UNIVERSITA' DEGLI STUDI DI VERONA

DEPARTMENT OF

Diagnostics and Public Health

GRADUATE SCHOOL OF

Natural Sciences and Engineering

DOCTORAL PROGRAM IN

Nanoscience and Advanced Technologies

Cycle / year XXXV/2019

POROUS SILICON: towards an optimized system for anticancer therapy

S.S.D. CHIM/03 - General and Inorganic Chemistry

Coordinator: Prof. Adolfo Speghini

Tutor: Prof. Nicola Daldosso

Doctoral Student: Dott.ssa Alessia Sambugaro

POROUS SILICON: towards an optimized system for anticancer therapy – Alessia Sambugaro
Tesi di Dottorato

ABSTRACT

Porous silicon (pSi) is a sponge-like material that is commonly obtained through electrochemical etching of a crystalline silicon wafer in hydrofluoric acid-based electrolyte medium. pSi particles of different size distribution can be obtained through fragmentation of the porous layer by means of ultrasounds or ball-milling. Due to quantum confinement effects, this material was discovered to be photoluminescent at room temperature The anodization technique produces a porosification of the material, resulting in elevated porosity, high surface-to-volume ratio and a large surface area, thus making pSi very attractive as a carrier in the perspective of drug loading and release in the field of NanoMedicine. Furthermore, the surface enables the binding of a broad range of different molecules (*e.g.*, polymers, drugs, dyes, magnetic nanoparticles, antibodies) leading to novel biomedical features, such as pH-responsiveness, magnetic properties and cell targeting. Its unique properties, together with biocompatibility, biodegradability and absence of immunogenicity, make this multifunctional platform perfectly suitable for nanomedicine applications that involve the delivery of drugs and the diagnostics.

This thesis work was aimed at developing novel strategies to improve the performances of pSi, starting from the achievements already accomplished, for applications in the anticancer therapy.

To do that, on the one hand surface modifications through coating and encapsulation (with polymers and cationic surfactant) as well as by decoration with magnetic nanoparticles were investigated. On the other hand, pSi particles were loaded with a variety of anticancer agents and tested on human cancer cell lines and cells of the immune system to explore their potential as valuable tools in support of clinically-established anticancer therapies.

Several experimental procedures have been successfully implemented, including magnetic nanoparticles decoration, surface charge modifications and coating with polymers with different properties. The prepared materials were thoroughly investigated by means of different techniques, among all photoluminescence spectroscopy, UV-Vis spectrophotometry, dynamic light scattering, HPLC, FT-IR. Several imaging techniques have been exploited, such as confocal microscopy, transmission

and scanning electron microscopy, optical microscopy and in vitro test were done also by means of biological assays.

The results here presented, associated with an acquired deep knowledge of the material, contribute to the improvement of a promising nanomedicine platform, adding a step towards its application in chemotherapy, immunotherapy and gene therapy.

TABLE OF CONTENTS

Introduction – Thesis presentation 8
CHAPTER 1 16
Nanomedicine against cancer 16
1.1. Passive and active tumor targeting 19
1.2. Drug delivery systems 22
CHAPTER 2 25
Porous silicon: basics, fabrication, functionalization and characterization 25
2.A. Background and introduction 25
2.A.1 Biodegradation 26
2.A.2 Fabrication 28
2.A.3 Surface modifications 32
2.A.4 Photoluminescence mechanism 33
2.B. Results and discussion 35
2.B.1 Fabrication and functionalization 35
2.B.2 Structural and optical characterization 39
2.B.3 Size reduction treatments 45
2.B.4 Surface charge modifications 49
2.B.5 Polymeric surface modification 53
2.C. Conclusions 63
CHAPTER 3 65
Porous silicon: infiltration with magnetic nanoparticles 65
3.A. Background and introduction 65
3.A.1 Magnetic resonance imaging: principles and contrast agents 65
3.A.2 Magnetic nanoparticles in diagnostics 69
3.A.3 SPIONs and porous silicon 72
3.B. Results and discussion 72
3.B.1 Preliminary investigations on commercial SPIONs in pSi 72
3.B.2 Iron oxide nanoparticles synthesis 76
3.B.3 Sonication treatments 79
3.B.4 Infiltration within porous silicon pores 82
3.C. Conclusions 88
CHAPTER 4 89
CHEMOTHERAPY 89
4.A. Background and aim 89

4.A.1 Chemotherapy drugs 89
4.A.2 Doxorubicin 89
4.A.3 Delivery of Doxorubicin 93
4.A.4 Porous silicon and doxorubicin 96
4.B. Results and discussion 98
4.B.1 Doxorubicin loading and release study 99
4.B.2 Coating with HA 101
4.B.3 In vitro cancer cell viability 104
4.C. Conclusions 115
CHAPTER 5 117
IMMUNOTHERAPY 117
5.A. Background and introduction 117
5.A.1 Dendritic cells 120
5.A.2 Pam3CSK4 123
5.A.3 Delivery of Pam3CSK4 125
5.B. Results and discussion 126
5.B.1 Preliminary investigations on porous silicon as drug delivery system 126
5.B.2 Pam3CSK4 loading and release study 133
5.B.3 Interaction with Human Dendritic Cells 137
5.C. Conclusions 148
CHAPTER 6 149
GENE THERAPY 149
6.A. Background and introduction 149
6.A.1 Porous silicon for gene delivery 152
6.B. Results and discussion 154
6.B.1 siRNA loading 154
6.B.2 Coating with HA and release study with a model drug 158
6.B.3 Co-delivery of doxorubicin and siRNA 160
6.C. Conclusions 164
CONCLUSIONS 165
Acknowledgements and collaborations 170
REFERENCES 171
Appendix A1: Characterization techniques 199
Appendix A2: In-vitro cellular studies 203
APPENDIX B 205

Introduction – Thesis presentation

Cancer stands as the second leading cause of mortality in the world (following heart diseases), according to the World Health Organization (WHO), and it is responsible for around 1 in 6 deaths globally with an estimation of more than 19 million new cancer cases diagnosed every year[1].

Depending on the diagnosis, on the tumor grade and on the general health situation of the patient, the current available approaches, administered alone or combined, are *surgery and radiotherapy,* also called “local treatments”, which are used to treat a specific tumor or area of the body and drug treatments (such as *chemotherapy*, *immunotherapy*, or targeted therapy) often called "systemic treatments" because they can affect the entire body. Alternative procedures, such as immunotherapy and gene therapy, during the last decade started to gain successful results, becoming in some cases approved and well-used medical practices. Targeted therapy is becoming more and more applicable although currently it is used for a limited number of tumors: this treatment exploits drugs or other substances to precisely identify and attack specific types of cancer cells, often labelled by molecular markers. For example, it can distinguish between healthy and cancer cells through identification of specific genetic alterations and thus inhibit tumor proliferation and cancer cells survival. Knowing this has led to the development of drugs that can selectively bind cell-cycle proteins, growth factors, modulators of apoptosis, molecules that promotes signaling or angiogenesis or enzymes. Targeted therapies can be carried out in several ways, among the others, angiogenesis inhibitors, monoclonal antibodies, proteasome inhibitors, signal transduction inhibitors. Moreover, stem cells and hormone therapies have been getting more and more attention in the last years.

However, nevertheless all the huge effort of medical research in finding and assessing new therapies, chemotherapeutic regimens are still in general the more effective in killing cancer cells. Their strength is commonly accompanied by many negative physical and mental implications, including weakened immune system, damage of healthy tissues and organs (e.g., cardiotoxicity) and depression, which are the result of their systemic and continuous administration. Another downside that threatens to hinder the therapeutic efficacy of anticancer treatments is multi-

drug resistance (MDR), a phenomenon, which usually occurs after multiple chemotherapeutic cycles, that causes a reduction of the efficiency of the anticancer drugs. Consequently, along with the standard treatments and combination therapies, both new drugs and new formulations based on drug delivery systems have been arising to overcome the present limitations. Besides the new approaches of precision medicine in cancer therapy, there is the need of new and more efficient ways to deliver chemotherapeutic drugs. Conventional drug delivery systems (e.g., syrups, tablets, capsules) are characterized by intrinsic limits such as poor bioavailability, non-regulated biodistribution, lack of control in the release of the drugs. Therefore, the development of tailored carriers in the nano scale have emerged to overcome the pharmacokinetics limitations related to the conventional drug administration routes.

The design of a nano-size carrier leads to many advantages:

- increased bioavailability and biodistribution
- help crossing the biological barriers
- enhanced tumor specificity
- lowered severe side effects by selectively administer the drugs to the targeted tumors
- protection of the drug from degradation
- overcame dose-dependent toxicity
- increased specificity against cancer cells

On the other hand, the alternative approaches of gene therapy and immunotherapy too often require the use of nanosystems to be able to properly work. The former because DNA molecules are not able to cross the cells membrane without a carrier, the latter to enable the delivery of immune cells and immunostimulatory agents to specific sites[2–4].

The currently available drug delivery systems, deeper discussed in the first chapter of this dissertation, can have different nature: organic materials (e.g., micelles, liposomes, exosomes, viral vectors, dendrimers), polymers, inorganic materials (e.g., metallic nanoparticles, iron oxide nanoparticles, carbona nanotubes, ceramics).

Among them, over the past decades, inorganic porous silicon particles have been demonstrated to have all it takes to be an optimal drug delivery system for cancer nanomedicine applications owing to its unique and outstanding properties. It is a

sponge-like material characterized by intrinsic porosity and photoluminescence. It can be produced by electrochemical etching of crystalline silicon wafers that produces nanostructures with large porosity, high surface to volume ratio and surface area, tunable pore size and photoluminescence (PL) at room temperature under UV excitation. PL emission wavelength depends on nanocrystal size and can be controlled as a function of the fabrication parameters. In addition, porous silicon features biocompatibility and easy biodegradation, absence of toxicity and chemical, mechanical and thermal stability, moreover, its surface can be chemically modified in order to bind different molecules or polymers, as well illustrated along this thesis work.

GOAL:

The topic of this thesis is the optimization of functionalized pSi particles as a drug delivery system for anticancer therapy, more specifically for chemotherapy, immunotherapy and gene therapy.

STARTING POINTS:

The achievements that have made the thesis studies feasible, reported in previous works, are:

(i) optimization of fabrication etching procedures[5,6]

(ii) surface functionalization with carboxylic and aminic groups was employed to stabilize the pSi properties in ethanol for long term conservation and to avoid degradation[5]

(iii) optimization of a size-reduction method based on ultrasounds[7]

(iv) biological stabilization with time was investigated to preserve photoluminescence in biological media: covalent attachment of organic (PEG and chitosan) and inorganic (TiO_2) coating was used for this purpose obtaining optical stability for over five months in aqueous media[8,9]

(v) preliminary drug and release tests in PBS were performed with Cbi (precursor of B12 vitamin) as drug test trial, that was efficiently loaded without losing its functionality and proved to be released with a slow rate[8]

(vi) evaluation of the interaction with human immune cells, resulting in neither toxic effects nor immunogenicity observed for the functionalized pSi microparticles

(vii) development of an easy, fast and cheap protocol to infiltrate SPIONs inside pSi pores for MRI applications[10].

MAIN THESIS ACHIEMENTS:

(i) Surface modifications that resulted in different performances of the material (i.e., negative to positive surface charge, pH-responsiveness, cancer cell targeting)

(ii) Infiltration of iron oxide nanoparticles which led to the addition of magnetic abilities to pSi particels

(iii) Immune response enhancement when mediating the internalization of an immunologic adjuvant by means of pSi particles

(iv) Improvement of the anti-proliferative effect of anticancer drugs when transported by pSi particles

(v) Co-encapsulation of a agene silencing agent and an anticancer drug

This thesis dissertation is organized in six chapters: the first three mainly talk about the material (porous silicon) description and its basics and optimized properties and the last three are dedicated to its applications in NanoMedicine in three different anticancer therapies: (i) chemotherapy, (ii) immunotherapy and (iii) gene therapy.

Besides the first introductory one, each of them is comprised of:

1) **a first introduction and review part** (*Background and introduction)* dedicated to the current state of knowledge of the subject,
2) **a second experimental part** *(Results and discussion)* dedicated to the empirical investigations and the achieved results in the thesis work.

Hereafter, a brief presentation of the contents of each chapter.

Chapter 1 – Nanomedicine against cancer, presents a brief but comprehensive introduction about drug delivery systems. The main properties and applications in

nanomedicine are presented and reviewed with an eye on anticancer therapy and the tumor targeting mechanisms associated with nanocarriers.

Chapter 2 – Porous silicon: basics, fabrication, functionalization and characterization, is a comprehensive section dedicated to the introduction of the material of this thesis: porous silicon. Starting from its discovery and from its interesting properties, both structural and optical, the main characteristics and fundamental studies along the years will be reviewed. In particular:

- Biodegradation routes in aqueous and basic media
- Fabrication procedures, how the parameters of the electrochemical process influence the product and the electrochemical mechanism,
- The most common surface modifications (i.e., oxidation, hydrosilylation and carbonization)
- Photoluminescence mechanism, the optical properties, with a special focus on the quantum confinement effect to explain the pSi light emission at room temperature.

The second half of the chapter deals with the experiments conducted within this thesis work to fabricate and functionalize the porous silicon microparticles and the post-functionalization procedures to reduce the average size and disaggregate the microparticles.

Two surface charge modification approaches by means of a cationic surfactant and poly-lysine, respectively are described.

It is then concluded with the optimization of the surface modification with two polymers to add new functionalities to the pSi platform, i.e., acetylated dextran that respond to pH variations and hyaluronic acid that targets the receptor CD44 over-expressed in certain cancer cells (prostate, lung, pancreatic and breast cancer).

Main goals achieved:

- Fabrication and functionalization (at Nanoscience Laboratory, University of Trento, Italy)
- Size reduction (at the facilities of University of Verona)

- Surface charge modifications with CTAB (at Biomedical Chemistry Laboratory, University of Verona, Italy) and poly-lysine (at Sailor's Lab, University of California San Diego, USA)
- Polymeric surface modifications with Acetalated Dextran (at Biomedical Chemistry Laboratory, University of Verona, Italy) and Hyaluronic acid lysine (at Sailor's Lab, University of California San Diego, USA)

Chapter 3 – Porous silicon: Infiltration with magnetic nanoparticles, starting from a previously optimized protocol that allows to add magnetic properties to pSi particles by decoration with commercial iron oxide nanoparticles, a further step forward along this direction was done by embedding the pSi carrier with self-produced iron oxide nanoparticles by means of pulsed laser ablation (degradation of iron bulk with a laser beam).

Main goals achieved:

- Synthesis of iron oxide nanoparticles (by NanoLaserLab, Pontifícia Universidade Católica do Rio de Janeiro)
- Magnetic infiltration of pSi (at Fluorescence Laboratory, University of Verona, Italy)

➔ **Publication**: A. Sambugaro, G. C. Concas, M. Gisbert, J. G. G. F. Paiva, T. Tahir, G. Perez, F. Enrichi, T. Del Rosso, N. Daldosso, *Light-emitting porous silicon decorated with magnetic iron oxide nanoparticles synthesized by Pulsed Laser Ablation* → Submitted.

In **Chapter 4 – Chemotherapy**, the first application studied within this thesis work in the anticancer therapy field is presented. The first part contemplates chemotherapy bright and dark sides: the success, the drawbacks and the successful solution that involves porous silicon particles. The second experimental part is dedicated to pSi as drug delivery system for the anticancer drug doxorubicin and a preliminary study with the antineoplastic drug docetaxel: loading, release, surface modifications. Investigated by means of dynamic light scattering photoluminescence spectroscopy, UV-vis spectroscopy and HPLC. It is concluded with in vitro cytotoxicity investigations on two different cancer cell lines (prostate and non-small lung cancer

cells) showing that the use of pSi as carriers lower the viability of the treated cells compared to the free drug.

Main goals achieved:

- Loading of doxorubicin and docetaxel (at Biomedical Chemistry Laboratory, University of Verona, Italy)
- Coating with hyaluronic acid (at Biomedical Chemistry Laboratory, University of Verona, Italy)
- Cytotoxicity investigations resulting in a general higher antiproliferation effect when delivering the drug by pSi (at Biomedical Chemistry Laboratory, University of Verona, Italy)

➔ **Publication**: Manuscript in preparation.

Chapter 5 – Immunotherapy. After a brief introduction about immunotherapy and the methods and the role of the dendritic cells in the mediation of the immune response, the chapter continues with the new (so far never reported in the literature) experimental results regarding the coupling of functionalized pSi microparticles with the toll-like receptor agonist Pam3CSK4 as immunotherapy adjuvant delivery system. This comprises loading and delivery study of the molecule, an extensive live-cell uptake analysis by means of confocal microscopy and the immunologic response evaluation of dendritic cells stimulation through quantification of the released cytokines by ELISA test.

Main goals achieved:

- Loading of Pam3CSK4 (at Department of Medicine, Division of General Pathology, University of Verona, Italy)
- Enhancement of the cytokines release when using pSi to deliver Pam3CSK4 to dendritic cells (at Department of Medicine, Division of General Pathology, University of Verona, Italy)
- Time-lapse confocal imaging allowed to follow the internalization by dendritic cells and their consequent morphological modifications (at CPT facilities, University of Verona, Italy)

➔ **Publication**: A. Sambugaro, M. Donini, E. Chiste', M. Scarpa, S. Dusi, N. Daldosso, *Porous silicon microparticles as efficient carriers for immunologic adjuvants* → Submitted.

The third example of pSi as drug delivery system for anticancer therapy: gene therapy is the topic of **Chapter 6 – Gene therapy**. This medical approach is briefly reviewed and the available paths to carry it out and the relationship between the gene silencing tool small-interfering RNA (siRNA) and porous silicon particles discussed. The experimental part consists in a preliminary study regarding the encapsulation of siRNA within porous silicon particles by means of a calcium-silicate shell precipitation and the coating with hyaluronic acid. Moreover, it is reported a first encapsulation study involving the co-delivery of siRNA and doxorubicin.

Main goals achieved:

- Encapsulation of siRNA by calcium silicate precipitation method (at Sailor's Lab, University of California San Diego, USA)
- Coating of siRNA-loaded pSi particles with hyaluronic acid (at Sailor's Lab, University of California San Diego, USA)
- Co-loading of siRNA and doxorubicin followed by coating with hyaluronic acid through layer-by-layer method (at Sailor's Lab, University of California San Diego, USA)

➔ **Publication**: Manuscript in preparation.

In the **Conclusions**, the main obtained results and the future perspective are summarized.

CHAPTER 1

Nanomedicine against cancer

Nanomedicine has been extensively studied during the last decades with the aim of exploiting the peculiar properties of the nanomaterials/nanosystems (i.e., materials characterized by nanometric structures) to the prevention and treatment of health diseases by developing novel therapeutic and diagnostic tools[11]. The idea of nanotechnology was introduced for the first time by the Nobel laureate, Professor Richard Feynman in 1959, during his famous lecture "There's Plenty of Room at the Bottom", when he encouraged the researchers to investigate at the molecular level and beyond[12]. Nanomaterials have been gained a lot of attention because at the nano-size their properties undergo interesting changes, resulting in, for example, modification of the melting point, super magnetism, photoluminescence in semiconductors, thermal conductivity, increased surface to volume ratio, enhanced mechanical strength[13–15].

Nanomaterials can find applications in the field of medicine as drug delivery systems (DDS). Drug delivery refers to the mechanism of transportation of a therapeutic substance into the body with the aim of overcoming pre-existent drawbacks related to conventional therapies (e.g., prolonging the drug efficacy, avoiding its degradation, minimizing the side effects) and imaging techniques.

The advantages of using nano-sized materials to deliver conventional and novel drugs are countless: they have the ability to transport and deliver large amount of payloads to selective targets, they can help enhancing the solubility of hydrophobic molecules and the stability in physiological conditions, reduce side effects related to systemic administration, improve the pharmacokinetics, they can be traced and used as advanced contrast agents[16]. Figure 1.1 shows the applications of nanomaterials in medicine.

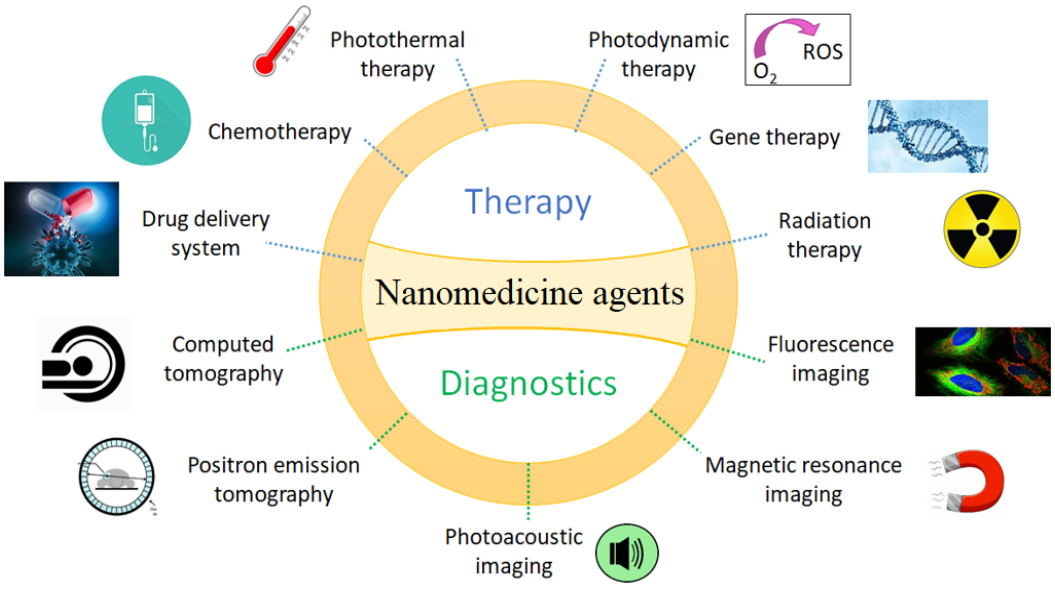

Figure 1.1. Examples of nanomaterials applications.

From the first nanodrug approved in 1995 to nowadays, the increasing number of publications, clinical trials and FDA-approved products reflects the growing interest in these materials. A first generation of nano-based systems has already been approved for the clinics as diagnostic and anticancer therapy tools, some examples are reported hereafter, while the second generation of nanomedicine systems is already under clinical evaluation and their demand is expected to keep growing[17,18] .

- Doxil®, the first nanocarrier-based drug approved by FDA in 1995 for the delivery of the anticancer drug doxorubicin by means of liposomes, was able to enhance the blood half-life of the drug from 5 minutes to 72 hours. This increased the tumor accumulation thus allowing the administration of a reduced amount of drug which benefits the patients by decreasing the risk of severe side effects such as cardiotoxicity[19].
- Abraxane® is another example of a nano-system that enabled the administration of a lower amount of the anticancer drug, in this case paclitaxel, by increasing its solubility. This albumin-based nanodrug was approved by FDA in 2005 for the treatment of metastatic breast cancer. The delivery of a reduced amount of drug (by 85%) resulted in lower side effects such as of hypersensitivity[20].
- An example di polymer-based nanodrugs is Oncaspar®, a PEGylated formulation of the enzyme L-asparaginase that is used for the treatment of

acute lymphoblastic leukemia. The combination with the polymer resulted in a prolonged circulation and retention time of the asparaginase, reduction of renal clearance and proteolysis and diminished side effects such as hypersensitivity[21].

- Approved nanosystems can also find application in diagnostics, Sinerem® and Endorem®, for example, are based on super paramagnetic iron oxide nanoparticles (SPIONs) coated with the polymer dextran, that demonstrated high biocompatibility and absence of cytotoxicity or inflammation. Moreover, they can target macrophages in arthritic joints, track T-cells and detect myocardial infarct and liver lesions[22].

The oncological sector, in particular, is the one that has gained more attention, both from an academic and industrial point of view, for the research and clinical translation of nanomedicine products.

Cancer, indeed, stands as the second leading cause of mortality in the world (following heart diseases), according to the World Health Organization (WHO), and in 2020 it was responsible for around 10 million deaths (nearly 1 in 6 deaths globally) with an estimation of more than 19 million new cancer cases diagnosed in the same year[1]. In terms of new cases, the most frequently diagnosed cancers are breast (2.26 million), lung (2.21 million), colorectal (1.93 million), prostate (1.41 million), skin (1.20 million) and stomach (1.09 million). While the most common causes of cancer deaths are lung (1.80 million deaths), colorectal (916.000), liver (830.000), stomach (769.000) and breast (685.000)[23].

Generally, cancer arises from the genetic mutation of normal cells that evolve into tumorigenic cells through a multistage, rapid and uncontrolled proliferation that leads from a pre-cancerous lesion to a malignant tumor. The tumor pathogenesis is the result of the interaction of several factors: genetics and age, lifestyle (e.g., alcohol and tobacco consumption, diet, physical activity), chemical (e.g., asbestos, water and air contaminants) and physical (e.g., ultraviolet and ionizing radiation) but also biological (i.e., infections from viruses, bacteria or parasites) carcinogens. Therefore, the way to contribute to prevent and reduce its incidence is to avoid as much as possible the risk factors and through early detection diagnosis and

screening[1]. Figure 1.2 summarizes the intrinsic and extrinsic events that might potentially lead to the tumor's formation.

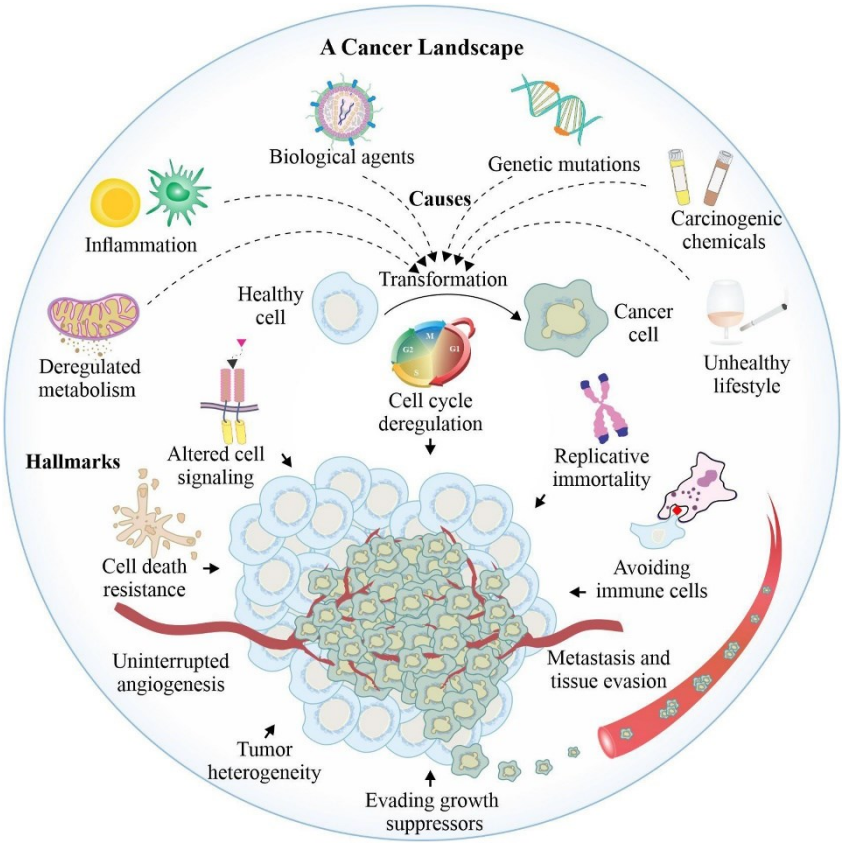

Figure 1.2. Schematic representation of the multiple factors that might lead to the transformation of a normal cell to a cancer cell and its different hallmarks[24].

Depending on the diagnosis and on the general health situation of the patient, the current available approaches are surgery, radiotherapy, gene therapy, immunotherapy and chemotherapy, and/or their combination. In this context, the presence of the already approved nano-drug delivery systems for anticancer therapies is already benefitting a number of patients, however, despite the progress made they are not applicable to every condition and are mostly administered systemically.

1.1. Passive and active tumor targeting

After the intravenous injection, in order to efficiently exert their functions, DDS not only have to transport and protect the payload from degradation, but they also need to be able to release their cargo only into the desired target, i.e., in the case of anticancer therapy DDS, into the tumor site, to avoid undesired systemic toxicity and

severe side effects. The tumor targeting associated with nanocarriers is correlated to controlled release of the payload, higher tumor-specificity, enhanced cellular uptake, improved pharmacokinetics and reduced systemic toxicity. The tumor targeting can be either passive or active.

Passive tumor targeting, commonly known as enhanced permeability and retention (EPR) effect, is a phenomenon, that was reported for the first time by Matsumura and Maeda in 1986, that consists in the progressive accumulation of macromolecules and nanoparticles (NPs) in the solid tumor vascularized area that leads to their retention into the tumor tissue[25]. To understand why this phenomenon occurs it is necessary to explain how the solid tumor growth works. A representation of the differences between healthy and tumorigenic tissues is shown in Figure 1.3.

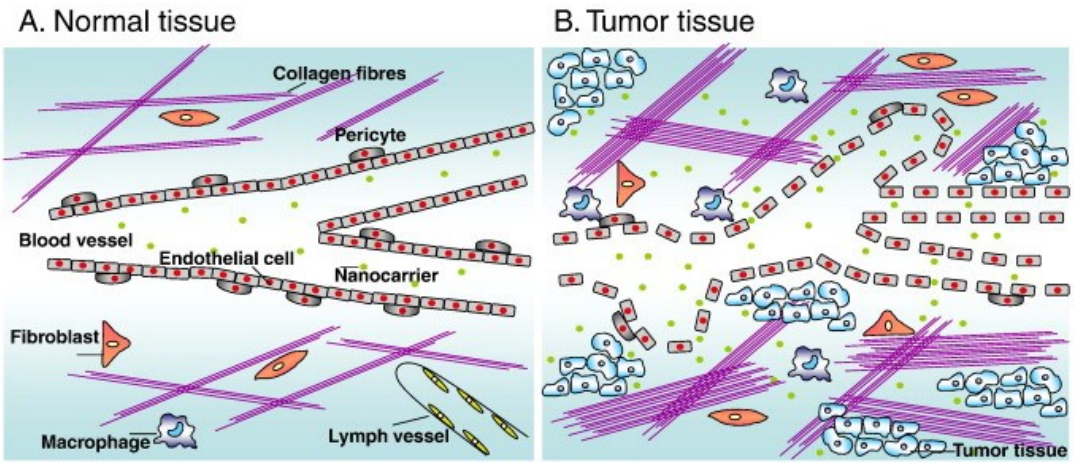

Figure 1.3. Differences between healthy (A) and tumorigenic (B) tissues[26].

Contrarily to the healthy tissues, due to the increased secretion of vascular epithelial growth factors and proangiogenic signals tumor that continuously stimulate the angiogenesis, the tumor blood vessels is characterized by irregular endothelium, disrupted basement membrane and lower amount of adjacent pericyte that results in higher permeability of the vascular walls. Thanks to this, the size of the inter-endothelial fenestrations can vary between 10 and 1000 nm, thus allowing the extravasation of macromolecules and carriers with appropriate size into the interstitial space, that, once entered into the tumor tissue, will be trapped for a prolonged time[26].

Although the majority of the nanosystems approved for the clinics rely on passive targeting, they encounter some limitations that are related to the tumor type and size, on the degree and heterogeneity of tumor vascularization and on the tumor site. Therefore, active targeting can provide a higher efficiency of the nanocarrier function[27]. Figure 1.4 reports a representation of the different mechanisms of passive and active targeting.

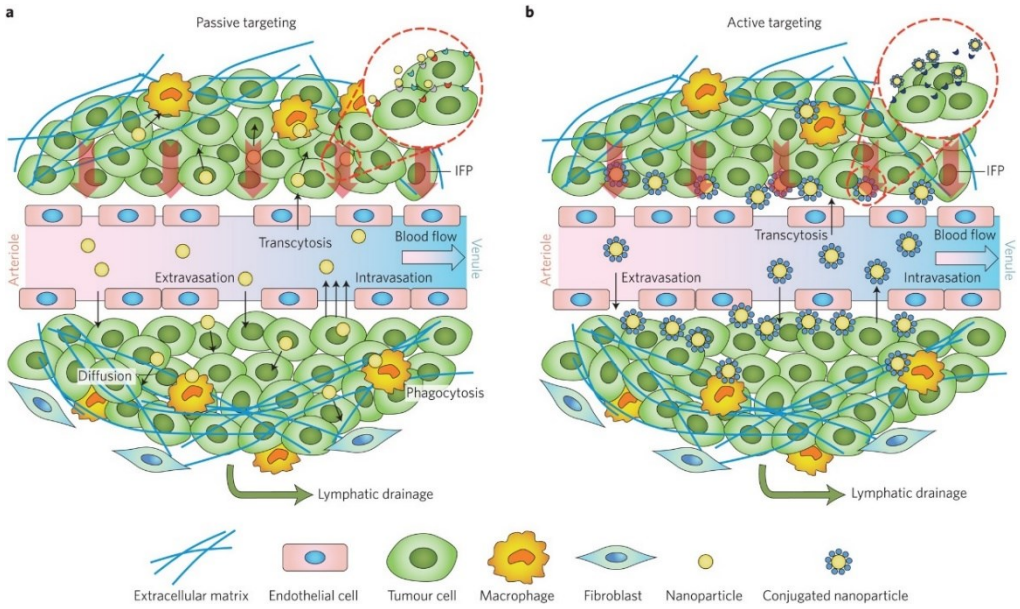

Figure 1.4. Schematic representation of passive (a) and active (b) targeting mechanisms[27].

In active tumor targeting the surface of the nanocarriers is functionalized by ligands that are able to recognize and bind tumor-associated receptors (e.g., CD44, HER2, folate receptor), biologically active surface molecules (e.g., growth factor receptors, cytokines receptors, cell-adhesion molecules) that are specifically overexpressed on the surface of tumor cells or part of the tumor microenvironment and not on healthy cells. Through this approach nanocarriers are on one hand able to selectively accumulate at the targeted tumor site and on the other to improve the internalization[28]. As it is possible to notice from the inset of Figure 1.4, in passive targeting (a) the nanosystems non-specifically interact with cell membrane receptors and are able to accumulate inside the tumor through the leaky vasculatures. On the contrary, in active targeting (b) the nanocarriers are usually conjugated with targeting ligands therefore they can recognize the tumor cells by binding specific cell membrane receptors resulting in a prolonged presence around the targeted cells[27].

However, the ligand-mediated targeting must rely anyway onto the EPR effect because to reach the receptors the nanocarriers need to be able reaching the cancer cells and thus accumulate into the tumor tissue. There are several targeting moieties available that can be selected to achieve the desired therapeutic effect improving targeted tumor accumulation, such as: antibody fragments and monoclonal antibodies, nucleic acid ligands (e.g., dendrimers), small molecules (e.g., transferrin and folic acid), peptides and proteins, and polysaccharides (e.g., hyaluronic acid). In addition, there are other parameters that might influence the cancer cell uptake, including homogeneous expression of the receptors in all the targeted cells, density of the targeting ligand, but also size, surface charge and shape of the nanocarrier[29,30].

1.2. Drug delivery systems

In this regard, the nature of the nano DDS influences the size, shape and surface charge and it can either be organic or inorganic[31].

The organic materials include:

- Lipidic nanomaterials (e.g., liposomes, micelles), partially hydrophilic and partially hydrophobic, this allows the entrapment of hydrophobic drugs through exposure of the hydrophilic part towards the aqueous media[32].
- Dendrimers, low viscosity branched globular macromolecules composed of a central hydrophobic monomers structure and functionalized peripheral branched hydrophilic groups. They are very versatile and can be functionalized in several ways[33].
- Polymers (e.g., PLGA, PEG and hydrogels, polymeric micelles), can be natural or synthetic, their shape varies from nanospheres, to nanosponges, or nanofibers and they are able to encapsulate hydrophobic molecules[34].
- Exosomes, biologically active cell membrane vesicles involved in cell-cell communications that can be isolated from the extracellular fluid and loaded with drugs[35].

While among the inorganic nanomaterials it is possible to find:

- Quantum dots, semiconductors nanocrystals, whose photoluminescence is tunable as a function of size and composition[36].

- Metallic, e.g., gold NPs can be produced in different shapes (nanospheres, nanocages, nanostars, nanorods), thus showing different optical and photothermal properties. They can be used as contrast agents in computed tomography (CT)[37].
- Magnetic, e.g., iron oxide NPs show strong magnetic properties therefore are useful for diagnostics (contrast agents for MRI), hyperthermia treatment, magnetic separation, drug de-livery and biosensors[22].
- Ceramic materials, e.g., mesoporous silica can be characterized by different porosity, shape and size by varying the synthesis procedure, moreover, they have an easily tunable surface[38].
- Carbon nanotubes, single or multiple concentric cylinders of graphene able to stimulate the neuronal growth and to increase the electrical signal in neural and cardiac cells. Moreover, their absorption in the NIR region, enables their application in imaging or PTT (photothermal therapy) and photothermal ablation (PTA) to ablate cancers cells[39].

Figure 1.5 shows an overview of the parameters (composition, physical characteristics, surface modifications, targeting ligands) that have to be taken into consideration when developing a nanomedicine carrier.

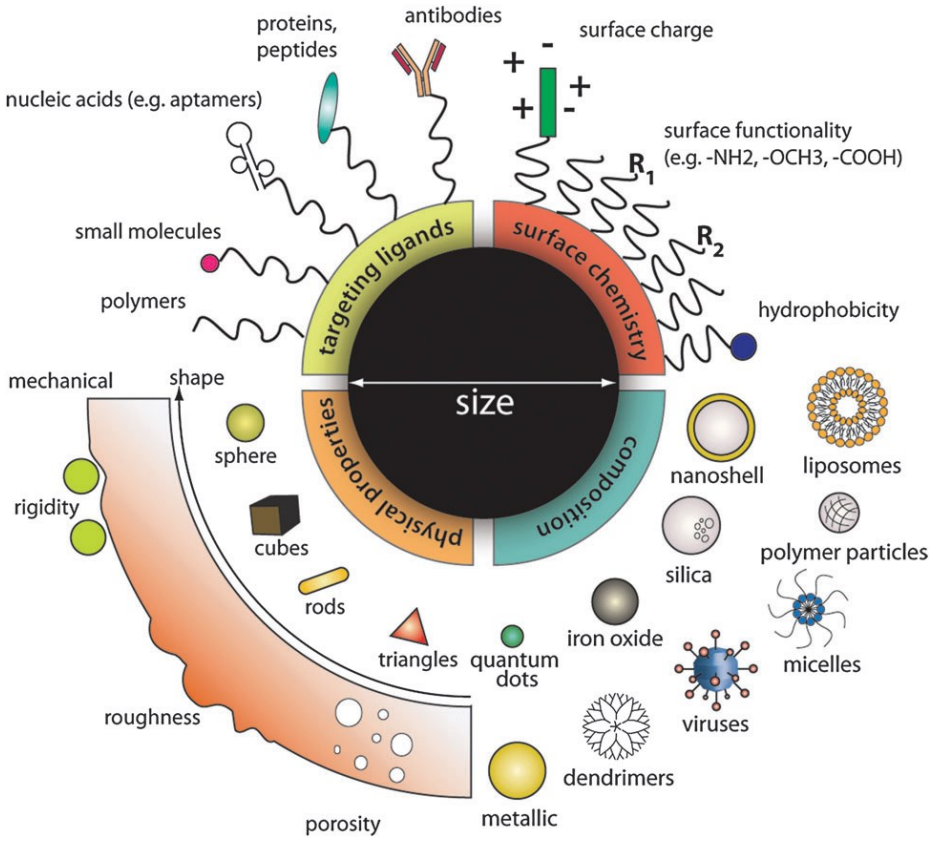

Figure 1.5. Schematic representation of the possible combinations for the development of DDS[31].

Among all the nanomaterials, inorganic porous silicon (pSi) has gained more and more attention for drug delivery and imaging applications thanks to its unique combination of properties such as intrinsic photoluminescence, porosity, biocompatibility and biodegradability, absence of toxicity and tunable surface. The main focus of this thesis work is related to the study and development of pSi-based drug delivery systems for the treatment of cancer. Starting from pSi production, properties and surface modifications (discussed in the next chapter) and continuing with the investigation of its possible application as diagnostic contrast agent (Chapter 3) and drug delivery system (Chapters 4, 5 and 6).

CHAPTER 2

Porous silicon: basics, fabrication, functionalization and characterization

2.A. Background and introduction

Porous silicon (pSi) was accidentally discovered in 1956 by Arthur Uhlir Jr. and Ingeborg Uhlir at the Bell Laboratories[40]. Indeed, while they were investigating the effects of the electrochemical polishing on crystalline silicon wafers in hydrofluoric acid solutions, they noticed the formation of a dark layer on the surface of the wafers that will then be named porous silicon (pSi). However, it was not until 1990, when Professor Leigh T. Canham first identified the photoluminescence at room temperature[41], and later demonstrated its biocompatibility in vitro[42], that this interconnected pSi wires started to gain interest first in photonics and then in the biomedical field. This was a milestone discovery because, being bulk silicon an indirect band gap semiconductor with a small energy gap, it went from being an inefficient absorber of light to a light-emitting material at room temperature. Due to the remarkable pioneering work of Prof. Canham, the number of scientific publications per year regarding pSi increased from just 10 in 1990 to 380 in 2022 (PubMed® database). Figure 2.1 shows the sponge-like structure of pSi with a schematic representation in panel (a) and a TEM image in panel (b).

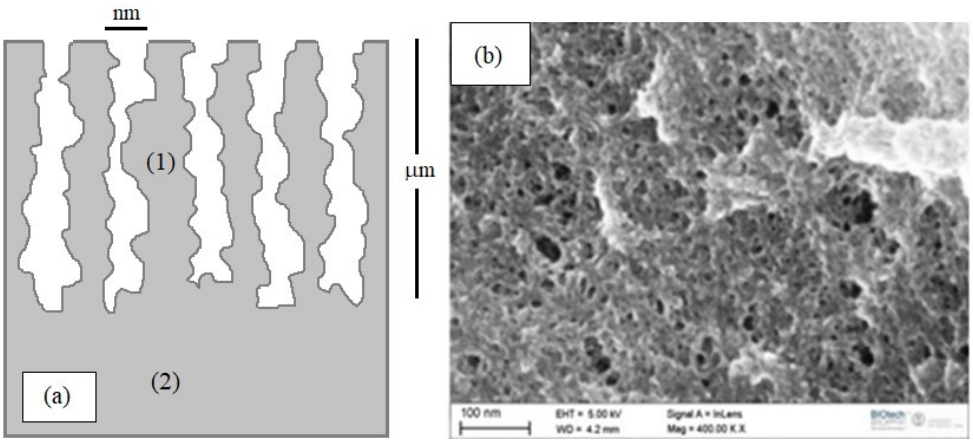

Figure 2.1 Porous silicon. Panel a: schematic picture of porous silicon (1) on a bulk silicon layer (2). Panel b: porous silicon typical sponge-like structure (100 nm scale)[43].

Over the last decades, pSi gained more and more attention as a system functional in nanomedicine applications such as optical biosensors, tissue engineering, biomolecular screening, but, most of all, as a drug delivery system[44,45].

The interest around pSi resides in its outstanding physicochemical and biological properties such as:

- large surface-to-volume ratio
- high surface area (up to 800-1000 m^2/g)
- tunable pore volume (around 0.9 cm^3/g) that allows to carry a large amount of different molecules
- high thermal, mechanical and chemical stability
- excellent biocompatibility and easy biodegradation
- low toxicity
- tunable surface that can be modified with different functional groups, polymers, molecules or targeting features to control the release of the payloads with a high selectivity for specific cells, organs or tissues, luminescence, biocompatibility and biodegradability[46–48].

In this regard, our group has been working for years to optimize and implement new functionalities to pSi particles. In particular, this thesis work is meant on one hand to investigate and improve the current properties and on the other to combine new features to this platform, through chemical and surface modifications, in order to exploit it as a tool in nanomedicine, especially as a drug delivery system for anticancer therapies (chapters 4, 5 and 6).

2.A.1 Biodegradation

Biodegradability and biocompatibility are two of the most relevant features of pSi for its application in the nanomedicine field. The in vitro biocompatibility was reported for the first time by Prof. Canham in 1995, who demonstrated the ability of pSi films to stimulate the growth of hydroxyapatite and associated the bioactivity of the material with the pore morphology, leading to its potential application for tissue engineering[42]. Since then, the biocompatibility and biomedical applications of pSi were extensively studied together with its immunologic compatibility and inflammatory response[49], not only in vitro but also in vivo[50–52]. For example, Cheng *et al.* investigated the toxicity and degradation of pSi microparticles for intraocular

drug delivery demonstrating that the material was stable and biocompatible[53]. Salonen and Foraker *et al.* proved the ability of pSi microparticles to carry and efficiently deliver drugs with low solubility in water through intestinal cells[54,55]. Park *et al.* demonstrated that after 8 hours in PBS pSi NPs were completely degraded, moreover, they tested pSi NPs in vivo in BALB/c mice proving that after 4 weeks they were completely cleared from the body via renal excretion[56].

The reason why pSi is easily and safely degraded in aqueous environment is clear by looking at the reaction of SiH_4 with water:

$$SiH_4 + 2H_2O \rightarrow SiO_2 + 4H_2$$

$$SiO_2 + H_2O \rightarrow Si(OH)_4$$

In aqueous media silicon hydrides are firstly oxidized, then Si-O bonds undergo through hydrolysis that degrades the silicon oxide to orthosilicic acid ($Si(OH)_4$), which is naturally absorbed by the body and can be found in several tissues and it is spontaneously excreted by renal clearance through urines[57].

Moreover, the oxidative hydrolysis of pSi is catalyzed by OH^-, a good nucleophile, therefore its dissolution rate increases as the pH becomes more basic, following the simplify reaction below:

$$Si + 2OH^- + 2H_2O \rightarrow [SiO_2(OH)_2]^{2-} + 2H_2$$

The doubly protonated form of silicic acid is one of the soluble species of silicon oxide and it is present when the media is highly basic (pH >12). Indeed the first and the second ionization constants (pKa) of $Si(OH)_4$ (the fully protonated water-soluble specie) are around 10 and 12, respectively, therefore, in acidic or neutral solutions the predominant form is $Si(OH)_4$[58].

It was demonstrated by Tzur-Balter *et al.* that when pSi is close to cancer cells its degradation is enhanced because of the upregulation of ROS present in the tumor microenvironment that, by oxidizing the Si, makes the degradation faster. This is particularly useful when using pSi as an anticancer drug delivery system, because while the carrier is being degraded the drug is released and able to attack the tumor[59]. In this regard, given the easy degradation of pSi in alkaline media, when there is the need to quantify the amount of loaded molecules inside its pores, the

popular method is to disperse the particles in a basic solution, such as potassium hydroxide (KOH). The dissolution frees the drug from the porous matrix enabling its quantification through appropriate technique[58].

2.A.2 Fabrication

Porous silicon can be produced by either a bottom-up or a top-down approach. The former involves physical and mechanical processes that create the pores by combining Si clusters with intermediated voids. The latter utilizes chemical and physical processes that, through porosification of a crystalline structure, create the pores. The available methods to produce pSi are more than thirty, either through wet or dry etching, through thermal or mechanical processes, through deposition or conversion reactions and they can lead to obtain macro (more than 50 nm pore size, panel c), meso (between few nm and 50 nm, panel b) or micropores (lower than few nm, panel a). (Figure 2.2)[60].

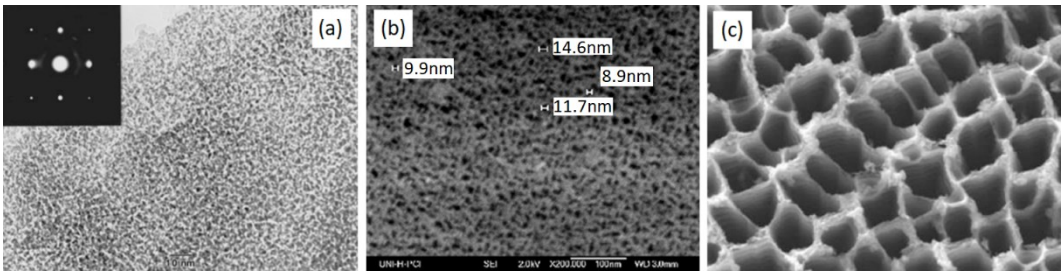

Figure 2.2. Examples of microporous (a), mesoporous (b) and macroporous (c) structures of porous silicon layers[61].

The most common way to fabricate pSi is through anodization, which is a top-down approach, that consists in the electrochemical etching of a crystalline silicon wafer in a hydrofluoric acid (HF) solution. To this purpose, a silicon wafer is placed inside an electrochemical cell: one side is in direct contact with one electrode, the anode, typically a conductive metal, and the other is separated from an electrolyte solution with the second electrode, the cathode, that usually consists in a platinum wire. The representation of a general anodization setup with the oxidation and reduction reactions happening at the electrodes is shown in Figure 2.3.

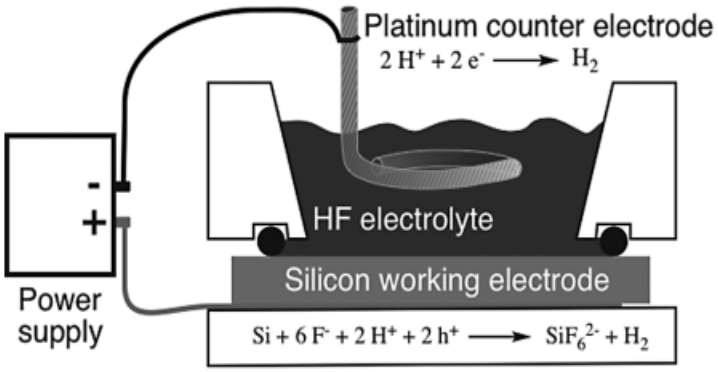

Figure 2.3. Schematic representation of an electrochemical cell and the reactions occurring at the two electrodes[58].

The presence of two electrodes is fundamental to close the electrical circuit and to keep the charge neutral: the anode removes electrons from the solution, while the cathode supplies electrons to it. Therefore, inside the electrochemical cell there are at least two reactions happening at the same time: an oxidation at the anode and a reduction at the cathode.

The flowing of the current through the HF solution partially dissolves the exposed silicon surface leading to the formation of a porous layer. Depending on the electrolyte solution, the wafer dopant, the crystallographic orientation, the temperature, the current density and the reaction time, it is possible to obtain different porosity, thickness and pore size. The mechanism of the electrochemical reaction is shown in Figure 2.4.

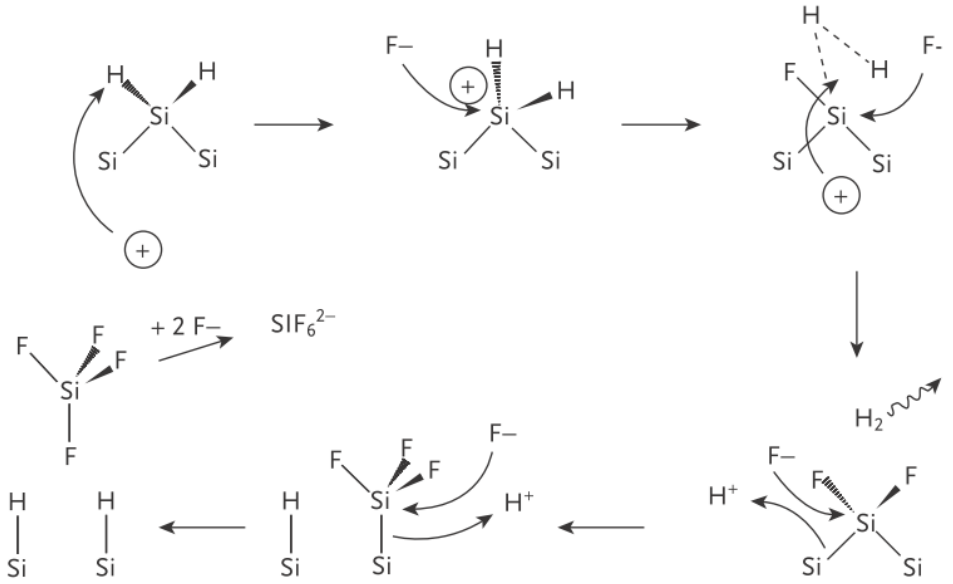

Figure 2.4. Electrochemical mechanism of the crystalline silicon wafer surface in HF solution during anodization[58].

As soon as the silicon wafer is in contact with the HF solution, the oxides on the silicon (Si) surface start to dissolve and the hydrogen atoms (H) take their place. Given the competition between the formation of Si-F, Si-H and Si-O bonds during the electrochemical corrosion, there will be a continue exchange between fluorine atoms (F) and H (Si-O only forms if the oxides are generated so fast they do not allow the attack of F, e.g., during electropolishing). When the first Si-F bond is formed it will be easily attacked by other two F atoms and then immediately removed from the surface, leaving the Si surface predominately bounded by hydrides species. This might sound strange because the Si-F bond is the most thermodynamically stable in the silicon chemistry. However, the H is less electronegative of F, consequently the Si-H bond is less susceptible, compared to Si-F, to be attacked by a nucleophile, thus its preferential formation. At the end of the electrochemical etching process there will be Si-H, SiH_2 and SiH_3 at the surface[58].

By changing the fabrication parameters such as current applied during the etching, the etch time and current density it is possible to control the pore size, thickness and porosity, respectively (Figure 2.5).

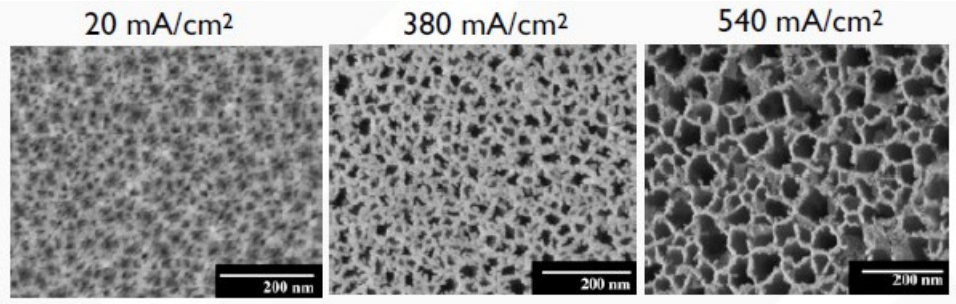

Figure 2.5. Influence of the current density on the morphology of porous silicon (image from Sailor et al.[62]).

The morphology of the final material depends also on:

- the electrolyte composition (e.g., ethanol, acetic acid, surfactants) and the hydrofluoric acid concentration: the higher is the HF concentration, the smaller are the produced pores
- the dopant of the wafer and its concentration[62]: the pores grow in the crystallographic directions, for n-type wafer, while in the current lines for the p-type wafers

In particular, porosity increases with current density, etching time and n-type wafer doping; it decreases with HF concentration and p-type wafer doping.

When obtained through electrochemical etching, the surface area can be as high as 800 m^2/cm^3, the pore size usually has a broad distribution between 3 and 20 nm (until 50 nm in some cases) and the porosity can vary from 20% to 95%. For p+-type Si <001> wafer the pores are formed towards the 001 direction, perpendicularly to the wafer surface, with a branched "fir tree" configuration[63].

The anodization procedure used to fabricate porous silicon during this thesis (deeply discussed in the next section of this chapter) allows to obtain mesoporous layers on the top of the p-type crystalline wafers, with an average diameter of 10-30 nm. After the electrochemical etching, pSi microparticles can be obtained by sonication or ball-milling, that fractures and disaggregates the porous silicon layer formed on the top of the Si wafer. This procedure can influence the size distribution, which is characterized by a fragments polydispersion with random size and shape, therefore, to solve this issue, it can be applied a sieving procedure with the mesh dimension dependent on the application[54]. The most common size-reduction techniques are reviewed in the following sections of this chapter.

2.A.3 Surface modifications

The hydride species present on the surface of a freshly etched pSi are unstable and highly reactive thus easily susceptible to oxidation and hydrolysis in air and water solutions. This is a fundamental issue to be addressed to get the success of pSi as a drug delivery system; therefore, an appropriate and controlled surface functionalization is needed to stabilize the material. The most common surface modification reactions are oxidation, hydrosilylation and carbonization[64].

- Oxidation: can be chemical, thermal or anodic[65–67].
  (i) Chemical one occurs either in water or by reagents such as H_2O_2, ozone, dimethyl sulfoxide (DMSO), pyridines, ketones, aldehydes, and creates a thin oxide layer on the surface.
  (ii) Thermal oxidation can be done either in air on in controlled atmospheres. By heating the samples between 60 and 100 °C Si-H are replaced by Si-O and Si-OH and at around 900 °C the surface is completely oxidized. With this method, the high temperature enables the introduction of oxygens atoms also within the Si-Si backbone leading to the formation of also Si-O-Si and $-O_ySiH_x$.
  (iii) Anodic oxidation is obtained by means of etching in acid solution (e.g., sulfuric acid).

  Oxidation treatments are often followed by further functionalization. Common reactions involve silanol-chemistry, for example by using (3-aminopropyltriethoxysilane) APTES or 3-aminopropyldimethylethoxysilane (APDMES) it is possible to introduce $-NH_2$ groups on the surface[68].
- Hydrosilylation: is a method used to stabilize the as-etched surface of pSi. Hydrides on the surface react with unsaturated molecules that can contain alkene (C=C), alkyne (C≡C) or carbonyl (C=O) groups that will result in Si-C-C, Si-C=C, Si-C-O, respectively. This reaction is catalyzed by thermal or light (white and UV) radiation or by Lewis's acids. This reaction allows additional functionalization at the end of the aliphatic chain[69–72].
- Carbonization: can be thermal or hydrothermal and involves the treatment of the as-etched pSi surface with acetylene at high temperatures.

(i) Thermal (TCPSi), consists in fluxing acetylene over 700 °C resulting in the formation of Si-C species and the removal of all the H obtaining a completely hydrophilic surface.

(ii) Hydrothermal (THCPSi), can be produced by pyrolysis of acetylene below 650 °C obtaining Si-C and Si-CH species on the surface which hydrophobic degree will depend on the temperatures and the amount of acetylene. If the pSi is subsequentially reacted with undecylenic acid at 120 °C (UnTHCPSi) it is possible to obtain carboxylic groups on the surface similarly to the hydrosilylation[73,74].

2.A.4 Photoluminescence mechanism

As mentioned at the beginning of this chapter, the discovery of the photoluminescence (PL) at room temperature was the event that catalyzed the research around porous silicon. There are four bands present in the emission spectrum of porous silicon, the photoluminescence can be observed from the UV to the near-infrared[75]:

- UV-band (350 nm, ps-ns) has been detected only in oxidized pSi and it has been connected to defective oxidized states;
- F-band (420-470 nm, 10 ns) in the blue-green region, it has been commonly observed in thermally or chemically oxidized samples and it has been related to contaminations by organic chromophores;
- S- band (400-1300 nm, 150 μs-ns for hydrogen-terminated surface and 590-1300 nm, μs range for surface with oxygen atoms) it is tunable depending on the condition of the fabrication of the sample. It has been attributed to the quantum confinement in nanocrystals, to the porosity and to the size distribution;
- IR-band (110-1500 nm, 10 μs - 10 ns), it has been found in absence and in presence of oxidized surfaces and associated to quantum-size effect. It increases at low temperatures.

Concerning the mechanism, for many years it was debated how the phenomenon was originated. The first model, based on the quantum confinement effect, attributed the tunable visible PL to the reduction of the dimensions (i.e., from crystalline to a skeleton of nanocrystalline silicon)[75]. Many other alternative models were proposed in the past based on the presence of hydrogenated amorphous

silicon, surface hydrides, siloxane, surface state and defects (based on the emission coming from carriers present at extrinsic centers on the pSi surface)[76,77].

Being crystalline silicon an indirect bandgap semiconductor, its radiative recombination probability, and thus the emission, is very low and in the infrared region[76]. Indeed, for the transition of an electron from the conduction band to the valence band there is not only the need of an available electron-hole pair but also of a phonon, making the process slow[78]. Crystalline bulk silicon, therefore, cannot be considered an ideal light-emitting material. However, when the size of the crystalline silicon is reduced to nanocrystalline, the edges of the conduction and valence bands gradually shift towards the center resulting in an increased bandgap (from 1.17 eV to more than 1.5 eV) thus improving the radiative transition rate without the need to be assisted by a phonon[41,43]. The PL is a consequence of the recombination of electrons and holes that are quantum-confined inside the nano-sized structures. A reduction in the dimensions shifts the PL towards lower wavelengths and enhance the energy of the electrons, which, being spatially confined, are easier to be excited to the conduction band. Structural and morphological analysis have proved the linear relationship between PL emission and nanostructured size. The main effects of quantum confinement are PL upshift and tunability, high quantum efficiency, also at long radiative lifetimes, and variation of the PL with the temperature.

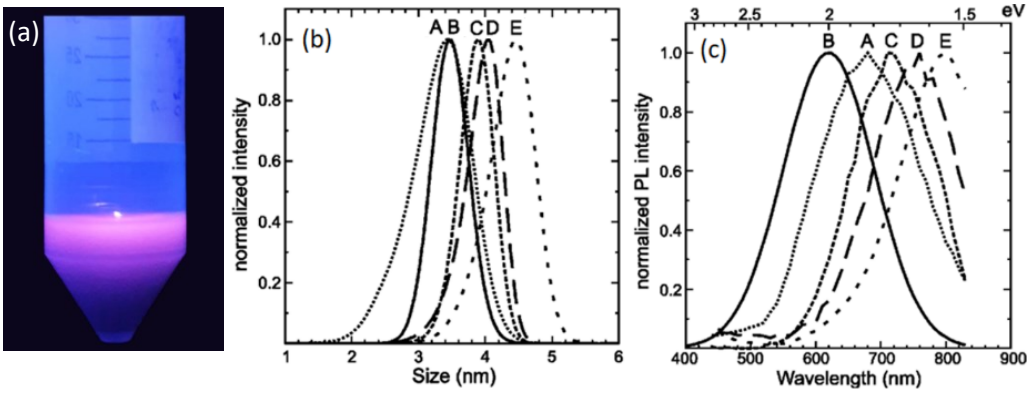

Figure 2.6. Visible PL emission of a pSi dispersion under UV excitation (panel a). Relation between size distribution of nanocrystals (panel b) and relative normalized photoluminescence spectra (panel c)[79].

From the picture in panel (a) of a pSi suspension excited by a black light it is appreciable the photoluminescence. By comparing the size distribution in panel (b)

with the emission spectra in in panel (c) it is possible to notice the clear correlation between the two of them: the larger the size, the higher the wavelength of the PL band. The effect of the quantum size only occurs for nanostructures smaller than 5 nm and to achieve an efficient light-emission the porosity of the samples should be at least the 80%. If the nanostructures are bigger than 10 nm, they will not show luminescence but instead they will absorb most of the incident light.

For the quantum confinement, depending on the size the PL energy for pSi is shifted towards lower wavelength compared to bulk Si. This behavior is described by the equation[80]:

$$E_{PL}(d) = E_0 + \frac{3.73}{d^{1.39}} + \frac{0.881}{d} - 0.241$$

E_0 corresponds to the bandgap of bulk silicon and it is equal to 1.17 eV, d is the size of the silicon nanocrystals and E_{PL} is the bandgap of porous silicon corresponding to the position of the maximum value of the emission band. This equation considers that the nanoparticles have a size distribution and that the bigger ones absorb more light without emission. The PL shifts towards the blue region as time passes. However, this model takes into consideration that there might be a discrepancy between the experimental results and the theoretical values. For example, a PL band centered around 670 nm, correspondS to a nanocrystal size of 3.5 nm.

2.B. Results and discussion

2.B.1 Fabrication and functionalization

The chosen fabrication method, for the production of the investigated pSi during this thesis work, was electrochemical etching. The steps needed to obtain the final functionalized pSi microparticles are shown in Figure 2.7.

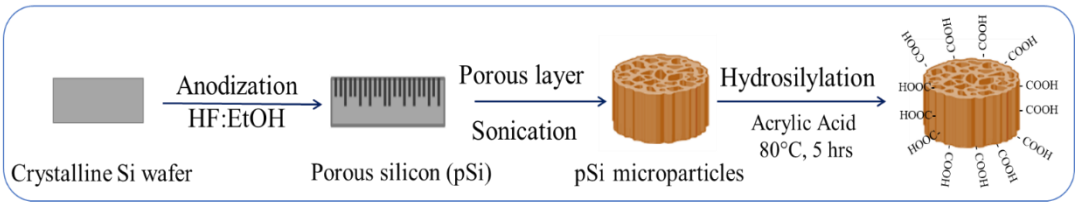

Figure 2.7. Representation of the fundamental steps needed to obtain the functionalized pSi microparticles.

The anodization procedure including the parameter for the electrochemical etching (i.e., electrolyte solution, etching time, current density) and the following functionalization were established from our group after many years of investigations, in order to define a protocol that leads to the desired optical and structural parameters[5,8]. The assessed protocol consists in the following steps:

1. Anodization of a crystalline silicon wafer
2. Removal of the porous layer
3. Fracture of the porous layer by means of ultrasounds to obtain the microparticles
4. Hydrosilylation reaction to obtain a carboxylic functionalization (labelled as pSi-COOH)

Moreover, with further functionalization of the carboxylic-functionalized microparticles by reaction with trioxa-1,13-tridecanediamine and dicyclohexylcarbodiimide, it is possible to obtain aminic-functionalized pSi microparticles (labelled as pSi-NH_2). The two functionalizations not only allow to have two opposite surface charges that enable the electrochemical interaction with both positive and negative molecules, but also result in different emission bands, reported in Figure 2.8.

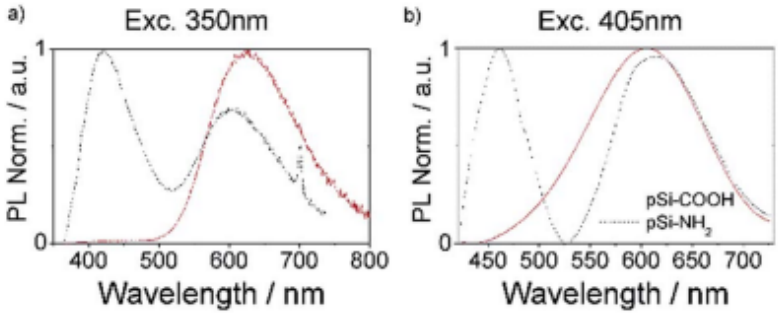

Figure 2.8. Emission spectra of functionalized pSi microparticles. The solid trace is for pSi-COOH and the dashed trace for pSi-NH_2. Panel a: excitation 350 nm. Panel b: excitation 405 nm[5].

The anodization was done by assembling a section of the boron doped p-type crystalline Si wafer (<100> oriented, 10–20 Ω/cm^2 resistivity, purchased from University wafers, Boston MA) in a PTFE cell filled with an electrolytic solution of ethanol with 16% HF and etched at a constant current of 80 mA/cm^2 for 15

minutes. The porous layer was removed from the wafer surface and transferred in toluene. To obtain the pSi powder, the layer was fragmented into microparticles by 20 min sonication in a thermal bath. The setup used for the fabrication (panel a) and the functionalization (panel b) of the pSi microparticles is visualized in Figure 2.9.

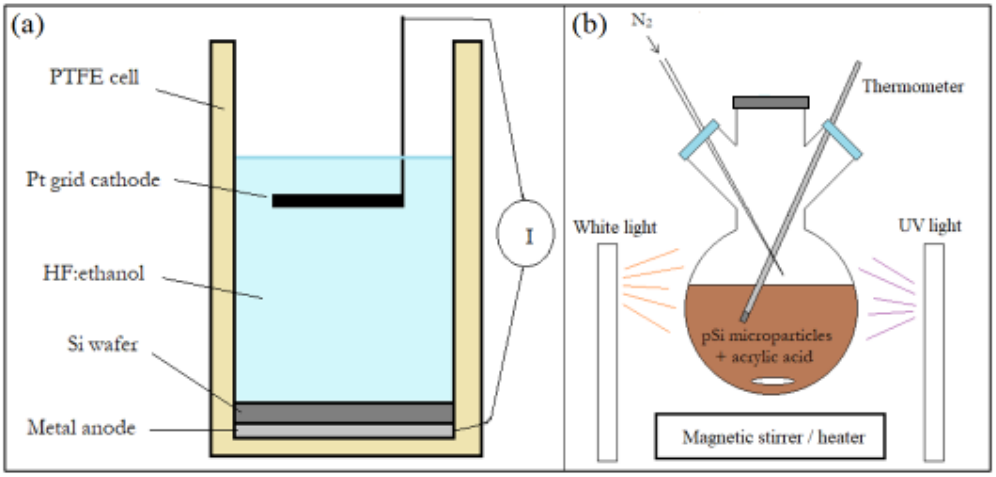

Figure 2.9. Schematic representation of the single electrochemical cell used for pSi porosification in HF:ethanol solution (panel a) and experimental setup used for the hydrosilylation of porous silicon microparticles (panel b).

The fabrication setup is composed of a PTFE cell containing the Si wafer on one side in direct contact with the metal anode and on the other side separated to the platinum cathode by a HF/EtOH solution. The circuit is closed passing through an electric generator that allows to adjust the voltage to obtain the desired current density. After the etching, the porous layer was removed and transferred in toluene and consequently sonicated for 20 minutes to obtain the microparticles and then stabilized by a light-driven hydrosilylation reaction. Figure 2.10 shows a picture of the as-etched silicon wafer during the removal of the porous layer, irradiated by a UV light.

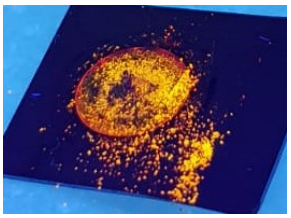

Figure 2.10. pSi during the removal of the as-etched porous layer, irradiated by black light.

UV and white light-promoted hydrosilylation of alkenes and alkynes is a one-step reaction that allows to obtain alkyl and alkenyl groups, respectively, on the surface of hydride-terminated porous silicon[81,82]. The carboxyl-functionalized pSi particles discussed in this dissertation were obtained by reaction with acrylic acid because it results in a reduced steric hindrance thus favoring the entrance inside the pores of the produced microparticles. In general, to carry out the reaction it is necessary to expose the freshly etched porous silicon microparticles to the chosen alkene (or alkyne) and illuminating them with UV and white light while heating at 80°C. Moreover, the reaction must be oxygen-free (e.g., anhydrous reagents and solvent) to avoid as much as possible the formation of undesired oxides species. Stewart and Buriak proposed two mechanisms to explain the role of the light: photolytic cleavage of Si−H bonds and exciton-mediated electrophilic-nucleophilic attack[81].

In the first case, the light induces the generation of silicon radicals from the homolysis of weak Si-H bonds which promptly interact with unsaturated C-C bonds forming a radical on the β-carbon which then removes a nearby hydrogen.

In the second model, unbound excitons generated in situ as a byproduct of the photoluminescence create a positive surface charge that leads to a nucleophilic attack from the alkene on the electrophilic silicon center, yielding to a Si−C bond characterized by a β-carbocation stabilized by a silyl group. Lastly, the strongly acidic β-silyl carbocation removes a hydride from a neighbor Si-H bond leading to a C-H bond, which is less polar, stronger and more stable.

The surface functionalization setup consists of a round-bottom flask containing the toluene suspension, coupled to a nitrogen flux and a thermometer, closed by a septum stopper to maintain the nitrogen atmosphere and catalyzed by UV and white lamps. The general hydrosilylation reaction is schematized in Figure 2.11.

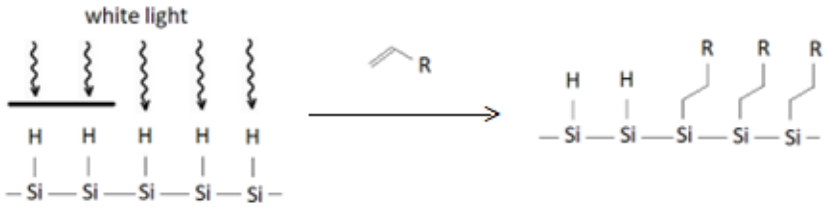

Figure 2.11. Hydrosilylation reaction to functionalize the pSi surface (R= -COOH).

To perform the reaction, 50 mM acrylic acid was added to the toluene suspension of pSi microparticles and stirred at 80°C for 5 hours. After that, the suspension was washed ten times with ethanol to remove the toluene containing the non-reacted acrylic acid. The introduction of carboxylic groups allows to store the sample, labelled as pSi-COOH, in ethanol at room temperature for years without degradation or loss of luminescence.

The preparation of the samples, whose fabrication procedure has been settled and is now well established[5], was performed in collaboration with Prof. Marina Scarpa, at the Nanoscience Laboratory in the Physics Department of the University of Trento.

2.B.2 Structural and optical characterization

Surface, structural (e.g., morphological) and optical properties of the functionalized pSi-COOH microparticles were investigated by FTIR spectroscopy, DLS and TEM and fluorescence spectroscopy, respectively. Details about the instruments and the measurements methods are reported in Appendix A.

Surface chemical characterization

The surface properties of the samples were investigated by FTIR to monitor the success of the hydrosilylation. Indeed, even if after the etching the particles were carefully handled (suspension in anhydrous toluene and carboxylic functionalization conducted in nitrogen atmosphere with anhydrous reagents) it is anyhow impossible to completely avoid the formation of oxide species at the surface. The presence of high amount of silicon oxides might affect the success of the reaction,

therefore it is fundamental to investigate the species present at the surface. Figure 2.12 shows the FTIR spectrum of the sample with the respective peaks assignation.

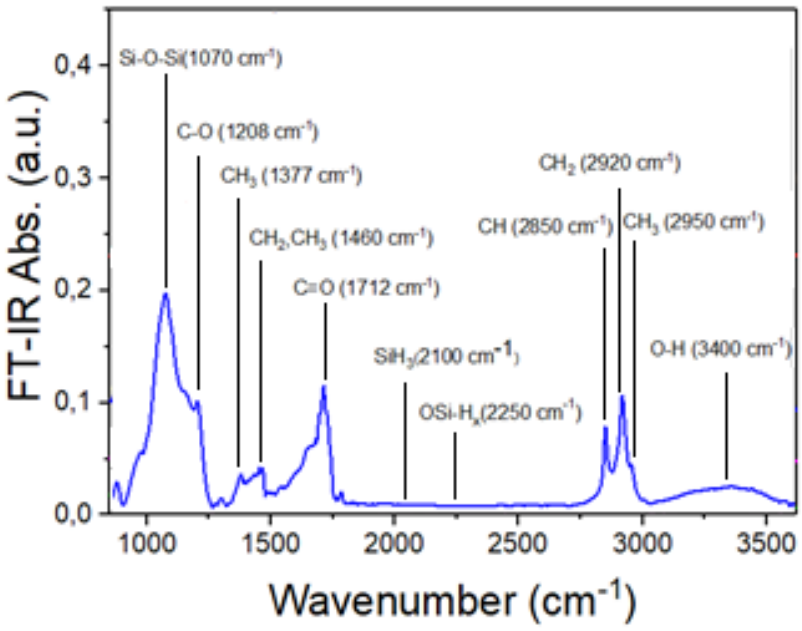

Figure 2.12. FTIR absorption spectrum of pSi-COOH microparticles. The most relevant absorption peaks are assigned.

In particular, it was investigated the presence of oxidized silicon groups, silicon hydrides species and the carbonyl group to verify the successful functionalization. The peak at 1070 cm^{-1}, due to the presence of Si-O-Si groups[83], together with the broad one at 3300 cm^{-1}, due to -OH, meant that the sample was partially oxidized. Peaks related to hydride species ($Si-H_x$), at 2100 and 2250 cm^{-1}, were irrelevant giving a first indication that the functionalization was effective and supported by the presence of the peak at 1712 cm^{-1} related to the carbonyl group (C=O) that confirmed the achievement of the hydrosilylation[84]. The decrease of hydride-related peaks intensity is compatible with the hydrosilylation, during the reaction, indeed, silicon-hydrogen bonds are replaced by the development of silicon-carbon ones. Moreover, the stretching modes of the alkyl-CH peaks between 2850 and 2950 cm^{-1} gave another proof to support the accomplished functionalization[85].

Structural properties

Electron Microscopy techniques, in particular TEM and SEM, by means of an electron beam probe interacting with the sample can give unique information about the morphology and estimate the average size and the porosity. Moreover, pSi electron

density is higher enough to not require the specific preparation for other kind of materials, thus, after its deposition on a TEM grid, can be right investigated. TEM, indeed, is a technique that gives information on the structural inner part of the sample by the passage of an electron beam through the sample. SEM, on the other hand, exploits the backscattering of electrons to investigate the surface giving information about the morphology.

Representative SEM images of the pSi-COOH microparticles samples are reported in Figure 2.13.

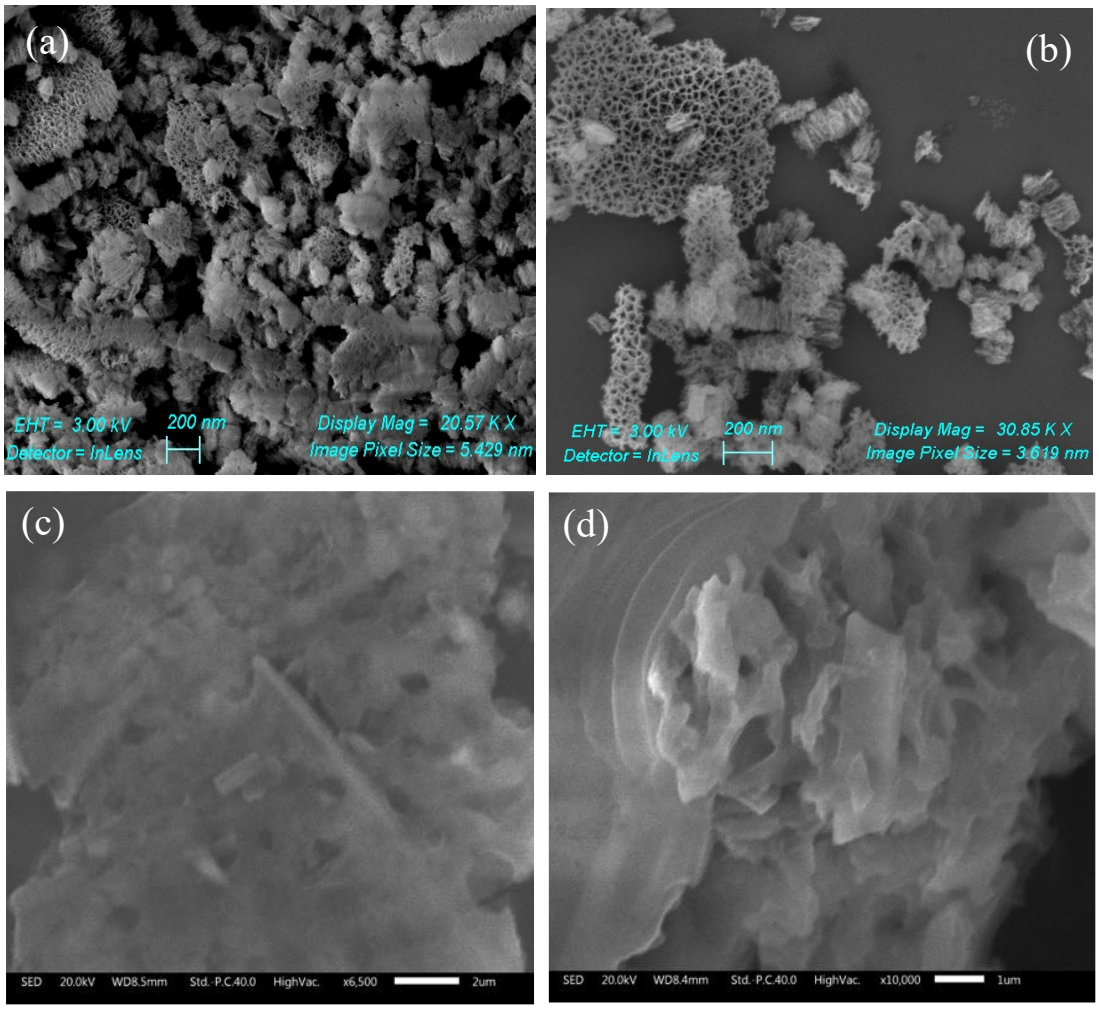

Figure 2.13. SEM images of pSi-COOH microparticles samples (200 nm, 200 nm, 2 μm, 1 μm scale).

A first look at the SEM images made possible to appreciate the sponge-like morphology typical of the material and the variations of the size distribution. Moreover,

since the images were acquired at high magnification (between 6.500X - 31.000X), the widespread presence of the porosity became clearer.

TEM measurements were coupled with EDX spectrometry to deeply investigate the elemental composition (Figure 2.14). EDX is based on the ability of high energy electromagnetic radiation (X-rays) to eject core electrons from an atom, the removal of these electrons leaves a hole that a higher energy electron can fill, and it will release energy as it relaxes. The energy released during this relaxation process is distinctive for every element on the periodic table thus can be used to identify what elements are present, as well as what proportion they are present in.

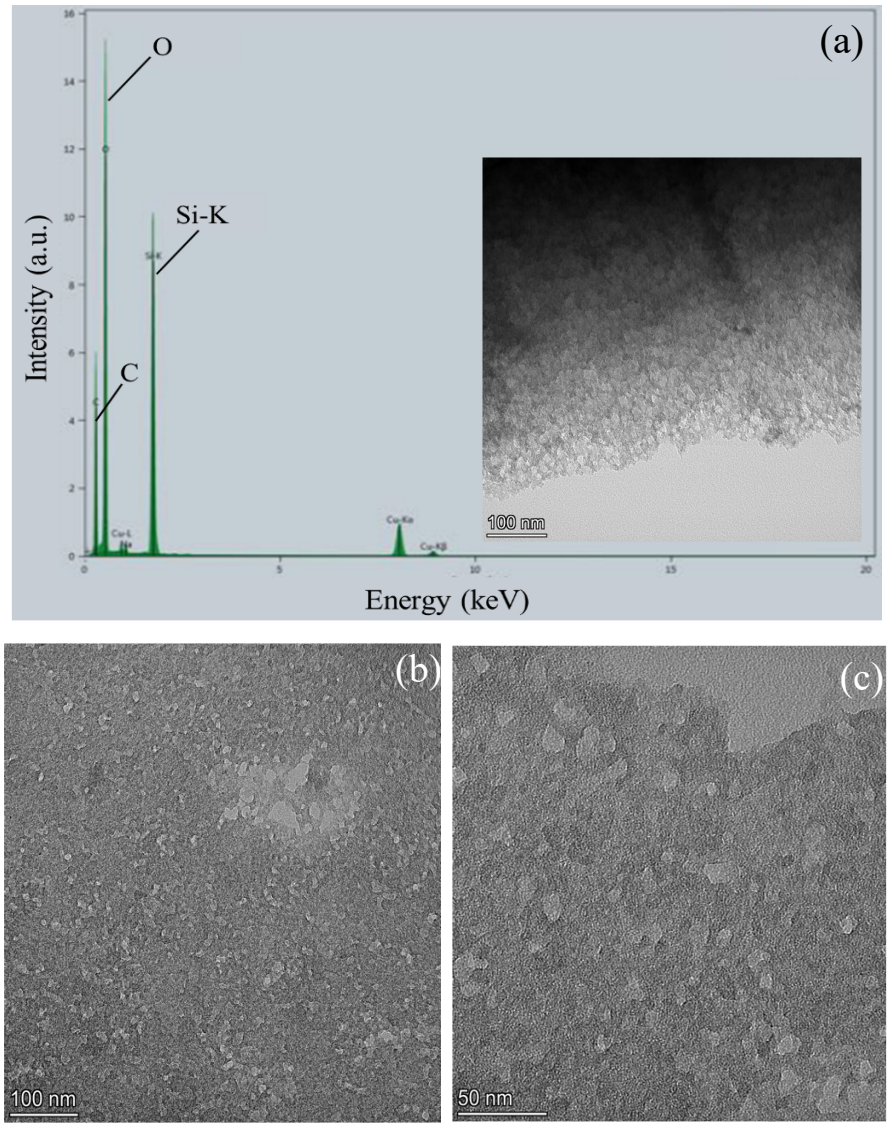

Figure 2.14. Panel (a): Elemental analysis performed on the region shown in the inset, for a representative sample of pSi-COOH. Panel (b) and (c): different magnifications of the TEM image in the inset (100 nm and 50 nm scale, respectively).

In the EDX spectrum (panel a) obtained from a representative TEM image in the inset the peaks with the highest intensity regard Si, as expected, but also O and C, confirming the success of the carboxylic functionalization. Cu peaks are high because it is the main component of the TEM grid used to analyze the sample. Panels b and c show a magnification of the TEM image in the inset of panel a. Panel c, in particular, was used as representative image of the pore size analysis, reproduced in Figure 2.15 with the respective pore measures.

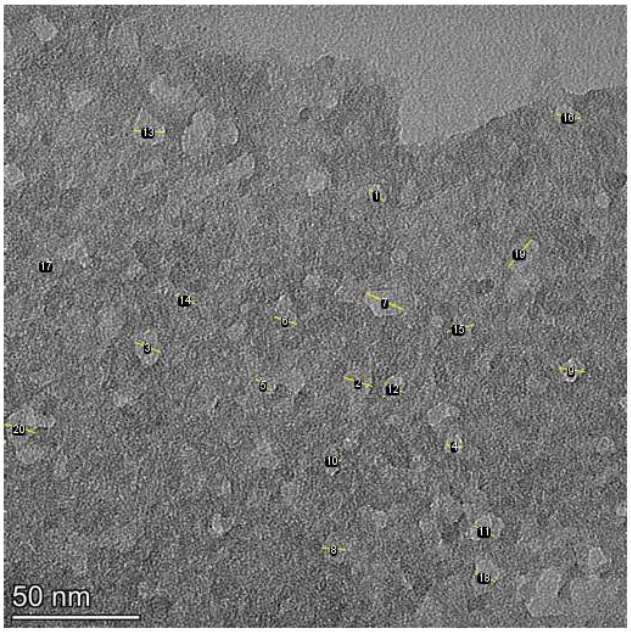

Reference number	Pore size (nm)	Reference number	Pore size (nm)
1	8	11	8
2	11	12	8
3	10	13	12
4	6	14	8
5	7	15	10
6	9	16	9
7	16	17	5
8	9	18	8
9	10	19	14
10	6	20	12

Figure 2.15. Pore size analysis on a representative TEM image.

The mean pore size was analyzed by ImageJ software, measuring the pore size of several sample in different portions, obtaining pores with a mean value of 9 ± 5 nm. The images obtained from the microscopy investigation showed that the pSi-COOH microparticles are mostly agglomerated, thus resulting in size values that were between 100 nm and a few microns.

To obtain information regarding surface charge and size distribution, pSi-COOH microparticles were analyzed by DLS. As expected, because of the presence of the carboxylic groups on the surface, the Z-potential was negative, while the average size before further fracture processes was between 900 and 780 nm. The average size and surface charge of some of the produced samples are reported in Table 2.1.

Sample	TEM		DLS	
	Porosity	Size (nm)	Size (nm)	Z-potential (mV)
pSi-COOH_1	16±6	900±470	1200 ± 220	-30 ± 3
pSi-COOH_2	16±5	820±510	1100 ± 250	-27 ± 1
pSi-COOH_3	17±3	730±650	1300 ± 260	-29 ± 2
pSi-COOH_4	5±1	780±630	1500 ± 480	-25 ± 1

Table 2.1. Average size and porosity obtained by the TEM images analysis and DLS and Z-potential values of some of the prepared samples (the mean values are presented along with the standard deviations calculated with 45 data points).

Optical properties

Photoluminescence spectroscopy was used to obtain information regarding optical emission, quantum yield (QY) and lifetime (i.e., the radiative fluorescence lifetime τr is related to the time the fluorophore remains on average in the excited state before emission takes place). The most significative optical results are reported in Figure 2.16.

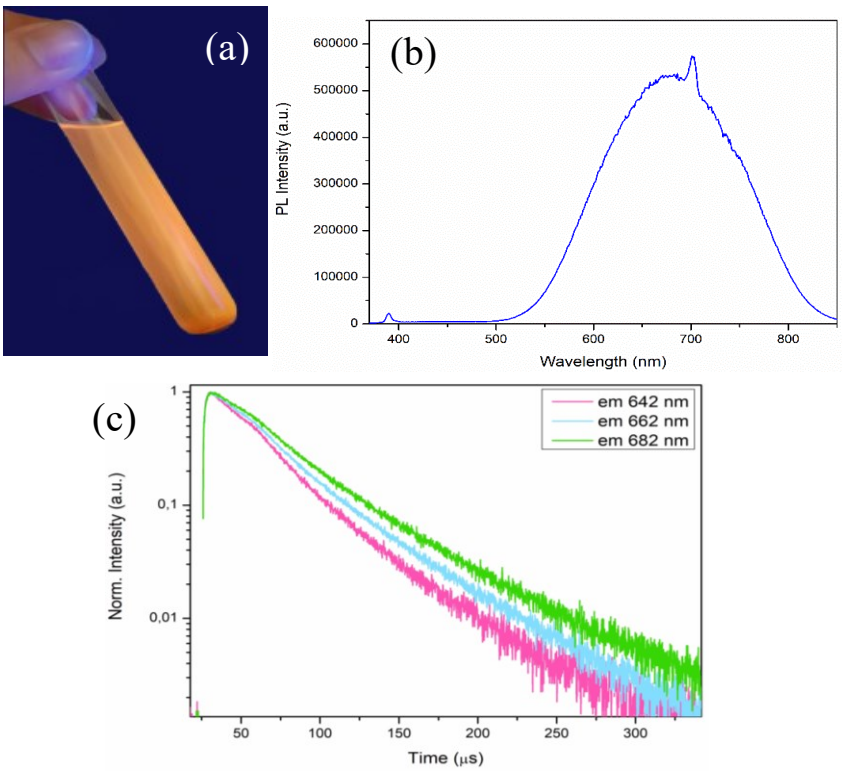

Figure 2.16. Panel (a): a picture of pSi-COOH microparticles before washings irradiated by black light. Panel (b): emission spectrum of pSi-COOH by excitation at 350 nm. Panel (c): PL decay curves of pSi-COOH by excitation at 350 nm varying λ_{em}.

In panel (a) is reported a picture of the pSi-COOH microparticles suspension after the functionalization and before the washings irradiated by a black lamp. As it is possible to notice, the particles at the bottom of the tube are reddish. The emission spectrum, indeed, shown in panel (b), collected by excitation at 350 nm, is characterized by a red band centered at 675 nm. The sharp peak at 390 nm is related to the Raman scattering of water and the peak at 700 nm is the second order of the excitation wavelength (i.e., 350 nm). The decay curves of the PL by excitation at 350 nm varying the emission wavelength is reported in panel (c). The exponential decay fit of the decay curves allowed to obtain the lifetime (τ) 28.0 ± 0.8 μs.

$$QY_S\% = QY_R \frac{I_S}{I_R} \frac{A_R}{A_S} x\ 100$$

Standard name	λ_{exc} (nm)	QY%
Rhodamine 101	470	100
Rhodamine 6G	488	94
2-aminopurine	280	60
Fluorescein	490	98
Quinine sulfate	350	58
Cresyl Violet	550	54
POPOP	365	97

Figure 2.17. Equation for the calculation of the QY through the comparative method and list of the most popular reference standard substances with the respective excitation wavelength and QY%.

To calculate the QY of our sample we applied the comparative method with the equation in Figure 2.17 using Fluorescein as a standard reference, the resulting QY was 0.8 %, comparable with previous findings[9].

2.B.3 Size reduction treatments

Even if the fabrication process of pSi is quite easy, the top-down approach does not allow to have a control of the average size and the size distribution. However, it is fundamental to know the average diameter of the particles and to have a sharp size distribution because these parameters, together with pore size and shape, have a huge influence on the biodistribution and the cellular uptake[56]. During the years,

scientists working on the pSi field have developed different method to reduce the size of the particles, the most common are ball-milling and ultrasonication[86].

Ball-milling

The key components of a planetary ball-mill are two grinding bowls and the grinding balls, they are usually made of either stainless steel or a ceramic material (i.e., zirconia), and depending on the starting size and on the desired final size they have a different diameter. Once filled with the sample and the spheres, the bowls are tightening closed and placed on a rotating platform. The grinding is achieved by a double rotation, one of the platforms and one of the bowls, with a planetary motion and the action of centrifugal forces. There are several parameters that dictate the final size of the sample: bowl volume, number and diameter of the grinding balls, the nature of the material, rotation speed and grinding time, moreover, it can be conducted in a dry or wet way.

Even if with this technique it is possible to obtain a considerate reduction in size (panel (a), Figure 2.18) there also a few drawbacks that come with it. Dry milling can oxidize the sample and wet milling requires a suitable solvent to avoid the passivation of the material, the stainless-steel grinding system might contaminate the powder with metal but having zirconia a lower density will yield different size distribution. To achieve consecutive size reductions, it would possible to repeat the milling procedure but this will result also in a reduction of the pore volume

We performed an experiment of size reduction by using the mill-ball. pSi-COOH microparticles ethanol suspension was placed inside stainless steel bowls with stainless steel spheres of 1 mm size and fractured. The experiment was done by using stainless steel bowls and balls (1 mm size) by three consecutive grinding cycles of three minutes each and other two cycles of 5 minutes each. The size distribution after every cycle is reported in Figure 2.18.

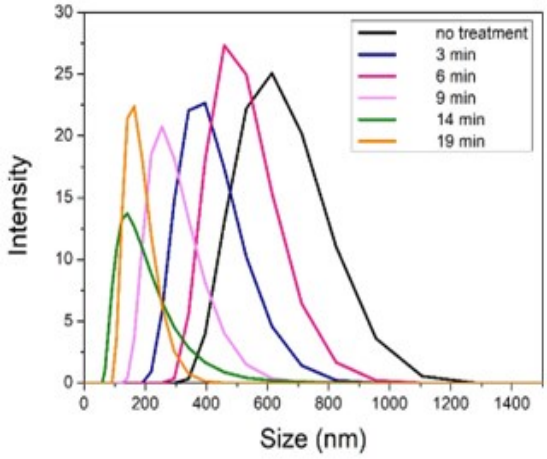

Grinding time (min)	Average Size (nm)	FWHM (nm)
0	615 ± 20	345 ± 10
3	370 ± 10	285 ± 10
6	490 ± 10	260 ± 5
9	260 ± 10	195 ± 5
14	155 ± 40	120 ± 5
19	145 ± 10	160 ± 5

Figure 2.18. pSi-COOH size distribution analysis by DLS - variation as a function of the time of milling treatment (the mean values are presented along with the standard deviations calculated with 45 data points).

The initial average size was 615 ± 20 nm, after the first cycle the size was reduced of almost half (370 ± 10 nm) but after the second cycle it seemed to start aggregate reach an average diameter of 490 ± 10 nm. Further grindings reduced more the size until around 200 nm. After the fifth cycle the average size was not decreasing anymore, reaching a value of 145 ± 10 nm. Moreover, by observing how the full width at half maximum (FWHM) became smaller (i.e., narrower size distribution) as the grinding time increased, it is possible to assume that the method not only is effective to reduce the size but also to homogenize the sample. This method, however, even if efficient in reducing the average size and size distribution is not time effective, because of the following weak points:

- small volume of the bowls resulting in a small amount of fractured particles, consequently more cycles are needed to reduce the size of the sample
- between every cycle it was necessary to cool down the sample because the medium was heated by the energetic process

Ultrasonication

Ultrasonication (US) is a fast and efficient approach that allows narrowing the size distribution and reducing the average size by fracturing and disaggregating the microparticles. The system is composed by a power supply connected to a probe through a transducer, the probe is immersed inside the suspension. Ultrasound

waves (frequency > 20 kHz) are transferred though the chosen medium creating cavitation phenomena thus there will be the formation, growth and, after a certain dimension, collapse of microbubbles. Ultrasonication releases a lot of energy, therefore this technique is commonly used also to homogenize emulsions[87]. The resulting size depends on the power density, the duration of the treatment, the size of the probe tip, and obviously on the nature of the sample and the chosen medium.

Our group previously assessed an efficient ultrasonication procedure to reduce and homogenize the size distribution of pSi-COOH microparticles without compromising the photoluminescence nor the pore size[7]. The procedure was optimized by varying concentration of the suspension, ultrasonication time and power density. We found that the duration of the treatment did not exert any effect on the average size reduction and established a protocol that consists in a concentration of 2 mg/mL and 42 W/cm^3 power density for 10 minutes of sonication. In Figure 2.19 are reported some representative data obtained with our optimized protocol.

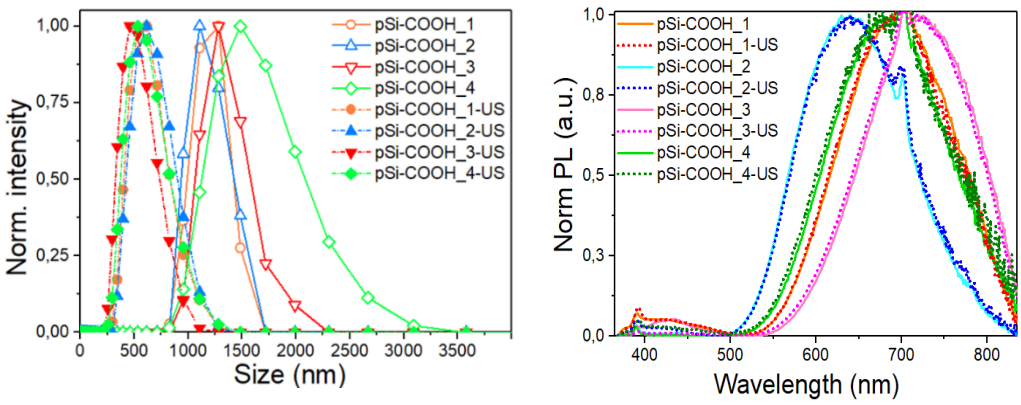

Figure 2.19. Panel (a): size distribution of different pSi-COOH microparticles by DLS analysis: as-prepared samples (solid lines) and after US (dotted lines). Panel (b): US treatment effect on the PL properties: normalized emission spectra (excitation wavelength at 350 nm) of different samples before (solid line) and after US (dotted line).

As it is possible to observe from panel a of Figure 2.19, with this easy and fast treatment we were able to fracture the microparticles and disaggregate the agglomerates leading to a reduction of the size and narrower size distribution (panel a), the distribution of sonicated samples (dashed lines) shifts towards lower values. For all the samples, the distribution shape has an elongated tail towards the higher dimension, this is a characteristic of samples prepared by a fracture mechanism, such as

sonication. From table 2.2, it is possible to notice a reduction to about half of the averaged size after the treatment (one third for sample pSi-COOH_4). The broadness of the size distribution, related to the FWHM, is generally unchanged, except for sample pSi-COOH_4: its FWHM value is halved and becomes comparable with the others. It is important to highlight that this procedure reduces the dimension of the bigger agglomeration of the particles, homogenizes the sample and prevents their agglomeration.

Sample	Diameter [nm]	
	as prepared	after US
pSi-COOH_1	1200 ± 230	580 ± 210
pSi-COOH_2	1100 ± 250	620 ± 220
pSi-COOH_3	1300 ± 260	480 ± 220
pSi-COOH_4	1500 ± 480	540 ± 230

Table 2.2. Average size of some representative samples from DLS analysis, before and after the ultrasonication process (the mean values are presented along with the standard deviations calculated with 45 data points).

Moreover, panel b shows that PL was not affected by the sonication treatment (continuous lines vs. dotted). The sonication treatment, indeed, does not act on the nanostructures responsible for the optical properties, but has an effect only on the microparticle dimension.

By comparing the ball-milling with the ultrasonication treatment, the first one allowed to obtain a higher size decrease (around 75 % *vs* 50%) and a reduction in the FWHM of about 50%, which for the second procedure was generally unaffected, thus resulting in a narrower size distribution. On the other hand, the latter resulted to be faster and easier, without contamination of the sample and with the possibility to fracture a higher amount of particles per cycle. All the pSi-COOH microparticles employed during this work of thesis were treated by consecutive ultrasonication treatments with the established protocol.

2.B.4 Surface charge modifications

As aforementioned, pSi-COOH microparticles are characterized by a negative surface charge (-27 ± 5 mV) due to the presence of the carboxylic groups that allow the electrostatic interaction between molecules with positive surface charge. This has been exploited to load through electrostatic interaction molecules such as

Pam3CSK4 and doxorubicin, an immune adjuvant and anticancer drug, respectively, that are characterized by positive surface charge. The use of these two examples in pSi will be deeply presented and discussed in Chapter 4 and 5, respectively. However, the COOH-functionalized surface represents a limitation when dealing with negatively charged or neutral molecules. Therefore, we investigated two different ways to obtain a modification of the surface:

(i) through binding with poly-L-Lysine (PLL)

(ii) through encapsulation with the cationic surfactant cetyltrimethylammonium bromide (CTAB).

As previously mentioned, the protocol that we established for the production of pSi particles allows also the functionalization with aminic groups[5]. However, for the purpose of loading doxorubicin (through electrostatic interaction with carboxylic groups) it was not useful.

Poly-L-Lysine

PLL is a cationic aminoacidic water-soluble polymer, composed of α-l-lysine structural units, that commonly finds application as a pre-coating agent to enhance cell attachment onto solid supports[88]. PLL is biocompatible and biodegradable and non-antigenic, the monomer α-l-lysin is considered fundamental for eukaryotes and prokaryotes and plays crucial roles in biological processes, such as injury recovery and protein functions, therefore thanks to these properties it finds application in the biomedical and pharmaceutical field. Since at physiological conditions its primary amino groups are protonated (pKa around 9.0), it is possible to exploit the electrostatic interactions between the positively charged PLL and a negatively charged material such as pSi-COOH[89]. Owing to this, PLL-based preparation have been investigated for coating preparations, bacterial biofilm and nanocarriers[90]. In Figure 2.20 is represented the procedure used to coat pSi-COOH with the PLL layer.

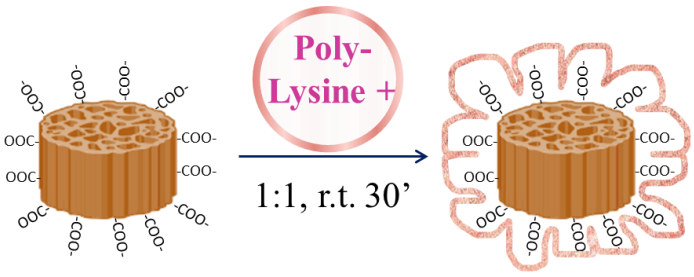

Figure 2.20. Representation of the coating procedure to obtain a poly-lysine layer.

The coating was obtained through electrostatic interaction by allowing to react pSi-COOH microparticles and PLL at a concentration of 5 mg/mL (70-150 kDa, water solution, pH 5) at a mass ratio 1:1 under mild agitation at room temperature for 1 hour. The sample was then thoroughly washed with ultrapure water to remove the non-bonded PLL. The success of the surface charge modification was investigated by Z-potential and size measurements with DLS, reported in Figure 2.21.

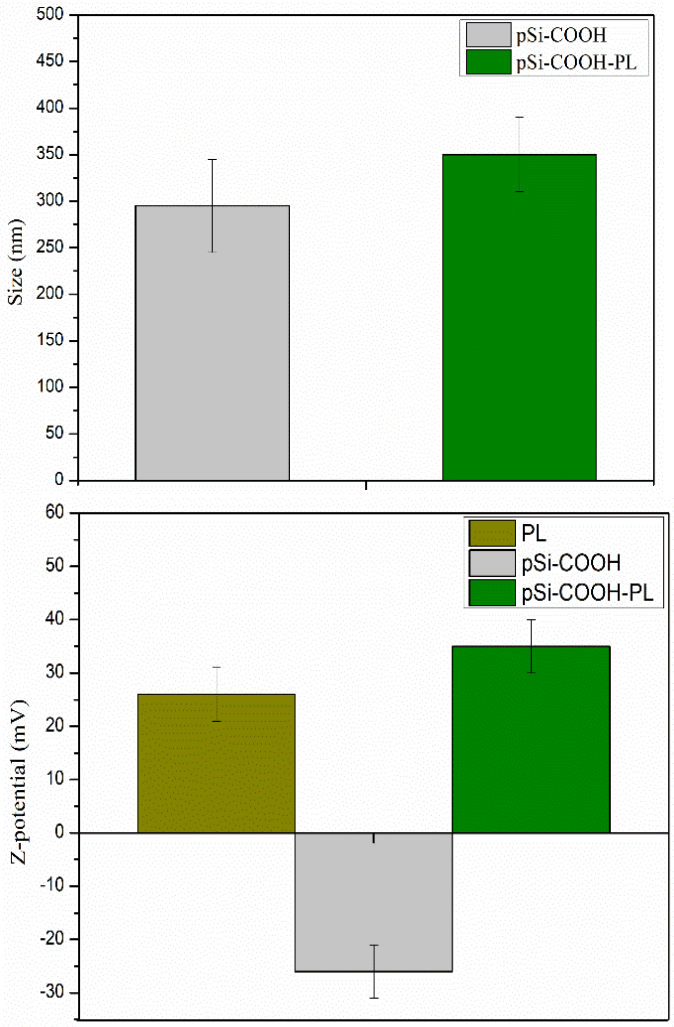

Figure 2.21. Average size and surface charge modification of pSi-COOH microparticles before and after the coating with PLL.

The surface charge after the conjugation resulted to be +35 ± 5 mV, proving the success of the method. In addition, the size had a slight increase (around 50 nm more) due to the presence of the layer of PLL around pSi. For this coating we used a PLL with a medium molecular weight therefore we did not expect a highly thick layer.

CTAB

CTAB is a cationic surfactant composed of a long chain with a cationic head and a hydrophobic tail. The hydrophobic groups are soluble in water and alcohol, in water media it can be found as CTA+ ions. Surfactants are usually applied to keep the particles dispersed in aqueous media but they can also be employed as cationic surface coating[91]. When CTAB is used at a concentration higher than its critical micellar concentration (CMC: 1.0 mM) it forms a bilayer through hydrophobic interaction of its hydrocarbon tails. Therefore, it can be used to encapsulate negative molecules or particles such as pSi-COOH through electrostatic force with the inner cationic head, ultimately resulting in a positive surface charge of the particles thanks to the outer cationic head[92]. The mechanism is shown in Figure 2.22.

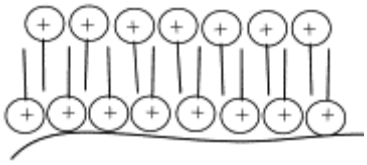

Figure 2.22. Simplified representation of CTAB bilayer[92].

Regarding our system, the cationic part of the surfactant is attracted by the negative pSi-COOH surface and will form a bilayer micelle that will ultimately result in the creation of a positive charge on the surface of the pSi-COOH samples (Figure 2.23).

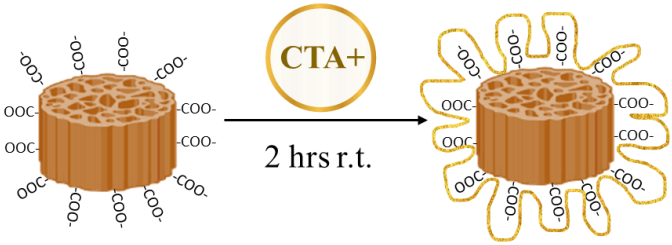

Figure 2.23. Representation of the coating procedure to obtain a poly-lysine layer.

pSi-COOH microparticles were energetically mixed with CTAB solution for two hours at room temperature, once with a concentration under the CMC (0.1 mM) and a second time with a concentration well above the CMC (13 mM), to find the best combination to obtain a positive surface charge on the particles. The samples were then thoroughly washed with ultrapure water (at least five times) to remove the free CTAB. Z-potential was then measured with DLS to check the obtained average surface charge, reported in Figure 2.24.

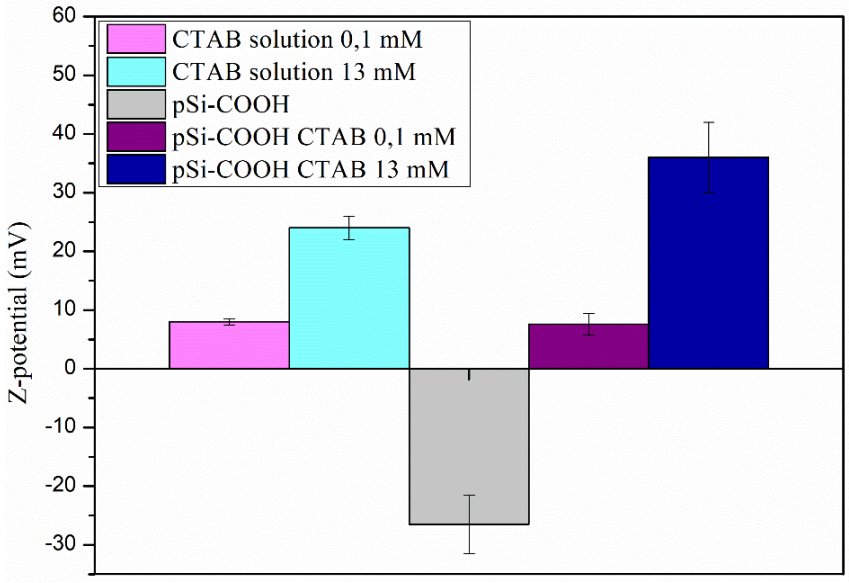

Figure 2.24. Surface charge modifications of pSi-COOH microparticles before and after encapsulation with different concentrations of CTAB.

The success of the encapsulation of pSi-COOH microparticles with CTAB was confirmed by the obtained positive surface charge: from -27 ± 5 mV of pSi-COOH to +8 ± 2 mV for the concentration under the CMC and to +36 ± 6 mV for the concentration over the CMC. Therefore, the mixing of the sample with a concentration of CTAB higher than its CMC resulted in a higher positive charge due to a higher amount of PLL bonded on the surface of pSi-COOH, thus in a more successful process.

2.B.5 Polymeric surface modification

We previously developed a PEG and chitosan coating by covalent attachment to pSi-COOH microparticles with the aim of stabilizing the optical properties in aqueous media and adding some useful features (such as increased biocompatibility and/or biomimetic behavior). Both PEG and chitosan allowed to stabilize the photoluminescence and protect the degradation of the particles for three months in buffer. Moreover, the pSi samples coated with PEG and chitosan were investigated as drug delivery carrier of cobalamin (Cbi, a vitamin B2 precursor) as a model drug, resulting in a high loading of the payload and a slow rate release[8]. These results confirmed the ability of pSi-COOH and pSi-NH_2 to act as an efficient drug delivery system and paved the way for the investigations of this thesis. During our previous investigations on the coating of pSi particles, we also reported the possibility to coat

pSi-COOH microparticles by means of an inorganic TiO_2 coating through atomic layer deposition. This allowed to obtain a uniform thin layer formation with tunable thickness, which was effective in prolonging the luminescence stability in aqueous media up to several months, with results similar to the PEG and Chitosan coatings[9]. With the aim of preserving the optical properties of functionalized pSi microparticles for its application in nanomedicine, in particular for its application as an anticancer therapy drug delivery system, we investigated two possible modifications of the surface of pSi-COOH by encapsulation with polymers.

Regarding this thesis work, two new polymers were studied and experimentally tested for their different features:

(i) acetalated dextran (AcDEX), as a pH-responsive coating

(ii) hyaluronic acid (HA), as a cancer cell targeting.

Acetalated dextran

AcDEX is a biocompatible and biodegradable polymer that can be obtained through acetalation of pendant hydroxyl groups on dextran, the resulting polymer is insoluble in water and soluble in organic solvents (e.g., ethanol, ethyl acetate, dichloromethane), in mildly acid aqueous media its acetals hydrolyze returning to the native dextran. Its on-step synthesis was reported for the first time by Bachelder et at al. in 2008[93].

Its solubility in organic solvents and hydrophobicity can be exploited for encapsulation of drugs (by either precipitation or emulsion) and the acid-triggered degradation can be useful for drug delivery applications. In particular, the pH-responsive feature of this polymer can be game changing when it is applied as a coating for anticancer delivery systems[94]. Indeed, its stability in physiological conditions (pH 7.4) allows to keep the drug inside the carrier while it is transported, avoiding leakage or typical degradation due to the biological fluid. However, as soon as the pH start to be mildly acid (about pH 5), like in the tumor microenvironment end endosomal compartments, the polymer will degrade releasing the payload at the targeted cancer cells. Moreover, it shows innate immunostimulant properties, enhancing MHC class I presentation and T cell activation. Therefore, it can stand as a great tool not only for the anticancer therapy but also in the cancer vaccines field[93]. Furthermore, AcDEX has already been investigated for example by Peine *et al.* for the

encapsulation of vaccine adjuvants such as polyinosinic:polycytidylic acid (poly I:C) and CpG and compared with PLGA, obtaining higher encapsulation efficiencies a significantly stronger immunostimulatory response than PLGA[95]. While Santos and collaborators reported the encapsulation of thermally oxidized pSi with AcDEX by means of glass-capillary based microfluidic chips in a co-flow configuration[96].

In collaboration with Prof. C. Nardon (Biomedical Chemistry Laboratory, Biotechnology Dep. - University of Verona) we synthetized AcDEX by dissolving 2 g of dextran (9-11 kDa) in 20 mL of DMSO in nitrogen atmosphere, followed by addition of 31.2 mg of pyridinium p-toluensulfonate (catalyst) and 6.8 mL of 2-methoxypropene and stirring at room temperature. Every 10 minutes for 40 minutes aliquots were taken out and quenched with 1 mL of trimethylamine (TEA, 0.01% v/v, pH 8). The setup of the reaction is pictured in Figure 2.25.

Figure 2.25. Setup for the synthesis of acetalated dextran.

After the quenching, the modified dextran was precipitated in distilled water and centrifuged. The pellet was washed twice thoroughly with TEA solution by Buchner filter funnel and freeze-dried for 48 hours, yielding a white powder.

Depending on the reaction time the number of cyclic acetals varies. Therefore, aliquots at different reaction times were analyzed by ^{1}H-NMR to find the best ratio of cyclic/acyclic content. The longer the length of the reaction, the higher the number of cyclic acetals formed at the expense of the acyclic ones. Acyclic and cyclic acetals have different hydrolysis rates. In fact, cyclic acetals are associated with slower degradation in mildly acidic media. The presence of only cyclic units would result

in a highly hydrophobic product with extremely slow degradation. Therefore, it is important to control their abundance.

The first NMR analysis was done after solubilization of the samples in DMSO. We then analyzed only the most interesting samples after the full hydrolysis achieved by addition of deuterium chloride (DCl) that resulted in the release of dextran, methanol and acetone whose concentration was different depending on the cyclic/acyclic content. The cyclic/acyclic content can be determined by comparing the relative concentrations of acetone and methanol: hydrolysis of an acyclic acetal yields one molecule of acetone and one of methanol, while hydrolysis of a cyclic acetal yields only one acetone molecule[97].

The magnification of an area of interest related to the first NMR spectra (without hydrolysis) related to the different reaction times is reported in Figure 2.26.

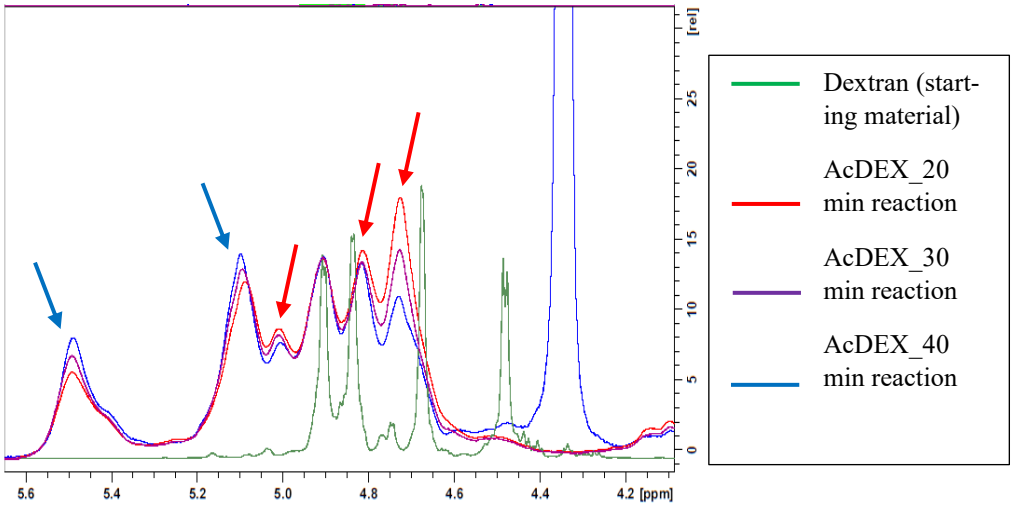

Figure 2.26. Overlap of the ^{1}H-NMR spectra related to the starting material and the products obtained at different reaction times.

The spectrum related to the first aliquot (after 10 minutes of reaction) is not reported because it was quite similar to the starting one. As it is possible to notice from the Figure 2.26, the longer the reaction length, the more intense the peaks at 5.5 and 5.1 ppm (indicated by blue arrows) and the less intense the ones at 5.0, 4.8 and 4.7 ppm (highlighted by red arrows). The increasing peaks were related to the cyclic acetals while the decreasing ones to the acyclic acetals, undergoing conversion into cyclic derivatives over time. We then did a second NMR analysis on AcDEX_20min and AcDEX_40min. After addition of DCl, the spectra were collected at 0, 20, 30, 60, 120, 150 minutes and 24 hours to follow the hydrolyzation of the

cyclic and acyclic acetals. We found that for AcDEX_20min the ratio between methanol and acetone was 1:2, respectively, therefore there were mostly acyclic acetals, whereas for AcDEX_40min the ratio was 1:4, hence mostly cyclic. Consequently, to do the encapsulation investigations we decided to use AcDEX_20min to avoid the high hydrophobicity related to the presence of the cyclic acetals.

To encapsulate pSi-COOH microparticles with AcDEX we applied the nanoprecipitation method that consists in the controlled injection of an organic water-miscible solution containing a high concentration of the polymer and the particles into an aqueous solution (where neither the polymer nor the particles are soluble), under mild stirring, containing a surfactant to help keeping the particles dispersed. The encapsulation happens through rapid solvent diffusion and precipitation. The solvents are then removed through evaporation under reduced pressure[98].

To perform the nanoprecipitation, we used a fluxmeter to obtain a controlled injection with a 3 mL/h flux rate connected to a syringe containing pSi-COOH microparticles (2 mg/mL) mixed with an AcDEX ethanol solution close to the saturation (10 mg/mL). The syringe needle was immersed in the aqueous solution containing 1% w/v of polyvinyl alcohol (PVA, 31–50 kDa, 1mg/mL) as surfactant. The setup of the process is reported in Figure 2.27.

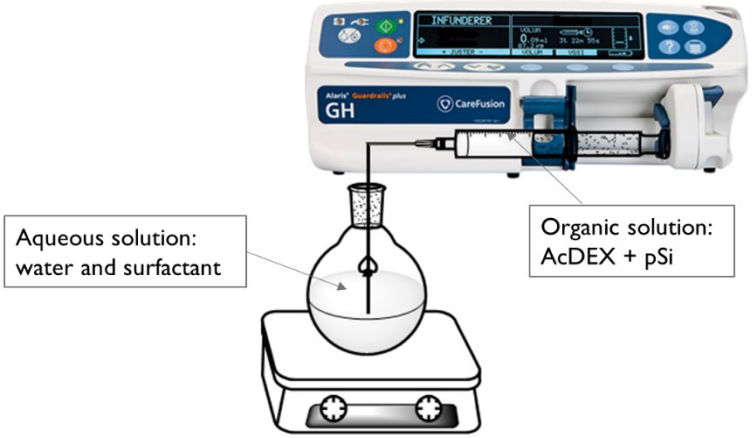

Figure 2.27. Representation of the setup used for the nanoprecipitation process.

Once the injection was concluded we evaporated the solvents by means of a rotary evaporator, washed five times with water to remove the PVA, freeze-dried and analysed the sample by means of DLS (Figure 2.28) and TEM (Figure 2.29).

It is worth noting that even if PVA was removed by washing thoroughly with water it is possible that some residues are still present within the samples, however, PVA presence should not interfere with the sample performance. On the contrary, it was reported by Shkodra-Pula *et al.* that PVA residues are able to stabilize the particles since it acts as cryo-protectant and it inhibits aggregation during the freeze-drying process. Moreover, beside being non-toxic it can protect the particles from enzymatic hydrolysis[99].

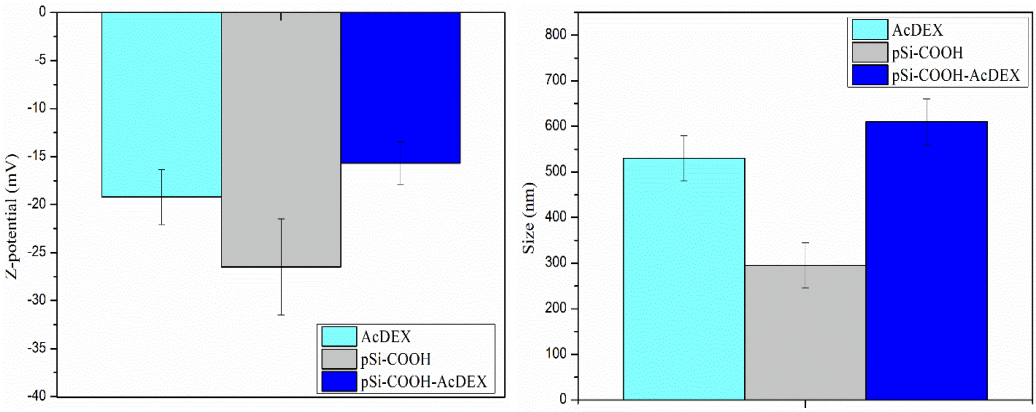

Figure 2.28. Z-potential and size distribution of pSi-COOH microparticles before and after encapsulation with AcDEX.

After the encapsulation the surface charge resulted negative (from -27 ± 5 of pSi-COOH to -16 ± 2 mV) and similar to the one of AcDEX (-19 ± 3 mV), in the same way the size of the samples after the encapsulation was higher compared to bare pSi-COOH and similar to the average diameter of AcDEX (from 530 ± 50 nm of bare AcDEX to 610 ± 50 nm of pSi-AcDEX).

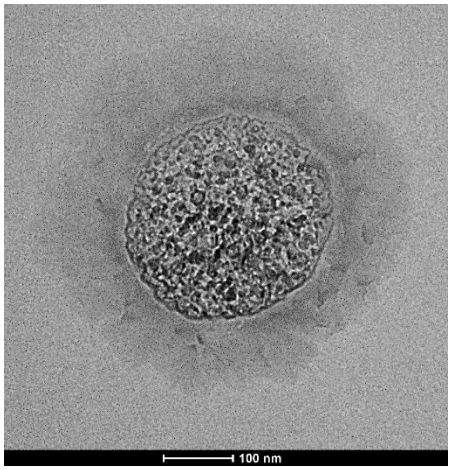

Figure 2.29. TEM image of a pSi-COOH microparticle encapsulated with AcDEX.

In the TEM image reported it is possible to notice the porosity of the pSi-COOH microparticle surrounded by the polymer layer that, since the sample was not stained before the TEM analysis, results almost transparent because its low electron density. Due to the low concentration of PVA in the nanoprecipitation process medium (1% w/v) and the intense washings done to remove it, we can reasonably exclude that the coating shown in the TEM image is made of the surfactant. PVA, indeed, has been reportedly used to coat pSi nanoparticles together with PLGA, however in higher concentrations (45 mg/mL) and with a longer reaction time (20 hours)[100], thus unmatching our above-mentioned method.

The drawback of using nanoprecipitation as encapsulation method is the lack of control of the size of the particles that leads to a wide size distribution. An alternative solution would be the use of a microfluidic device as already successfully demonstrated by Fontana *et al.*[96]

Hyaluronic acid

Hyaluronic acid (HA), also known as hyaluronan, is a natural, biodegradable and biocompatible polymer composed of repeated disaccharide units of D-glucuronic acid and N-acetyl-D-glucosamine linked by β (1–3) and β (1–4) glycosidic bonds, part of the glycosaminoglycan family. It does not show toxicity nor immunogenicity and it is non-inflammatory[101]. Its structure enables cross-linking and the possibility to conjugate and encapsulate several kinds of molecules. HA is a major component of the extracellular matrix and it is involved in several cellular mechanism such as innate immunity, wound healing, proliferation, regulation of cell adhesion, cell migration[102]. Thanks to its ability to easily bind water molecules and to form gels, it finds application in the cosmetic industry and surgery[101].

However, it has attracted the interest of many researchers because of its ability to target cluster of differentiation-44 (CD44), its main membrane receptor[103]. CD44 is a cell-surface glycoprotein that can be found in every mammalian cell that is involved in several biological functions like cell adhesion, cell migration, modulation of cells interaction. Moreover, the receptor is over-expressed in solid tumors such as lung, pancreatic, prostate and triple-negative breast cancer. Therefore, the application of HA for anticancer therapy has been investigated with the aim of targeting CD44 and limiting the accumulation of anticancer drugs in healthy cells, improving

their delivery and the cancer cell uptake with very low toxicity[102]. All these features make HA a very interesting material for drug delivery.

HA binding with other molecules can happen either through covalent or electrostatic interactions. In the first case the binding is stronger and HA needs to be activated before being coupled, in the other case the binding is weaker but it is ready to be conjugated and it does not involve the use of chemicals.

Therefore, as a first step of our investigations of HA as a targeting moiety for pSi drug delivery system, we compared the coating of the pSi particles with HA activated and non-activated and we optimized the coating by testing different weight ratios.

To study the optimization of the HA coating we used aminated-pSi particles because the aminic group enabled the electrostatic interaction with the carboxylic groups of the polymer, a schematic representation of the process is pictured in Figure 2.30.

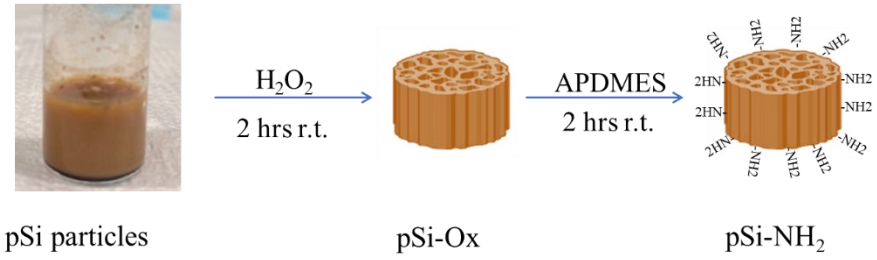

Figure 2.30. Schematic representation of the amination process.

We started by sonicating pSi flakes overnight at room temperature (r.t.), followed by three washings with ethanol (EtOH). The particles were then resuspended in hydrogen peroxide to oxidize them, sonicated, mixed for 2 hours at r.t. and then washed three times with EtOH. To obtain the functionalization with aminic groups, the oxidized pSi particles were mixed with 3-aminopropyldimethylethoxysilane (APDMES) for two hours at r.t. and then washed one time with a 50% v/v EtOH solution and twice with EtOH. The confirmation of the success of the amination was confirmed by measuring the surface charge by DLS: it resulted to be +26 ± 5 mV. Meanwhile, during the amination process, HA activated and non-activated were prepared simultaneously. HA acid was solubilized in distilled water (5 mg/mL) and stirred energetically for two hours at r.t., the HA solution was then split in two vials: one for the non-activated and the other one for activated. The first was

ready to be tested, the second one needed a further step for the activation. Acetonitrile was added drop wise (650 µL) followed by 2.5 µL of N-methylmorpholine (NMM) and 2.5 mg of 2-chloro-4,6-dimethoxy-1,3,5-triazine (CDMT) and stirred for two hours. The coating of the pSi-NH_2 particles was tested for three mass ratio HA:pSi 5:1, 3:1, 1:1 by stirring vigorously the particles with the polymer, both activated and non-activated, at r.t. for two hours.

To investigate which HA gave a more stable coating, we washed the coated-pSi particles for five times and analyzed the surface charge of the particles after every washing by means of DLS to investigate the possible agglomeration or the loss of the coating: the smallest variation in Z-potential, the more stable the coating. The Z-potential comparison is reported in Figure 2.31.

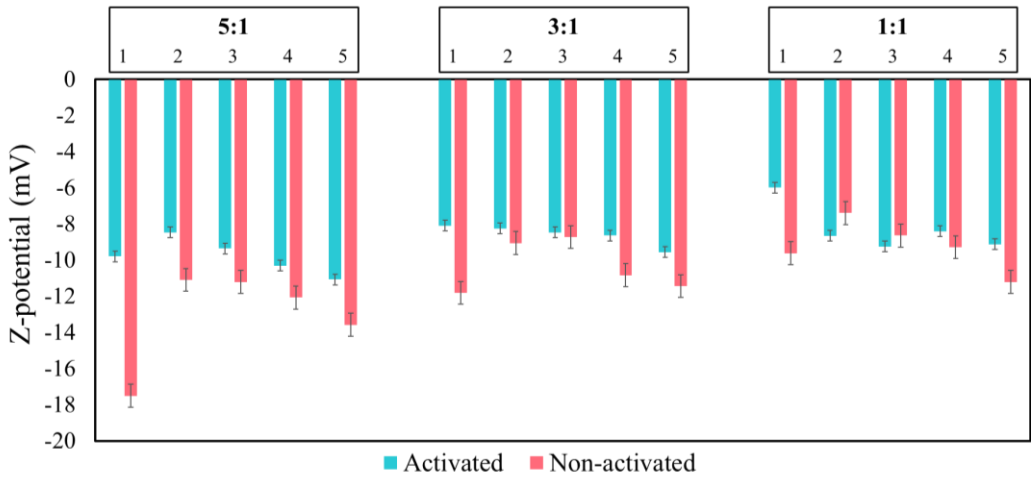

Figure 2.31. Z-potential comparison for HA coating with and without activation during five washings.

The negative surface charged confirmed the success of the coating, moreover, after five washings the less variable surface charge were the one related to the ratio 3:1 and to the ratio 1:1. In Figure 2.32 are compared the size distribution variations and thickness of the coating by means of DLS and SEM, respectively, of the ratio 3:1.

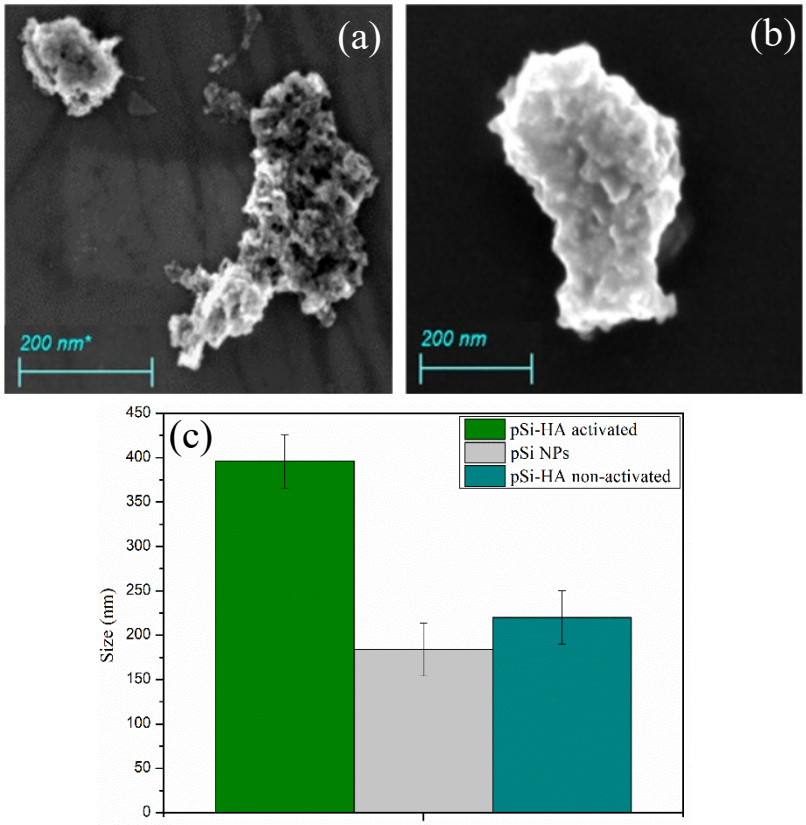

Figure 2.32. Panel (a) and (b) SEM images of pSi coated with HA non-activated and activated, respectively. Panel (c) size distribution of pSi coated with HA non-activated and activated.

As it is possible to observe from the SEM images, the coating is thicker when the HA is activated (panel b) probably due to the strength of covalent binding that leads to the conjugation of a higher amount of polymer. This is confirmed also by the size measurements: pSi particles after the coating with non-activated HA have an average diameter similar to the one of the bare pSi (220 ± 30 nm vs. 184 ± 40 nm, respectively), while the coating with the activated version leaded to obtain a size that is almost the double compared to the bare pSi (396 ± 30 nm vs. 184 ± 40 nm of pSi).

Moreover, since the Z-potential measurements did not differ too much between the activated and the non-activated and since the thicker coating might be an obstacle for the release of the payload of the pSi particles, the best solution is to not activate the HA and, thus, to have a faster process with less chemicals involved.

To prove the efficiency of the HA coating to prevent the particles aggregation, we measured the size of the pSi particles coated with non-activated HA (3:1) every twelve hours for three days (Figure 2.33).

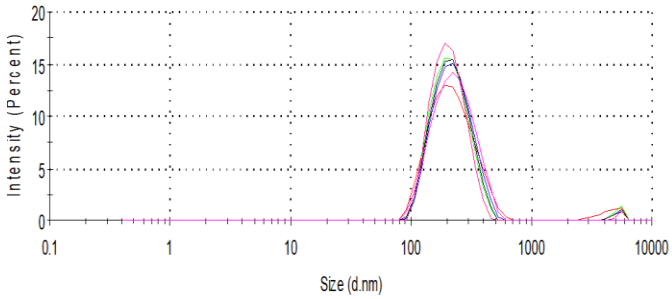

Figure 2.33. Size distribution of HA-coated pSi particles over 72 hours.

The size distribution was constant during the 72 hours (220 ± 30 nm), therefore we can conclude that the HA helped avoiding particles aggregation.

2.C. Conclusions

The pSi-COOH microparticles samples under investigation were prepared with the well-established protocol of electrochemical etching in HF:ethanol solution. From a chemical and structural point of view, we obtained a good reproducibility among the fabricated samples. Concerning the structural properties and the average size of the microparticles, the results obtained by TEM images analysis are consistent with the results of DLS technique, despite the difference in sensitivity and the limitation in the statistical significance of the analyzed images.

The surface modifications discussed in this chapter served as starting point for the following experiments related to the applications in the anticancer therapies:

- surface charge modification with CTAB
  - → binding of docetaxel (Chapter 4 – Chemotherapy)
  - → coating of pSi-DOX with hyaluronic acid (Chapter 4 – Chemotherapy)
- surface charge modification with poly-L-Lysine
  - → binding of doxorubicin (Chapter 6 – Gene therapy)
  - → binding of siRNA after doxorubicin loading (Chapter 6 – Gene therapy)
  - → coating with hyaluronic acid (Chapter 6 – Gene therapy)

Moreover, the encapsulation with acetal-modified dextran and hyaluronic acid resulted in the addition of new functionalities to our drug delivery platform:

- Acetalated dextran → ability to respond to pH variations
- Hyaluronic acid → ability to target specific tumorigenic cells (prostate, lung, triple-negative breast and pancreatic cancer).

CHAPTER 3

Porous silicon: infiltration with magnetic nanoparticles

3.A. Background and introduction

3.A.1 Magnetic resonance imaging: principles and contrast agents

Magnetic resonance imaging (MRI) is a primary investigation technique that has been used in clinics for medical diagnosis for more than 40 years[104]. Its success resides in the absence of invasiveness and the high resolution. Indeed, thanks to its deep penetration, it can give information about the internal structure and functionality of human and animal body by employing ionizing electromagnetic radiation without exposure-related hazard. The application of MRI to human and animal bodies is feasible because they are mainly composed of water, H_2O. Therefore, thanks to the use of RF (radiofrequency) signals in presence of an external magnetic field, it is possible to obtain the nuclear magnetization of the hydrogen ions (H^+ i.e., protons) available in the body-water and, through processing of the signals, create high-quality images of the body in any plane[105]. The working principle of MRI is summarized in Figure 3.1.

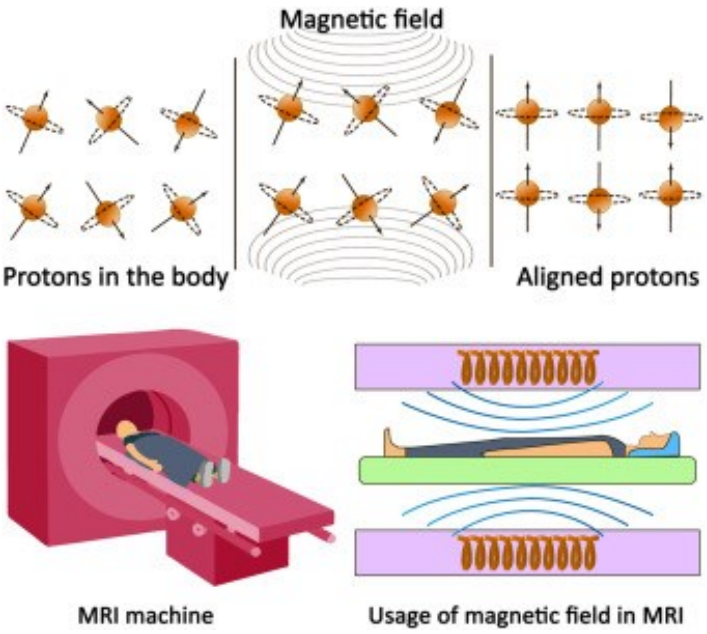

Figure 3.1. Visual representation of the working principle of MRI technique[106].

To obtain MR images, the patient is placed inside a large magnet (i.e., the MRI scanner) that creates a strong external magnetic field forcing the nuclear spin of the protons of the body under investigation to align with it. Then, the application of an RF pulsation causes the perturbation of the magnetization of the protons spins. As soon as the RF is turned-off, the protons tend to return to their equilibrium state and while realigning with the magnetic field they release energy that is collected and transformed in contrast images[106].

In particular, when RF pulsation stops, the return to the equilibrium state generates two types of proton relaxation, as shown in Figure 3.2:

- Longitudinal relaxation time (T_1), which indicates the time needed for the protons to return parallel to the external magnetic field direction (z axis)
- Transverse relaxation time (T_2), which indicates the time needed for the protons diphase (x, y plane)

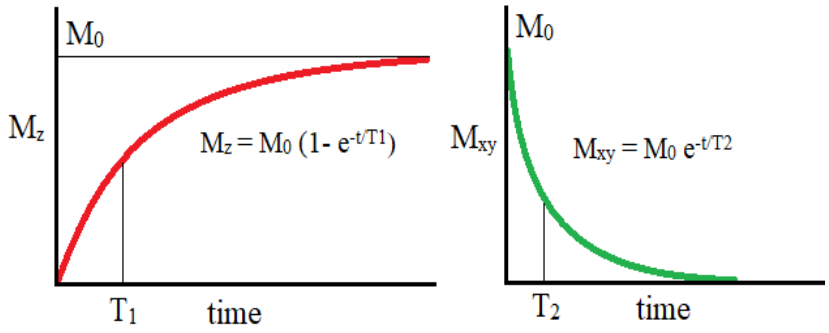

Figure 3.2. Proton relaxation caused by the RF turning off: longitudinal (T_1) and transversal (T_2) relaxation times determination.

The two relaxation times are characteristic for every tissue composition and their variation between the tissues provides the main sources contrast, therefore, it is generally possible to distinguish the contrast between healthy and non-healthy areas. In Figure 3.3 is reported an MRI scan where it is shown the opposite contrast between a T_2-weighted image (panel a) and a T_1-weigheted image (panel b).

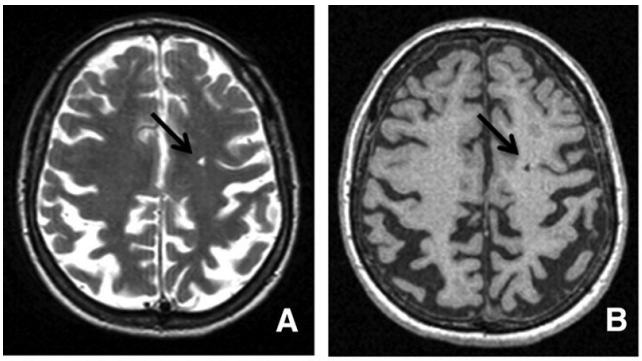

Figure 3.3. MRI scans based on T2 (panel a) or T1 (panel b) relaxation times. Arrows indicate cavities containing infarcts[107].

As it is possible to notice, MR images have high spatial resolution and are characterized by contrast between the soft tissues that comes from the sensitivity to water molecules (i.e., protons) concentration and the differences in the relaxation times.
In clinics, if for some tissues the variations of T_1 and T_2 are too small to be detected, it is required the use of exogenous materials, called contrast agents (CAs), to increase the contrast between the analysed tissues and the surroundings. Typically, CAs shorten prominently one of the two relaxation times throughout coordination with water molecules, thus, they are categorized as T_1 or T_2 contrast agents. The first are defined positive CAs, they enhance the signal intensity, providing a brightened positive contrast image.
The latter, as the opposite, are called negative CAs, they decrease the signal intensity resulting in a darken negative contrast image[108]. Characteristic for every CAs is the relaxivity, that is defined as the degree of relaxation rate of the water present in the tissues and is termed r_1 or r_2 for either T_1 or T_2 respectively[109]:

$$\frac{1}{T_1} = r_1 \times [CA_1] \qquad or \qquad \frac{1}{T_2} = r_2 \times [CA_2]$$

They can be obtained by a linear fit of the relative relaxation rate ($1/T_1$ or $1/T_2$) as a function of the contrast agent concentration [CA], as shown in Figure 3.4.

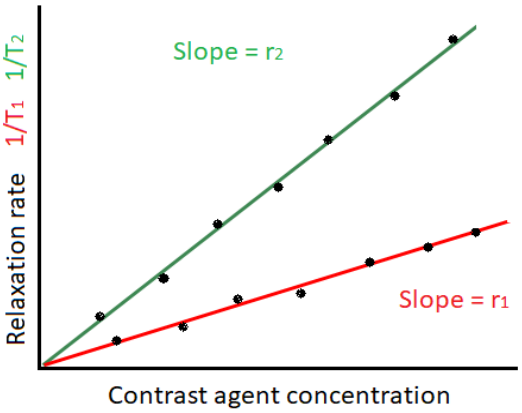

Figure 3.4. Contrast agent relaxivity obtained from the relaxation rate against the CA concentration.

The CAs most employed in clinics are positive contrast agents made with paramagnetic chelates of lanthanide metals (i.e., gadolinium), being the paramagnetic ions close to the water molecules results in their coordination thus shortening the longitudinal relaxation time and increased contrast. Even if they are commonly used, gadolinium(III) chelates show some issues such as low detection sensitivity, toxicity and short blood circulation time[110]. Therefore, alternatives to overcome the long-term safety of these molecules are currently investigated from several research groups, such as nanoparticles and metal complexes with magnetic properties, such as super paramagnetic iron oxide nanoparticles (SPIONs) or magnetic ions entrapped in carriers (e.g., micelles or liposomes)[108]. Moreover, systems able to deliver CAs to a specific target and stimuli-responsive carriers of CAs have been developed to enhance their efficacy[111]. Figure 3.5 summarize the alternatives to gadolinium(III)-based chelates to increase the contrast in MRI.

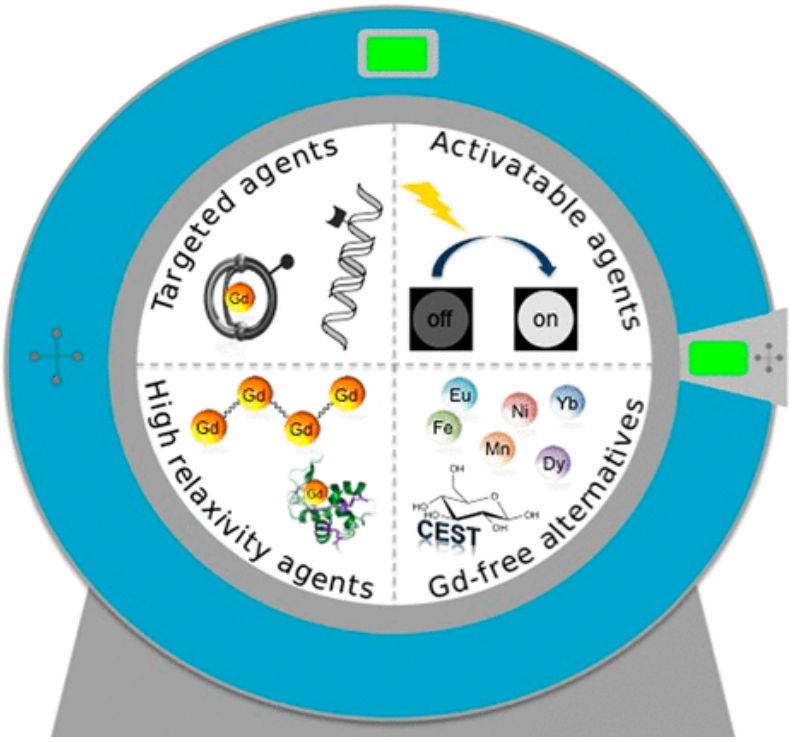

Figure 3.5. Representation of the available alternatives to gadolinium-based CAs[111].

Alternatives to gadolinium(III)-based CAs aim not only at lowering the well-known toxicity that characterize the current ones, by increasing the relaxivity and avoid the metal ion release, but also at giving new useful properties. Therefore, molecules able to alter their relaxivity in response from external stimuli (e.g., pH enzymatic activity, ion flux, temperature, redox potential) such as Yb-DO3A-oAA , a redox potential-responsive agent able to detect NO in the presence of O_2 through an irreversible covalent conversion to binuclear species bridged through a triazene thus losing its contrast ability, or systems able to target specific molecules, such as the fibrin-targeting contrast agent EP-2104R that by selectively binding the protein formed by the enzyme thrombin were prolonging the local contrast enhancement thus efficiently detecting thrombus in carotid arteries, heart, deep veins, aorta, pulmonary emboly. Moreover, molecules able to generate MR image contrast through different mechanisms such as chemical exchange saturation transfer, direct detection and relaxation are being investigated[111].

3.A.2 Magnetic nanoparticles in diagnostics

During the last decades, magnetic nanoparticles have been extensively studied for diagnostic purposes because of their unique properties. Not only their capacity to

generate magnetic fields and to influence their surroundings, resulted in their application in MRI, but also their ability of being guided through an external magnetic field makes them interesting candidates as drug delivery systems and as a tool in cell separation and cell tracking, furthermore their ability to be heated subsequently the action of an oscillating magnetic field can be exploited for anticancer photodynamic and magnetic hyperthermia therapies. In addition, they are biocompatible at low-cost manufacturing[112].

Among all, SPIONs gained attire over the years thanks to their low toxicity, biodegradability and easy fabrication, but mostly because of their paramagnetic nature. These materials, indeed, are characterized by different magnetic domains with their own magnetic moment towards different directions, thus in absence of an external magnetic field they do not show magnetic abilities. On the contrary, when a magnetic field is applied, the domains become aligned with the filed leading to the exhibition of their magnetic properties. Once the magnetic field is removed their magnetic features cease[113]. Moreover, their small size allows to be less likely taken up from the macrophages thus allowing an easier biodistribution. This led to the approval from the FDA of several formulations based on those nanoparticles, such as GastroMARKT™, Umirem®, Feridex®/Endorem®, while there are many others in ongoing clinical trials[114]. Their ability to modify the relaxation time of the water molecules they interact with, led to their application as CAs. In particular, they are classified as negative contrast agents because they darken the images by acting on T_2.

However, many studies proved that, at high concentrations, they can cause toxicity or cytotoxicity, plus they tend to agglomerate, moreover they are hydrophobic and non-water soluble. Therefore, they are usually administered once engineered with proper surface modifications and/or coatings with organic and inorganic materials such as micelles, liposomes, porous particles, polymers and hydrogels (e.g., PEG, PLGA, chitosan, dextran), with the aim of stabilizing them, avoiding agglomeration and slowing their degradation and introducing hydrophilic properties[106,115]. Figure 3.6 summarize some available carriers for magnetic NPs.

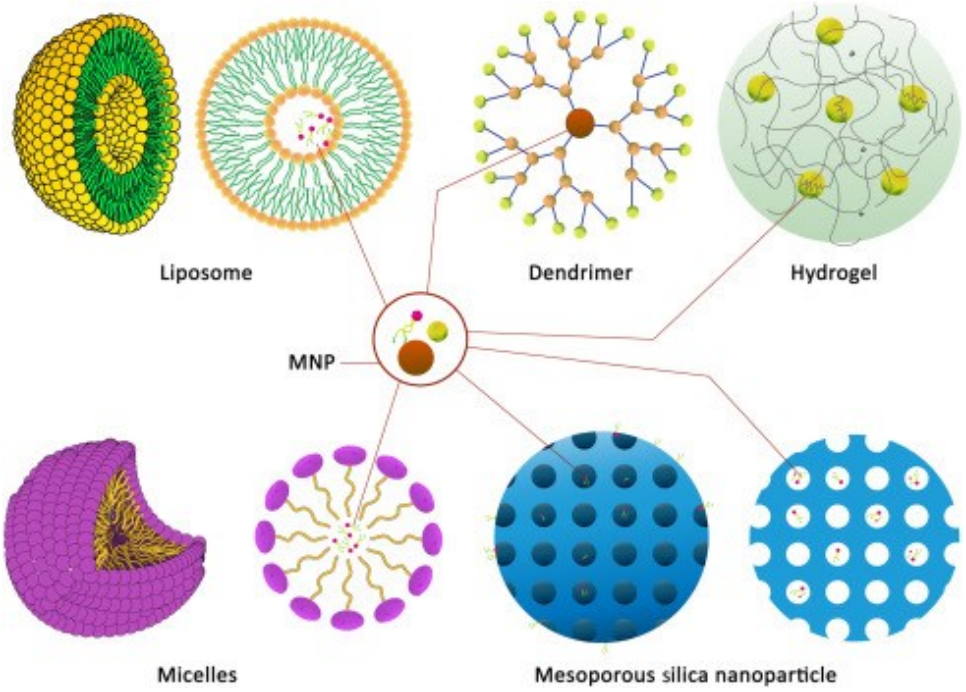

Figure 3.6. Representation of some of the available coatings for magnetic NPs.

On this matter, when Malvindi *et al.* conducted a study on A549 and HeLa cells to compare the cytotoxicity of bare SPIONs and thin silica shell-coated SPIONs they found that the in situ degradation of bare iron oxide NPs was high. On the contrary, by modifying the surface of the NPs (i.e., with a coating) it was possible to obtain lower oxidative stress and iron homeostasis alteration, compared to bare SPIONs, without affecting their cell internalization efficiency. In addition, engineering the surface allows to avoid their oxidation in air that can cause to lose the magnetic ability, plus a coating open the possibility to bind drugs and targeting ligands[116].

The delivery of SPIONs by a drug delivery system can have several benefits for both the carrier and the payload. On one hand it helps improve the properties and abilities of the loaded magnetic nanoparticles and on the other it gives interesting new features to the carrier. Indeed, the presence of nanoparticles with magnetic properties on a system that is already functional to deliver drugs, enables their application not only as a therapy tool but also in diagnostics. Hence, the development of such systems could lead to the application in the field of theranostics (therapy and diagnosis)[108].

3.A.3 SPIONs and porous silicon

In this regard, porous silicon, thanks to its high porosity, biocompatibility, high surface to volume ratio and tunable surface, stands as a suitable platform for the delivery of magnetic nanoparticles such as SPIONs. By reviewing the literature about the association of pSi with iron oxide NPs it is possible to find some successful studies that are worth noting. Gu *et al.* reported the trapping of magnetite NPs in the porous structure of the silicon-derived nanoparticles by means of a thermal oxidation/dehydration procedure followed by the loading of the anticancer drug doxorubicin[117]. While Serda *et al.* managed to entrap a large amount of SPIONs inside the protective nanopores of discoidal pSi microparticles and discovered that not only the relaxation times became shorter, depending on the iron oxide NPs concentration, but also the delivery to target sites was facilitated[118]. In another case, pSi nanorods were successfully coated with SPIONs for magnetic guidance and decorated with a peptide to enable targeting and improve their internalization by the cancer cells[119].

With the goal to overcome the issues related to the administration of bare SPIONs, a few years ago our group started to investigate the infiltration of SPIONs within the pores of pSi-COOH microparticles. To begin, we chose commercial magnetic nanoparticles to work with more applicative and reproducible experiments and to demonstrate the feasibility of the combination of porous silicon and SPIONs. These fundamental preliminary results are briefly reported in the following paragraph since they served as a foundation for the further investigations done within this thesis work[10].

3.B. Results and discussion

3.B.1 Preliminary investigations on commercial SPIONs in pSi

When approaching to the study of pSi-COOH combined with iron oxide NPs, our aim was to add another important functionality to our system: magnetic ability. Indeed, the addition of magnetic properties would allow the traceability of pSi particles by MRI, thus the application in diagnostics.

For this purpose, an infiltration protocol was optimized to efficiently decorate luminescent pSi microparticles with commercial SPIONs that are characterized by a high magnetic susceptibility, which allows a stronger and more rapid response to an external magnetic field.

During the characterization of the just bought magnetic material we realized that, as the opposite on what was declared by the company, it had a negative surface charge (-25 ± 5 mV) (due to the presence of an anti-agglomerant salt). That was incompatible with the electrostatic binding of our pSi microparticles. The latter, indeed, bear carboxylic groups on the surface, making it negative (-30 ± 5 mV), thus the need to find a molecule able to act as a bridge between the two. The choice fell on cyclohexane diamine ((±)-trans-1,2-Diaminocyclohexane), a molecule that bears two amino groups that, after being protonated, can connect the magnetic and the pSi negatively charged surfaces through an electrostatic binding. The infiltration method is schematized in Figure 3.7.

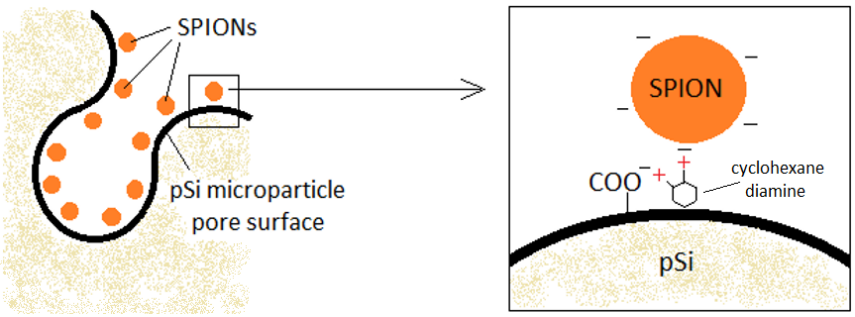

Figure 3.7. Representative portion of the pSi surface, not in scale, and pSi-SPIONs interaction.

To confirm the effective infiltration of SPIONs within pSi-COOH, we analyzed the samples with TEM and S/TEM that allows to combine the morphological investigation with composition analysis by EDX mapping. We obtained a map (Figure 3.8) as a function of the atomic elements' presence (i.e., Si, O, Fe).

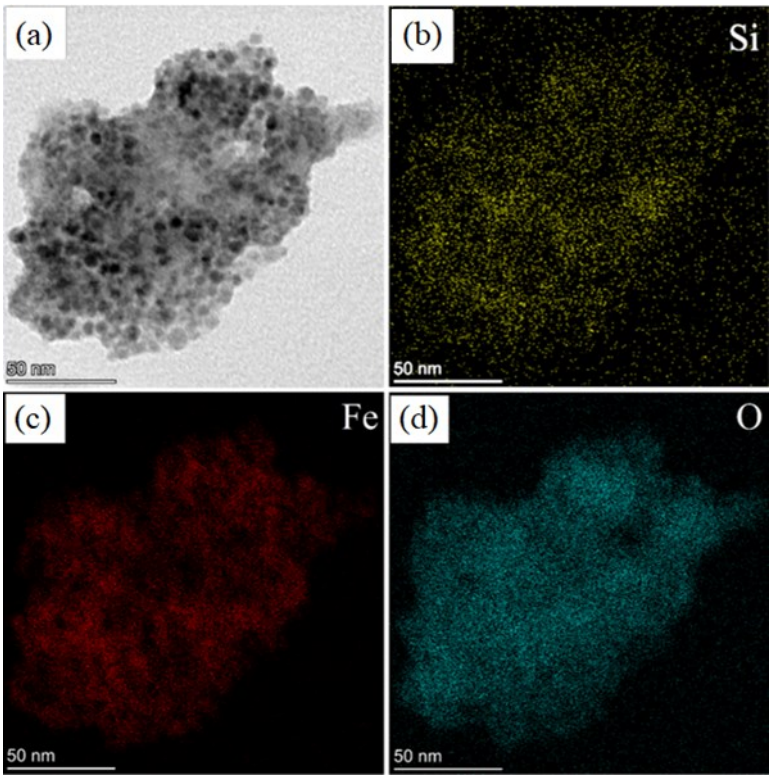

Figure 3.8. STEM (BF) images of a single pSi-SPIONs microparticle at 50 nm scale (panel a) and elemental mapping of Si (panel b), Fe (panel c) and O (panel d).

By analysis of the map of Si (panel b), Fe (panel c) and O atoms (panel d): there is a quite perfect overlap between the positions of the elements and the morphological image. The overlap between Fe and O distribution is clear and related to the composition of the SPIONs (i.e., Fe_3O_4), while the overlap between Fe, O and Si atoms (main component of the pSi structure) means that the SPIONs are on the porous silicon surface confirming the successful infiltration. Furthermore, the weakness of signal coming from the Si atoms is related to the pSi structure characterized by a lot of pores in a crystalline silicon matrix. After proving the efficacy of the SPIONs infiltration protocol and their infiltration inside pSi by electrostatically attraction, the magnetic pSi microparticles were further analyzed to deeply investigate their magnetic properties. It was first verified that the pSi-SPIONs microparticles were attracted by a magnet, as a clear evidence of the magnetic properties addition to the system (Figure 3.9).

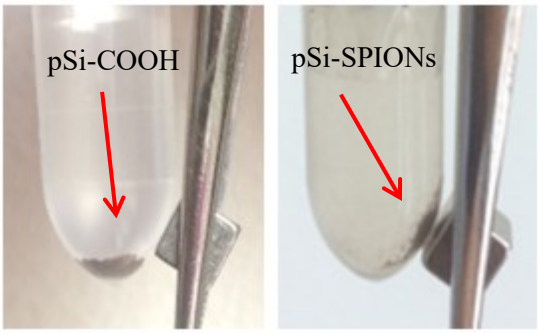

Figure 3.9. Evidence of the pSi-SPIONs microparticles magnetic properties, differently from pSi-COOH microparticles, not attracted by the magnet.

After that, according to the fact that the diagnostic application of SPIONs as contrast agents in MRI depends on their ability to modify the relaxation times of water, we investigated the magnetic parameter (i.e., the relaxivity). For SPIONs alone, the longitudinal relaxivity (r_1) resulted to be about 1.1 $(mmol)^{-1}s^{-1}$ and the transverse relaxivity (r_2) about 5.5 $(mmol)^{-1}s^{-1}$. As expected for such nanoparticles, the transversal relaxation time is higher than the longitudinal one with a r_2/r_1 ratio of about 5 (Figure 3.10, panel a). Therefore, the T_2 of bare and infiltrated pSi microparticles were investigated obtaining for magnetic pSi microparticles r_2 3.2 $(mL/mg)\ s^{-1}$. For bare pSi no variation was detected by varying the concentration. r_1 was negligible for both bare pSi microparticles and pSi-SPIONs samples, as it is shown in panel (b) of Figure 3.10.

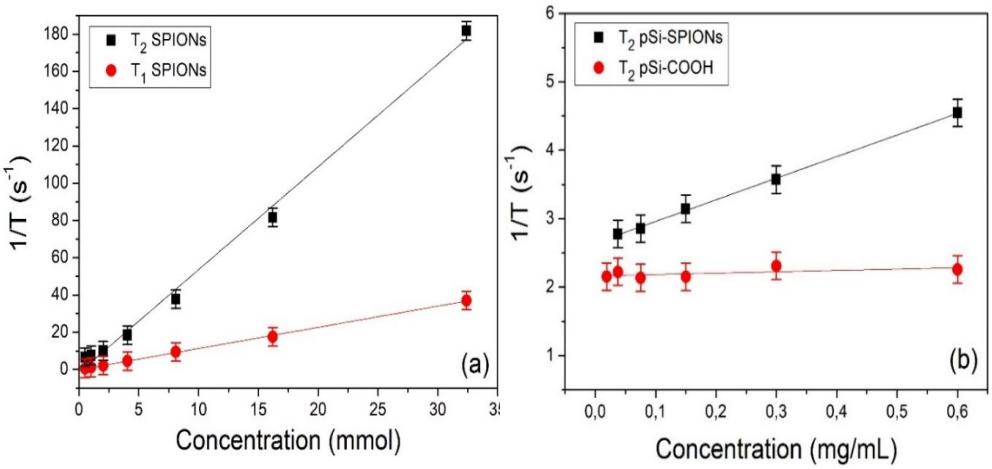

Figure 3.10. Relaxivity determination: $1/T_1$ and $1/T_2$ relaxation rates of SPIONs as a function of the iron concentration (panel a) and $1/T_2$ relaxation rate of pSi-SPIONs and pSi-COOH microparticles as a function of the microparticles concentration (panel b). In a 7T external magnetic field.

With these investigations we demonstrated the possibility to add magnetic properties to the pSi-COOH microparticles through decoration with commercial SPIONs by developing a fast and easy procedure. MRI measurements confirmed the ability of pSi-SPIONs to act as negative MRI contrast agent, with variation of the transversal relaxivity (3.2 (mL/mg) s^{-1}) compared to bare pSi-COOH microparticles, which, as expected, do not have magnetic properties nor influence on the spin's orientation.

3.B.2 Iron oxide nanoparticles synthesis

Starting from our previous findings, in collaboration with the group of Prof. Tommaso Del Rosso (NanoLaserLab, Department of Physics, Pontifícia Universidade Católica do Rio de Janeiro), we investigated the decoration of pSi-COOH microparticles with self-produced iron oxide nanoparticles that, on the contrary to the commercial SPIONs, show a positive surface charge thus allowing to perform an easier and faster procedure that avoids the use of chemicals (such as HCl and cyclohexane diamine used for the bridge) and intermediate protocol steps.

SPIONs can be produced by physical (i.e., pulsed laser ablation, ball milling, gas-phase deposition), chemical (i.e., co-precipitation, hydrothermal synthesis, microemulsions) or even biological (by means of plants or bacteria) methods. Depending on the method, they will have different characteristics in terms of size, shape and magnetic features that will then determine their future field of application[113]. Among all, pulsed laser ablation (PLA) is the procedure that was used to obtain the iron oxide nanoparticles that we studied in combination with pSi-COOH microparticles.

One of the main advantages of using PLA to fabricate nanoparticles is that during the synthesis it is possible to maintain a high control of the conditions (i.e., temperature, pressure, density), moreover it is fast, cost-effective and simple, and since it does not require any chemicals there are no harming by-products compared to a chemical method[120]. Furthermore, the NPs produced through this method present a relatively broad size distribution, this is suitable with our pSi delivery systems because it is characterized by a wide range of pore size thus allowing the infiltration of NPs with different average size.

Laser ablation consists in a laser beam irradiating a metal precursor bulk placed on the bottom of a cell containing a solution medium, such as water, ethanol, acetone, toluene, dimethyl sulfoxide. A representation of the synthesis configuration is reported in Figure 3.11.

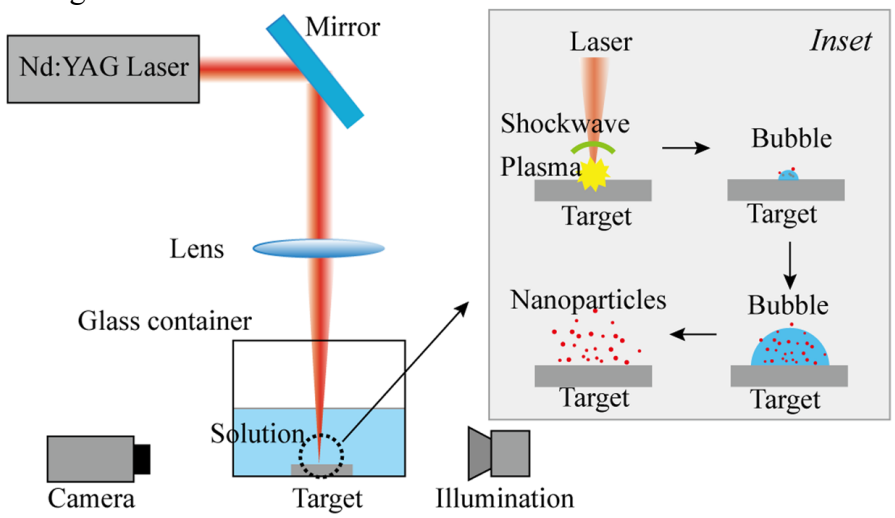

Figure 3.11. General experimental setup for the production of nanoparticles with laser ablation (Image from Hua et al.[121]*)*

The ablated material reacts with ionized species of the target and the solvent, generated from the high pressure and temperature of the plasma, to produce metastable particles through nucleation and growth. Adjusting the parameters of the laser beam, such as wavelength, diameter, intensity, allows to fabricate particles with different properties[113]. In particular, to obtain the iron oxide nanoparticles that we worked with, we used iron bulk as solid target and water as solvent medium, moreover the synthesis was done either in air or in 100% argon atmosphere, considering that the gaseous species participate to the final chemical and physical properties of the nanoparticles.

More specifically, the target material used for the synthesis of iron NPs in water was a disk of pure iron (99.99% purity). The synthesis was conducted either in air or in 100% argon atmosphere. To remove surface oxides, the disk was twice ultrasonically cleaned in ultrapure water, once in trichloroethylene, once in ethanol and once in acetone for 10 minutes each after being carefully scrubbed with sandpaper and dried in oven for 24 hours. The cleaned iron disk was then rinsed in 2 mL of ultrapure deionized water before being exposed to a nanosecond laser beam (λ=532

nm, 10 Hz pulse repetition rate) across the air-liquid interface. The experimental setup is shown in Figure 3.12.

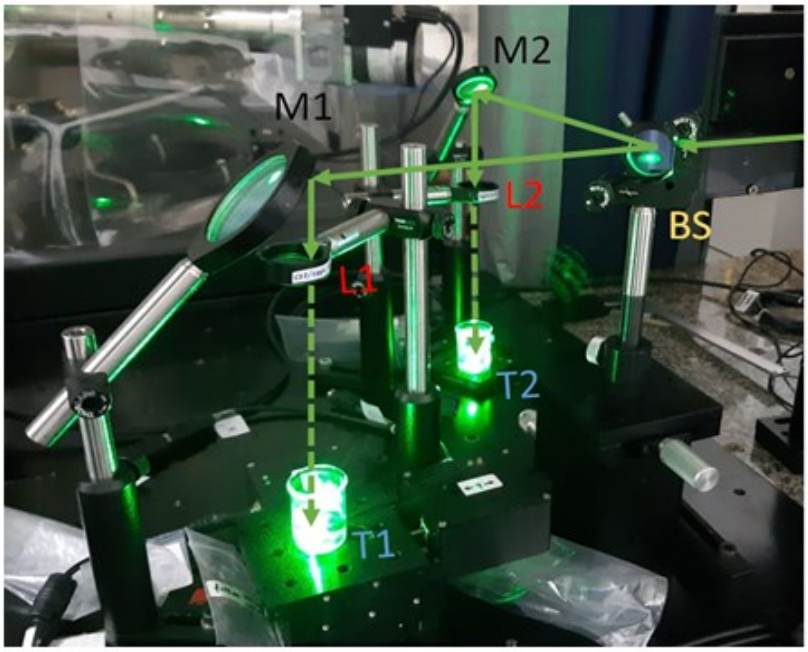

Figure 3.11. PLA experimental setup. The laser pulse is coming from the right direction to the left. BS is the beam splitter, M1 and M2 are the mirrors, L1 and L2 are the lenses, T1 and T2 are the metal targets immersed in water.

By changing the distance between the lens and the target (focal length: 13 cm), the concentration of the colloidal dispersion of iron oxide NPs was regulated to maximize the fluence of the laser beam at the sample plane on the order of 0.2–0.4 J/cm^2. The length of the laser ablation procedure was 6 hours. The synthesis was conducted in open environment (atmospheric air) and controlled environment (100% Ar). After separation of the precipitated NPs from the colloidal solution by means of a magnetic bar, the NPs were washed several times with deionized water. In each ablation cycle, the total mass-concentration ratio of NPs was under 65 μg/32 ± 2 μg/mL and measured by inductively coupled plasma mass spectrometry (ICP-MS). After the synthesis, samples (named Fe-Air and Fe-Ar for the presence of air or argon, respectively, during the fabrication) were characterized by means of TEM (Figure 3.12) the structural and morphological analysis and DLS to determine average size and surface charge.

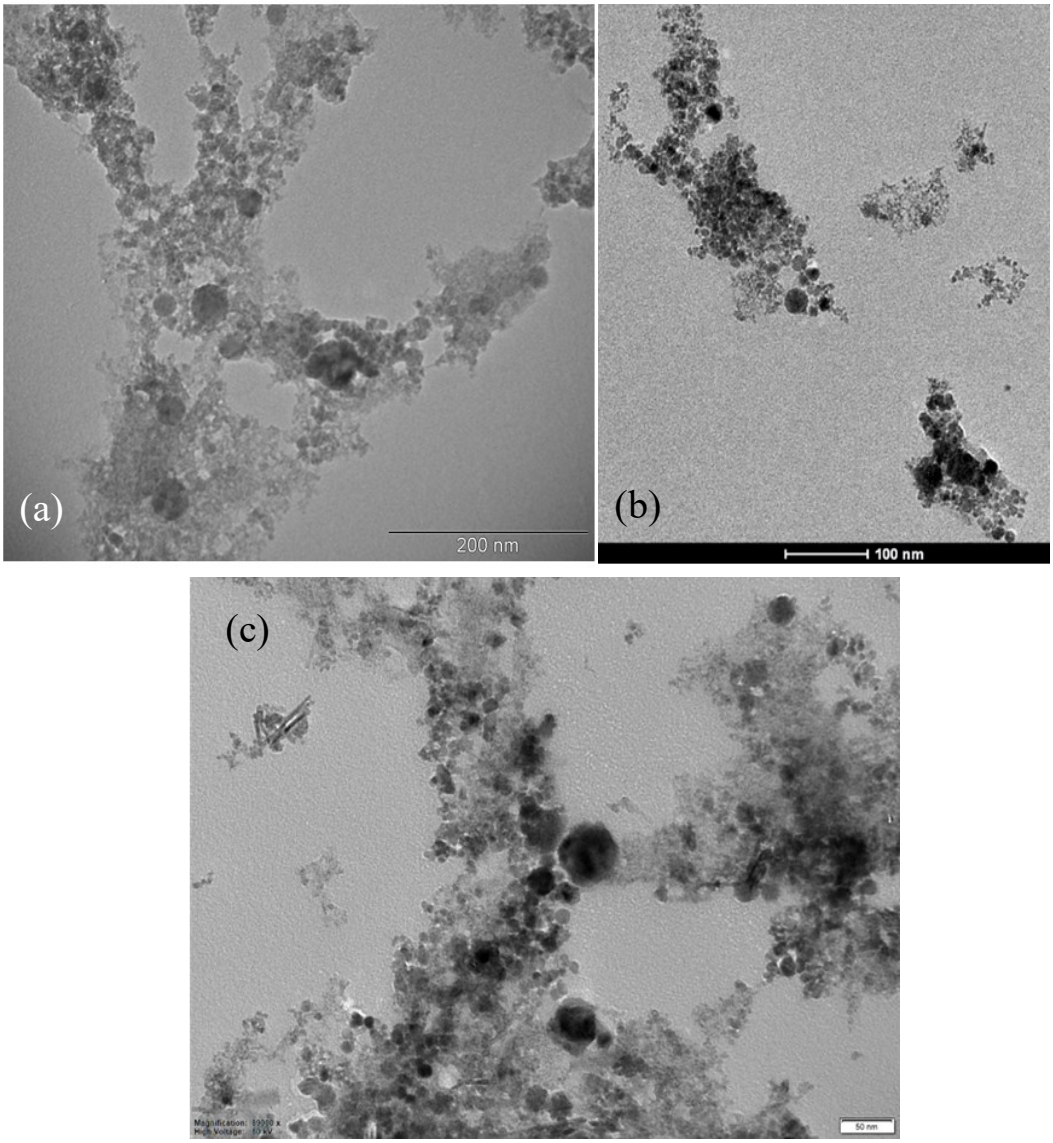

Figure 3.12. TEM Images of sample Fe-AIR (panel a, 200 nm scale) and Fe-Ar (panel b, 100 nm scale and panel c, 50 nm scale).

From TEM images we evaluated that the size was around 6 nm, although the NPs were aggregated in agglomerates that were between 100 and 500 nm. DLS measurements confirmed that the size was between 100 and 300 nm for both of the samples.

3.B.3 Sonication treatments

To allow the access of all the iron oxide NPs inside the pSi pores it was necessary to separate the agglomerated samples. Therefore, the two samples were first treated in a sonication bath for 20 minutes and measured with DLS obtaining values of 100 ± 50 nm for Fe-AIR and two populations peaked at about 90 ± 30 nm and 390 ±

100 nm for Fe-Ar, with a very low surface charge (-3 ± 5 mV for Fe-AIR and +4 ± 5 for Fe-Ar). To further reduce the agglomerated size, an ultrasonication (US) treatment for 1 minute with frequency of 20 kHz and power of 70 W, repeated for 5 cycles, was performed. After the ultrasonication, Fe-Air seemed well dispersed but, on the contrary, Fe-Ar appeared flocculated and still aggregated (Figure 10, panel (a) and (b) respectively). DLS analysis was, thus, needed to check the size and surface charge after the ultrasonication treatment. Size modifications are compared in panel (c) Figure 3.13.

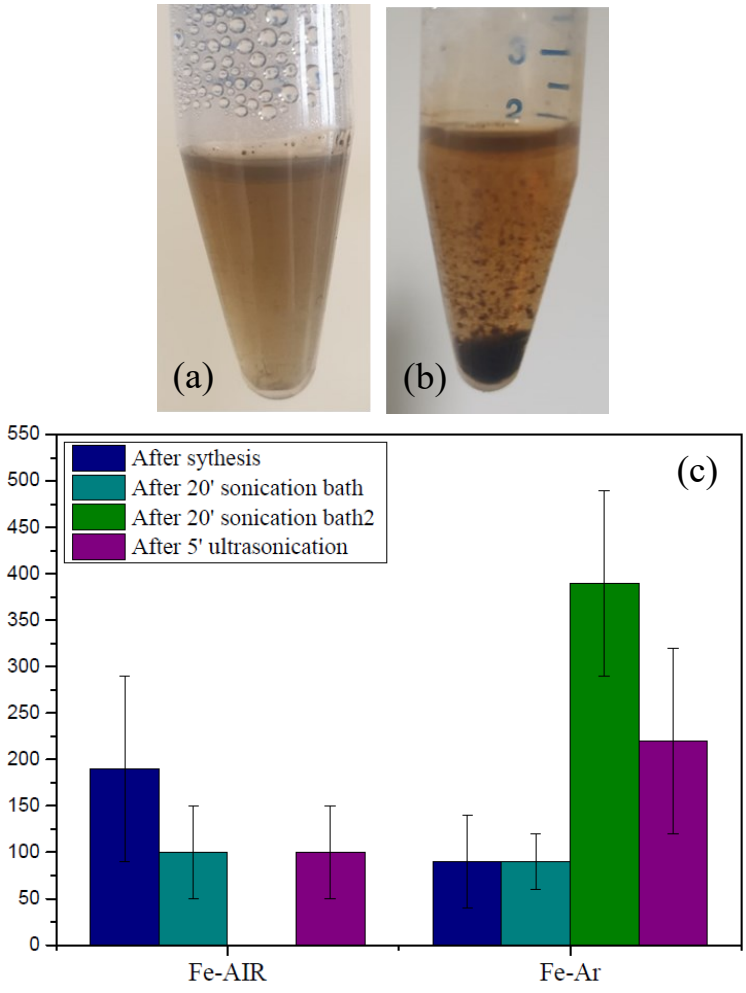

Figure 3.13. Samples Fe-AIR (a) and Fe-Ar (b) after ultrasonication treatment. Size comparison before and after treatments (c).

After the US treatment, highly positive surface charges were measured for both the samples (+22 ± 5 mV for Fe-AIR and +25 ± 5 for Fe-Ar) indicating that the NPs were effectively more dispersed than before. However, the size resulted to be around 100 ± 50 nm for Fe-AIR and around 220 ± 100 nm for Fe-Ar. For the first,

the US seemed to have worked, as hypothesized from their aspect, since the size decreased. For the latter, the diameter that is slightly bigger probably because of the flocculation.

To better investigate how the distribution of the NPs was affected by the ultrasonication treatment the samples were also analyzed by TEM (some representative images are in Figure 3.14).

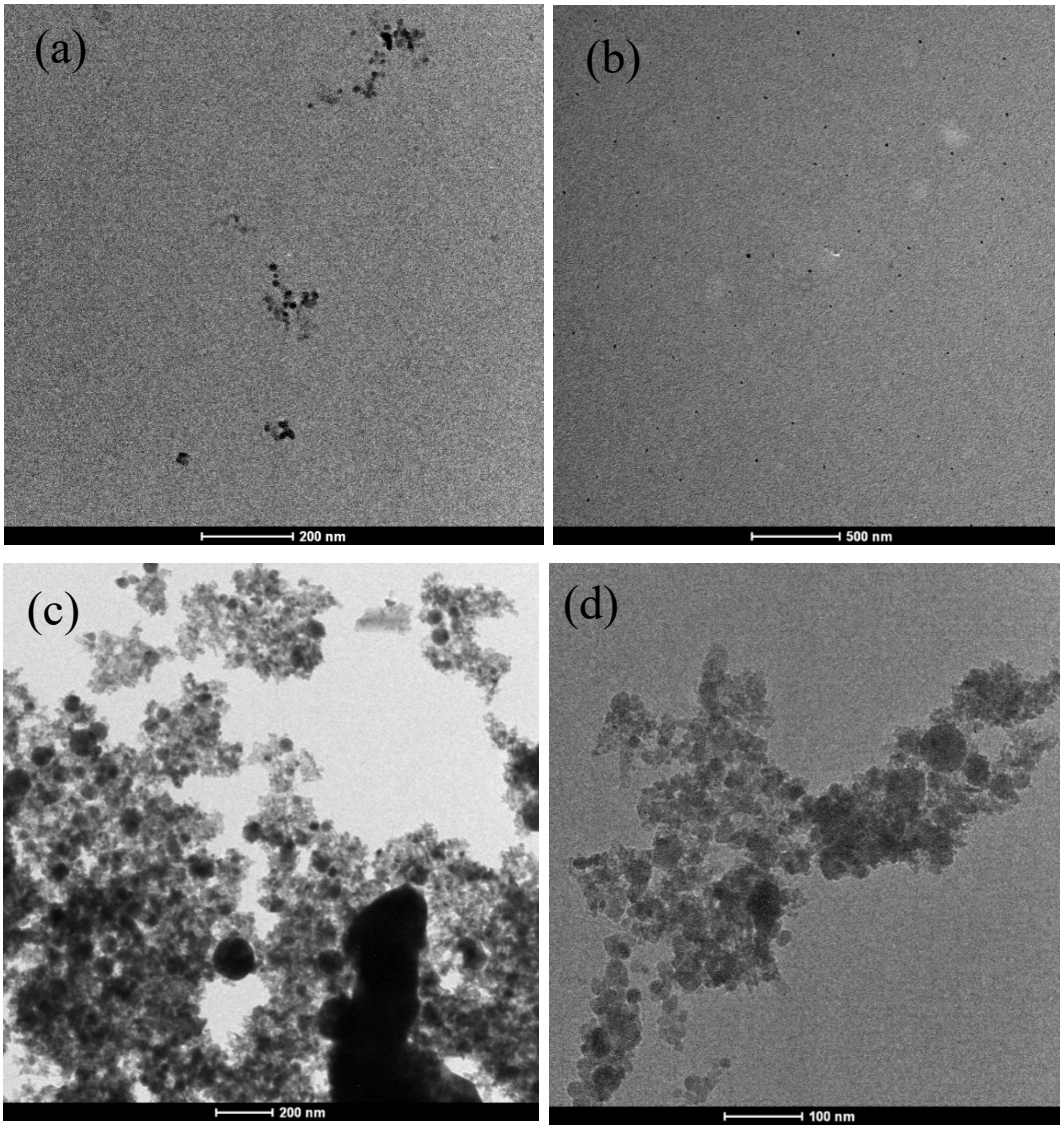

Figure 3.14. TEM Images of sample Fe-AIR after ultrasonication (200 nm and 500 nm scale, panel a and b) and sample Fe-Ar after ultrasonication (200 nm and 100 nm scale, panel c and d).

When acquiring TEM images of Fe-AIR, the sample seemed well dispersed (panel b) and the aggregates were measuring around 200 nm (panel a). However, for Fe-

Ar the presence of big aggregates of more than 500 nm seemed more spread, thus validating the data obtained from the DLS measurements. Therefore, to separate the visible micro-sized aggregates from the smaller nano-sized particles to facilitate the infiltration with the pores of the pSi microparticles, the iron oxide nanoparticles samples were left depositing overnight and the supernatant (containing the smaller particles) was collected for the two samples for the infiltration procedure.

3.B.4 Infiltration within porous silicon pores

The pSi microparticles, functionalized with carboxylic groups, were prepared according to the procedure described in Chapter 2, then dried for 5 hours in a 50 °C oven. The infiltration was performed following our previously assessed protocol. However, in this case, since the Fe NPs are characterized by a positive surface charge, there was no need to exploit a cyclohexane diamine bridge, pSi microparticles, indeed, had a surface charge of -26.5 ± 5 mV while the iron oxide nanoparticles of +22 ± 5 mV and +25 ± 5 mV for Fe-AIR and Fe-Ar, respectively. pSi microparticles were dried and resuspended in the iron oxide NPs water suspensions (0.3 mg/mL) for two days at room temperature, then washed twice with ultrapure water. A first proof of the success of the infiltration was checked by simply placing a magnet on the side of the suspension. As clearly shown by the pictures in Figure 3.15, the pSi microparticles are attracted by the magnet only after infiltration with Fe NPs (panel b).

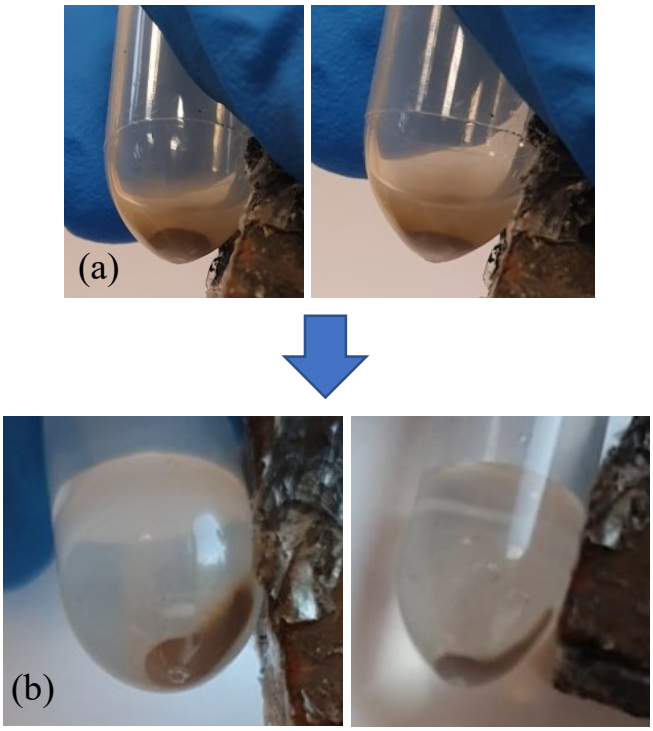

Figure 3.15. pSi microparticles before (panel a) and after (panel b) infiltration of Iron Oxides NPs (sample Fe-Ar).

From this simple test it is possible to notice that only part of the pSi microparticles is attracted to the magnet, probably because the infiltration was not homogenous for the whole sample. Moreover, the human eye obviously is not able to distinguish nano-sized particles, consequently, it was necessary to perform a deeper analysis by TEM to have a comprehensive view of the structural morphology of the infiltrated samples. TEM images acquired for pSi microparticles infiltrated with Fe NPs synthetized in air and in argon are shown in Figure 3.16 panel a and b, respectively.

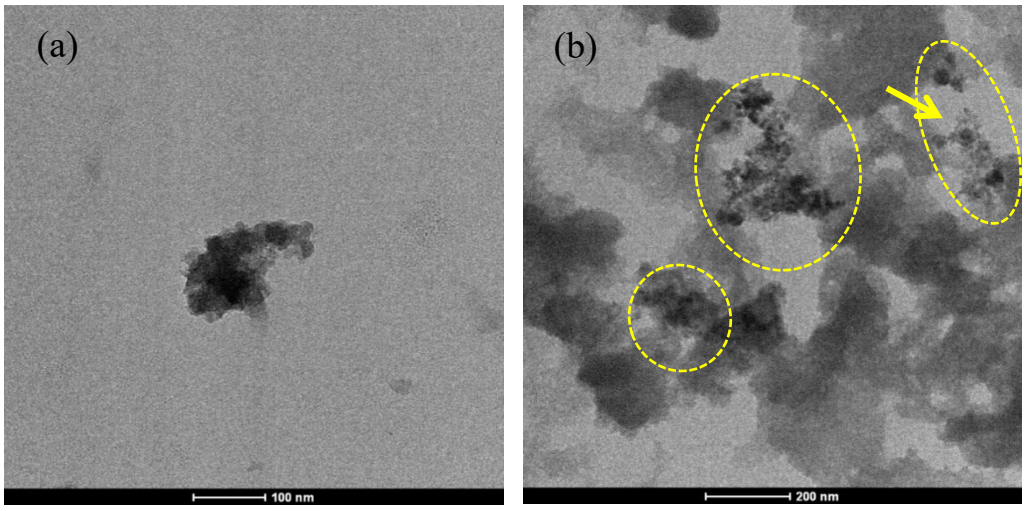

Figure 3.16. TEM images of pSi microparticles infiltrated with sample Fe-AIR (panel a, 100 nm scale) and sample Fe-Ar (panel b, 200 nm scale).

By observing the TEM images, it is possible to deduct that the Fe NPs are partially infiltrated in the pSi, as it is may be noticed in the highlighted areas in panel (b) of Figure 3.16. This is consistent with the pictures in panel (b) of Figure 3.15: part of the pSi it is not attracted to the magnet thus, it is supposedly non-bonded with iron oxide NPs. Moreover, size and surface charges after infiltration were checked with DLS (Figure 3.17 and 3.18, respectively).

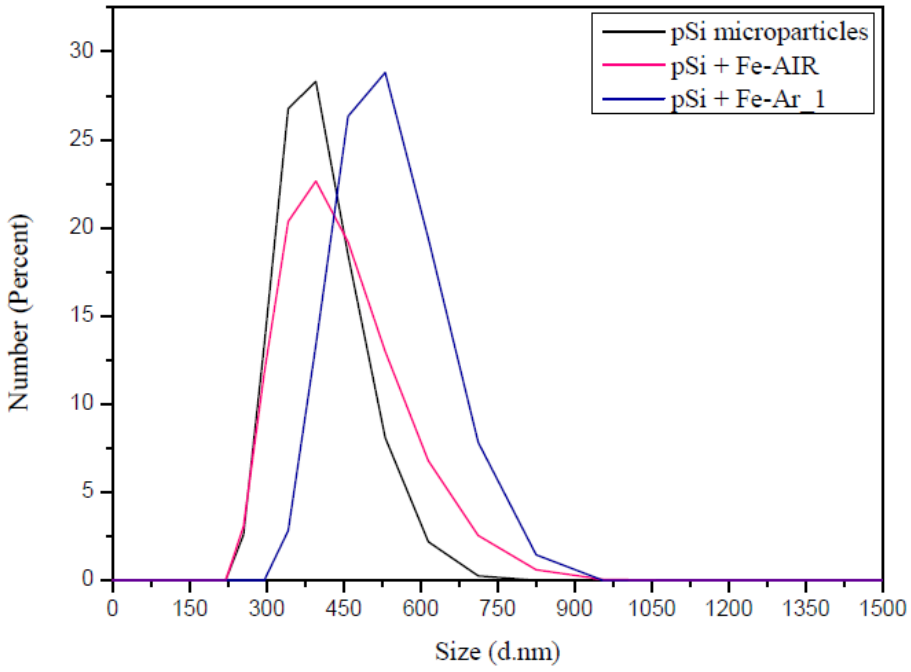

Figure 3.17. Size distributions of pSi microparticles before and after infiltration with Fe NPs (DLS measurements).

From the DLS measurements (Figure 3.17) it is clear that the pSi size was not affected by the infiltration of Fe-AIR, however, when infiltrated by Fe-Ar, the size increased of around 100 nm. This is agreement with TEM observations. The average size of pSi microparticles is not really modified by the combination with Fe-AIR, Figure 3.16 panel (a) show that infiltrated Fe NPs follow the shape of the pSi structure. However, if we consider the Fe-Ar ones (Figure 3.16 panel b), they do not always follow the morphology of pSi (highlighted by the yellow arrow) but go beyond the pSi structure. This is probably due to agglomerated Fe NPs that are

attached to surface of the silicon-derived material making the resulting diameter slightly increased.

Furthermore, by comparing the surface charges before and after the infiltration (Figure 3.18), there is another confirmation of the success of the infiltration.

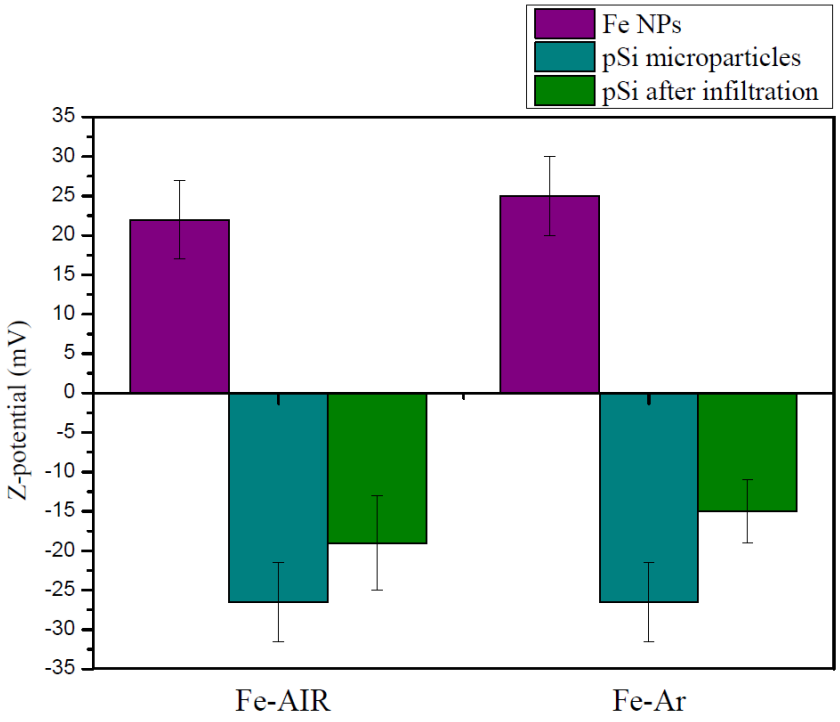

Figure 3.18. Surface charge modification before and after infiltration process.

pSi Z-potential after infiltration, indeed, is still negative for both iron oxide NPs made in air or argon, although partially reduced in its values (from about -25 mV to about -20 and -15 mV, respectively). This can be considered a proof of the presence of iron oxide NPs that, with their positive surface charge, are able to make the pSi one a little less negative.

Following our understanding, and to investigate if with a higher concentration of iron oxide NPs would be possible to improve the infiltration, the experiment was repeated with same procedure (only with Fe-Ar) by doubling the amount of iron oxide NPs incubated with pSi.

The DLS analysis showed that after the infiltration the size of pSi microparticles is slightly higher (from 350 to 530 nm) and Z-potential is less negative (from -27 to -12 mV) compared to the bare pSi microparticles, both the data are analogous to the previous experiment. In Figure 3.19 panel (a) and (b) is reported the comparison

between bare pSi and pSi after the first (pSi + Fe-Ar_1) and second (pSi + Fe-Ar_2) experiment in size distribution and surface charge respectively.

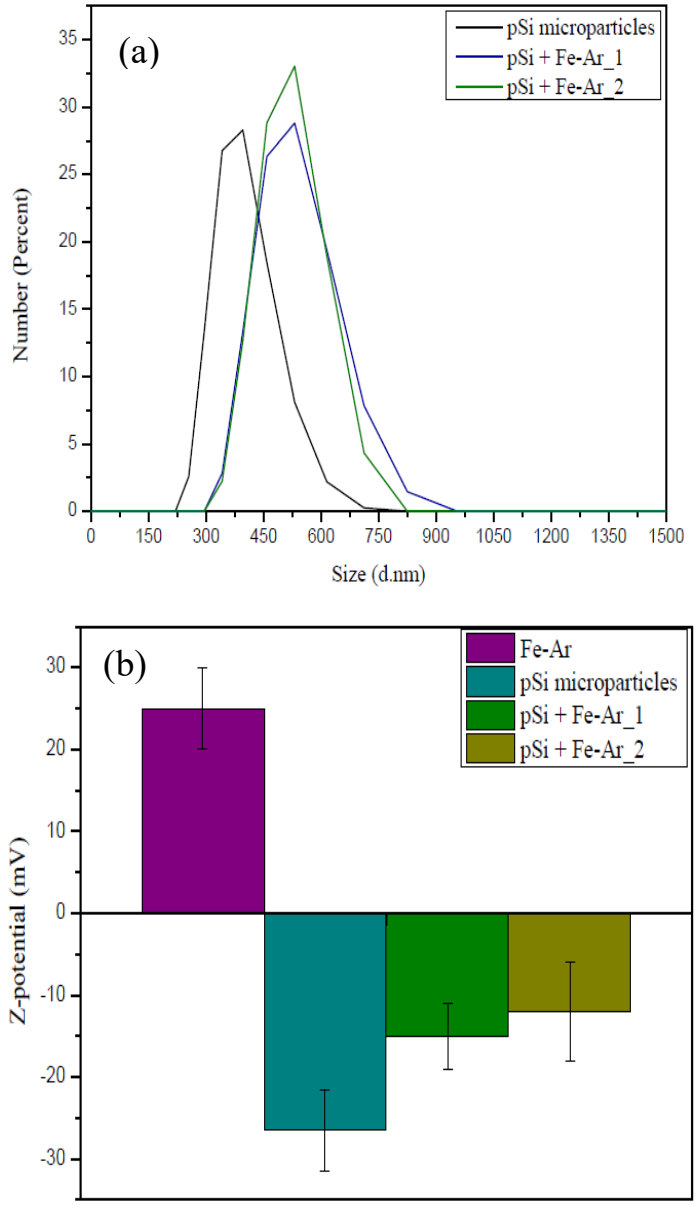

Figure 3.19. Size distribution (panel a) and Z-potential (panel b) comparison between bare pSi and pSi infiltrated with Fe-Ar after the first (Fe-Ar_1) and second (Fe-Ar_2) infiltration.

From the results obtained from DLS measurements it is possible to notice that doubling the amount do not change the mean diameter of the magnetic pSi (530 ± 80 nm). The surface charge is slightly lower compared to the first infiltration (-12 ± 6

mV) probably because in this case the amount of infiltrated iron oxide NPs is higher, as expected with an increased quantity of incubated NPs.

The infiltration was, once again, successful: as shown in Figure 3.20, the modified pSi microparticles (named Fe-Ar_2) are attracted to the magnet.

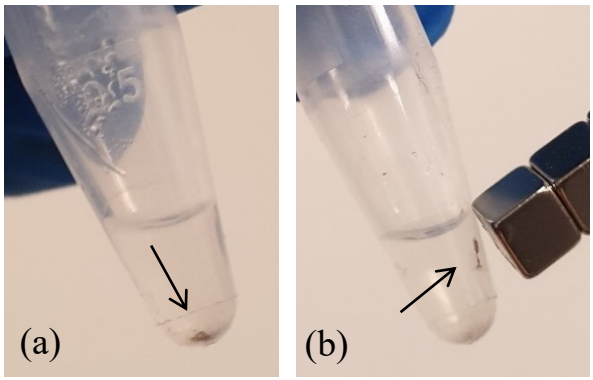

Figure 3.20. magnetic pSi in absence (panel a) and presence (panel b) of a magnet.

During this second experiment the infiltrated pSi microparticles were separated from the non-infiltrated through a magnetic separation. All of the particles visible in Figure 3.20 are, indeed, attracted to the magnet. As for the other samples, pSi + Fe-Ar_2 was analyzed by TEM (Figure 3.21).

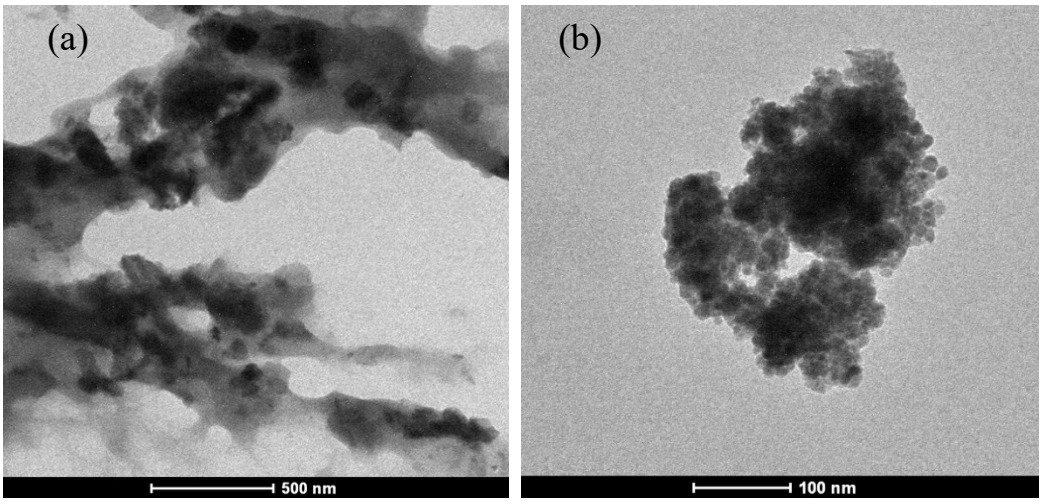

Figure 3.21. TEM images of pSi +Fe-Ar_2 (panel a 500 nm scale and panel b 100 nm scale).

From the image of panel (a) there seems to be a spread presence of iron NPs (darker areas) inside the structure of pSi microparticles, although other experiments with higher amount of iron NPs are needed to better understand if the pores of the pSi

have already reached their “saturation” or if there are still free binding sites left. On the magnified image of panel (b) there is a clear presence of a high quantity of iron NPs that cover all the pSi surface.

3.C. Conclusions

In this chapter, we applied a procedure that we previously optimized to add magnetic properties to the well-known properties of carboxyl-functionalized pSi microparticles, through infiltration of iron oxide nanoparticles produced by pulsed laser ablation. They can easily enter the different sizes of the pores because of their relatively broad size distribution and interact with the negative porous silicon surface by electrostatic interaction thanks to their positive surface charge, which was proved by means of TEM and by attraction to a magnet of the infiltrated pSi microparticles.

Concerning the use of magnetic pSi microparticles as contrast agent in MRI, we already planned to investigate how the relaxivity changes in function of the amount of successfully infiltrated pSi microparticles.

These encouraging new results combined with the previous successful ones[10], although they need further investigations, open the way to pSi microparticles to be used as negative MRI contrast agent.

CHAPTER 4

CHEMOTHERAPY

4.A. Background and introduction

4.A.1 Chemotherapy drugs

Since their first use in the mid-1900s to nowadays, chemotherapy drugs have been widely and commonly used as a standard practice to treat different form of cancers[122]. Their efficacy is, however, preceded by their bad reputation due to the many and harsh side effects that they come with. Some of the most common are physical such as vomiting, diarrhea, weakened immune system, dyspnea, chest pain, fatigue, rash but also mental like depression and anxiety. To demonstrate how chemotherapy affects the patient's life, Pearce *et al.* in 2017 performed a study, evaluating 449 chemotherapy patients, recording that 86% of the recipients reported at least one side effect and 27% a grade IV (potentially life threatening) side effect (fatigue and dyspnea were the most frequent)[123]. The main reason for the high frequency and roughness of the reported adverse effects is that those drugs are administered systemically and not selectively on tumors, therefore, since they are able to kill not only cancerous but also healthy cells.

4.A.2 Doxorubicin

The approved chemotherapeutic drugs are countless: only between the 2016 and the 2021 there were 207 approvals by FDA of cancer drugs for application in oncology and malignant hematology[124]. moreover, they can be administered through several possible routes: direct injection into the patient's veins, pills, intramuscular and intra-abdominal injections (mostly used if the solid tumor is in a specific accessible location), topical administration[24]. The currently most applied drugs are reported in Table 4.1 with the relative treated cancer.

Drugs	Target
Altretamine	B-cell chronic lymphocytic, leukemia, lymphoma, non-Hodgkin's lymphoma
Busulfan	Chronic myelogenous leukemia

Carboplatin	Advanced cervical, endometrial, esophageal, head and neck, melanoma, testicular, bladder and small and non-small cell lung cancer, thymoma, ovarian carcinoma, and sarcoma, metastatic breast cancer, skin carcinoma, refractory Hodgkin and non-Hodgkin's lymphoma, retinoblastoma
Chlorambucil	Chronic lymphocytic leukemia, lymphomas, and Hodgkin's disease
Cisplatin	Testicular cancer, ovarian cancer, bladder cancer, head and neck cancer, esophagus cancer, small cell and non-small cell lung cancer, non-Hodgkin's lymphoma
Cyclophosphamide	Lymphoma, multiple myeloma, leukemia, ovarian cancer, breast cancer, small cell lung cancer, neuroblastoma, sarcoma
Doxorubicin	Leukemia, Hodgkin’s lymphoma, sarcomas, breast cancer, bladder cancer, stomach cancer, ovary, lung cancer
Epirubicin	Breast cancer
Etoposide	Testicular and lung cancer, lymphoma, leukemia, neuroblastoma, ovarian cancer, Kaposi's sarcoma, Ewing's sarcoma and glioblastoma multiforme
Mitoxantrone	Prostate cancer, leukemia, breast cancer and non-Hodgkin's lymphoma
Oxaliplatin	Colorectal, metastatic pancreatic and gastric cancer
Thiotepa	Adenocarcinoma, thyroid and bladder cancer, Hodgkin's and non-H lymphomas
Capecitabine	Metastatic breast, gastric and colorectal cancers
Cytarabine	Leukemia and non-Hodgkin's lymphoma
Decitabine	Myelodysplastic syndromes (MDS)
Gemcitabine	Metastatic ovarian cancer, metastatic non-small cell lung cancer, and metastatic pancreatic adenocarcinoma, breast cancer, ovarian cancer, bladder cancer
Fluorouracil	Breast cancer, malignant neoplasm of colon, malignant neoplasm of pancreas, malignant neoplasm of stomach, rectal and superficial basal cell carcinoma
Raltitrexed	Advanced Colorectal Cancer, Pleural Mesotheliomas
Tegafur	Advanced Gastric Cancer
Paclitaxel (Taxol®)	Kaposi's sarcoma and cancer of the lung, ovarian, and breast
Docetaxel (Taxotere®)	Breast, non-small cell lung, prostate and head and neck cancer, gastric adenocarcinoma

Ixabepilone (Ixempra®)	Breast cancer, head and neck cancer, melanoma, lung cancer, non-Hodgkin's lymphoma, prostate cancer, renal cell carcinoma
Methotrexate	Leukemia, choriocarcinoma, breast, lung, head and neck cancer, advanced non-Hodgkin's lymphoma
Vinblastine	Breast cancer, testicular cancer, lymphomas, neuroblastoma, Hodgkin's and non-Hodgkin's lymphomas and Kaposi's sarcoma
Vincristine	Acute lymphocytic leukemia, Hodgkin and non-Hodgkin's lymphomas, Wilms' tumor, neuroblastoma, rhabdomyosarcoma

Table 4.1. Most common chemotherapeutic drugs and their respective tumor target[24].

Among all, one of the most famous and widely used is Doxorubicin (DOX), approved by FDA in 1974[125], DOX, once called Adriamycin® when firstly isolated in 1967 by Farmitalia Research Laboratories, is a cytotoxic antibiotic part of the class of anthracyclines (together with e.g., Daunorubicin, Epirubicin, Idarubicin), a group of drugs extracted from the bacterium Streptomyces peucetius that finds application in cancer chemotherapy[126]. DOX is commonly used - sometimes coupled with other therapies - in both adults and children, to treat hematological neoplasms (e.g., leukemias, Hodgkin's lymphoma, sarcomas) and solid tumors (e.g., breast, bladder, stomach, ovary, lung).

Its ability to efficiently kill cancer cells is accompanied by many negative implications. Doxorubicin, indeed, has the ability to intercalate between DNA base pairs leading to the inhibition of the action of the enzyme topoisomerase II (TOP2) (responsible for relaxing of topological strain in DNA) that ultimately results in the apoptosis of the cancer cells. The exact mechanism is however not fully known and another one proposed consists in the generation of reactive oxygen species (ROS) by DOX that cause oxidative stress to mitochondria[127]. Either way, DOX action, especially when present in high quantities, can have a negative impact on healthy tissues and organs such as liver, kidney or heart, by generating severe injuries that might as well be fatal for the patient. Specifically talking about cardiotoxicity, which is the most common side effect related that, indeed, exerts cardiotoxic effects by inducing apoptosis in cardiomyocytes that leads to irreversible heart injury[128]. Moreover, its ability to target proliferative cells (cancer and normal) without tumor specificity can also cause bone marrow suppression[129], its accumulation in the liver

and kidneys can lead to hepatotoxicity and nephropathy and its use is also associated with neuropathy and other severe side effects[130]. Other downsides related to use of DOX that limit its application are, beside the already cited dose-dependent toxicity and low specificity against cancer cells, fast degradation and multi-drug resistance (MDR).

MDR is a phenomenon that causes a reduction of the efficiency of cytotoxic drugs against cancer cells resulting in the failure or not efficacy of the chemotherapy treatment. It represents a burden that a slice of the scientific community (also with drugs like antibiotics) has been investigating with the aim of understanding it and finding innovative therapies to try to get rid of it. The success of doxorubicin and many other chemotherapeutic agents is majorly affected by intrinsic and acquired resistance of several kind of cancer cells and, as a consequence, higher doses of anticancer drugs are administered to the patients to obtain an effective therapeutic effect but at the same time they are affected with more severe side effects.

The development of the resistance has been ascribed to different unrelated mechanisms (pictured in Figure 4.1) such as overexpression of the drug efflux transporters, decrease in uptake of the agents or their inactivation, alteration of cell cycle checkpoints, inhibition of the apoptotic signals, DNA repair processes, modification of the drug targets[131].

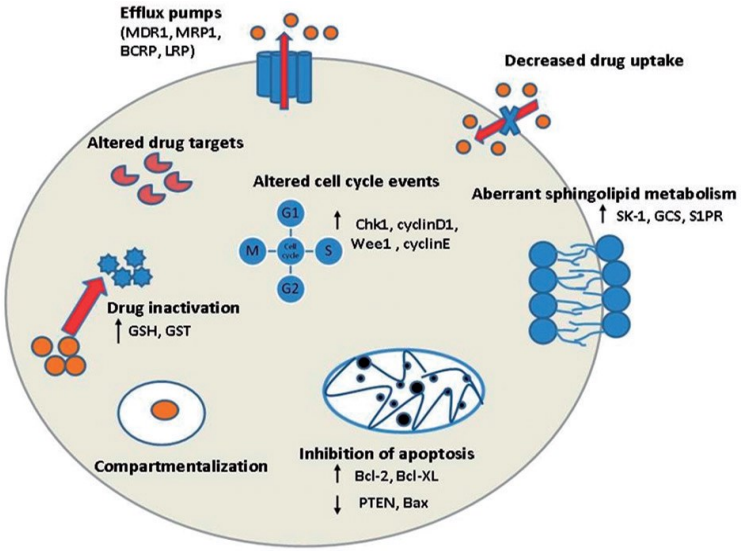

Figure 4.1. Schematic representation of the resistance mechanisms in cancer cells (Image from Kartal-Yandim et al.[131])

Different approaches have been proposed to try reversing the resistance such as: application of P-gp modulators i.e., suppressors of P-gp activity and expression, which prevents intracellular accumulation of DOX leading to the failure of the treatment, the use of drug delivery systems, gene therapy to reduce the expression of pathogenic genes for example with the use of RNA interference (RNAi), immunotherapy, combination therapy by coupling either different chemotherapeutic drugs between each other or with RNAi[132–134].

Consequently, many researchers have been studying new drugs and alternative administration paths with a selective or patient-specific therapeutic approach with the aim of improving the patient's quality of life while being treated. Nevertheless, most chemotherapeutic drugs are still in use due to their effectiveness, even if they come with a tough price.

4.A.3 Delivery of Doxorubicin

During the last three decades carriers for the delivery of anticancer drugs have been extensively investigated because of their ability to prolong blood circulation of the drug and enhance the bioavailability and distribution, their capacity to protect the patient from many side effects, but also because their tunable surface enables the binding of targeting molecules that can improve the selectivity for the cancer cells leading to the accumulation of the drug only where it is needed.

Doxorubicin-based chemotherapy has been the subject of the research of several scientific groups for the development of novel delivery systems able to help overcoming the drawbacks above described. Among the others, the most popular is Doxil®: composed of doxorubicin surrounded by a nano-sized PEGylated liposomal coating (Figure 4.2), it made history for being the first nanocarrier-based drug approved by FDA, in 1995[135].

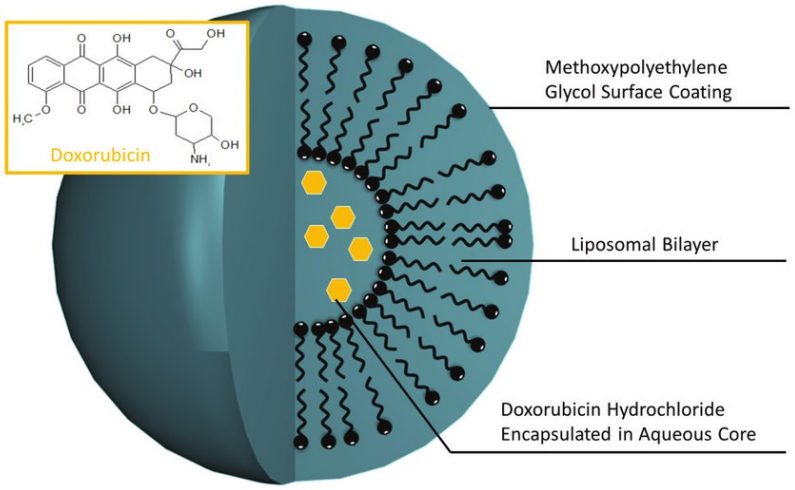

Figure 4.2. Doxil® structure[135].

There are several advantages by using an encapsulated version of DOX, such as:
- prolonged circulation time (circulation half-life time of ~ 90 h and DOX presence in the circulation of > 350 h),
- high loading of the drug (> 90% drug encapsulation),
- the possibility of a selective release to the tumor cells
- protection of the patient to side effects like cardiotoxicity compared to the soluble version of the drug. Moreover, thanks to the EPR effect (discussed in Chapter 1), the system is "passively targeted" allowing a direct release of doxorubicin to cancer cells[19]. In 2000, EMA approved a non-PEGylated liposome-based carrier for doxorubicin named Myocet®. The absence of the PEG resulted in the absence of palmar plantar erythrodysesthesia (PPE), a harsh side effect that was reported with the first version.

Currently, there are more than fifteen (data updated in 2022) nanoparticles-based drugs approved for the treatment of cancer. Table 4.2 summarized them in terms of nano-carrier, drug and main therapeutic indication. The nature of the nano-systems can be lipidic, polymeric, iron oxide nanoparticles or albumin-based.

Name	**Nanoplat-form**	**Drug**	**Therapeutic indication**	**Approval**
Non-targeted chemotherapy				
Doxil/Caelyx	PEG, lipo-some	Doxorubicin	Ovarian cancer, HIV-re-lated Kaposi's Sarcoma, Multiple Myeloma	FDA (1995)

				EMA (1996)
DaunoXome	Liposome	Daunorubicin	HIV-related Kaposi's Sarcoma	FDA (1996)
Onivyde	PEG, liposome	Irinotecan	Post-gemcitabine metastatic pancreatic cancer	FDA (2015)
Myocet	Liposome	Doxorubicin	Metastatic breast cancer	EMA (2000)
Marqibo	Liposome	Vincristine sulfate	Philadelphia chromosome-negative acute lymphoblastic leukemia	FDA (2012)
Mepact	Liposome	Muramyl tripeptide phosphatidyl ethanol amide	Non-metastatic, resectable osteosarcoma	EMA (2009)
Vixeos	Liposome	Cytarabine:daunorubicin (5:1 M ratio)	High-risk acute myeloid leukemia	FDA (2017) EMA (2018)
Lipusu	Liposome	Paclitaxel	Breast, lung and ovarian cancer	
Oncaspar	PEGylated Asparaginase	Asparaginase	Acute lymphoblastic leukemia	FDA (1994)
Genexol-PM	Polymeric micelle	Paclitaxel	Metastatic breast cancer, pancreatic cancer	South Korea (2007)
Elgard	PLGA	Leuprolide acetate	Prostate cancer	FDA (2002)
Neulasta	PEGylated protein	Granulocyte-colony Stimulating Factor	Non-myeloid malignances (reduce the risk of infection in patients with non-myeloid malignances receiving myelo suppressive anticancer therapy associated with febrile neutropenia)	FDA (2002) EMA (2002)
Zinostatin Stimalamer	Styrene-malic acid	Neocarzinostatin	Primary unresectable Hepatocellular carcinoma	Japan (1994)

Abraxane	Albumin NPs	Paclitaxel	Lung cancer, metastatic breast cancer, metastatic pancreatic cancer	FDA (2005) EMA (2008)
Hyperthermia				
NanoTherm	Iron oxide NPs	NA	Glioblastoma	EMA (2011)
Abbreviations: FDA, US Food and Drug Administration; EMA, European Medicines Agency; miRNA, micro-RNA; HIV, human immunodeficiency virus; PEG, Polyethylene glycol; NPs, nanoparticles; NA, not applicable.				

Table 4.2. Overview of the nanoparticles-based drugs for cancer therapy approved for the clinics.[136]

Lipid-based nanoparticles are one of the most popular kind of nanomedicine approved by FDA because of their interesting properties: they are easy to produce, they have a self-assembly behavior, they can transport a large amount of drugs, moreover they have high bioavailability and tunable chemical and biological properties. Polymers are able to fit in a wide range of applications because of their high loading capacity, easy biodegradation and high bioavailability, but mostly because they can be modified depending on the nature of payload (e.g., hydrophobic or hydrophilic, positive or negative surface charge) and most of the is able to respond the external stimuli. Albumin-based, even if largely used, are facing many challenges, including high price, sources of human serum albumin limited, they can exert biological effects on the organism and they have a low availability, therefore for their future use they need to be improved and new synthesis technique needs to be found[136].

4.A.4 Porous silicon and doxorubicin

Among all the drug delivery systems, the inorganic approach is quite rare. The great potential of inorganic porous materials resides in the combination of outstanding properties, such as large surface-to-volume ratio, optical features, high mechanical and chemical stability with biocompatibility, ability to transport and protect a high amount of drug. Moreover, they can be functionalized to react to external stimuli (e.g., change in temperature or pH). Consequently, they find application not only as drug delivery systems but also as imaging agents. The most popular inorganic

materials are metallic (e.g., gold and silver NPs), magnetic (e.g., iron oxide NPs), ceramic materials (e.g., mesoporous silica and porous silicon) and based on graphene.[137–139]

Among all, porous silicon has been taken more and more into consideration as a promising drug delivery system thanks to its unique features such as large surface area, high porosity, tunable pore size, intrinsic photoluminescence, non-immunogenicity and non-toxicity, easy biodegradation, and tunable surface (described more in detail in Chapter 2)[140].

When first approaching to the investigation of porous silicon for the delivery of anticancer drugs, we decided to start from doxorubicin (DOX), one of the reference chemotherapeutic drugs. Since its first clinical application it has been widely studied and it can be considered a "gold standard" in anticancer therapy. We began by reviewing the available literature about porous silicon coupled with DOX to define a method that served as a starting point to our investigations. As a matter of fact, there are different silicon-derived particles coupled to DOX, such as:

i) Xu *et al.* developed a co-delivery of DOX and Paclitaxel by thermally oxidized pSi coated with poly(beta-amino ester) (PAE) and Pluronic F-127 to HeLa cells;[141]
ii) Janoniene *et al.* tested the delivery of DOX on human breast adenocarcinoma (MCF-7) cells by undecylenic acid-modified thermally hydrocarbonized pSi (UnTHCPSi) particles coated with PEG and grafted with VD11-4-2 as a targeting molecule;[142]
iii) Oxidized pSi coated with dextran was successfully studied by Park *et al.* in vitro on HeLa and metastatic human breast cancer (MDA-MB-435) and in vivo on MDA-MB-435 tumor bearing mice;[56]
iv) Xia *et al.* reported vinylaniline-terminated pSi nanoparticles tested in vitro on a murine breast cancer (4T1) and human umbilical vein endothelial (HUVEC) cells and in vivo in 4T1 tumor-bearing mice for photothermal therapy.[143]

Within this thesis work, we investigated the loading and the release of doxorubicin in optimized carboxyl-functionalized pSi particles. Moreover, we did a preliminary

investigation on the loading of another approved and commonly used chemotherapeutic drug: docetaxel (DTX). To enable the binding of this hydrophobic drug, the particles were coated by the cationic surfactant CTAB as described in Chapter 2.
Finally, we investigated the antitumor efficacy of the anticancer drugs delivered via functionalized pSi particles by monitoring the cytotoxic effect of the two formulations on two different human cancer cell lines, representative of aggressive neoplasia:

(i) PC3: castration-resistant prostate cancer;
(ii) A549: non-small cell lung cancer

As far as we know, it is the first time that the combination of carboxyl-functionalized pSi particles loaded with doxorubicin or docetaxel has been tested against these model cell lines.

4.B. Results and discussion

Starting from the methods used in literature, we loaded the doxorubicin within the pSi-COOH microparticles prepared and functionalized as described in Chapter 2, by stirring them overnight with a water solution of the drug. After the removal of the supernatant containing the non-loaded drug and a couple of washing cycles with water, the loaded particles were stirred with a cation surfactant (CTAB) to obtain a positive surface charge that in turn enables the coating with the negatively-charged hyaluronic acid (HA). As described in Chapter 2, coating the particles with HA has several benefits: it makes the particles well-dispersed, it helps keeping the payload (i.e., the drug) inside the pores of the particles but its main function is to target tumors that overexpress the protein CD44, such as triple-negative breast, pancreatic, lung and prostate cancer[102]. Therefore, after loading with the anticancer drug and coating with HA, our drug delivery system was tested in vitro on prostate and lung cancer cells. The steps needed to obtain the final complete drug delivery system are summarized in Figure 4.3.

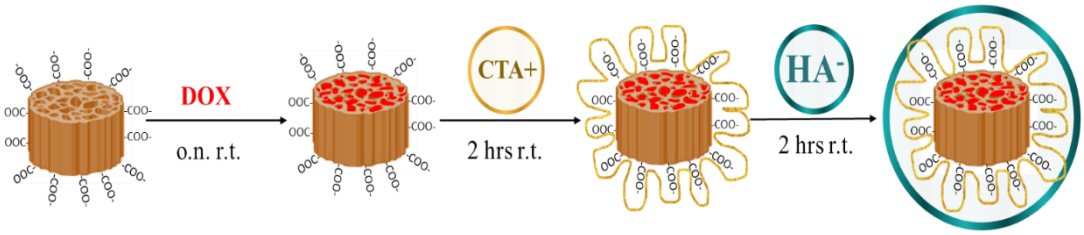

Figure 4.3. Overview of the steps needed to obtain the complete drug delivery system.

4.B.1 Doxorubicin loading and release study

pSi-COOH were produced as described in detail in Chapter 2. Doxorubicin was loaded within pSi microparticles by using a simple immersion method. After drying overnight in a 50 °C oven, to completely remove the ethanol, pSi-COOH microparticles were added to an ultrapure water solution of DOX with a weight ratio of 10:3 (pSi:DOX). The suspension was then mildly stirred over night at room temperature (Figure 4.4). After that, the suspension was washed 3 times to remove the free DOX and replaced with fresh ultrapure water. The DOX-loaded pSi particles were labelled as pSi-DOX.

Figure 4.4. pSi-DOX suspension after overnight loading.

To quantify the loaded amount of DOX within the pores of micro-silicon particles, the loaded pSi microparticles were added to a 0.1 M solution of KOH. As already discussed in Chapter 2, pSi particles are easily degraded in basic solutions[58]. Afterwards, an equal volume of 0.1 M HCl was added for pH neutralization. UV−Vis absorption and fluorescence spectroscopy were used to evaluate the amount of DOX present in the solution since, according to the literature, it shows a maximum absorption at 495 nm and the excitation and emission wavelengths are at 495 and 595 nm, respectively (Figure 4.5)[144].

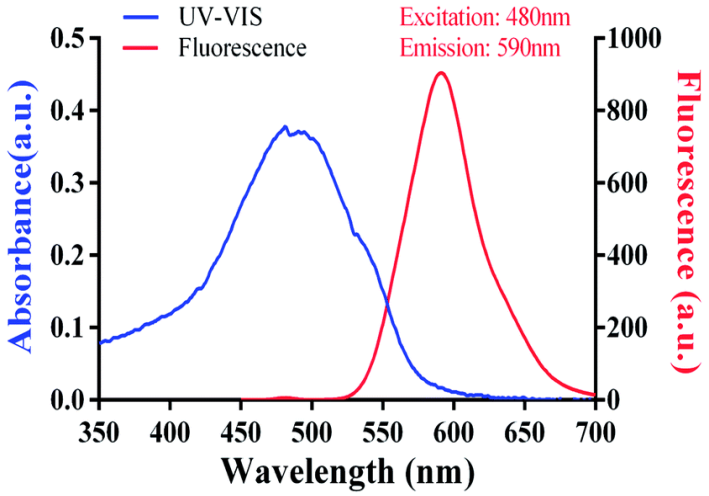

Figure 4.5. Emission and absorbance spectrum of doxorubicin in water[144].

The absorbance and emission intensities were correlated to the concentration of DOX though a calibration curve of a standard (Figure 4.6 panel a), obtained by measuring the signals of known concentration of the drug.

Loading capacity (LC%) was calculated by using the following equation:

$$LC\% = \frac{mass\ of\ loaded\ drug}{mass\ of\ loaded\ particles} \times 100$$

The obtained loading capacity was 34 %. This value is coherent to the one obtained from other groups with a similar system[56,145]. On the other hand, other groups found a higher loading capacity when the binding occurred through stronger bonds (e.g., 16 times higher by π-stacking[146] and 6 times higher when mediated by the presence of bovine serum albumin[147]). Therefore, it is possibly the nature of the electrostatic binding that limits the amount of the loaded drug.

The in vitro release of DOX was studied with a dialysis method in PBS buffer by means of HPLC coupled with a PDA and fluorescence spectroscopy detectors. After the loading of DOX within pSi microparticles, the suspension was transferred in a dialysis tube (cut-off: 12 kDa) and gently stirred in PBS. The amount of released drug was obtained by collecting aliquots at set times and replacing the removed aliquot with the same amount of fresh PBS. The aliquots were then analysed by HPLC, and the concentration was obtained by means of a calibration curve. The obtained calibration and release curves are reported in Figure 4.6 in the panel a and b, respectively.

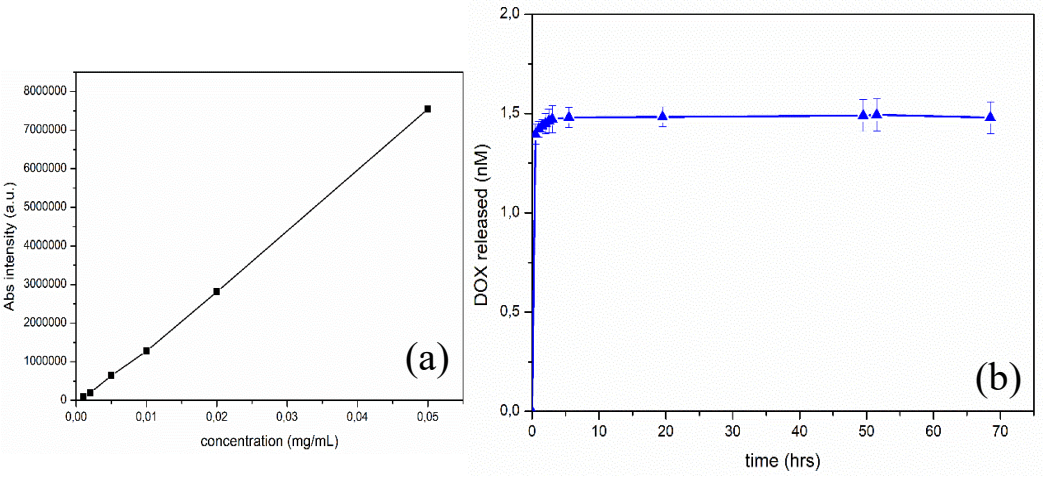

Figure 4.6. Calibration curve of standard DOX (panel a). Determination of the release rate: DOX concentration measured at set times (panel b).

The release profile shows a burst release of the loaded DOX within the first 30 minutes, releasing about the 90% of DOX. The plateau was reached after around 5 hours with a continuous release for 70 hours. The fast release is probably due to the weak electrostatic interaction between the pSi particles and the drug.

4.B.2 Coating with HA

Hyaluronic acid (HA) coating was performed following the procedure described in Chapter 2. Briefly, sodium hyaluronate (40 kDa) was dissolved in ultrapure water. Meanwhile, pSi particles loaded with the drug were incubated with a CTAB solution for 2 hours to obtain a positive surface essential for the electrostatic binding of HA (negative surface charge). After washing the particles to remove the non-bonded CTAB, the HA solution was added to the particles with a weight ratio of 3:1

HA:pSi, stirred vigorously for 5 hours and then washed three times with ultrapure water.

To assess the efficiency of the procedure, Z-potential measurements were used to monitor the surface modification process, therefore the surface charge was checked at every step and reported in Figure 4.7.

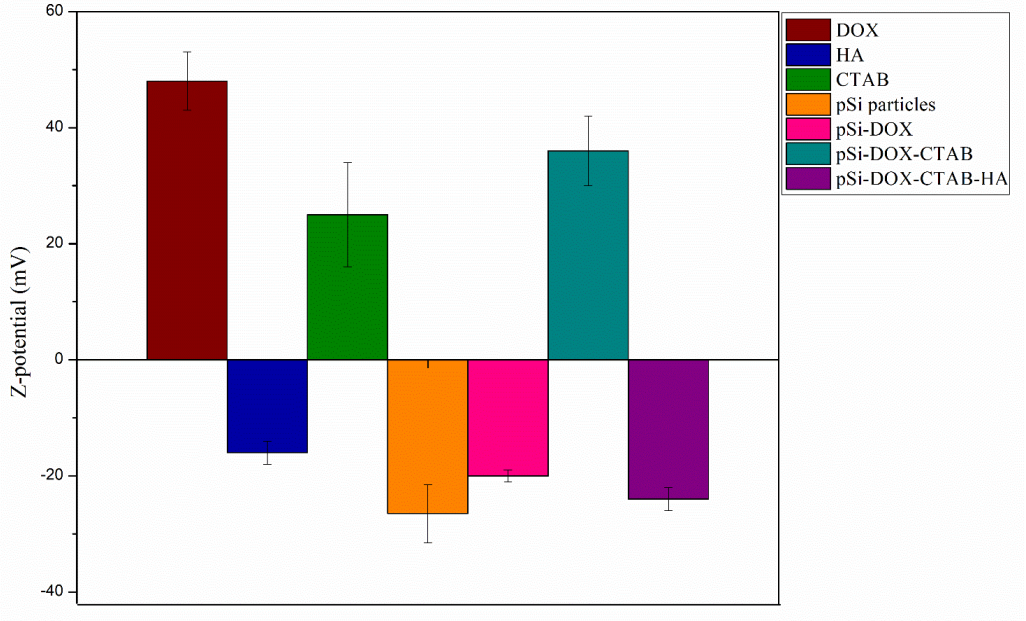

Figure 4.7. Z-potential distribution following the surface modifications of pSi particles.

Considering that carboxyl-functionalized pSi and doxorubicin have opposite surface charge (-27 ± 5 mV and +48 ± 5 mV, respectively), their binding occurs through electrostatic interaction. Hyaluronic acid has negative charge (-16 ± 2 mV), therefore there was the need of changing the pSi charge to allow their combination. The cationic surfactant CTAB was considered a good candidate to work as a "bridge" between the two of them since it is composed of a cationic head and a hydrophobic tail. As already discussed in Chapter 2, the cationic part of the surfactant will be attracted through electrostatic force by the negative pSi surface and, through hydrophobic interaction of the CTAB hydrocarbon tails, there will be a surfactant bilayer that ultimately results in the creation of a positive charge on the surface of the particles where HA will be able to interact.

The Z-potential values reflect the surface state and allow the monitoring of every step of the process:

Step 1 → pSi-DOX: the value was still negative (-20 ± 1 mV) as expected since the drug was mainly inside the pores.

Step 2 → pSi-DOX-CTAB: the addition of CTAB resulted in a recharging of the surface with an increase of its value up to +36 ± 6 mV. By coating the negatively charged pSi particles with CTAB, it was possible to obtain a positive surface that was fundamental to allow the coating by electrostatic interaction with the negative HA (-16 ± 2 mV).

Step 3→ pSi-DOX-CTAB-HA: after the coating with the last layer, obtained by vigorously stirring pSi in a HA solution, the surface resulted to be negative with a Z-potential of the order of -24 ± 2 mV suggesting the successful coating with the polymer.

Some preliminary investigation regarding the loading of another anticancer drug, docetaxel (DTX), have also been performed. Docetaxel is an approved potent anti-cancer drug obtained from the European yew tree *Taxus baccata L*. that promotes and stabilizes the assembly of microtubules, thus helping to avoid their depolymerization. Its co-administration with other chemotherapies for patients with early breast cancer results in a significant reduction in mortality. Moreover, it is highly active in the treatment of metastatic breast cancer. But it is also efficient against other solid tumors such as non-small cell lung cancer, prostate cancer, gastric adenocarcinoma and head and neck cancer. DTX efficiency in killing cancer cells is however associated not only to improvement in overall survival but also to high toxicity and severe side effects such as peripheral neuropathy and neutropenia. Therefore, its combination with drug delivery systems could improve its efficacy by lowering the side effects[148].

After the functionalization with carboxylic groups, pSi particles surface was modified by coating with the cationic surfactant CTAB, fabrication and surface modification are described in Chapter 2). Docetaxel was then loaded though the same method used for doxorubicin with a weight ratio of 10:1 (pSi:DTX). The loading capacity was evaluated by measuring the absorbance at 229 nm obtaining a value of 40%. This value is comparable to the results found by Vakili-Ghartavol *et al.* (34-67%) using liposomes instead of pSi[149], probably the presence of CTAB bilayer makes the pores surface less accessible to the drug.

4.B.3 In vitro cancer cell viability

As already discussed, pSi toxicity in vitro and in vivo has already been widely studied and, thanks to its ability of being easily degraded in biological environment, its administration can be considered safe[50,53,150].

For this purpose, to perform cytotoxicity tests, PC3 and A549 cells were first thawed out and then grown in Kaighn's Modification of Ham's F-12 Medium (F-12K) and Dulbecco's Modified Eagle's Medium (DMEM), respectively, supplemented with the antibiotics Streptomycin and Penicillin (1% w/v) and 10% v/v FBS (fetal bovine serum). Cells were then incubated in 75 cm^2 culture flasks in a humidified atmosphere of air and CO_2 (5%) at 37°C and then harvested and seeded in a 96-well plate in F-12K or DMEM complete medium (6000 and 7000 cells/well, respectively). After around 24 hours the confluence was appropriate (70-75%), thus PC3 and A549 cells were treated for 72 hours with a range of concentrations of pSi particles loaded with the anticancer drugs DOX and DTX and, as a control, pSi bare particles, DOX solution and DTX solution (the concentrations were chosen considering the loading capacities). Moreover, we tested pSi-CTAB and CTAB solution as a control for the pSi-DTX evaluation.

The cell viability was evaluated by AlamarBlue™ assay, a colorimetric test based on the measurement of metabolic activity of the cell: resazurin is a dye that undergoes reduction upon metabolization, and the reduced dye is highly fluorescent. Thus, a decrease of fluorescence is related to a decrease of dye metabolization and therefore of cell viability (as discussed in Chapter 5). An example of a well-plate after the reaction with resazurin is shown in Figure 4.8.

Figure 4.8. Part of a well-plate after reaction with resazurin.

The section of the well-plate shown was treated with concentrations from 0.56 to 0.015 mg/mL of bare pSi from column 2 to 6 and pSi-DOX from 7 to 11 (every well

of the column was treated with the same concentration, columns 1 and 12 are controls).

The color pink, related to bare pSi, means that cells are viable, thus excluding the cytotoxicity of the material. Conversely, the pSi-DOX toxicity is increasing linearly with the concentration revealing a color gradient which intensity decreases from left to right (from blue to pink, from more viable to less viable cells).

In addition, we used the MTT assay, another colorimetric test that likewise measures the cellular metabolic activity, as a control, for the dose-response activity of DOX and DTX solutions. MTT solution is made of a yellow tetrazolium salt (3-(4,5-dimethylthiazol-2-yl)-2,5-diphenyltetrazolium bromide) that can be reduced through a redox reaction by metabolically active cells to purple formazan crystals. Once the solution is added to the cell layer, if the cells are metabolically active (i.e., viable), by passing through their mitochondrial inner membrane, the MTT reagent is reduced to formazan by the mitochondrial dehydrogenase. Therefore, the more intense the purple color the higher the viability and the metabolic activity of the cells[151]. We did not use the MTT assay for pSi-based formulations because, as reported by Laaksonen *et al.,* pSi particles are able to reduce the MTT reagent, thus resulting in higher cellular viability.[152]

Consequently, to evaluate the chemotherapeutic effect, cells were incubated with resazurin (or MTT) for three to five hours at 37°C. The plates were shacked for 5 minutes at room temperature and analyzed by TECAN plate reader at 595 nm (565 nm). Untreated cells in medium were used as a control. To evaluate cell viability (%) after AlamarBlue™-assay the following equation was applied:

$$\%\ vitality = \frac{\frac{1}{\sum Abs_{treated\ cells}} - \frac{1}{\sum Abs_{resasurine\ blank}}}{\frac{1}{\sum Abs_{control\ cells}} - \frac{1}{\sum Abs_{resasurine\ blank}}} \cdot 100$$

While to evaluate the cell viability (%) after the MTT test the following equation was applied:

$$\%\ vitality = \frac{abs\ mean\ value\ of\ the\ sample\ (after\ background\ sub)}{abs\ mean\ value\ of\ the\ ctrl\ (after\ background\ sub)}\ x\ 100$$

We first assessed the presence of a dose-response effect (i.e., the lower the sample concentration the higher the viability) in PC3 and A549 cells treated with free DOX (Figure 4.9), free DTX (Figure 4.10), pSi-DOX (Figure 4.11) and pSi-DTX (Figure 4.12)

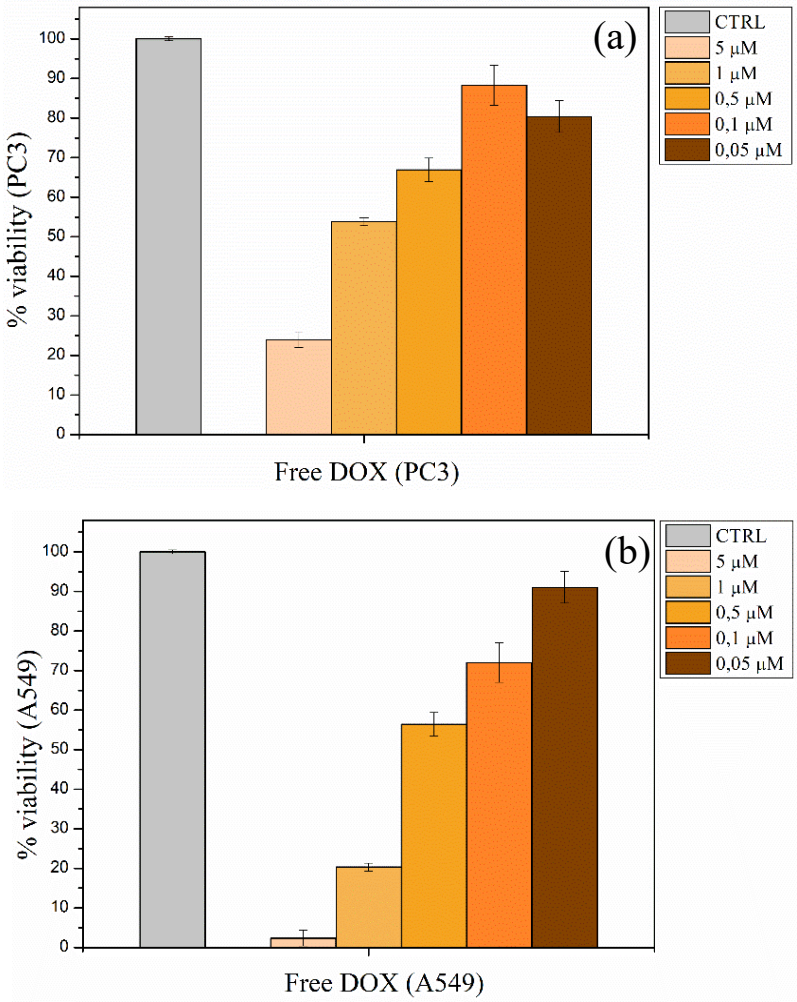

Figure 4.9. Dose-response of free DOX on PC3 (panel a) and on A549 (panel b).

In agreement with literature data, Doxorubicin affects cell viability of both PC3 (panel a) and A549 (panel b) cells [153,154]. In panel a we can observe that starting from a concentration of 0.05 to 5 µM the vitality decreased in a dose-dependent way from 80 to 24% for PC3, while in panel b decreased from 91 to 2%, also in a dose-dependent mode, for A549, highlighting a higher cytotoxic effect on the latter cell line for concentrations higher than 0.1 µM. The data reported are coherent with what recorded, for example, from Shu *et al.* who found that at 0.1µM the

viability was around 85% and at 1 µM was around 45%, therefore similar to our 88% and 54%[155]. For the A549 cell line, Melguizo *et al.* reported a viability of around 90% at 0.05 µM, around 55% at 0.5 µM and around 10% at 5 µM, that are coherent compared to our 91, 56 and 2%, respectively[156].

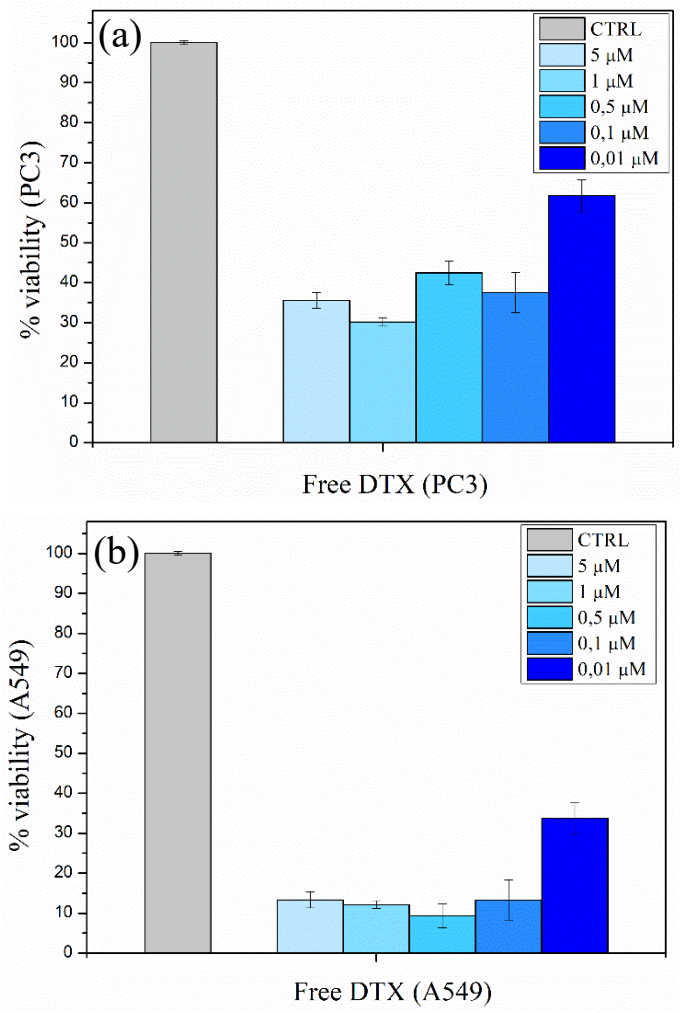

Figure 4.10. Dose-response of free DTX on PC3 (panel a) and on A549 (panel b).

When treating PC3 with free DTX (Figure 4.10 panel a) we found that the viability almost halved (from 62% to 37%) when increasing the concentration of one order of magnitude (from 0.01 to 0.1 µM) and then remained consistent at around the 35% even when increasing the concentration ten-fold (from 0.1 to 1 µM). Cancino-Marentes *et al.* reported a viability of around 80% when treating PC3 with DTX at 0.01 µM, this value decreased linearly until 0.025 µM and from that point on remained constant even if increasing the concentration[157]. Therefore, our results were

in line to what found from Cancino-Marentes and co-workers. This can be due to the fact that even if DTX is commonly used as a standard treatment for prostate cancer it is usually accompanied by chemoresistance so probably when testing concentrations > 25 nM the drug reaches its highest toxic effect. This behavior can be found also when treating A549 cells with DTX (Figure 4.10 panel b) and it was coherent with what declared by Chen *et al.*: at 0.01 μM they found that the viability was around 40%[158], similar the 34% that we reported. However, the drug seemed more effective on this cancer cell line: at 0.1 μM the viability was around 13% for A549 versus 37% for PC3.

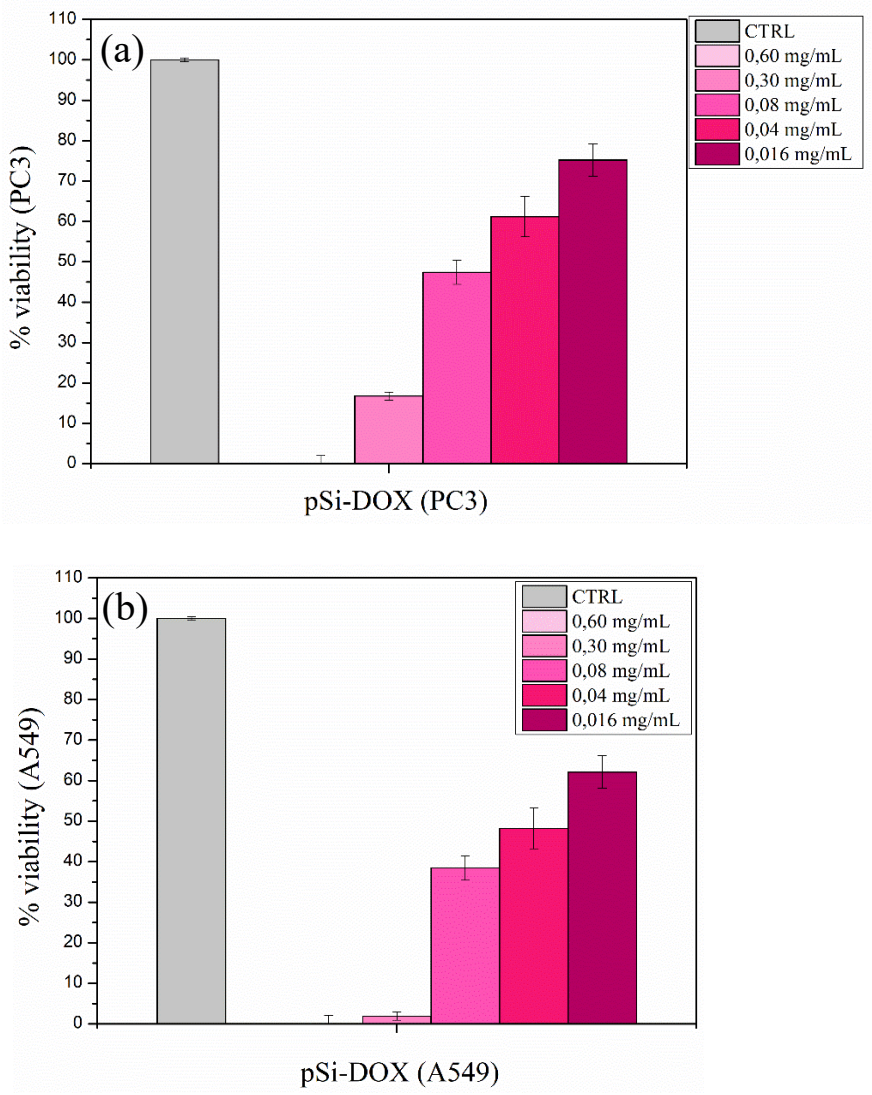

Figure 4.11. Dose-response of pSi-DOX on PC3 (panel a) and on A549 (panel b).

When the action of doxorubicin was mediated by the presence of pSi, the dose-dependent cell viability trend was very similar to the one observed for the free drug:

from a particles concentration of 0.016 to 0.60 mg/mL the vitality decreased from 75 to 0% for PC3 (panel a) and from 62 to 0% for A549 (panel b). This points out that the drug was stable and its action was not modified by the presence of the inorganic carrier. Moreover, at a first look it is possible to notice that the viability was generally lower when using pSi particles as a carrier. The comparison between the same concentration of free DOX and DOX transported by the pSi particles (evaluated considering the 34% loading capacity) is reported in Figure 4.13 to better highlight potential differences.

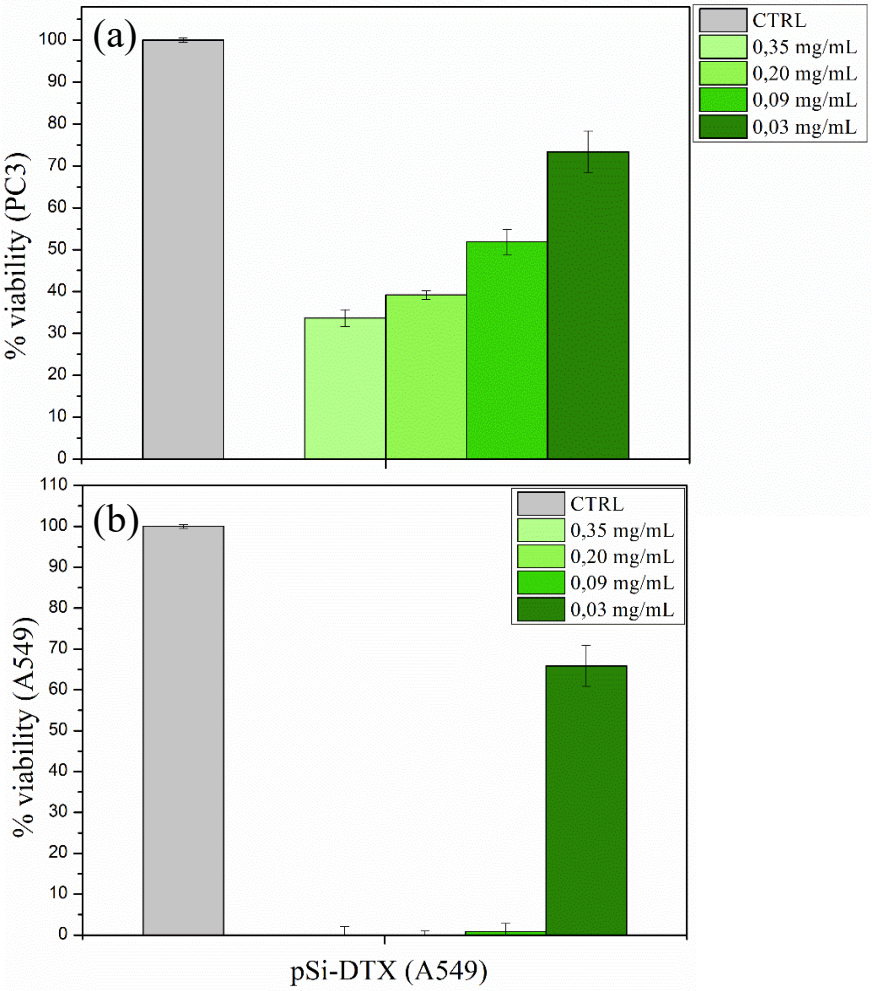

Figure 4.12. Dose-response of pSi-DTX on PC3 (panel a) and on A549 (panel b).

On the contrary to pSi-DOX, the biological response of pSi-DTX did not follow the same trend of the response of free DTX. In fact, if we consider the actual amount of loaded DTX (40% loading capacity), the pSi-DTX formulations with concentrations between 0.03 and 0.2 mg/mL delivered an amount of drug between 0.1 and 0.01 μM. Therefore, related only to a small part of the free DTX-response graph.

To clarify if the presence of pSi resulted in a higher cytotoxic effect within this narrow actual DTX concentration range (0.1-0.01 μM), amounts of free DTX and DTX delivered by pSi (evaluated considering the 40% loading capacity) are compared in Figure 4.14. At first glance the two formulations seemed effective in reducing the cell vitality of both cell lines. In particular, the "half maximal effective concentration" (EC_{50}), commonly defined as the concentration of the formulation needed to cause half of the maximum possible response to the treatment (in this case to cause a reduction of the 50% of the viability), were evaluated as reported in Table 4.3.

EC_{50}	PC3	A549
DOX	0.56 mg/mL (0.9 μM)	0.33 mg/mL (0.6 μM)
pSi-DOX	0.08 mg/mL	0.04 mg/mL
DTX	0.008-0.08 mg/mL (0.01-0.1 μM)	<0.008 mg/mL (<10 nM)
pSi-DTX	0.09 mg/mL	0.01 mg/mL

Table 4.3. EC_{50} values evaluated for the free drugs and the formulations tested on PC3 and A549 (the concentration of psi-DOX and pSi-DTX are referred to the formulations).

DOX EC_{50} values are comparable to the ones found by Shu *et al.* (0.75 μM) on PC3 and by Melguizo *et al.* (0.71 μM) for A549[155,156].

DTX EC_{50} values are coherent to the values reported by Cancino-Marentes *et al.* (20 nM) on PC3 and by Kuo *et al.* (7.6 nM) on A549[157,159].

It is interesting that when using pSi to deliver doxorubicin, the EC_{50} had a sevenfold reduction for PC3 and around eightfold for A549 compared to the free drug. This highlights a stronger cytotoxic effect when mediating the delivery of doxorubicin by means of pSi. However, when transporting docetaxel with pSi the EC_{50} was similar to the free drug on PC3 and 1.25-fold higher when considering A549. Therefore, in the case of DTX, the delivery mediated by pSi did not influence the half maximal concentration.

To sum up, we compared the cytotoxicity induced by the free drug versus the drug vectorized by the carrier (considering the loading capacity calculated in the previous section), untreated cells (CTRL) and bare pSi particles (pSi CTRL), considered

here as a control at the same concentration of the formulations (for pSi-DTX also pSi-CTAB and CTAB were used as a control). Free DOX vs pSi-DOX is reported in Figure 4.13 while free DTX vs pSi-DTX in Figure 4.14.

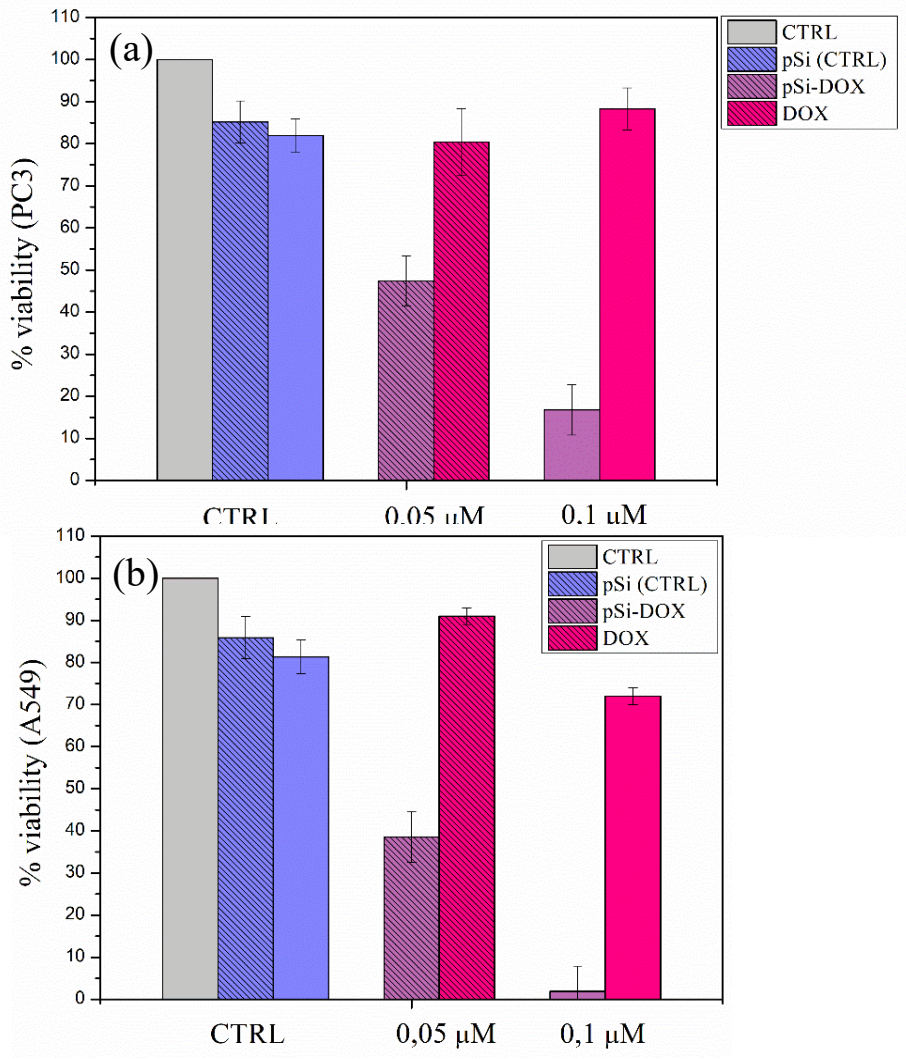

Figure 4.13. Cytotoxicity induced by free DOX vs. DOX encapsulated in pSi, on PC3 (panel a) and A549 (panel b).

Bare pSi particles were found to be non-cytotoxic (82-85% cell viability) at concentrations between 0.1 and 0.3 mg/mL (blue and dense pattern columns) in both PC3 and A549. On the other hand, DOX-loaded pSi particles in two different concentrations induced a significant decrease in the cell proliferation in both PC3 and A549 cell lines, compared to the free DOX:

(i) pSi-DOX vs free DOX (0.05 μM) → PC3: viability decreased from 80 to 47% with pSi-DOX

(ii) pSi-DOX vs free DOX (0.1 μM) → PC3: viability decreased from 88 to 17% with pSi-DOX

(iii) pSi-DOX vs free DOX (0.05 μM) → A549: viability decreased from 91 to 39% with pSi-DOX

(iv) pSi-DOX vs free DOX (0.1 μM) → A549: viability decreased from 72 to 2% with pSi-DOX

The decrease in cell viability in both PC3 and A549 cell lines after exposure to doxorubicin, mediated by pSi particles, is probably due to a synergic effect between the payload and the carrier or to an intracellular release of doxorubicin upon internalization. A cytotoxic effect due to pSi can be ruled out because at the same concentration bare pSi do not exert antiproliferative effects.

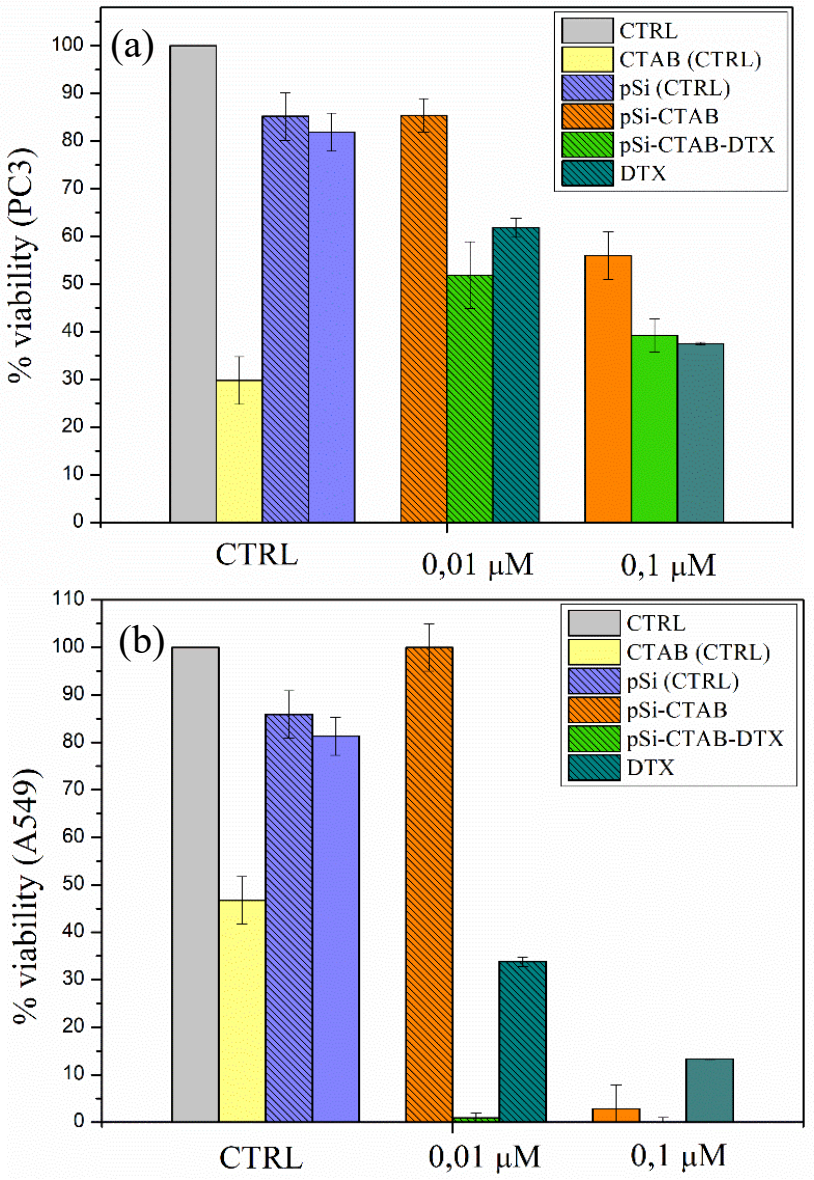

Figure 4.14. Cytotoxicity induced by free DTX vs. DTX encapsulated in pSi, on PC3 (panel a) and A549 (panel b).

The absence of toxicity of bare pSi particles at concentrations between 0.1 and 0.3 mg/mL was confirmed in both PC3 and A549 cell lines.

In the case of pSi-DTX it is worth reminding that to be able to conjugate DTX to pSi particles it was necessary to use CTAB as a "bridge". Consequently, also CTAB and pSi-CTAB were tested on the two cell lines to investigate any possible contribution. CTAB alone, indeed, at 20 µM concentration led to 30% cell viability in PC3 and 50% in A549.

When used to coat pSi, it was at a concentration of 12 μM, therefore one might suppose that part of the cytotoxicity derives from it. However, when the cells were treated with pSi-CTAB the viability was always higher compared to the same concentration of pSi(-CTAB)-DTX in PC3 and at a concentration of 0.1 mg/mL in A549. The only case with low viability recorded with pSi-CTAB is at a concentration of 0.3 mg/mL in A549, probably due to the aggregation of the particles or other factors that need to be further investigated.
DTX-loaded pSi particles induced a significant cell viability decrease at two different concentrations only in the A549 cell line proliferation compared to free DTX, whereas a similar cytotoxicity in PC3 cells, in particular:

(i) pSi-DTX vs free DTX (0.01 μM) → PC3: viability decreased from 62 to 52% with pSi-DTX
(ii) pSi-DTX vs free DTX (0.1 μM) → PC3: similar viability (~37%) with pSi-DTX and free DTX
(iii) pSi-DTX vs free DTX (0.01 μM) → A549: viability decreased from 34 to 1% with pSi-DTX
(iv) pSi-DTX vs free DTX (0.1 μM) → A549: viability decreased from 13 to 0% with pSi-DTX

After the exposure to docetaxel mediated by pSi particles the cell viability is comparable to the exposure to free DTX. Therefore, except for pSi-DTX at 0.01 μM on A549, we can exclude a synergic effect between pSi and the drug. This is, however, consistent to what previously discussed regarding the dose-response of free DTX (Figure 4.10): when treating with concentrations higher than 0.025 μM the drug has already reached its highest toxic effect and from that point on the effects on cell proliferation remain unchanged. This might be related to drug resistance phenomena. In this case we are discussing two concentrations, 0.1 and 0.01 μM, but we lack information between them and in particular at 0.025 μM. Therefore, it would be interesting to investigate the cell viability at concentrations between 0.01 and 0.1 μM.

4.C. Conclusions

We were able to efficiently load the anticancer drugs doxorubicin and docetaxel to carboxyl-functionalized pSi particles. Moreover, we were able to cover the doxorubicin-loaded pSi particles with hyaluronic acid to add a cancer targeting functionality (cytotoxicity still needs to be assessed). The cytotoxic activity of the pSi formulations (pSi-DOX and pSi-DTX) was tested on two human cancer cell lines, associated with aggressive prostate (PC3) and non-small cell lung (A549) cancers. We obtained interesting results:

(i) pSi-DOX EC_{50} had a sevenfold reduction in PC3 and around eightfold in A549 compared to the free drug
(ii) pSi-DTX EC_{50} was similar to the free drug in PC3 and 1.25-fold higher in A549
(iii) pSi-DOX had an antiproliferative effect higher than the free drug at different concentrations on PC3 (viability went from around 85 to 47-17%, depending on the concentration) and on A549 (viability from 90-70 to 39-2%, depending on the concentration)
(iv) pSi-DTX had a cytotoxicity comparable to the free drug on both the cell lines even at different concentrations.

Therefore, we obtained a significant improvement of anticancer properties when mediating the delivery of doxorubicin by means of pSi. When DTX was coupled to pSi there was almost no difference in the cell viability. This is probably due to the investigated concentrations (0.1 and 0.01 μM). Indeed, it was reported in the literature that after around 25 nM, DTX-induced antiproliferation reaches a plateau and the cell viability remains constant[157,158].

Further investigations are needed, especially between 0.1 and 0.01 μM, to understand the behavior of docetaxel and the influence of pSi as a carrier. One possible way to overcome the drug resistance in vivo of both DOX and DTX would be the implementation of a co-delivery. By taking advantage of the presence of a second anticancer agent, this would allow to decrease the concentration of the studied drugs, thus hampering the onset of the drug resistance.

Moreover, it still has to be investigated the targeting ability of the HA coating and its possible effects on the cell viability of the here reported cancer cell lines.
With these preliminary investigations we demonstrated the potential of using pSi-COOH particles as a delivery system for anticancer drugs: the synergic interaction between pSi and doxorubicin resulted in larger cytotoxic effects on the tested cell lines compared to the free drug, thus paving the way for their application as a chemotherapy tool.

CHAPTER 5

IMMUNOTHERAPY

5.A. Background and introduction

Immunotherapy is a cancer treatment approach that has earned successful achievements among the last few decades[160]. The principle on the bottom of it is that if cancer cells are being targeted it is possible to boost the immunologic response and therefore to find and kill more cancer cells.

The firsts to hypothesized that cancer can be treated by modulating the immune system were the German medical doctors, Wilhelm Busch[161] and Friedrich Fehleisen[162], during the 19th century: they noticed the regression of tumors in patients after infection by erysipelas, a bacterial skin infection. A few years later, in 1981, the American surgeon William Coley, sometimes referred to as the "Father of immunotherapy"[163], in order to report evidence of the efficacy of the practice, started a research project that consisted in inoculating patients with inoperable cancers with the extracts of inactivated bacteria S. pyogenes and Serratia. With the use of the so called "Coley's toxins", he was able to achieve the regressions of tumors in more than 1000 patients. Although, the lack of scientific protocols and inability to reproduce the results together with the development of radio and chemo therapies precluded the diffusion of this treatment as cancer therapy regimen[164].

The effectiveness of the principle of using bacteria to treat cancer was definitively established with a trial conducted by Morales *et al.*[165] in 1976 where they employed the tuberculosis vaccine to prevent the relapse of non-muscle invasive bladder cancer. The foundation of this study resides in a 1959 work by Old *et al.*[166] who demonstrated the anti-tumor effects of the Bacille Calmette-Guérin (BCG) bacteria in mice with bladder cancer. BCG therapy was so effective that has continued to be used nowadays. It would be legit to mention that Old was also a discoverer of the tumor necrosis factor (TNF-α) in 1975[167]. TNF-α is an important pro-inflammatory cytokine, produced by macrophages and monocytes, that regulates inflammatory and immune responses. It is responsible for signaling events, such as proliferation and differentiation but it is also able to induce necrosis or apoptosis[168]. Nowadays

(as of August 2022), there are more than seventeen immunotherapy agents approved for several cancer types (e.g., lymphoma, leukemia, melanoma, lung, bladder, triple-negative breast, kidney, colorectal) and more than twenty ongoing clinical trials[169]. An example of the promising efficacy of immunotherapy is ipilimumab, the first immunotherapy treatment approved for advanced melanoma in 2011: over the 20% of the recipients of the treatment enrolled during the first clinical trial are still alive without a recurrence[163].

Depending on the type of cancer, immunotherapy can be carried out in different ways (Figure 5.1), such as:

- injection of monoclonal antibodies to precisely target cancer cells,
- inhibition of immune checkpoints to achieve a stronger immune response,
- administration of immunomodulators (e.g., immunomodulatory drugs, cytokines, BCG) to enhance immune response against cancer,
- adoptive cell therapy to improve the immune system ability to kill cancer cells by isolating cells (i.e., natural killer, dendritic and cytotoxic T cells) from the patient and then re-injecting them back once activated,
- cancer vaccines to help boost the immune systems against cancer cells.

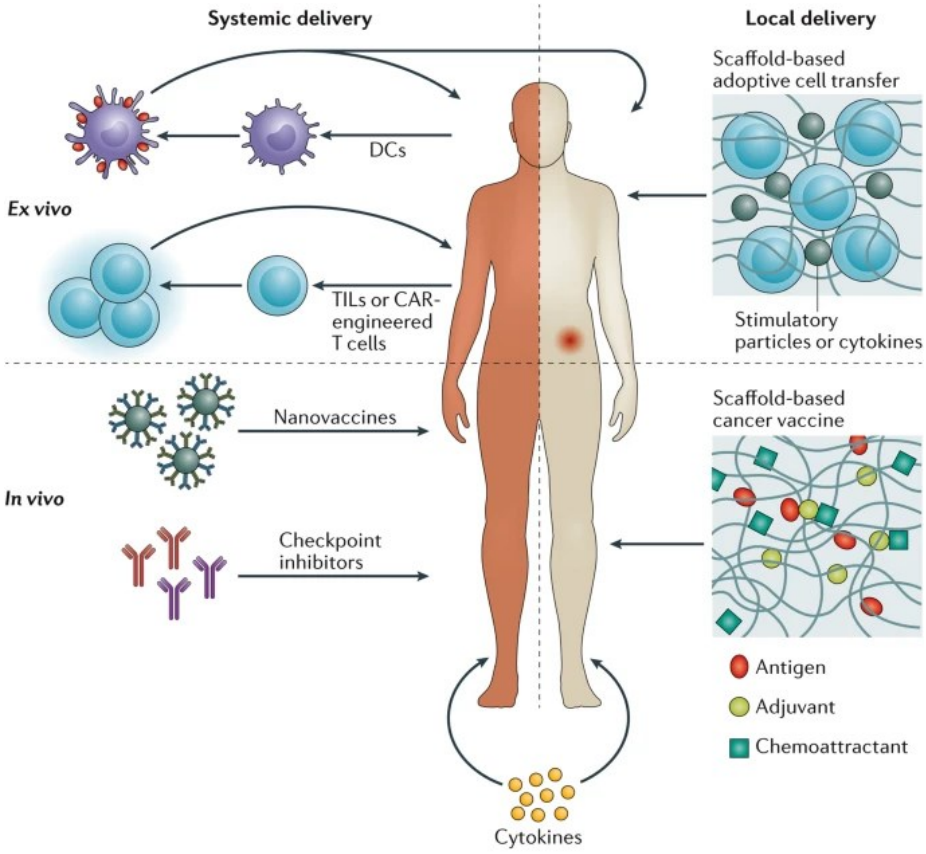

Figure 5.1. Visual representation of systemic (left) and local (right) immunotherapeutic administration paths. Upper left, ex vivo delivery: adoptive cell therapy, that reinject activated immune cells (i.e., DCs, T-cells). Lower left, in vivo delivery: immune-checkpoint inhibitors, immunomodulators (i.e., cytokines) and nanovaccines. Upper right: adoptive cell transfer through a carrier. Lower right: cancer vaccination by loading adjuvants and antigens on a drug delivery system[3].

However, so far, those administration pathways of immunotherapy can be effective merely for certain tumors and only a limited number of patients can respond positively to the treatment which are sometimes associated with unwanted side effects related to systemic toxicity, therefore, the scientific research on this field is still in progress to try to improve this promising therapy[170,171]. A solution can be found in the use of delivery vehicles (i.e., drug delivery systems, already discussed in Chapter 1), which are not only able to protect the patients from adverse events but also to avoid systemic administration in favor of a localized delivery of immune cells and immunostimulatory agents to specific sites[3,4].

5.A.1 Dendritic cells

Dendritic cells (DCs) are antigen-presenting cells (APCs) that play a fundamental role in the activation of the immune response and the development of innate immunity. DCs take their name from their long and spiky arms (i.e., dendrites) that are used to move and to capture the pathogens. In their immature state they are rounded with uniformly smooth cell surface and crowned by short dendrites, however, after maturation caused by external stimuli, their morphology changes to a bigger flattened shape, rougher surface, and longer dendrites. These morphological changes are fundamental for the modification of the immunological functions related to the mature state [172–174]. Figure 5.2 shows the different maturation states of DCs towards immunity.

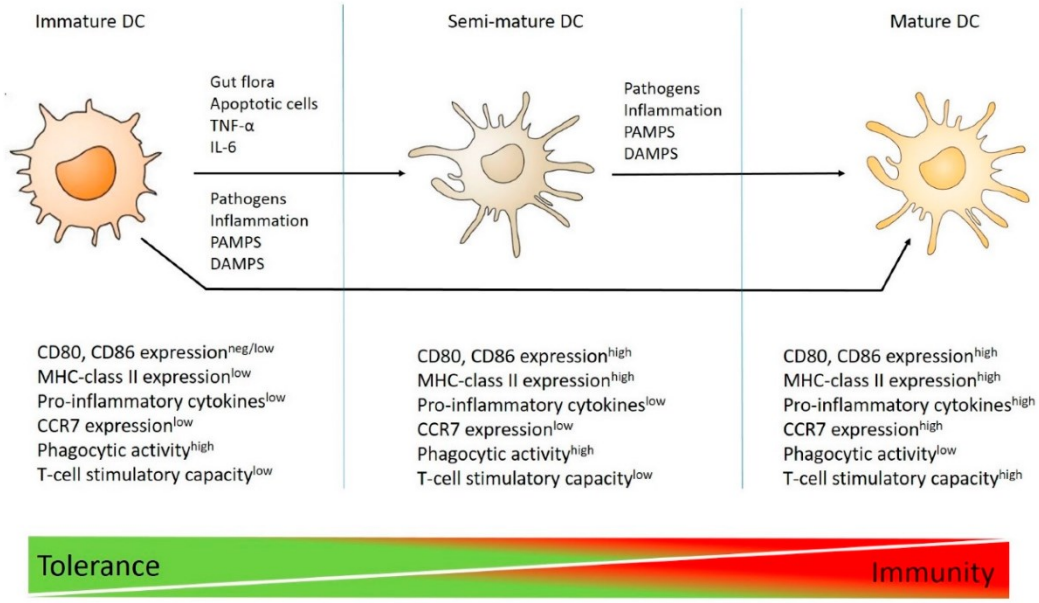

Figure 5.2. Maturation states of DCs[175].

In the immature state DCs sample the surrounding environment through their pattern recognition receptors (PRRs) (e.g., toll-like receptors (TLRs), complement receptors (CRs), NOD-like receptors (NLRs)), internalize and process exogenous antigens through a continuous phagocytosis and endocytosis. However, they are not able to produce proinflammatory cytokines, such as TNF-α, IL-23 and IL-12, nor upregulate costimulatory molecules (i.e., CD 80 and CD86). They can differentiate in their semi-mature state in presence of apoptotic cells, lactobacilli from the gut flora, TNF-α. In this state they can express costimulatory molecules and MHC-class

II, but they are still not able to release high levels of proinflammatory cytokines. Both immature and semi-mature DCs can reach the fully mature state in presence of high level of inflammatory and microbial signals (e.g., cytokines and microbial ligands). This results in the release of high quantities of proinflammatory cytokines, elevated expression of costimulatory molecules and the ability of antigens processing and presentation. Moreover, the occurrence of these events further leads to enhanced immunogenicity and T-cell priming, ultimately triggering the immune response[175,176].

Among all the PPRs present on the DCs surface, TLRs are transmembrane proteins that can be found not only on the surface but also inside immune cells like macrophages and DCs. These receptors are able to recognize typical pathogens structures called pathogens-associated molecular pattern (PAMPs) in the extracellular environment and consequently to alert the immune system[177]. In this regard, when we previously investigated the stimulation of the activation of immune systems cells induced by our silicon-derived carrier[9] (deeply discussed in the following paragraphs), we used as positive control some endotoxins representative of typical PAMP molecules called bacterial lipopolysaccharides (LPS), that are recognized from TLR 2 (as many other PAMPs) and can cause a very intense cytokines release[178].

Uptake processes of DCs can happen by phagocytosis, micropinocytosis and receptor-mediated endocytosis (Figure 5.3).

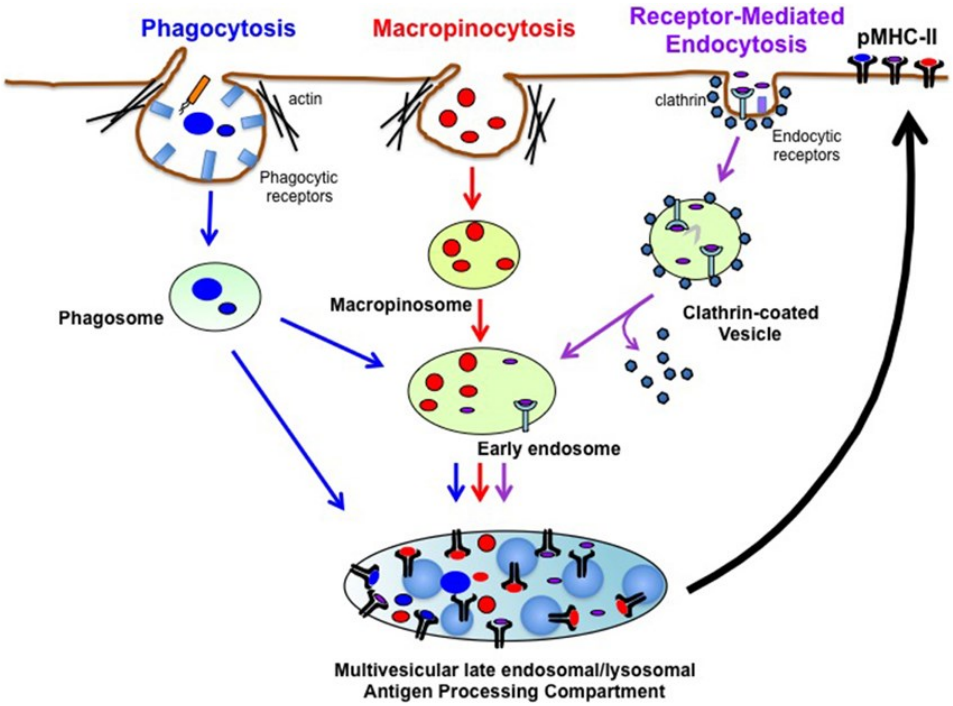

Figure 5.3. Representation of the available pathways of antigens uptake in DCs[179].

Phagocytosis is usually implemented when the antigen molecules that have to be taken up are rather large and non-soluble, it can be either non-specific or receptor-mediated and it forms big endocytic vesicles called phagosomes (>0.5 μm). Macropinocytosis, on the other hand, happens when there are soluble molecules (i.e., antigens and nutrients) that are internalized by forming less larger vesicles (0.2-5 μm) called macropinosomes, it is non-specific but actin-dependent. While receptor-mediated endocytosis necessary involves antigen binding to the membrane receptors of DCs. In this case, the antigens are mostly small soluble molecules and engulfed in small vesicles (0.1 μm) that can be coated or not with clathrin (a self-assembly protein)[179].

As reported by Jia J *et al.*[180], nanoparticles can influence the internalization and the immune response promoted by DCs in different ways, depending on their physicochemical properties. For example, the size can determine the recognition and the endocytosis pathway: the smaller the nanoparticles are, the easier is for the cells to engulf them[181]. The surface charge also plays a crucial role, i.e., positive Au nanoparticles were shown to be more efficiently taken up compared to the negative

ones[182]. However, the efficiency of the uptake does not depend on just one of those factors, ligands, shape, coatings, and their combinations can affect the internalization process.

When treating a patient with immunotherapy or for in vitro investigations, DCs are usually isolated from the blood monocytes of the patient, stimulated, and then re-injected into the patient to boost the immune response against cancer cells[183]. For the experiments reported in the following section we applied an established protocol to isolate them, briefly, monocytes separated from blood samples of human donors were stimulated for 5 days with IL-4 (interleukin 4) and GM-CSF growth factor to induce differentiation into DCs[184].

To promote the tumor antigen presentation of DCs, cancer vaccines are typically coupled with an immunologic adjuvant to help increase the DCs stimulation and the immune response. Few adjuvants, like aluminum hydroxide are FDA approved and already used in clinics, but new generation of adjuvants based on TLR recognition is currently under studies[185].

One path, that is currently under investigation, is the use of nanosystems as carriers to transport cancer these vaccine adjuvants: a local administration paired with lower doses can help reduce the side effects and systemic toxicity related to cancer treatments and vaccinations. Moreover, they can be modified to target their uptake to certain cells or labeled to be tracked once internalized by the cells[186].

Our study fits within this branch of research, indeed, we investigated the delivery of an immunologic adjuvant, Pam3CSK4, loaded within pSi-COOH microparticles.

5.A.2 Pam3CSK4

Palmitoyl-3-cysteine-serine-lysine-4 (Pam3CSK4), see Figure 5.4, is a synthetic lipopeptide member of PAMPs and activator of the pro-inflammatory transcription factor NF-κB, that can recognize and bind TLR 1 and 2[187].

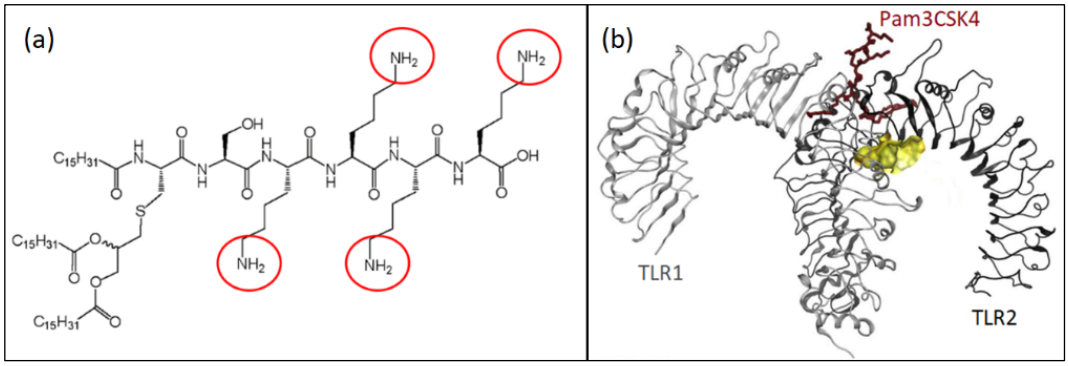

Figure 5.4. Structure of TLR agonist, Pam3CSK4. The amine groups are marked (panel a); Representation of TLR1/2 heterodimer to recognize Pam3CSK4 (panel b)[188].

Pam3CSK4 gained interest for the development of a new adjuvant in the field of immunotherapy and cancer vaccines because it's a TLR 1/2 ligand (Figure 5.5) whose receptors can be found on the surface of DCs which engagement leads to their activation and maturation thus triggering adaptive and innate immune response.

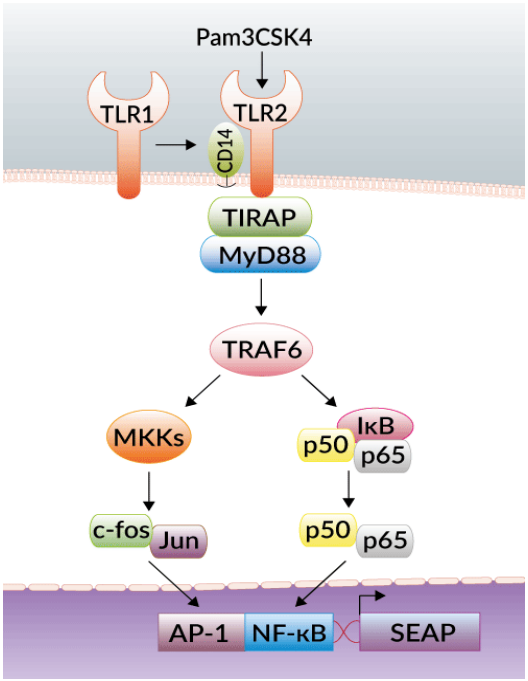

Figure 5.5. Signaling pathway of TLR 2 and TLR 1 activation after binding with Pam3CSK4. (Image from InvivoGen website)

However, TLR ligands like Pam3CSK4 present some issues that thwart their clinical application such as poor bioavailability, fast degradation and absence of selectivity of action[189,190].

Therefore, the only way to avoid those obstacles is using a carrier that allows not only to transport the molecules and to protect them from degradation but also to improve their availability with a controlled release that enables to reach the selected receptors and prolong their activation with a predictable duration. Moreover, by using a delivery system it is also possible to target DCs, i.e., with CD40, in order to achieve a higher selectivity and efficacy of the treatment and to prevent non-specific activation of immune responses that can cause unwanted side effects like triggering regulatory processes[189,191].

5.A.3 Delivery of Pam3CSK4

Over time, the encapsulation of Pam3CSK4 has been studied with different kind of carriers: Lamrayah *et al.* and Megy *et al.* investigated the entrapment in PLA nanoparticles supported by means of molecular modelling, Alkie *et al.* compared the innate response induced by Pam3CSK4 soluble and encapsulated in PLGA, while Katebi *et al.* combined the same system with an antigen to achieve a targeted delivery. Other examples of delivery systems for the studied molecule are an N-trimethyl chitosan carrier formulated by Bal *et al.* to apply Pam3CSK4 for nasal and intradermal vaccines and an ARC4 and ARC7 -based system developed by Haddadi *et al.* to deliver it to mice[190,192–196].

Nevertheless, as far as we know, no reports are available in the literature about the association of Pam3CSK4 with mesoporous silicon nanostructures (i.e., pSi microparticles).

It was chosen, among other adjuvants, to be loaded within pSi microparticles because it can fit inside the particle's pores[7] and because it features multiple binding sites. Its acylated amino termini, in fact, not only mimics the bacterial LPS ones (in which resides their stimulatory activity) using a similar signalling pathway[197], but, if protonated, they allow an electrostatic binding between the molecule and the carboxylic groups present on pSi-COOH. Moreover, there is a labelled form available that can be exploited for imaging studies and characterization through its photoluminescence.

5.B. Results and discussion

5.B.1 Preliminary investigations on porous silicon as drug delivery system

In previous studies that served as pillars of this thesis, we proved the ability of pSi to transport and release in vitro a small and positively charged molecule, cobinamide (Cbi), which is a vitamin B12 analogue that allowed us to investigate the effect of the surface chemistry of pSi on drug stability, loading amount and release profile. Cbi was attached through an electrostatic interaction to the -COOH groups present on the surface and on the pores of pSi particles, the weak binding enabled a slow release in PBS (pH 7.4). Furthermore, the carboxylic functionalization combined with the PEG coating helped controlling the redox activity of the particles towards the drug that, as a result, did not degraded[8].

After assessing the ability of our system to efficiently load and release a drug and after demonstrating that through appropriate coating it was possible to maintain the intrinsic photoluminescence for a prolonged time, cytotoxicity and immunogenicity needed to be evaluated for applications in the biomedical field. Indeed, when developing a drug delivery system, it is fundamental to corroborate its safety to avoid unwanted side effects that might happen during the future clinical use.

In our case, we wanted to verify that our particles do not have toxic effects on human immune cells, nor they stimulate the release of cytokines or the generation of oxygen free radicals. For this purpose, we studied the interaction of our pSi-COOH particles with cells of the immune system, following the steps pictured in Figure 5.6. More specifically, we investigated monocytes, dendritic cells and lymphocytes viability, Cytochrome C reduction and the release of the cytokines TNF-α and IL-6 (inflammatory and immune-stimulatory cytokines involved in the systemic acute phase) and IL-12 (related to the natural killer cells and the T lymphocytes).

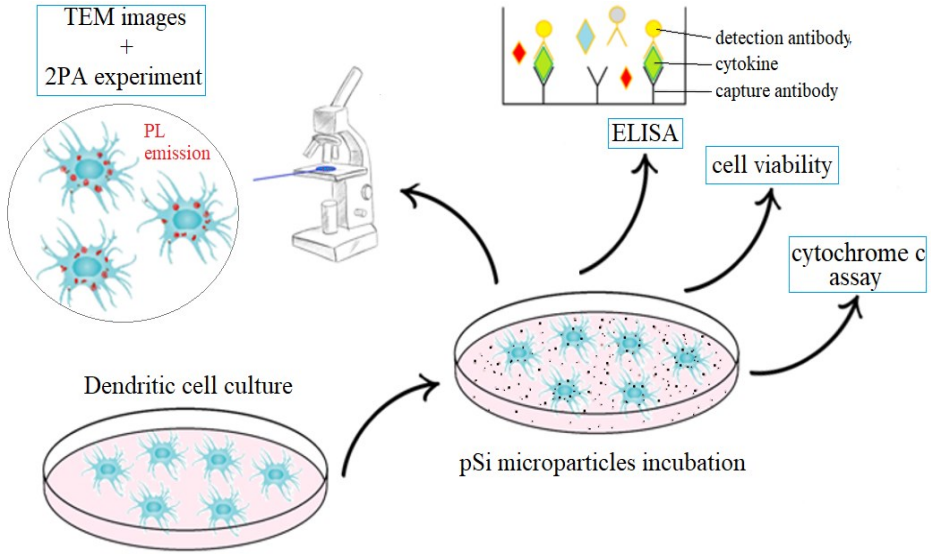

Figure 5.6. Experimental steps to perform cell viability tests, immune assay and cell imaging.

The ROS production was evaluated by cytochrome c reduction assay. Indeed, the superoxide anion reduces the cytochrome c (a molecule isolated by horse heart and added to the cells in the assay).

To investigate the cells viability and immunogenicity we used the alamarBlue™ assay for the first and enzyme-linked immunosorbent assay (ELISA) for the second. AlamarBlue™ is an assay based on the measurement of metabolic activity of the cell: resazurin is a dye that undergoes reduction upon metabolization, and the reduced dye is highly fluorescent. Thus, a decrease of fluorescence is related to a decrease of dye metabolization and therefore of cell viability (Figure 5.7).

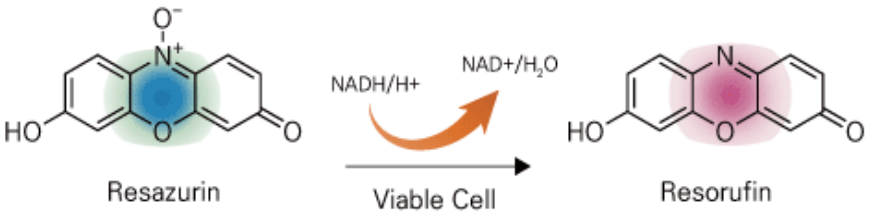

Figure 5.7. Reduction reaction of resazurin that allows to quantify cell viability (image from Biomax© website).

ELISA is a biological test that allows to quantify the macromolecules (peptides, proteins, antibodies) present in the supernatant of cell cultures.

The working principle of ELISA is that the presence of any antigen can be detected, through an enzymatic reaction, after its binding to an antibody attached at the bottom of a well-plate. The reaction is colorimetric thus it will be converted in a measurable fluorescence signal with an intensity proportional to the cytokines concentration. In Figure 5.8 is reported an overview of the steps needed to perform a sandwich ELISA assay, representative of the one we used.

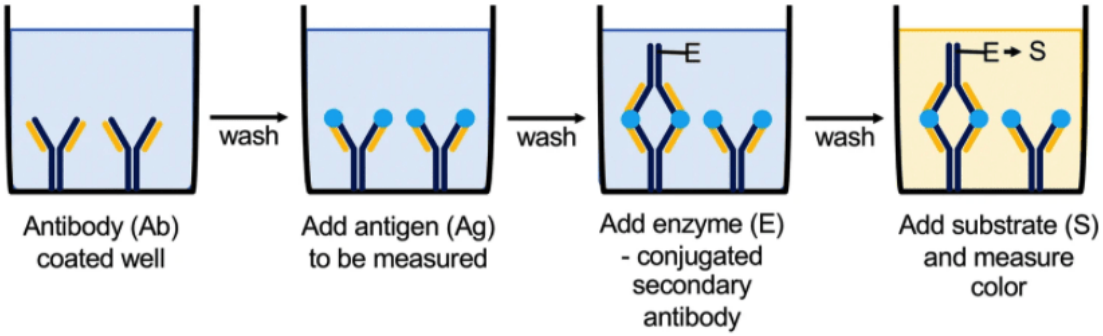

Figure 5.8. Overview of sandwich ELISA that allows to quantify the protein concentration through a colorimetric reaction. (image from Boguszewska et al., 2019[198]*).*

The internalization of our carrier was investigated by two-photon absorption, TEM (not shown) and optical microscopy after staining with May-Grunwald-Giemsa that allows to clearly distinguish the nucleus (Figure 5.9).

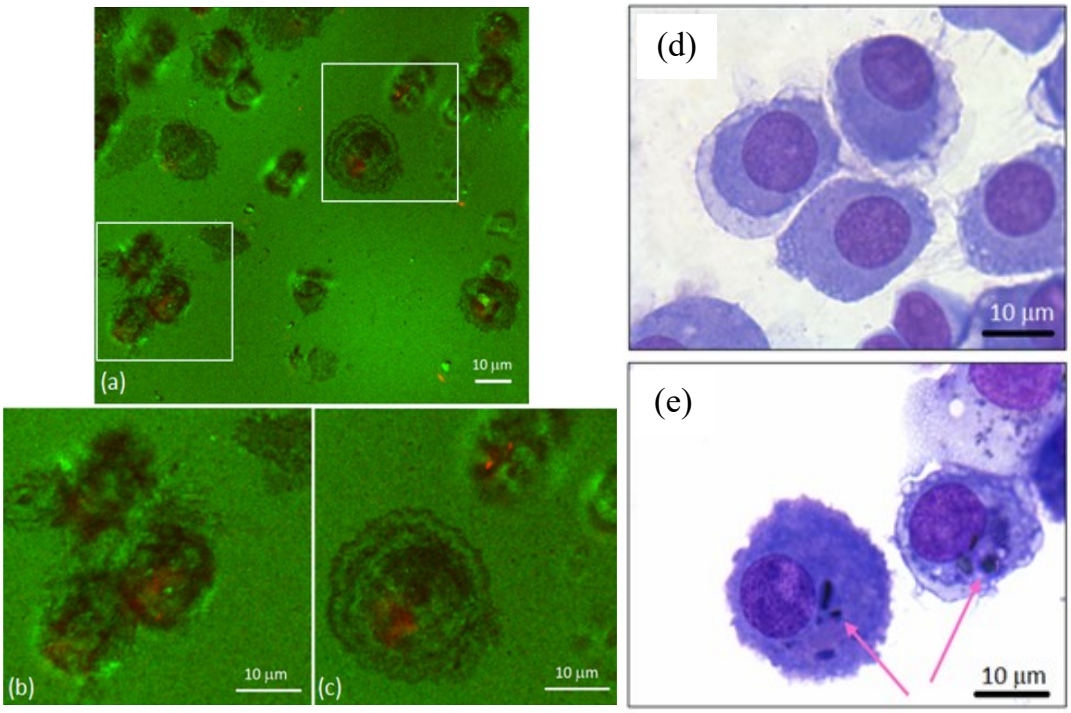

Figure 5.9. Two photon absorption image of pSi–TiO_2 microparticles internalized in DCs. The cells are represented in green color scale, while the PL of the microparticles in red color scale (panel a). Zoom of the highlighted areas (panel b and c). Optical microscopy of May-Grunwald-Giemsa-stained DCs: cells cultured in the absence (panel d), or presence of pSi-TiO_2 microparticles. Ingested particles are indicated by arrows (panel e)[9].

The two photon absorption images (panel a, b and c) clearly show that the microparticles (in red-color scale) were preserving their photoluminescence and internalized by the cells (in green-color scale) and did not exert toxic effects since there cells were alive and not showing apoptosis. Through the optical microscopy images (panel d and e) it was possible to localize the presence of the pSi particles in the cytoplasm and outside the nucleus (indicated by the pink arrows) and to confirm that the cells were healthy (well-defined nucleus and homogeneous shapes) and not in the apoptotic phase.

After cytochrome c reduction assay, we found that pSi microparticles were not able to induce O_{2-} release, neither in combination with LPS. Therefore, they do not induce the production of toxic oxygen radicals. With the viability assay we demonstrated that pSi-COOH did not induce any cytotoxic effect in the cells of the immune system (monocytes and lymphocytes), indeed, the viability was higher than

90% even at high microparticles concentration (100 μg/mL). While by means of ELISA assay, we were able to confirm that after incubation with pSi microparticles DCs were not to produce cytokines (IL-12, IL-6, and TNF-α) on the contrary of LPS, that were used as a positive control, that induced a high release of all the investigated cytokines. Moreover, when DCs were co-stimulated with LPS and microparticles we observed a dose-dependent increase of the released cytokines as compared with DCs stimulated with LPS alone, a so called "priming effect" that will be discussed deeply in the next paragraph.

Consequently, we demonstrated that after being efficiently internalized by DCs, our silicon-based carrier not only does not exert toxic effects on neither dendritic cells nor lymphocytes or monocytes, but also they do not have an immunogenic effect[9].

Priming effect

When studying cells stimulation, it is important to consider also the priming effect and how it can affect the reaction of cells to treatments. By definition, cell priming is an event that occurs when an antigen and antigen-specific T helper cell precursors meet for the first time[199]. As a result, cells will be prepared into lineage-specific differentiation that involves, for example, cells activation and molecular signaling, and will result in a more efficient immune response against upcoming pathogens. The antigen presentation provided by DCs primes naive T lymphocytes and it's fundamental for the generation of effector and memory T-cells[200]. Moreover, during this event DCs operate other important functions like the expression of co-stimulatory ligands to promote cell-to-cell interactions and the release of cytokines, which regulate cellular communication and stimulate T-cell responses. The combination of these two phenomena triggers the T-cell expansion, the immune response length and the development of effector T-cells functions that results in killing only the malignant or virus infected cells carried by cytotoxic T-lymphocytes[200,201]. Figure 5.10 summarizes the fundamental steps that take place during the immune response to cancer cells.

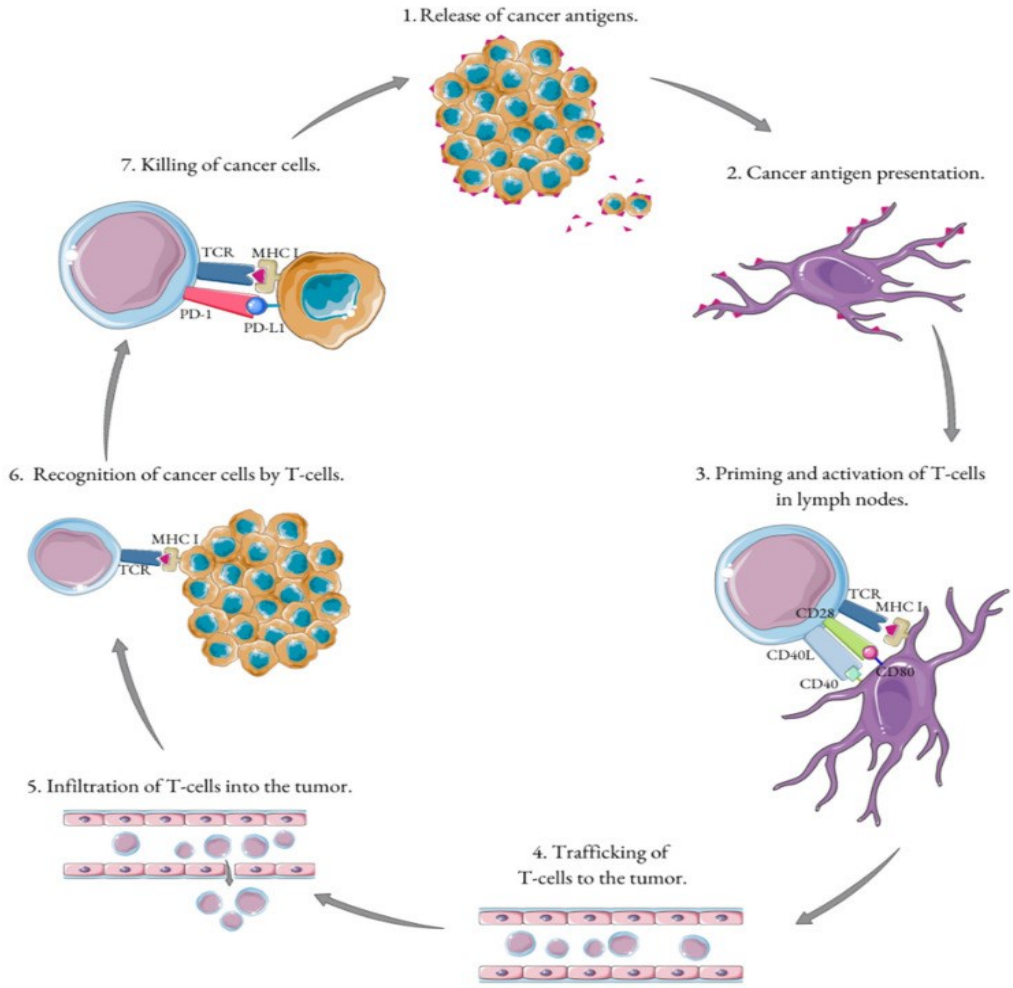

Figure 5.10. Schematic overview of cancer immunity cycle (from Karwacki J et al., 2022[201]).

During our previous studies, cited in the latter paragraph, we considered worth addressing the possibility of a priming effect of bacterial components (i.e., LPS), that can be found in the biological environment, caused by our silicon-derived system. In fact, if the priming occurs, it might lead to negative side effects like allergy or autoimmunity. Therefore, we investigated if the combination of our particles and LPS might stimulate a higher release of cytokines provided by DCs.

In Figure 5.11 it is reported the quantification of cytokines (TNF-α, IL-6 and IL-12) released upon incubation of DCs with just pSi-COOH microparticles, LPS and a co-treatment of the two of them.

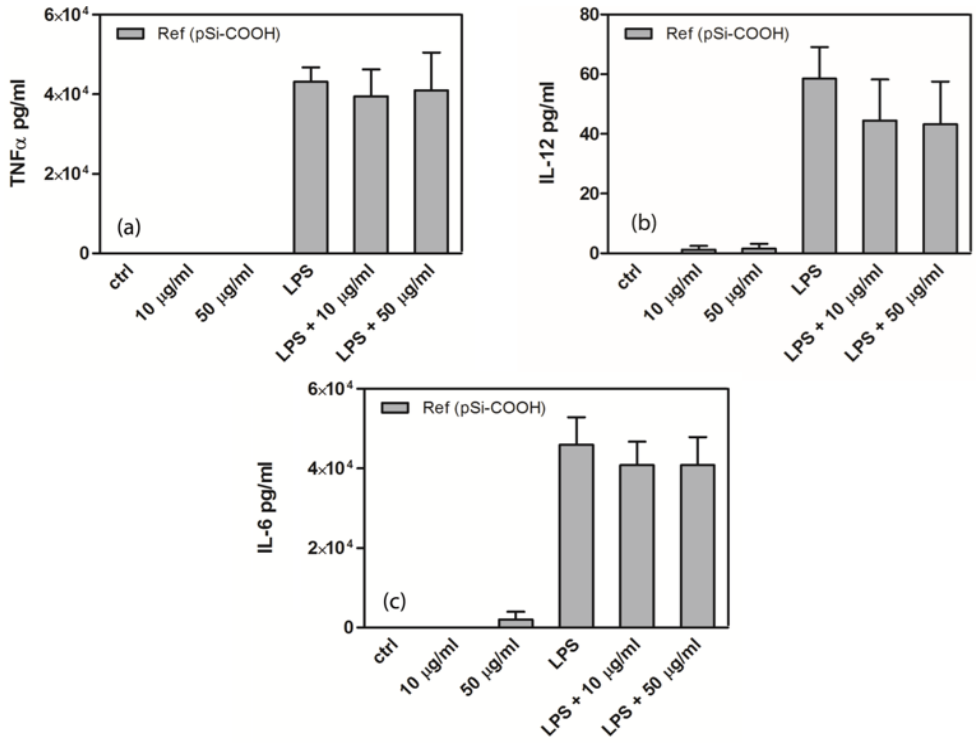

Figure 5.11. Evaluation of cytokine secretion by DCs upon incubation with different pSi-COOH microparticles with and without the addition of 100 ng/mL LPS: TNF-α (panel a), IL-12 (panel b) and IL-6 (panel c). The results are expressed as the mean value and standard deviation of five independent experiments. LPS served as positive control.

We obtained two important findings. First, the treatment with just pSi particles did not induce the release of cytokines, thus for further investigations we can exclude an immunogenic effect of our pSi particles. Second, a priming effect was not observed for any of the examined cytokines, in fact, when DCs were incubated with pSi and LPS together the amount of released cytokines was not higher compared with LPS alone[9].

When first approaching to the part of this thesis work related to the immunotherapy field, the findings, obtained from our group, used as starting points can be summarized as the followings:

- pSi particles are taken up by DCs with a non-receptor mediated mechanism. Microscopy images revealed that the carrier is mainly distributed inside vacuoles and its photoluminescence is preserved even when endocytosed.
- Absence of toxicity of our silicon-derived carrier against dendritic cells, monocytes and lymphocytes: cells viability was not affected even at high

concentrations (up to 50 μg/mL).

- The production of reactive oxygen species (ROS) was not detected when the immune cells were treated with pSi alone or in combination with LPS: they do not induce oxidative damage.
- pSi particles do not show immunogenicity: the cytokines released from DCs after incubation with our carrier (for concentrations up to 50 μg/mL) are irrelevant.

Those results suggested that pSi particles might be an interesting candidate as drug delivery system in the field of immunotherapy thanks to its absence of toxicity and immunogenicity, its high surface to volume ratio and its long-lasting photoluminescence.

The first step of our investigations regarding pSi microparticles as drug delivery system for an immunotherapy adjuvant was to assess the effective loading of the chosen molecule in our pSi microparticles by means of optical and confocal microscopy. After that, the quantification of the loaded molecule and in a release study in buffer (PBS), to evaluate the release rate of *Pam3CSK4 in vitro, by* means of fluorescence spectroscopy. For this reason, the experiments were conducted with a rhodamine-labelled version available of the adjuvant: Pam3CSK4-R, with an intense PL emission at 578 nm when excited at 555 nm. To correlate the concentrations with the rhodamine signal it was used the method of external standard, thus a calibration curve of known concentrations of Pam3CSK4-R was created.

5.B.2 Pam3CSK4 loading and release study

Different concentrations of Pam3CSK4 (5 and 10 μg/mL) were loaded within pSi microparticles by using an immersion method. After drying overnight in a 50 °C oven, to completely remove the ethanol, the pSi microparticles (see Chapter 2 for fabrication and functionalization) were added to a solution of Pam3CSK4 in 2-(N-morpholino) ethane sulfonic acid (MES) buffer (pH 5.8). The suspension was then incubated overnight under mild rotation at room temperature. After the loading time, the suspension was washed 3 times to remove the free Pam3CSK4 and replaced with fresh buffer. The supernatant was kept for the quantification.

Pam3CSK4-R (used for characterization purpose only) was loaded following the same procedure.

To assess whether the loading of Pam3CSK4 within pSi microparticles was successful or not we used confocal microscopy. In fact, as already said, pSi has an intrinsic photoluminescence and Pam3CSK4 have a rhodamine-labelled version, thus they can easily be traced by excitation with at 405 nm for the first (λ_{em} 650 nm) and at 555 nm for the latter (λ_{em} 578 nm). Emission and excitation spectra of Pam3CSK4-R are shown in Figure 5.12.

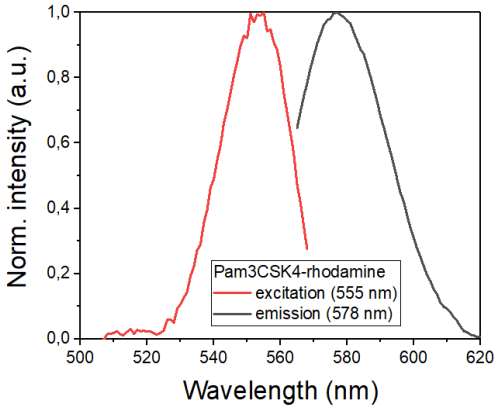

Figure 5.12. Normalized excitation (PLE) and emission (PL) spectra of Pam3CSK4-R.

The sample was measured after the loading and the washings by deposition of a drop on a microscope glass slide. The obtained images are reported in Figure 5.13 (panels a, b, c 100 µm scale and magnifications in panels d, e, f 25 µm scale). To better highlight the merging of the two images, pSi microparticles signal was set up as green while Pam3CSK4-R was set up as red.

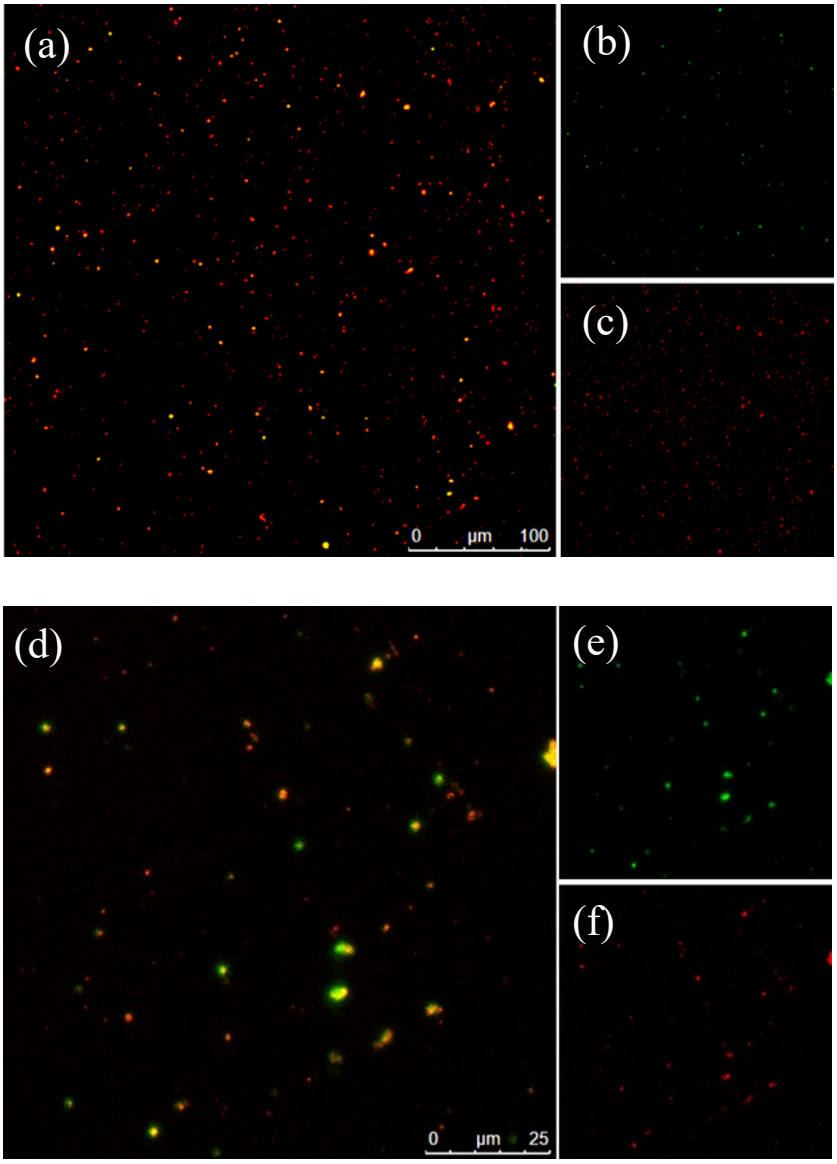

Figure 5.13. Confocal microscopy images of merged (panels a and d) and separate signals (panels b and c, panels e and f) of pSi microparticles, upon 405 nm excitation (in green) and rhodamine, upon 555 nm excitation (in red), respectively (panels a, b, c 100 µm scale and panels e, f, g 25 µm scale).

The merging of the two signals (green for pSi and red for Pam3CSK4-R) shows a good overlapping, therefore confirming the loading. The presence of red points without any corresponding green point could be due to the low signal intensity of pSi. As a matter of fact, it should be noted that the quantum yield is about 70% for rhodamine and only a few % for pSi, so the latter can be hard to detect when compared to first.

Quantification of loaded Pam3CSK4-R

After having confirmed the ability of the carrier to load Pam3CSK4, experiments with Pam3CSK4-R in two different concentrations were performed in MES buffer to find the best concentration ratio in order to optimize the loading within the pores. After the loading time, the samples were centrifuged and the supernatant containing the non-loaded Pam3CSK4-R was removed and kept, PBS buffer was added to the loaded pSi particles. Several sonication steps, centrifugations, removal of the supernatant and substitution with fresh PBS buffer were conducted to allow the whole loaded Pam3CSK4-R to be quantified. The amount of loaded plus non-loaded Pam3CSK4-R was compared to the initial amount incubated with pSi particles to confirm the success of the quantification method. To obtain the unknown concentrations of Pam3CSK4-R the external standard method was applied by creating a calibration curve of known concentration of the lipopeptide by means of photoluminescence spectroscopy.

Loading capacity (LC%) and encapsulation efficiency (EE%) were calculated by using the following equations:

$$LC\% = \frac{mass\ of\ loaded\ drug}{mass\ of\ loaded\ particles} \times 100$$

$$EE\% = \frac{mass\ of\ total\ added\ drug - mass\ of\ non\ loaded\ drug}{mass\ of\ total\ added\ drug} \times 100$$

Evaluation of loading capacity (LC%) and encapsulation efficiency (EE%) was conducted by quantification of the loaded Pam3CSK4-R and comparison with non-loaded Pam3CSK4-R. The obtained loading capacity was 0.30% for the sample with lower concentration and 0.49% for the sample with higher concentration. As expected, the encapsulation efficiency was the same for the two samples, 34%. The slightly difference between the loading capacity of the two samples suggested that doubling the concentration doesn't allow to load double Pam3CSK4-R.

In vitro release study

To investigate the release rate of loaded Pam3CSK4-R in a buffer, the loaded particles were dispersed in PBS and stirred. The PL intensities were converted into concentrations by the calibration curve. The obtained calibration and release curves are reported in Figure 5.14 in panel a and b respectively.

The release of the molecule was studied in buffer (i.e., PBS) by photoluminescence spectroscopy. After the loading of Pam3CSK4-R into pSi microparticles, the sample was dispersed in PBS with mild agitation at room temperature. At set times (20, 40, 60, 90 and 120 min) supernatants were collected and replaced with fresh PBS and measured by fluorescence spectroscopy. As for the quantification, a calibration curve was created to correlate the intensity of the rhodamine PL signal to its concentration.

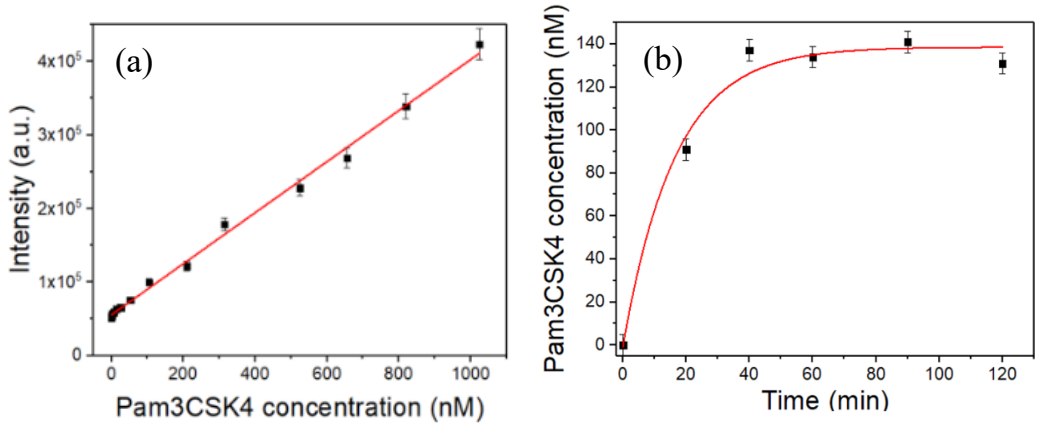

Figure 5.14. Calibration curve to obtain Pam3CSK4-R concentration from PL intensity signals (of rhodamine) (panel a). Determination of the release rate: Pam3CSK4-R concentration measured at set times (panel b).

The release curve shows that after 20 minutes about 64% of Pam3CSK4-R has been released. After 40 minutes, 100% reaching a plateau. This indicates that the molecule isn't strongly bonded within the pSi pores, accordingly to the electrostatic nature of the bonding. The release rate plays a crucial role because it allows the encapsulated adjuvant to be not immediately accessible as the soluble one but, instead, by carrying it with our drug delivery system it's released in a controlled way.

5.B.3 Interaction with Human Dendritic Cells

The investigation of the interaction of pSi particles with human dendritic cells was done in strict collaboration with Marta Donini and Prof. Stefano Dusi at the Department of Medicine, Division of General Pathology, University of Verona.

Upon approval of the Ethical Committee for the "Sperimentazione Clinica delle province di Verona e Rovigo (Prot. no. 46134, October 4th, 2016)" and after written

informed consent, buffy coats from the venous blood of normal healthy volunteers were obtained from the Blood Transfusion Centre at the University Hospital of Verona upon approval of the Ethical Committee of "Azienda Ospedaliera Universitaria Integrata di Verona" (Prot. no. 5626, February 2nd, 2012). Peripheral blood mononuclear cells were isolated using Ficoll Hypaque and Percoll (GE Healthcare Life Science) density gradients. To generate dendritic cells (DCs), monocytes were incubated at 37 °C in 5% CO_2 for 5–6 days at 106 mL in 6-well tissue culture plates (Greiner, Nurtingen, Germany) in RPMI 1640 medium, supplemented with heat-inactivated 10% low endotoxin FBS, 2 mM L-glutamine, 50 ng/mL GM-CSF, and 20 ng/mL IL-4. The final DC population was 98% CD1a+, as measured by FACS analysis. The immune response activation was evaluated by using ELISA assay to quantify the release of the cytokines (TNF-α and IL-12). For live-cell confocal imaging, DCs were transferred in a 8-well μ-slide and treated with soluble Pam3CSK4-R and pSi microparticles loaded with Pam3CSK4-R right before starting to acquire the frames. Frames were acquired every 1.5 minutes for the first hour, every 15 minutes for the following 4 hours and every 1 hour over night for 17 hours, by exciting the rhodamine labelling with a 555 nm laser.

Live-cell confocal imaging

When we investigated the interaction between our Pam3CSK4-R loaded pSi-COOH microparticles with DCs, the first step was to confirm their uptake. Therefore, we captured some confocal images (Figure 5.15) of DCs incubated with our loaded drug delivery system.

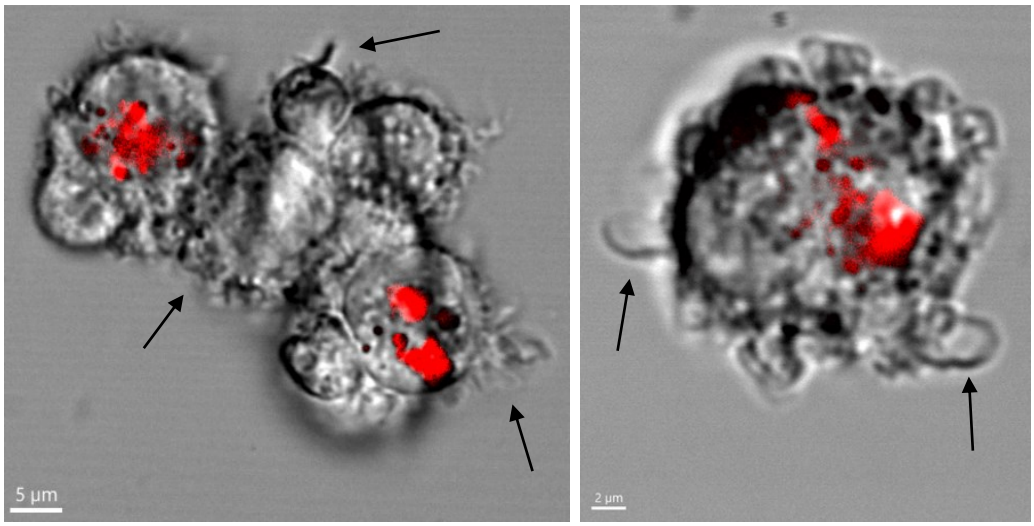

Figure 5.15. Confocal images (5 µm scale left and 2 µm scale right) of DCs incubated with loaded-pSi-COOH microparticles.

From these images it is possible to appreciate the red signal coming from pSi-COOH loaded with Pam3CSK4-R that have just been phagocytosed by the cells, thus giving a first confirmation of the successful uptake. The presence of the short dendrites (some indicated by arrows) all over their surface it is a typical feature of the immature state of this type of immune cells. Indeed, their morphology in the immature state is typically rounded with uniformly smooth cell surface and crowned by short dendrites. Once the payload will be released from the carrier, the DCs will evolve in their mature state thus changing their morphology into a bigger flattened shape, rougher surface, and longer dendrites.

To better investigate the effects on DCs of soluble Pam3CSK4-R vs loaded within pSi microparticles, time-lapse confocal imaging was performed to compare the kinetics of uptake, morphology modifications and localization of the drug carried by pSi microparticles when added directly into the incubation medium. In Figure 5.16 are reported the confocal frames captured every 15 minutes (the frames acquired in between are not reported) with the red channel (excitation at 532 nm) for DCs treated with soluble Pam3CSK4-R (left panels) and pSi particles loaded with the same molecule (right panels).

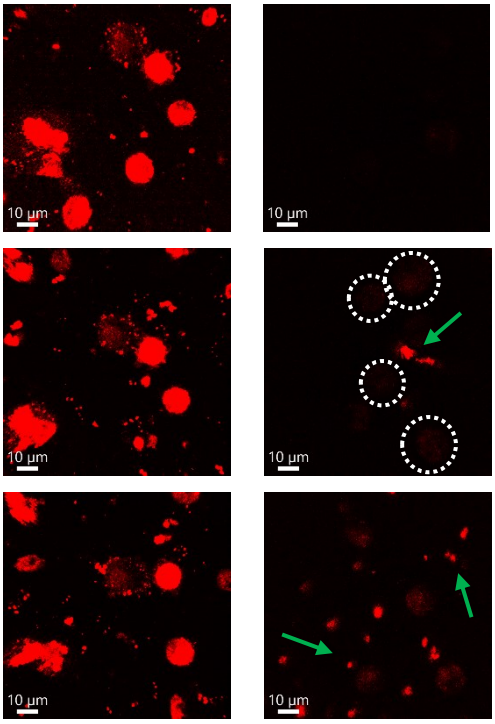

Figure 5.16. Live-cell confocal images (532 nm laser excitation, frames at 0, 15 and 60 minutes) of DCs treated with soluble Pam3CSK4-R (left panels) and with pSi microparticles loaded with Pam3CSK4-R (right panels) (10 µm scale).

When treated only with free Pam3CSK4-R (left panels of Figure 4), the cells had ready internalized it during the first 15 minutes. Indeed, the first frame was acquired 15 minutes after the treatment (due to the settings time) and it clearly shows the presence of the red emission of the labelled TLR ligand inside the cells. On the contrary, when the cells are treated with Pam3CSK4-R loaded within pSi microparticles (right panels of Figure 5.16), it is difficult to notice the slight rhodamine signal in the first frame. From the second frame the emission coming from the labelled molecule inside the cells is starting to become visible (white circles). Moreover, there is a clear red signal coming from loaded pSi particles floating inside the wells (large bright red spots indicated by green arrows) and not taken up by the DCs probably because of their large dimensions (i.e., agglomerations of pSi microparticles). By comparing the frames collected at 60 minutes, there is a clear difference between the intensity of the red signals: for DCs incubated with just soluble Pam3CSK4-R, indeed, the intensity is analogous to the one of the floating loaded-pSi particles (green arrows), meanwhile the one coming

from the cells is quite feeble. This represents a significant proof of the delayed presence of Pam3CSK4-R inside the DCs when treated with the vectorized molecule instead of the soluble one.

Focusing only on the DCs treated with Pam3CSK4-R loaded inside pSi microparticles, in Figure 5.17, where confocal frames steadily acquired for 23 hours are reported, we can observe that the signal started to become clearly visible only around four hours from the beginning of the treatment. Moreover, it is possible to notice that the more the minutes pass the clearer becomes the rhodamine signal.

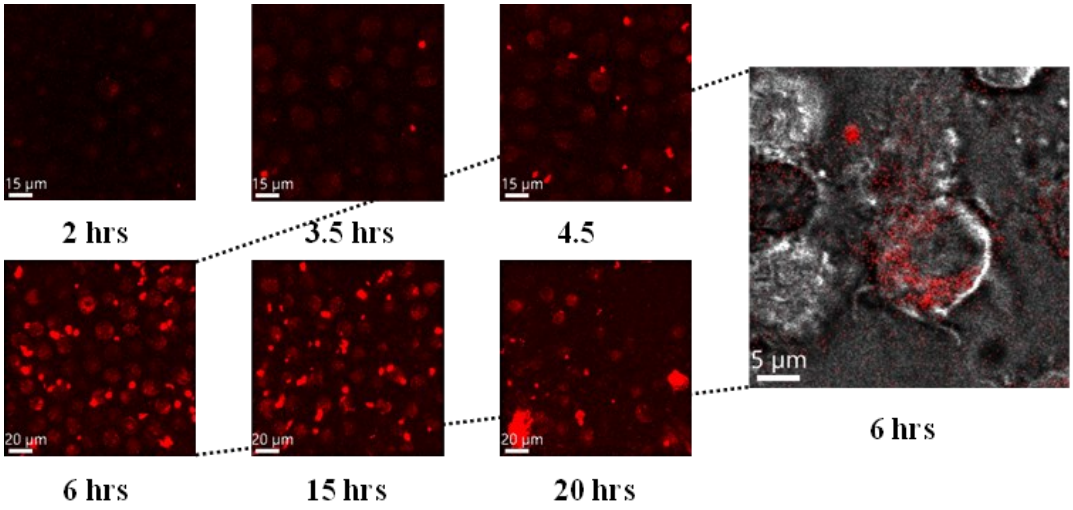

Figure 5.17. Left: overnight frames (2, 3.5, 4.5, 6, 15 and 20 hours after the stimulation) of live-cell imaging of DCs treated with pSi microparticles loaded with Pam3CSK4-R displayed through the red channel (15 and 20 µm). Right: inset from the 6 hours frame of live-cell imaging of DCs treated with pSi microparticles loaded with Pam3CSK4-R and their distribution (5 µm scale).

As the confocal images show, the slower phagocytosis leads to a slower display of the red signal, when the Pam3CSK4 is inside the pSi microparticles is indeed not immediately accessible to the cells. As proved, also by means molecular modelling, by Tamiru *et al.* and Lamrayah *et al.* , for different delivery systems but with the same molecule, once DCs are incubated with free Pam3CSK4 its internalization is instantaneous, but the TLR ligand is consumed right away[193,202]. On the contrary, when Pam3CSK4 is entrapped inside the pores and on the surface of the carrier, a lower amount is steadily accessible to the cells but its availability lasts for a longer time. The small amount of ligand attached on the surface of the drug delivery

system will rapidly bind the receptors available on the surface of the cells, thus the presence of a low intensity red signal during the first four hours. Whereas it's only after going through endocytosis, when the pSi particles will release the payload inside the cells, that Pam3CSK4 will bind the TLR 2 that can be found in the endosomes[203], hence the later display of the rhodamine signal.

From the images of Figure 5.17, additionally, the wide presence of the cells started to decrease around six hours. The apoptosys events increase, indeed, is caused by the progression of time and the heating coming from the laser beams that are addressed to the cells and essential for the confocal analysis. In addition, the strong red signal allows to investigate the presence of Pam3CSK4-R inside the cells: the molecule does not enter the nucleus, but it can be found spread into the cytoplasm. In the inset in Figure 5.17 is pictured the magnification of the frame, six hours after the stimulation, to show the distribution of Pam3CSK4-R inside the cells. From the overlap between the BF image and the one obtained by excitation with the laser it is clear that there is an absence of the red signal coming from the nucleus, instead, it is spread all over the cytoplasm and in the dendrites. The floating point with the highest intensity of the rhodamine signal outside the cells corresponds to the loaded pSi microparticles inside the well.

Another proof of the delayed stimulation caused by the loaded molecule compared to the soluble one can be found by observing the morphology of the dendritic cells. As demonstrated by Xing *et al.* and Verdijk *et al.*, the DCs's transition from immature to mature is associated with morphological changes that are essential for the variation of the immunological functions related to the mature state, thus considering the modifications in the morphology as the foundation of their phenotype and function. From their findings, when DCs are in their immature status they show a typical rounded shape with uniformly smooth cell surface. On the contrary, when the mature status is reached, their size become larger, the shape longer and flatter and the surface rougher. Moreover, they display longer protrusions (e.g., pseudopods, podosomes, filopodia, lamellipodia) and ruffles on the cell membrane[173,174].

Concerning the confocal images acquired during our experiments, DCs displayed the morphology characteristic of the mature state with a huge difference in terms of

time in case they were stimulated with soluble Pam3CSK4-R or loaded within the pSi microparticles. In Figure 5.18 are shown the confocal images of the mature DCs, in panel a and b in the first case and in panel c and d in the second one.

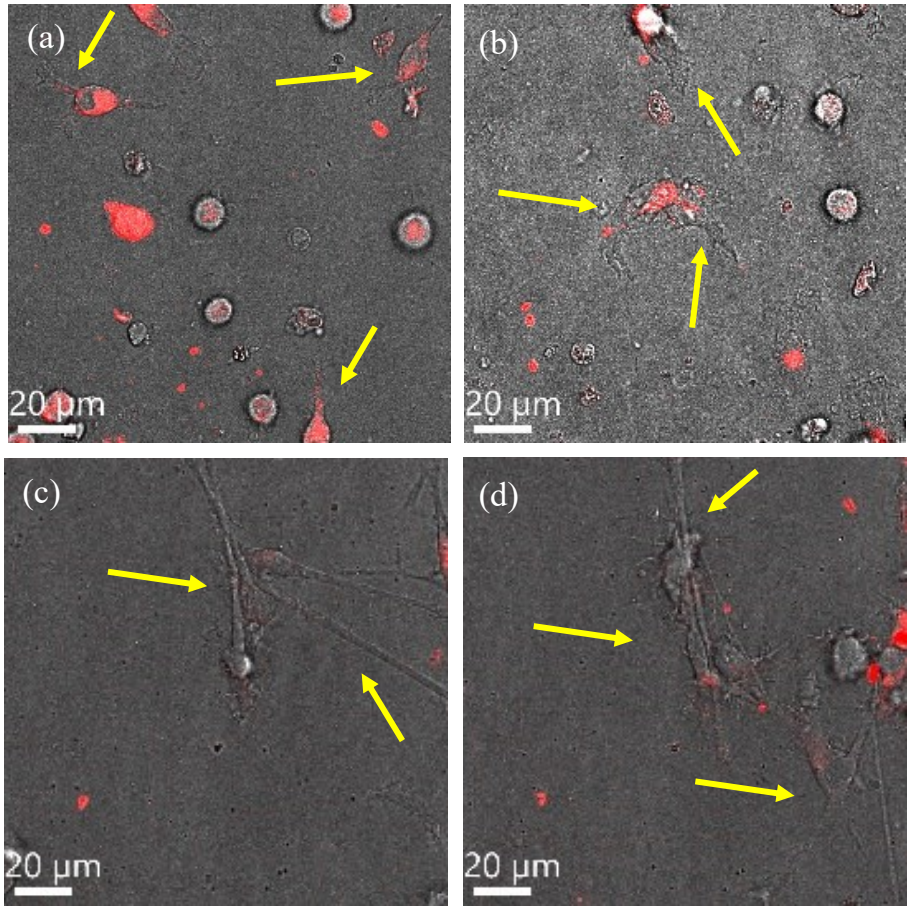

Figure 5.18. Live-cell confocal images (532 nm laser excitation) of DCs treated with soluble Pam3CSK4-R (panel a and b) and with pSi microparticles loaded with Pam3CSK4-R (panel c and d) (20 µm scale).

As displayed in Figure 5.18, in both cases DCs have a longer, larger and flatter form, their shape is irregular and they display protrusions and longer dendrites on their surface (indicated by yellow arrows), as described by Xing *et al.* and Verdijk et al[173,174]. However, the images in panel a and b were acquired at 45 minutes 1 hour, while the ones in panel c and d were acquired after 15 hours from the treatment. The impossibility to find DCs with the morphology typical of the mature status during the first 15 hours after stimulation, can be considered a further proof of the delayed maturation of DCs in response to the treatment with a carrier loaded with the TLR ligand instead of the free ligand.

Evaluation of the immunostimulatory ability

Since the aim of this study is to overcome the obstacles that the administration of the immunologic adjuvant implies (i.e., poor bioavailability and fast degradation), it is fundamental to assess whether Pam3CSK4 loaded within pSi microparticles is able to maintain its function without being degraded and to stimulate human DCs to release more cytokines compared to the soluble one.

To this goal, we first assessed the dose dependent stimulatory effect of the treatment of DCs with loaded pSi microparticles. Therefore, DCs were stimulated for 18 h pSi microparticles loaded with different concentrations of Pam3CSK4 (1 μg/mL, 5 μg/mL and 10 μg/mL). The resulting secretions of cytokines IL-6, IL-12 and TNF-α is reported in Figure 5.19.

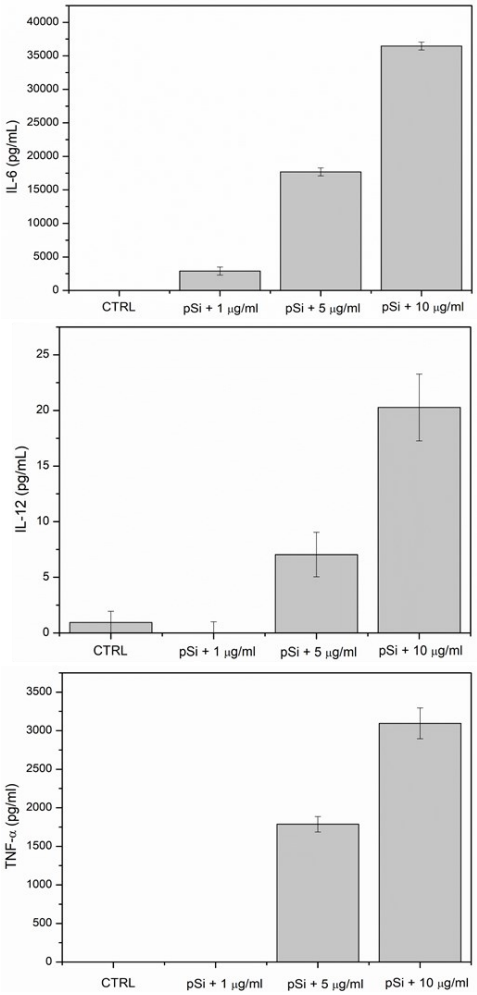

Figure 5.19. Evaluation of IL-6, IL-12 and TNF-α cytokines secretion by DCs, upon 18 h incubation with pSi-COOH microparticles loaded with different concentrations of Pam3CSK4. Ctrl refers to the DCs without stimulation.

By observing the trend of all analysed cytokines, shown in Figure 5.19, the dose-dependency (stimulation increases with the concentration) in the activation of DCs by stimulation with our silicon-derived carrier is confirmed: for example, for IL-6, a factor of about 6 from 1 to 5 μg/mL and then about the double from 5 to 10 μg/mL. Similarly, although not with the same ratio for IL-12 and TNF-α thus demonstrating a clear dependence between the concentration of Pam3CSK4 loaded and the amounts of secreted cytokines. Given that the higher amount of released cytokines was obtained by stimulation with pSi microparticles loaded with 10 μg/mL of Pam3CSK4, we applied this concentration for the following stimulations.

Consequently, human dendritic cells were treated for 18 hours with: bare pSi microparticles, Pam3CSK4 loaded within pSi microparticles and comparable amounts of soluble Pam3CSK4. The stimulatory effect of our delivery system was investigated by assessing the released of the pro-inflammatory cytokines IL-6 and TNF-α present in the supernatant of the treated cells by means of ELISA assay. Before collecting the supernatants, the treated DCs were observed by optical microscopy as reported in Figure 5.20.

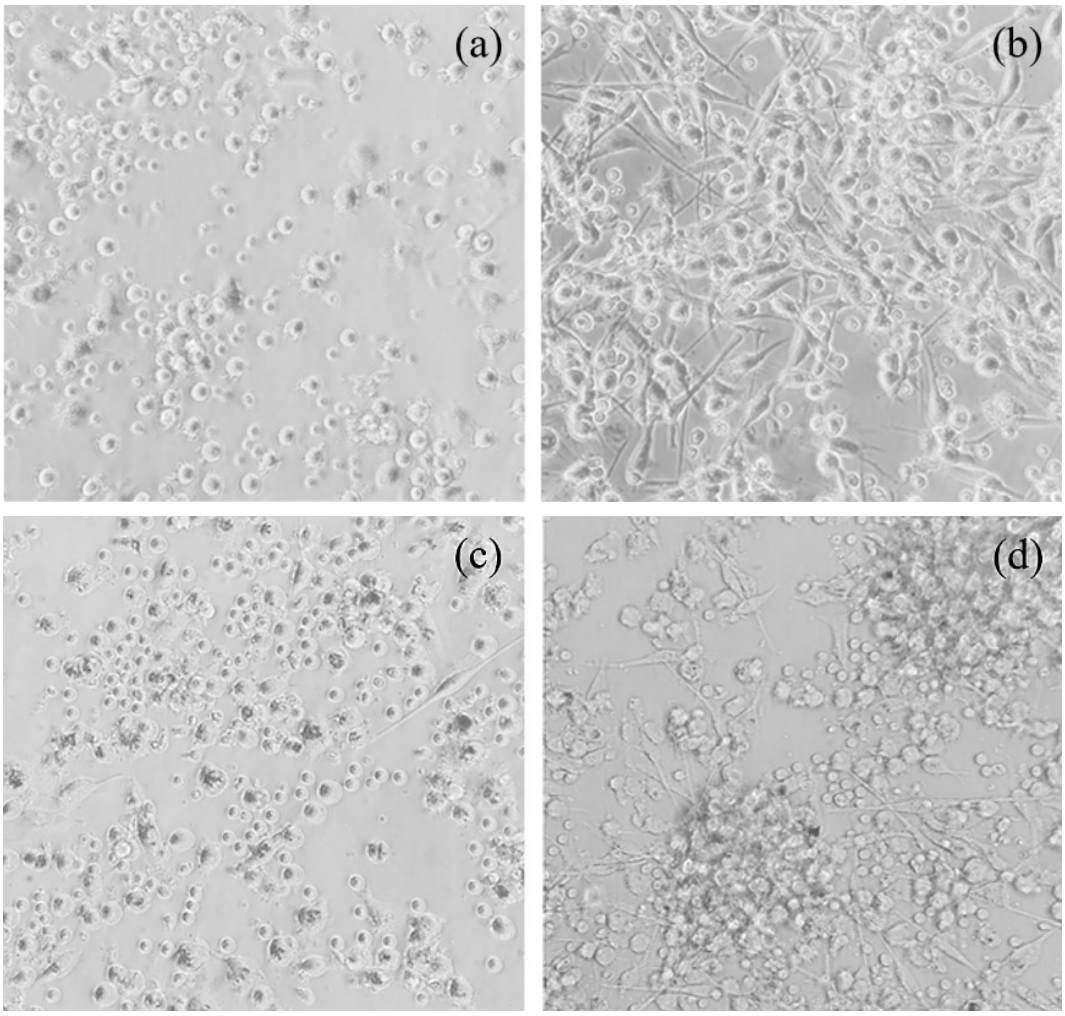

Figure 5.20. Optical microscope images of DCs untreated (panel a), incubated with free Pam3CSK4 (panel b), bare pSi-COOH microparticles, (panel c) and pSi-microparticles combined with comparable amount of Pam3CSK4 (panel d).

Figure 5.20 shows that both untreated DCs (panel a) and DCs incubated with un-loaded pSi-COOH microparticles (panel c) are well distributed and round-shaped, indicating that they have not been stimulated. Differently, cells treated with free Pam3CSK4 (panel b) and loaded within pSi-COOH microparticles (panel d), undergo a typical shape change, i.e., strong elongation of their dendrites, after phagocytosis of the immunologic adjuvant that support the occurrence of the expected activation.

Subsequently, supernatants were collected and analysed by ELISA assay to evaluate DCs stimulation. The resulting secretion of cytokines (IL-6 and TNF-α) is reported in Figure 5.21.

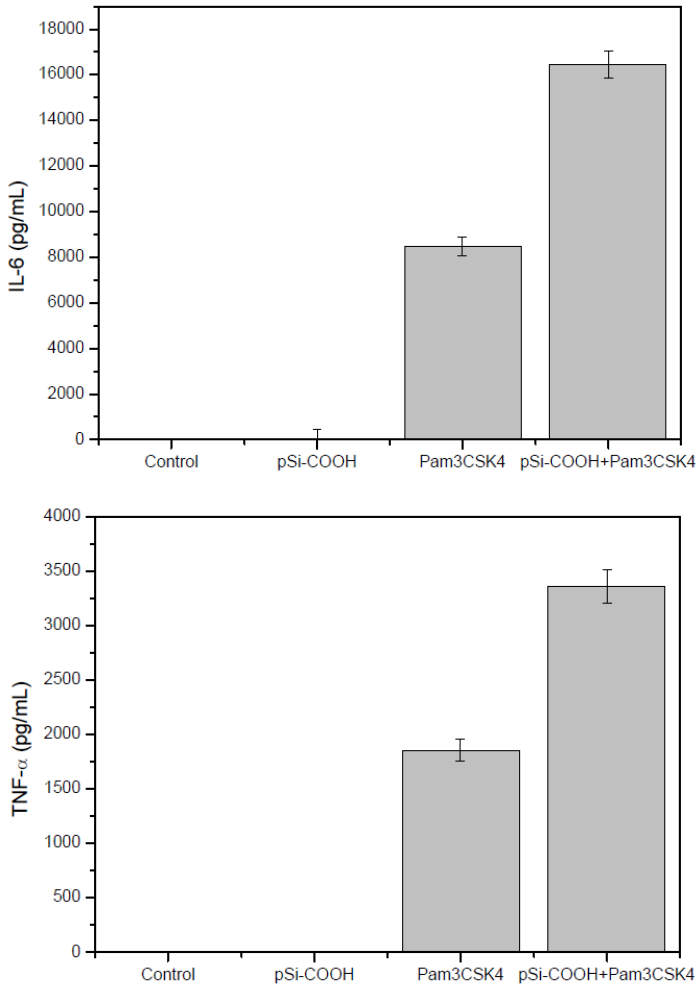

Figure 5.21. Evaluation of IL-6 and TNF-α cytokines secretion by DCs, upon incubation with pSi-COOH microparticles, Pam3CSK4, and pSi-COOH microparticles incubated with comparable amounts of soluble Pam3CSK4. Ctrl refers to the DCs without stimulation.

By quantifying the analysed cytokines, shown in Figure 5.21, it is possible to confirm that unloaded pSi microparticles did not activate the DCs (the cytokines values are comparable to the control, DCs alone), corroborating our previous results[9]. Moreover, comparing the values of Pam3CSK4 alone, and those related to comparable concentration of Pam3CSK4 loaded within our silicon-derived delivery system, it's evident that loaded Pam3CSK4 not only maintains its ability to stimulate human DCs, but the delivery via pSi microparticles resulted in a considerable enhancement of the cytokines secretion.

A suitable explanation of this experimental finding might be that when the DCs are

incubated with free Pam3CSK4 their activation is instantaneous because the molecule is free to immediately bind the TLR 2 that are expressed on the surface of the cells. In that way, the stimulation is exhausted in a short time because the ligand will then go through degradation processes and will not be available for long. On the other hand, when using pSi microparticles as a carrier, the small amount of Pam3CSK4 bonded on their surface will first engage the TLR 2 on the membrane. Then, after internalization, the bigger amount of Pam3CSK4 loaded inside the pores will be continuously released to bind the receptors expressed inside the endosomes. As a result of the release action of the delivery system, stimulation will occur continuously, as hypothesized by the molecular modeling made by Lamrayah *et al.*[190], allowing to achieve a higher cytokines release, on the contrary of the soluble molecule that is consumed right away.

5.C. Conclusions

We reported for the first time the coupling of the immunologic adjuvant Pam3CSK4 with the pSi microparticles and their following stimulation of dendritic cells. The combination of the TLR ligand with our drug delivery system allowed to achieve a prolonged stimulation of the DCs that ultimately resulted in an enhanced release of the cytokines (IL-6 and TNF-α) compared to the soluble version of the ligand. Moreover, the pSi microparticles did not affect human DCs viability, nor induce pro-inflammatory cytokine release by these cells[5,9]. By means of live-cell confocal imaging we were able to follow the kinetic of internalization of the microparticles and the increased presence of the adjuvant inside the cells. Furthermore, the technique allowed us to point out the modification in the morphology of the stimulated DCs.

An enhancement of the cytokines secretion due to the synergic interaction between pSi microparticles and Pam3CSK4 was observed, that might lead to an application in vaccination and cancer immunotherapy. As far as we know, neither reports on the association of Pam3CSK4 with pSi microparticles nor on the effect of Pam3CSK4-loaded pSi microparticles on the activity of human DCs have been provided. Moreover, pSi microparticles have been scantly used for the development of cancer vaccines[204,205]. Therefore, the results reported here provide the first demonstration that pSi microparticles represent a good tool to stimulate human DCs by

transporting an active Pam3CSK4.

CHAPTER 6

GENE THERAPY

6.A. Background and introduction

Gene therapy is a branch of medical treatments that aims at remedying genetic, degenerative and infectious diseases and also cancer, through modifications at genetic level, by transferring genetic material into human cells[206]. The history of gene modifications dates back at the first decades of the XX century but only in 1989 the first clinical protocol for the treatment of patients with cancer with foreign genes was approved by the director of the National Institutes of Health (NIH). Followed by that, the first successful gene therapy clinical trial was started on a four-year-old girl who was born with severe combined immunodeficiency (SCID), by W. French Anderson and colleagues, in 1990[207,208]. When talking about the history of gene therapy, it is fundamental to mention the discovery, during the first decades of 2000, of clustered regularly interspaced short palindromic repeats (CRISPR) and its associated protein (Cas9) that was worth in 2020 a Nobel Prize in Chemistry to E. Charpentier and J. Doudna for their contribute to the development of the CRISPR–Cas9 gene-editing tools. This technology allows to precisely alter the genome by combining the enzyme Cas9 nuclease with single-guide RNA (sgRNA) to recognize and bind precise genetic sequences (related to phages or other invaders) and cut the targeted DNA[209].

Gene therapy is a treatment that from the beginning of the 21st century has gained interest and consideration and the amount of the related products had a huge enhancement over the years. There are currently forty gene therapy products approved (either by FDA, EMA or the Chinese State Food and Drug Administration (SFDA)). Gendicine, was the first one to be approved, in 2003, by SFDA for the treatment of head and neck cancer[210] and only ten years later the number of the clinical trials was already almost doubled. In 2022, three products were approved (i.e., Zynteglo,

Bluebird's Skysona and CSL's Hemgenix)[211] and in 2023 at least five gene therapies including the first one based on a CRISPR technology are expected to be approved. Considering the new genetic tools available (e.g., CRISPR and zinc fingers nucleases), the development of these therapies is expected to increase even faster[212].

Even though gene therapy started as a cure for genetic diseases, the biggest amount of gene therapy clinical trials of the last decade are related to the treatment of cancer[207]. As already mentioned in Chapter 1, the development of cancer is the result of the combination of different factors including genetics. Hence, therapies mediated by gene editing are an emerging alternative for the treatment of cancer and sometimes can be considered a better choice compared to the conventional drug treatments, especially when the manifestation and the progress of cancer is the consequence of gene mutations. The most frequent addressed tumors are blood cancers (i.e., leukemia, myeloma, lymphoma), melanoma, gastrointestinal cancer and nervous system cancer[207].

Gene-based treatments can operate in three ways:

- Gene editing, through specific nucleases (i.e., zinc fingers, CRISPR-Cas, TALENs)
- Gene replacement, direct delivery into the cells through plasmid and viral vectors
- Gene silencing, through small-interfering RNA (siRNA), short hair-pin ribonucleic acid (shRNA) and micro ribonucleic acid (miRNA).

The introduction of genetic material into the cells can be carried out throughout two strategies: ex vivo and in vivo. The first one involves the genetical engineering and transplantation into the patient of gene-manipulated stem cells either autologous or from a healthy donor. The latter requires a vector, that can be classified as viral or non-viral (e.g., lipid nanoparticles or polymers), to deliver the gene drugs to the targeted cells. It necessary to use a delivery system because naked DNA molecules have a large size (owed to the presence of two negatively charged phosphate groups), they are hydrophilic and they can be easily degraded by the enzymes nuclease, therefore it is not easy for them to cross the cells membrane without a carrier[2]. Figure 6.1 shows a schematic representation of the two methods.

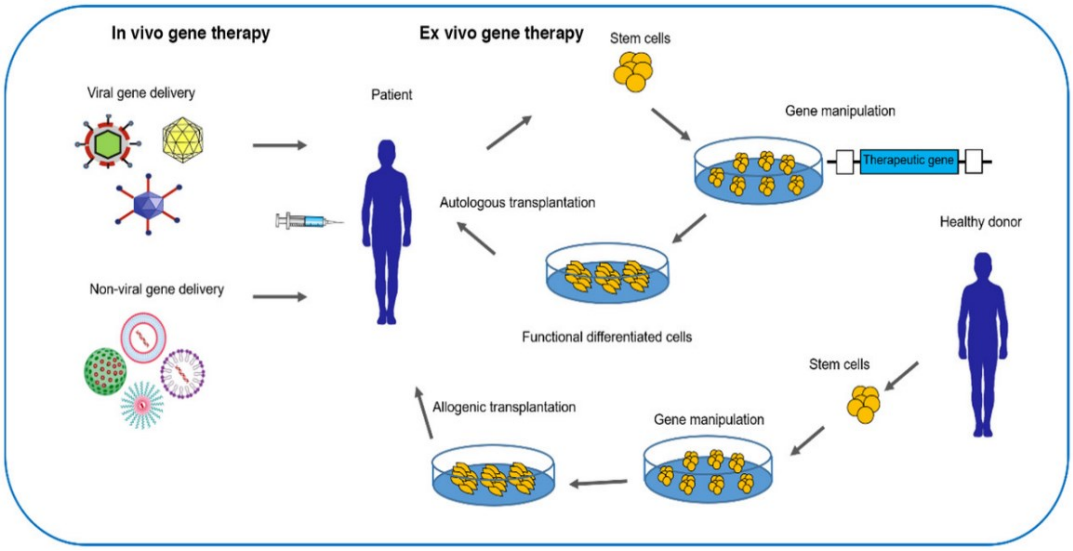

Figure 6.1. Schematic representation of the available methods for the application of gene therapy. (Image from Shahryari et al.[212]*)*

Viral vectors are the most common kind of vectors and they have been extensively used during the past three decades because they are able to infect and transfer their therapeutic genes into the nucleus of the host cell in an efficient way. In order to be safe and not able of replication nor infection, the virus genes are replaced with therapeutic genes. The most commonly used are retrovirus, lentivirus and adeno-associated virus because they allow a transgene expression that lasts for a longer time. Viral vectors found a wider range of applications compared to the non-viral ones because of their highly efficient transfection ability, their extremely specific gene delivery and the possibility to be easily engineered. However, when used to treat solid tumors, being replication-deficient they are not able to infect all the cancer cells thus it is not possible to completely cease the metastasis and the cancer cell growth. On the other side, the use of replicating vectors that enables a continued infection, replication and oncolysis might results in unwanted side effects such as oncogenicity, cytotoxicity and immunogenicity. Therefore, the use of non-viral gene delivery systems is often preferred because they can be modified to target cells or tissues, they do not show immunogenicity, they are safer, easy to be synthetized and more reproducible with a lower cost, even if they are less efficient and with shorter gene expression duration[207,212]. Most non-viral vectors are indeed biocompatible materials such as liposomes, plasmid, chromosomes, biopolymers and nanoparticles and they usually transport RNAs (e.g.,

siRNA, shRNA, miRNA), DNAs (e.g., plasmid DNA, DNA interference), antisense oligonucleotides (ASOs), CpG oligodeoxynucleotides (CpG-ODNs). In order to be successful, a gene therapy delivery system needs to have suitable properties such as large pore size to allocate the payload, non-immunogenic, biocompatible, high cell specificity, good encapsulation efficiency[213].

6.A.1 Gene silencing - Porous silicon for siRNA delivery

It should be noted that the gene silencing technique differs from the gene therapy in a narrow sense. The target of the first one is in the cytoplasm and its effects are reversible, controllable and highly specific while the second one's target is the nucleus and its action is permanent[214,215].

The mechanism of action that siRNA uses to silence the delivery of specific gene's messages starts with the direct sequence-specific cleavage: endogenous double-stranded RNA is identified and cleaved by Dicer (a ribonuclease protein) into the siRNA duplex, a double stranded molecule 21 to 23 nucleotide long, comprised of a passenger and a guide strand. After siRNA binding and subsequent activation with the multiprotein component complex RNA-Induced Silencing Complex (RISC), the endonuclease Argonaute 2 (AGO2) (part of the RISC) unwind the duplex. Consequently, while the passenger strand is being degraded, the RISC-bound guide strand directs the activated complex to the target mRNA, which is then cleaved by the enzyme AGO2 resulting in the interruption of mRNA translation. The high selectivity of siRNA resides in the guide strands which only binds fully complementary mRNA causing the silencing of specific genes[216–218]. The stages that compose the silencing action of siRNA are schematically represented in Figure 6.2.

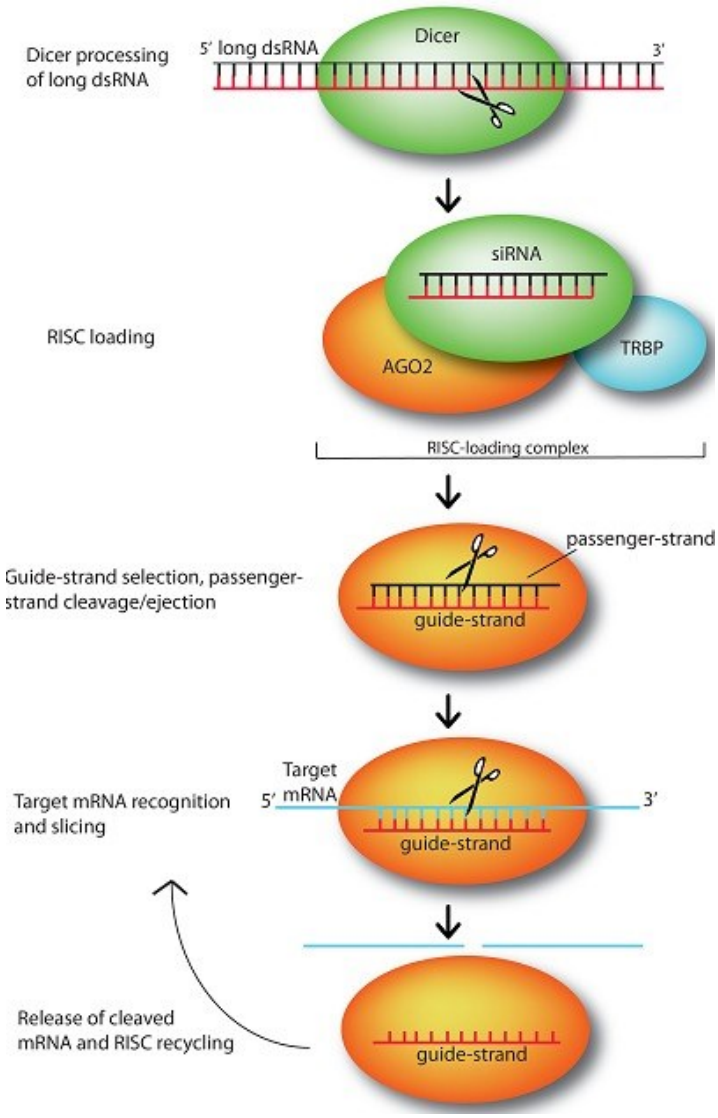

Figure 6.2. Summary of the stages that compose the gene silencing mechanism operated by siRNA. (Image from Dana et al.[218]*)*

After its discovery in 1999, the scientific interest regarding siRNA grew over the years and with that also the number of clinical trials involving it. siRNA started as a therapeutic for the treatment of genetic diseases, but it progressively found application in cancer therapy. The success of this oligonucleotide in cancer treatment resides in its ability to silence gene expression, that leads to the inhibition of the cancer cells growth. However, due low stability in physiological conditions, its systemic administration in the soluble form would result in rapid degradation by nucleases and renal clearance. Furthermore, it is hardly capable to reach the cytoplasm of the selected cells and exerts immunogenic effects, therefore, it needs a carrier to be shielded by and to facilitate its delivery to the targeted cells[219,220].

In this context, porous silicon with its features, extensively described in Chapter 2, stands as a good candidate for the delivery of gene therapeutics. In fact, several successful studies (mostly involving siRNA) have been published during the last few years. For example, Tanaka *et al.* were able to obtain a prolonged gene silencing for three weeks in an ovarian cancer mouse model by loading nanoliposomes containing siRNA into mesoporous silicon particles[221], while Tieu *et al.* demonstrated that by adding salt or urea to the siRNA solution it was possible to obtain a higher loading into amine-modified porous silicon nanoparticles[222]. A system composed of cationic amino acid-functionalized porous silicon nanoparticles loaded with pDNA was developed by Chaix *et al.* acting on HEK293 cells with an efficiency 300 times superior to the bare nanoparticles[223], and a self-sealing porous silicon-calcium silicate core-shell method was used by Kang *et al.* to deliver siRNA to injured brain through cell targeting and cell-penetrating peptides with an improved delivery in vivo compared to non-targeted nanoparticles[224].

6.B. Results and discussion

6.B.1 siRNA loading

In collaboration with Professor M. J. Sailor at the University of California San Diego, we did some preliminary investigations with the aim of combining within porous silicon nanoparticles the transport of siRNA and the targeting ability of hyaluronic acid. As previously said, siRNA is a nucleic acid with high instability and low efficiency to cross cell membranes[219], consequently, the loading within the pores of pSi that have the proper size to accommodate the molecule (siRNA is approximately 7.5 nm long and 2 nm large [225]) will result in its protection from degradation. Lastly, the coating with hyaluronic acid completes the gene delivery system by enabling a localized delivery to the targeted cancer cells (i.e., prostate, breast, pancreatic, lung) overexpressing the CD44 (as discussed in detail in Chapter 2).

To load siRNA into porous silicon, we followed a procedure (schematized in Figure 6.) that was optimized by Sailor's group for calcium silicate core-shell[224].

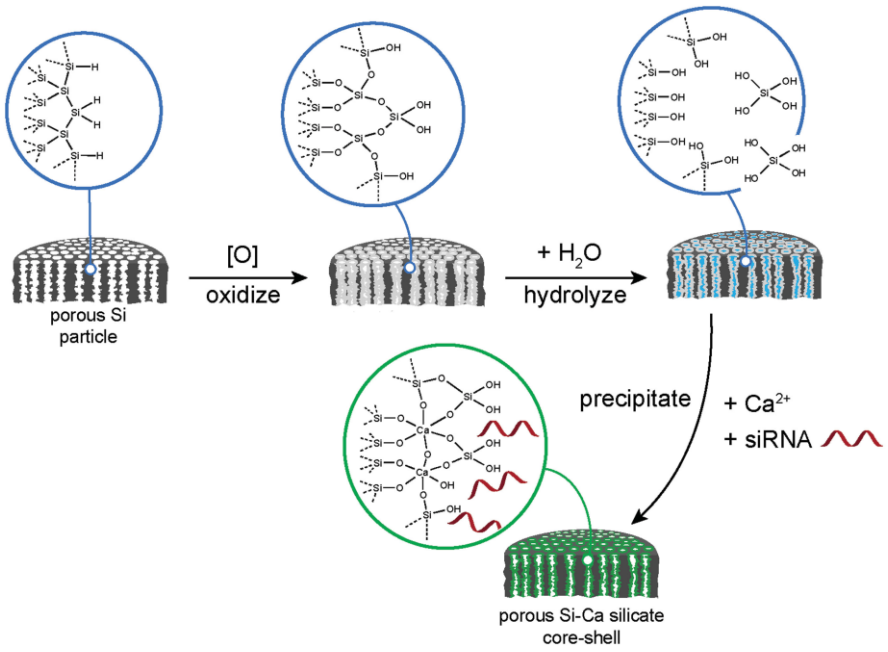

Figure 6.3. Representation of the calcium silicate core-shell method applied for the loading of ICG and siRNA (Image from Kang et al.[224])

This one-step process, through the precipitation of an insoluble shell of calcium silicate, allows to load and protect at the same time high concentrations of the payload. To do that, it is necessary to have high concentration of calcium(II) ion (e.g., from $CaCl_2$ or $MgCl_2$) and silicate that derives from the dissolution of the silicon oxides present on the surface of the pSi particles. More in detail, pSi particles were first stirred in an aqueous solution of siRNA for a few minutes to allow, through partial hydrolyzation of the oxide layer, the release of orthosilicic acid $Si(OH)_4$ in the surroundings of the pSi. Then, the addition of a highly concentrated solution of $CaCl_2$ (as a source of Ca^{2+} ions) immediately starts the precipitation process of the calcium silicate layer that simultaneously seals the pores and traps the drug inside them. The loading of the drug through this method enables at the same time a slower release of the payload (~5 times slower than by electrostatic interaction) and of the degradation of the pSi particles from hydrolysis and oxidation in aqueous media (~30% less degraded compared to bare pSi), but also to achieve the encapsulation of a higher amount of drug compared to the electrostatic interaction, i.e., 20–25% for the first versus 5–8% for the latter[224].

Considered the high cost of siRNA, a preliminary study to set up the same protocol was conducted with dye indocyanine green (ICG) as a model drug. In Figure 6.4 are summarized all the steps needed for the creation of the complete targeting gene delivery system.

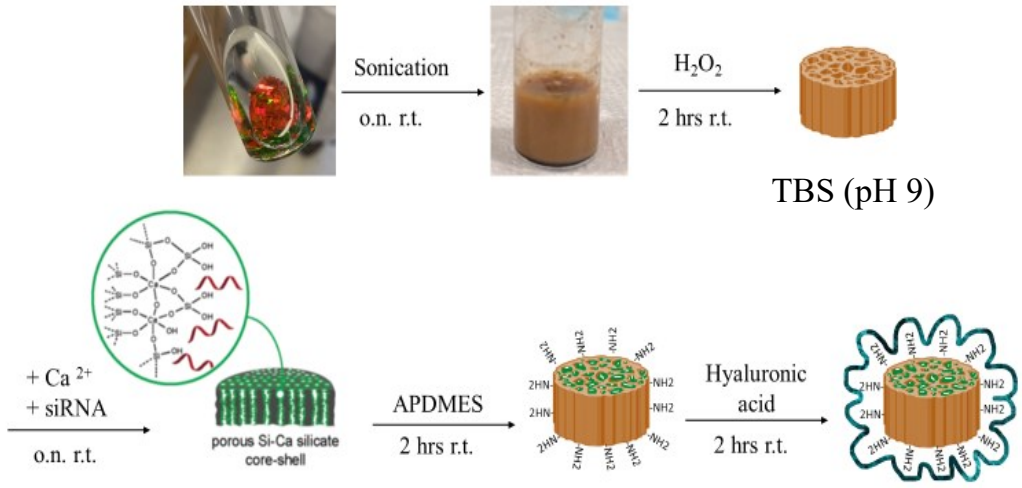

Figure 6.4. Schematical representation of the steps needed to obtain the gene delivery system.

The pSi particles were obtained by overnight sonication of silicon flakes in ethanol followed by three washings. They were then oxidized by hydrogen peroxide (H_2O_2) and, after the washings, they were resuspended in tris buffer saline (TBS) (pH 9). These two steps are fundamental for the success of the encapsulation of the drug, indeed, when the pSi particles are in a water solution at mildly alkaline pH, the oxide layer on their surface will start to hydrolyze and solubilize, freeing ortho-silicic acid $Si(OH)_4$. After a few minutes, a solution of the drug and a highly concentrated solution of $CaCl_2$ were added to the particles buffer suspension. While the drug and the Ca^{2+} ions were diffusing inside the pores of the carrier, the Ca^{2+} present in the solution reacted with the $Si(OH)_4$ already released to generate a calcium silicate precipitate that confined the payload inside the structure of the porous carrier. After an overnight loading, the particles were washed for three times with ultrapure water to remove the non-encapsulated drug. Figure 6.5 shows a picture of the ICG

loaded-pSi particles suspension before and after the loading, the green color comes from ICG.

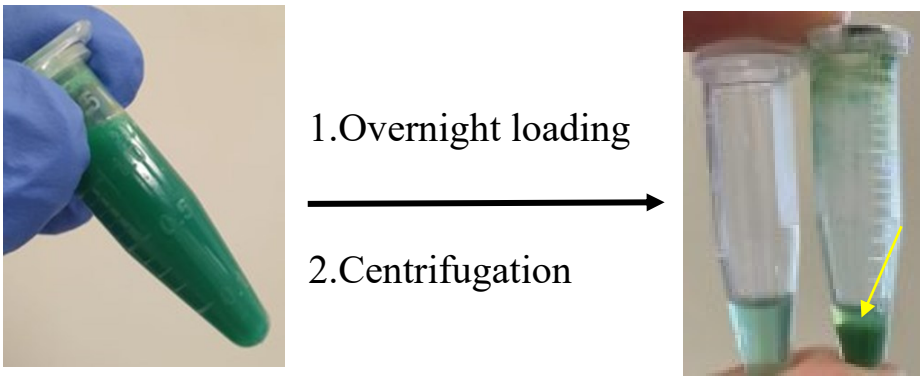

Figure 6.5. Loading of ICG within pSi particles.

The light green color of the supernatant compared to the clearly green pellet (indicated by the yellow arrow) after the loading and separation through centrifugation suggested that most of the ICG was effectively loaded inside the pores of pSi particles.

To determine the mass loading and the encapsulation efficiency, the particles were dissolved with KOH and the payload quantified by UV-VIS spectrophotometry, as already explained in Chapter 2. They were 42% and 37% respectively. This can be considered a quite good result. Indeed, in a previous work the encapsulation of ICG by using the same calcium-silicate method was compared between pSi and microporous silica nanoparticles resulting in 11% and 2.6% of mass loading, respectively. Moreover, they evaluated the mass loading of ICG also for liposomal nanoparticles and porous calcium silicate nanoparticles (obtained by mixing ICG, $CaCl_2$ and silicic acid) obtaining values of 16.5% and 57.7%, respectively[226]. Therefore, we were able to obtain a three times higher amount of loaded model drug.

6.B.2 Coating with HA and release study with a model drug

Before coating the loaded particles with hyaluronic acid, it was necessary to aminate them, by reaction with APDMES, to obtain a positive surface charge that enabled the electrostatic interaction between the particles and the negatively charged polymer, as represented in Figure 6.6.

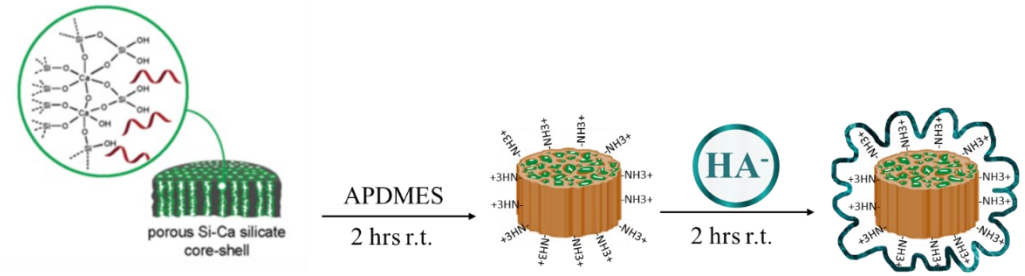

Figure 6.6. Simplified representation of the hyaluronic acid (HA) coating through electrostatic interaction with aminated-pSi particles.

After the confirmation of the success of the amination by means of DLS (Z-potential: +15 mV ± 5), the loaded particles were coated with HA (with a method that was already optimized and discussed in Chapter 2) and confirmed by the Z-potential measurement, obtaining a surface charge of -14 ± 5 mV.

The release study of the so-combined system was performed by stirring the IGC-loaded and HA-coated pSi particles in PBS buffer at 37°C in presence of hyaluronidase (HAase, 800 U/ml). This human enzyme is present in a large amount in cancers such as prostate, breast, colon and bladder ones, and it is known to break the hyaluronic acid by cutting the glycosidic acid bond[227] (Figure 6.7).

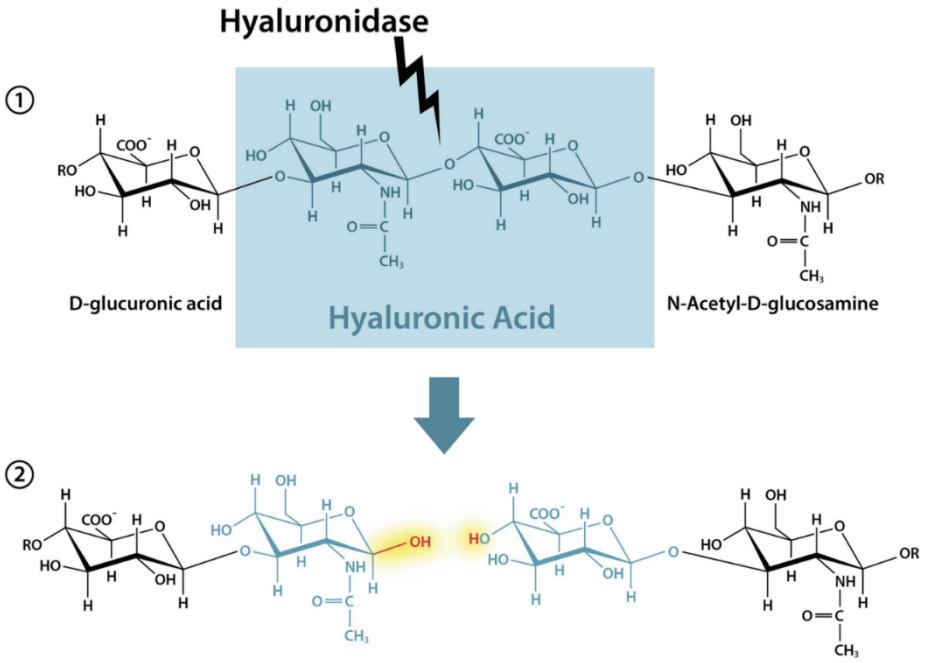

Figure 6.7. Mechanism of the hyaluronidase enzyme action on hyaluronic acid [228].

Therefore, it helped the release of the ICG drug and mimed what would occur if the system would reach the targeted tumor cells. The release curve and the calibration curve used to convert the absorbance intensity to the concentration of ICG are reported in Figure 6.8.

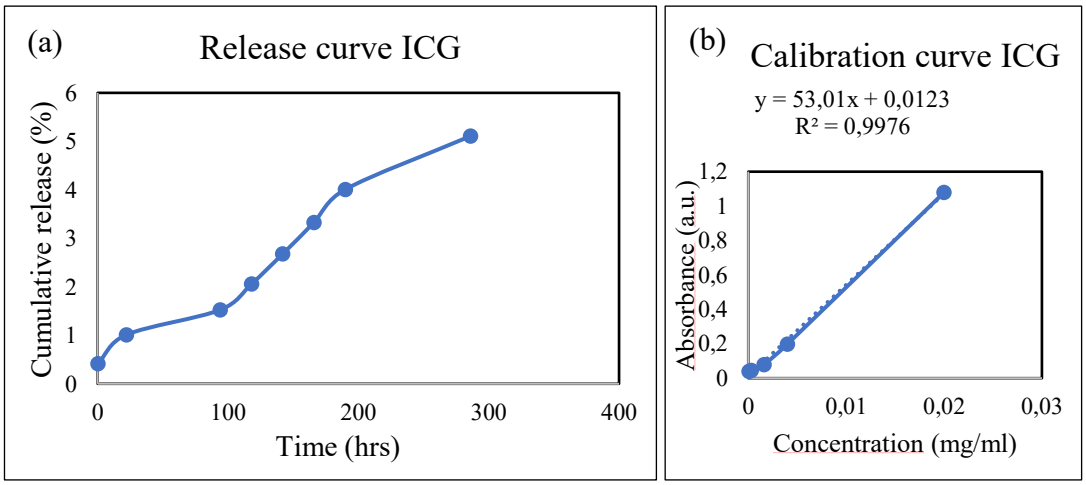

Figure 6.8. Release study of ICG in PBS (panel a) and calibration curve (panel b)

The slow release of ICG can be ascribed to the presence of the calcium-silicate shell that, if on one side allowed the loading of a higher amount of drug, on the other the shell was dissolving slowly therefore the release resulted prolonged in time.

The good results obtained with the loading of the model drug led us to eventually repeat the experiment with siRNA (5'- rCrArA rCrArC rGrCrC rUrGrA rUrUrC rUrCrU and 5'- rArHrA rHrUrA rGrArG rArArU rCrArG rGrCrG, MW 14.634,9). For the encapsulation of the oligonucleotide we applied the same aforementioned protocol but working with RNAase-free solvents and in a bio-safe environment to avoid contamination. Briefly, pSi particles were oxidized and resuspended in RNAase-free TBS (pH 9), after a few minutes a solution of the drug and a highly concentrated solution of $CaCl_2$ were added to the particles buffer suspension and mixed overnight at room temperature. After the washings with RNAase-free water to remove the non-encapsulated RNA, the mass loading was calculated with the method previously described resulted in 5.2%. Considering the previous results obtained by Sailor and co-workers with this method (20-25% mass loading[224]) we expected a higher value, probably there mistakes were made during the encapsulation process or there was a contamination. However, the average mass loading through electrostatic interaction is usually between 5 and 8%, therefore the obtained result can be considered a good starting point to further investigations.

6.B.3 Co-delivery of doxorubicin and siRNA

After the successful loading of siRNA and doxorubicin within our pSi carrier (see Chapter 4) and the optimized coating with hyaluronic acid (HA) (Chapter 2), we combined the co-delivery of siRNA and doxorubicin in a targeted mode, i.e., by using the HA coating.

Combination therapy is considered a possible solution to efficiently overcome anticancer drug resistance. The co-delivery of anticancer molecules usually leads to improved cytotoxicity against cancer cells because of a synergetic effect of the drugs. This, often, allows to administer a lower amount of drug thus reducing side effects and risk of developing resistance[133]. There are several studies concerning the application of combination therapy for cancer. Hereafter some representative examples of siRNA coupled with doxorubicin are briefly reviewed.

- Tieu *et al.* developed a system composed of doxorubicin and siRNA loaded pSi particles with incorporated nanobodies via PEG to target prostate cancer cells. Their system on one hand successfully inhibited the expression of MRP1 (multidrug resistance-related proteins) by about 74% and on the

other was able to increase the cytotoxicity compared to free DOX(14% and 32% of cell viability after 72 hours treatment, respectively)[229].

- Wu *et al.* designed discoidal pSi microparticles loaded with siRNA and DOX and tested them on two mouse models of triple negative breast cancer resulting in enhanced efficacy of the cytotoxic effect of DOX and efficient suppression of the cancer cells proliferation and metastasis[230].
- Meng *et al.* co-delivered siRNA targeting P-glycoprotein drug exporter and DOX by mesoporous silica particles functionalized with PEI-PEG and tested them on the resistant breast cancer cell line MCF-7/MDR. They obtained an 8% increased retention effect and permeability at the tumor site and a synergetic inhibition of cancer growth in the in vivo model[231].
- Ding *et al.* combined the delivery of DOX and siRNA by multi-layering rattle mesoporous silica particles. The first layer was made with the polymer PEI to allow the electrostatic interaction with siRNA followed by the loading of DOX inside the pores. The last layer was a hyaluronic acid coating embedded with cell penetrating peptide to prevent the leakage of the drugs and achieve the targeting of breast cancer in vivo. They obtained an improved anticancer effectiveness compared with the chemotherapy alone[232].

Having cleared the above cited literature and aiming at assessing an easy and efficient procedure for the co-loading of pSi particles we applied a layer-by-layer method, as shown in Figure 6.9.

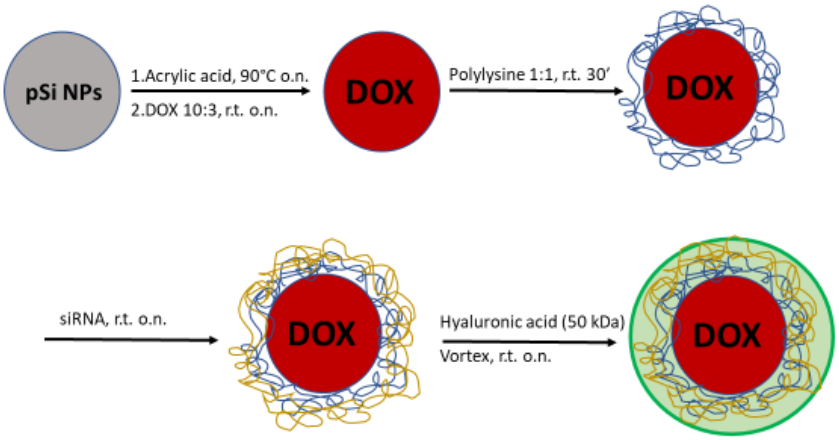

Figure 6.9. Representation of the layer-by-layer procedure applied to create the codelivery system.

The nanoparticles were functionalized with carboxylic groups by a hydrosilylation reaction, as described in Chapter 2, and doxorubicin was loaded by an immersion method, as discussed in Chapter 4. After that, to allow the electrostatic interaction between the carrier and siRNA, we did a coating with poly-L-lysine by stirring the particles with a poly-lysine solution in a weight ratio 1:1 at pH 5, to obtain a layer of positive surface charge. The polymer and particles were powerfully stirred for thirty minutes at room temperature and then washed twice with RNAase-free water. The particles were then added to the siRNA solution and mixed overnight at room temperature. after the washings with RNAase-free water the mass loading was calculated obtaining a value of 2%. The low mass loading could be due to multiple factors, the pores of the carrier are less accessible because of the poly-lysine layer therefore there is less surface to allow the binding, moreover, the oligonucleotide was loaded through electrostatic interactions and not by using the previously discussed calcium-silicate method. Therefore, further investigations are needed to improve the amount of loaded oligonucleotide and optimize the loading method. Lastly, a layer of HA was obtained by using the method reported in Chapter 2 to avoid the leaking of the loaded siRNA and as a targeting functionality.

To follow all the different phases of the procedure, we performed DLS measurements, looking at the surface potential and at the size of the “built-up” system. Figure 6.10 reports the size and Z-potential distributions (panel a and b, respectively), after each step.

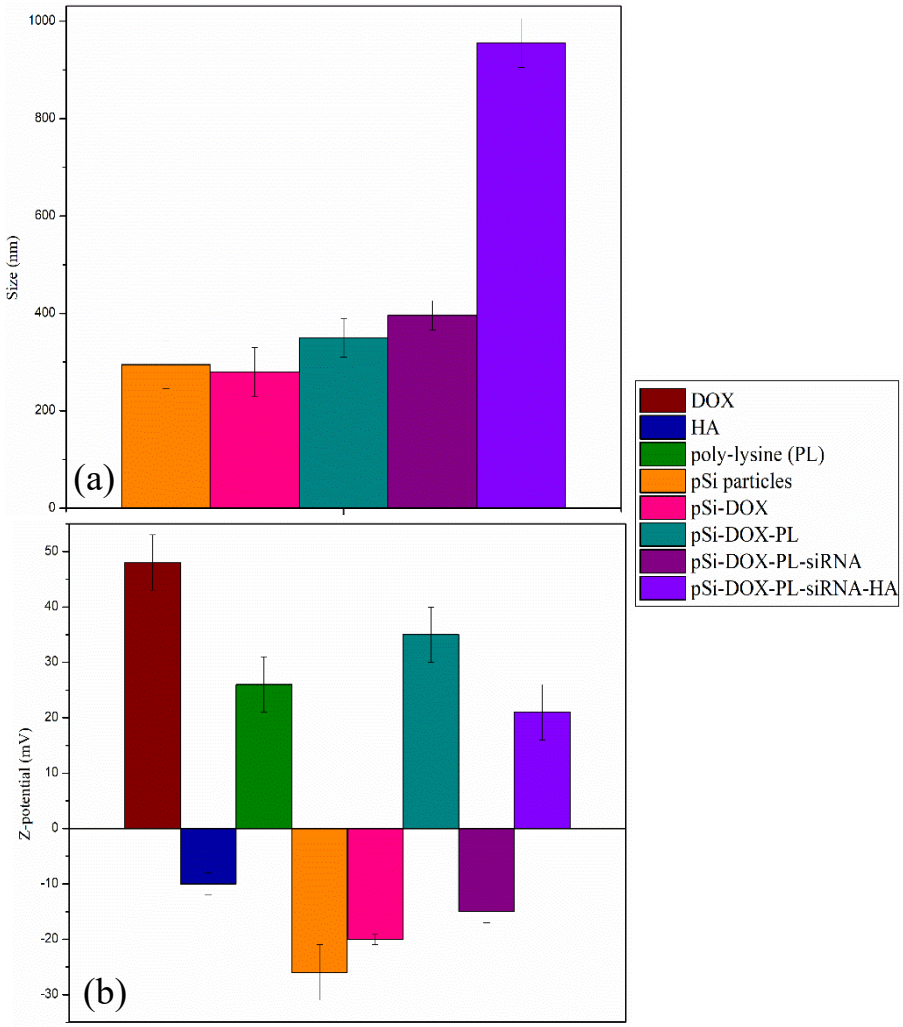

Figure 6.10. Size (panel a) and Z-potential (panel b) distributions measured after every modification of the carrier.

Step 1 (pSi-DOX): as expected, after the loading of DOX neither the size nor the surface charge changed because the drug is well infiltrated inside the pores, therefore it does not influence these parameters.

Step 2 (pSi-DOX-PL): the coating layer of poly-lysine gives a slight increase to the average size and a positive surface charge of about +35 mV thus enabling the electrostatic interaction first with siRNA and then with HA.

Step 3 (pSi-DOX-PL-siRNA): The siRNA binding is confirmed by the change of surface charge, on the other hand, resulted in a modest expansion of the mean diameter of the particles, probably owed to the small amount of bonded oligonucleotide, as expected by the 2% of mass loading.

Step 4 (pSi-DOX-PL-siRNA-HA): after the final layer with hyaluronic acid the particles became almost double their size. However, being HA negative, we did not expect a positive surface charge in the end. This might be due to different factors: either the amount of reacted polymer was not high thus the coverage of the particles was not homogenous, or there was an agglomeration of the particles, supported by the huge mean diameter.

6.C. Conclusions

From these preliminary investigations we were able to obtain some positive results:

- Efficient loading of siRNA within the pSi pores with a calcium-silicate shell precipitation method
- Successful loading of doxorubicin and siRNA within the same carrier by means of a poly-lysine layer
- Effective coating with hyaluronic acid of both pSi particles loaded with siRNA alone and in combination with doxorubicin through a layer-by-layer method.

The investigations will continue on one hand, to study the release, optimize the loading of the drugs and the coating with hyaluronic acid, on the other, in vitro test on cancer cell lines will be performed to examine the antiproliferative effect and the drug resistance in the direction of finding a future application for pSi particles in the field of gene therapy delivery.

CONCLUSIONS

In this PhD Thesis work, porous silicon microparticles were deeply studied to assess their use as a drug delivery system in anticancer therapy. The project aim was to study and optimize the ability of pSi particles, by means of functionalization and surface modifications, to efficiently transport and deliver clinically-established anticancer agents. The final goal was the enhancement of the cytotoxic and immunogenic effects through the synergistic interaction between the payload and the pSi particles.

In the first part of this Thesis the main experimental results are about the preparation of the studied inorganic system. Specific surface modification/functionalization and different coatings were studied and realized. In the last chapters, the application of pSi particles as drug carriers were demonstrated for cancer, immuno and gene therapy.

The main results achieved are summarized hereinafter chapter by chapter.

In Chapter 2 we realized a **surface charge modification** (from negative to positive) by means of the cationic surfactant CTAB and of the positively-charged synthetic aminoacidic chain poly-lysine. By either creating micelles, in the first case, or a coating, in the latter, the presence of a positive layer enables the electrostatic binding with negatively charged (macro)molecules. We hence investigated the coating with the negatively-charged polymer hyaluronic acid (HA) by electrostatic interactions, and with the biopolymer acetal-modified dextran by nanoprecipitation. The presence of these two polymers not only helps **avoiding** unwanted **leakage** of the payload, leading to a higher **stability** for the pSi particles, but also adds two new important functionalities to our platform:

(i) Acetalated dextran → **ability to respond to pH variations**

(ii) Hyaluronic acid → **ability to target specific tumor cells** (prostate, lung, triple-negative breast and pancreatic cancer)

Moreover, the ability to modify the surface charge enabled the possibility of loading anticancer agents as shown in the chapters 4 and 6.

In Chapter 3 we succeeded in adding **magnetic properties** to the functionalized pSi microparticles by using a previously optimized protocol for the infiltration of commercial magnetic nanoparticles. We used **iron oxide nanoparticles** fabricated with a new method. The magnetic nanoparticles were fabricated by a pulsed laser ablation in water and, being positively-charged, were able to interact with the negative carboxylic groups present on the pSi surface. We demonstrated the success of the infiltration by attraction to a magnet and by means of DLS and TEM analysis.

Chapter 4 was focused on the application of pSi particles as a carrier for the chemotherapeutic drugs **doxorubicin** and **docetaxel**. After efficiently loading the anticancer molecules, we tested the cytotoxic activity in vitro against two human cancer cell lines (PC3 and A549). We obtained some promising results:

(i) Doxorubicin-loaded pSi particles on PC3 → 33-67% reduced cell viability compared to the control free drug (depending on the concentration);
(ii) Doxorubicin-loaded pSi particles on A549 → 53-56% reduced viability compared to the control free drug (depending on the concentration);
(iii) Docetaxel-loaded pSi particles on PC3 → cytotoxic effect comparable to the control free drug;
(iv) Docetaxel-loaded pSi particles on A549 → 13-32 % reduced cell viability compared to the control free drug (depending on the concentration).

Another interesting achievement was to the covering of the doxorubicin-loaded pSi particles by hyaluronic acid; this adds an active cancer targeting functionality to the system that will be tested at the biological level in the near future.
Overall, the results point out a deal of potential in oncology for the here studied inorganic platform. In fact, the synergic interaction between pSi and the clinically-established drugs resulted in a generally **higher cytotoxic** effect on the tested cell lines **compared to the free drug**, thus paving the way to their potential use in chemotherapy.

In Chapter 5, the potential of pSi as a vehicle for the delivery of the **immunologic adjuvant** Pam3CSK4 (ligand of the toll-like receptors of dendritic cells) was clarified. We previously demonstrated the absence of immunogenicity and toxicity of

the carboxyl-functionalized pSi particles on human immune cells. On the one hand, we investigated the kinetic internalization of the payload and the morphological changes that are associated to the maturation of the human dendritic cells that occur during the immune response by means of confocal imaging. On the other hand, we quantified the release of cytokines correlated to the human dendritic cells maturation that is related to the stimulation with Pam3CSK4-loaded pSi particles. We collected the following results:

(i) Dendritic cells maturation followed by stimulation with the immunologic adjuvant is delayed when using the carrier;
(ii) When the uptake of Pam3CSK4 is mediated by the presence of pSi, the continuous release of the payload enables a **prolonged stimulation** of the dendritic cells;
(iii) The **release** of the **cytokines** IL-6 and TNF-α, followed by the stimulation with the immunologic adjuvant, is **higher** when using pSi to deliver it to the dendritic cells.

To the best of our knowledge, neither the association of Pam3CSK4 with pSi microparticles nor the effect of Pam3CSK4-loaded pSi microparticles on human dendritic cells have been reported yet. Therefore, these results provide the first demonstration that pSi microparticles represent a good tool to stimulate human dendritic cells by transporting an active Pam3CSK4 that might lead to an application in the immunotherapy practice.

Chapter 6 regarded a preliminary investigation of pSi particles coated with hyaluronic acid for the targeted delivery of a gene silencing molecule – a small-interfering RNA (**siRNA**) – and the co-delivery with doxorubicin.

(i) Efficient loading of siRNA within the pSi pores with a calcium-silicate shell precipitation method;
(ii) Successful loading of doxorubicin and siRNA within the same carrier by means of a poly-lysine layer;
(iii) Effective coating with hyaluronic acid of both pSi particles loaded with siRNA alone and in combination with doxorubicin through a layer-by-layer method.

With this preliminary study we looked into the ability of pSi to be a carrier not only for the delivery of siRNA but also for the co-delivery of siRNA and doxorubicin. The coating with hyaluronic acid completes the system, adding a targeting functionality and keeping the particles well-dispersed. These first promising steps are in the direction of finding a future application for pSi particles in the field of gene therapy delivery.

In conclusion, among the several nanomaterials studied for anticancer therapy, pSi microparticles stand out, particularly, for the absence of toxicity and for their intrinsic diagnostic and therapeutic assets. The findings discussed in this Thesis are a fundamental step towards the exploitability of this material as a carrier of anticancer agents in different branches of the medical treatments against cancer (i.e., chemotherapy, immunotherapy and gene therapy) which may be traced by optical and/or magnetic resonance imaging.

FUTURE PERSPECTIVES

During this PhD work we were able to improve the pre-existent performances of pSi as a multifunctional platform by means of different surface modifications that lead to novel abilities including pH-responsiveness, magnetic properties and cancer cell targeting.

The versatile pSi-based formulations optimized and biologically investigated in vitro during this project point out a great promise for dendritic cells activation, drug delivery, active tumor targeting, diagnostics and gene silencing. However, the possibility to exploit the loaded pSi particles as effective tools for anticancer therapy is challenging. The applied in-vitro models own some limitations and do not have the complexity of real tumor tissues, including the presence of biological barriers and the key role of the immune system. Therefore, more comprehensive investigations in-vitro and evaluations in in-vivo models are required to fully clarify the potential of this platform.

From the diagnostics point of view:

- the magnetic ability of the iron oxide decorated-pSi particles has to be tested to evaluate their potential as contrast agents;

-The encapsulation with acetalated dextran must be optimized and the pH responsiveness has to be examined.

From a targeting point of view:

- The targeting ability of hyaluronic acid coated pSi-based drug delivery systems needs to be assessed for example by working with specific CD44-overexpressing human cancer cell lines.

- The immunologic adjuvant delivery could be improved by adding a dendritic cell targeting ability.

The siRNA delivery investigations are only at the beginning and require further investigations in vitro such as improvement of the loading capacity, release studies and in-vitro testing on cancer cell lines.

Regarding future developments, we already started to investigate the possibility to couple pSi with other molecules, in particular with metal-based compounds characterized by anticancer and anti-inflammatory abilities.

Acknowledgements and collaborations

The **fabrication and functionalization of the pSi particles** used for the investigations of Chapter 1 -5 of this thesis were done in collaboration with Prof. Marina Scarpa at the Nanoscience Laboratory, Physics Department of the University of Trento (Italy).

The **synthesis of iron oxide nanoparticles** by pulsed laser ablation was done in collaboration with Prof. Tommaso Del Rosso at NanoLaserLab, Physics Department of the Pontifícia Universidade Católica do Rio de Janeiro (Brazil).

The investigation of the interaction of pSi particles with **human dendritic cells** was done in collaboration with Doc. Marta Donini and Prof. Stefano Dusi at the Department of Medicine, Division of General Pathology of the University of Verona (Italy).

The **surface modifications**, loading and delivery test with **anticancer drugs** and the **in vitro test on cancer cell lines** were done in strict collaboration with Prof. Chiara Nardon at the Biomedical Chemistry Laboratory, Biotechnology Department of the University of Verona (Italy).

All the experiment reported in Chapter 6 including the **fabrication** of the pSi particles, the **loading of siRNA** and the **optimization of hyaluronic acid coating** were done in collaboration with Prof. Michael J. Sailor in Sailor's Lab, Department of Chemistry and Biochemistry of the University of California San Diego (UCSD) (USA). The research done at (UCSD) was primarily supported by NSF through the UC San Diego Materials Research Science and Engineering Center (UCSD MRSEC) DMR-2011924. The authors acknowledge the use of facilities and instrumentation supported by NSF through the UC San Diego Materials Research Science and Engineering Center (UCSD MRSEC) DMR-2011924.

Most of the measurements performed at the University of Verona were done with access and support at the instrumentations by **CPT** (Centro Piattaforme Tecnologiche).

REFERENCES

1. Sung, H. *et al.* Global Cancer Statistics 2020: GLOBOCAN Estimates of Incidence and Mortality Worldwide for 36 Cancers in 185 Countries. *CA: A Cancer Journal for Clinicians* **71**, 209–249 (2021).
2. Mali, S. Delivery systems for gene therapy. *Indian J Hum Genet* **19**, 3–8 (2013).
3. Weiden, J., Tel, J. & Figdor, C. G. Synthetic immune niches for cancer immunotherapy. *Nat Rev Immunol* **18**, 212–219 (2018).
4. Gowd, V. *et al.* Advancement of cancer immunotherapy using nanoparticles-based nanomedicine. *Seminars in Cancer Biology* **86**, 624–644 (2022).
5. Daldosso, N. *et al.* Orange and blue luminescence emission to track functionalized porous silicon microparticles inside the cells of the human immune system. *J. Mater. Chem. B* **2**, 6345–6353 (2014).
6. Ghafarinazari, A. *et al.* Isoconversional kinetics of thermal oxidation of mesoporous silicon. *Thermochimica Acta* **623**, 65–71 (2016).
7. Chistè, E., Ischia, G., Scarpa, M. & Daldosso, N. Ultrasonication effect on size distribution of functionalized porous silicon microparticles. *Mater. Res. Express* **6**, 075006 (2019).
8. Ghafarinazari, A. *et al.* Hybrid luminescent porous silicon for efficient drug loading and release. *RSC Advances* **7**, 6724–6734 (2017).
9. Chistè, E. *et al.* TiO2-coated luminescent porous silicon micro-particles as a promising system for nanomedicine. *J. Mater. Chem. B* **6**, 1815–1824 (2018).

10. Chistè, E. *et al.* Porous Si Microparticles Infiltrated with Magnetic Nanospheres. *Nanomaterials* **10**, 463 (2020).
11. Webster, T. J. Nanomedicine: what's in a definition? *Int J Nanomedicine* **1**, 115–116 (2006).
12. Bayda, S., Adeel, M., Tuccinardi, T., Cordani, M. & Rizzolio, F. The History of Nanoscience and Nanotechnology: From Chemical–Physical Applications to Nanomedicine. *Molecules* **25**, 112 (2019).
13. Guo, D., Xie, G. & Luo, J. Mechanical properties of nanoparticles: basics and applications. *J. Phys. D: Appl. Phys.* **47**, 013001 (2013).
14. Zhang, Z., Li, J. C. & Jiang, Q. Modelling for size-dependent and dimension-dependent melting of nanocrystals. *J. Phys. D: Appl. Phys.* **33**, 2653 (2000).
15. Sun, C. Q. Size dependence of nanostructures: Impact of bond order deficiency. *Progress in Solid State Chemistry* **35**, 1–159 (2007).
16. Yao, Y. *et al.* Nanoparticle-Based Drug Delivery in Cancer Therapy and Its Role in Overcoming Drug Resistance. *Front Mol Biosci* **7**, 193 (2020).
17. Shi, J., Kantoff, P. W., Wooster, R. & Farokhzad, O. C. Cancer nanomedicine: progress, challenges and opportunities. *Nat Rev Cancer* **17**, 20–37 (2017).
18. Wang, R., Billone, P. S. & Mullett, W. M. Nanomedicine in action: an overview of cancer nanomedicine on the market and in clinical trials. *J. Nanomaterials* **2013**, 1:1 (2013).
19. Barenholz, Y. (Chezy). Doxil® — The first FDA-approved nano-drug: Lessons learned. *Journal of Controlled Release* **160**, 117–134 (2012).

20. Yuan, H. *et al.* Albumin Nanoparticle of Paclitaxel (Abraxane) Decreases while Taxol Increases Breast Cancer Stem Cells in Treatment of Triple Negative Breast Cancer. *Mol Pharm* **17**, 2275–2286 (2020).

21. Avramis, V. I. & Tiwari, P. N. Asparaginase (native ASNase or pegylated ASNase) in the treatment of acute lymphoblastic leukemia. *Int J Nanomedicine* **1**, 241–254 (2006).

22. Nelson, N. R., Port, J. D. & Pandey, M. K. Use of Superparamagnetic Iron Oxide Nanoparticles (SPIONs) via Multiple Imaging Modalities and Modifications to Reduce Cytotoxicity: An Educational Review. *Journal of Nanotheranostics* **1**, 105–135 (2020).

23. Ferlay, J. *et al.* Cancer statistics for the year 2020: An overview. *International Journal of Cancer* **149**, 778–789 (2021).

24. Anand, U. *et al.* Cancer chemotherapy and beyond: Current status, drug candidates, associated risks and progress in targeted therapeutics. *Genes & Diseases* (2022) doi:10.1016/j.gendis.2022.02.007.

25. Matsumura, Y. & Maeda, H. A New Concept for Macromolecular Therapeutics in Cancer Chemotherapy: Mechanism of Tumoritropic Accumulation of Proteins and the Antitumor Agent Smancs1. *Cancer Research* **46**, 6387–6392 (1986).

26. Danhier, F., Feron, O. & Préat, V. To exploit the tumor microenvironment: Passive and active tumor targeting of nanocarriers for anti-cancer drug delivery. *Journal of Controlled Release* **148**, 135–146 (2010).

27. Jiang, W. *et al.* Designing nanomedicine for immuno-oncology. *Nat Biomed Eng* **1**, 1–11 (2017).

28. Zeromski, J. Significance of tumor-cell receptors in human cancer. *Arch Immunol Ther Exp (Warsz)* **50**, 105–110 (2002).

29. Rosenblum, D., Joshi, N., Tao, W., Karp, J. M. & Peer, D. Progress and challenges towards targeted delivery of cancer therapeutics. *Nat Commun* **9**, 1410 (2018).

30. Attia, M. F., Anton, N., Wallyn, J., Omran, Z. & Vandamme, T. F. An overview of active and passive targeting strategies to improve the nanocarriers efficiency to tumour sites. *Journal of Pharmacy and Pharmacology* **71**, 1185–1198 (2019).

31. Strategies for the intracellular delivery of nanoparticles - Chemical Society Reviews (RSC Publishing). https://pubs.rsc.org/en/content/articlelanding/2011/cs/c0cs00003e.

32. Torchilin, V. P. Recent advances with liposomes as pharmaceutical carriers. *Nat Rev Drug Discov* **4**, 145–160 (2005).

33. Wong, A. D., DeWit, M. A. & Gillies, E. R. Amplified release through the stimulus triggered degradation of self-immolative oligomers, dendrimers, and linear polymers. *Adv Drug Deliv Rev* **64**, 1031–1045 (2012).

34. Torchilin, V. P. Micellar nanocarriers: pharmaceutical perspectives. *Pharm Res* **24**, 1–16 (2007).

35. Kalluri, R. & LeBleu, V. S. The biology, function, and biomedical applications of exosomes. *Science* **367**, eaau6977 (2020).

36. Hasan, A. *et al.* Recent Advances in Application of Biosensors in Tissue Engineering. *Biomed Res Int* **2014**, 307519 (2014).

37. Huang, P. *et al.* Folic acid-conjugated Silica-modified gold nanorods for X-ray/CT imaging-guided dual-mode radiation and photo-thermal therapy. *Biomaterials* **32**, 9796–9809 (2011).

38. He, X., Wu, X., Wang, K., Shi, B. & Hai, L. Methylene blue-encapsulated phosphonate-terminated silica nanoparticles for simultaneous in vivo imaging and photodynamic therapy. *Biomaterials* **30**, 5601–5609 (2009).

39. Fabbro, A. *et al.* Adhesion to Carbon Nanotube Conductive Scaffolds Forces Action-Potential Appearance in Immature Rat Spinal Neurons. *PLoS One* **8**, e73621 (2013).

40. Uhlir Jr., A. Electrolytic Shaping of Germanium and Silicon. *Bell System Technical Journal* **35**, 333–347 (1956).

41. Canham, L. T. Silicon quantum wire array fabrication by electrochemical and chemical dissolution of wafers. *Appl. Phys. Lett.* **57**, 1046–1048 (1990).

42. Canham, L. T. Bioactive silicon structure fabrication through nanoetching techniques. *Advanced Materials* **7**, 1033 (1995).

43. Lehmann, V. & Gösele, U. Porous silicon formation: A quantum wire effect. *Appl. Phys. Lett.* **58**, 856–858 (1991).

44. Tasciotti, E. *et al.* Mesoporous silicon particles as a multistage delivery system for imaging and therapeutic applications. *Nature Nanotech* **3**, 151–157 (2008).

45. Wang, C.-F. *et al.* Multifunctional porous silicon nanoparticles for cancer theranostics. *Biomaterials* **48**, 108–118 (2015).

46. The structural and luminescence properties of porous silicon: Journal of Applied Physics: Vol 82, No 3. https://aip.scitation.org/doi/10.1063/1.366536.

47. Salonen, J., Kaukonen, A. M., Hirvonen, J. & Lehto, V.-P. Mesoporous Silicon in Drug Delivery Applications. *Journal of Pharmaceutical Sciences* **97**, 632–653 (2008).

48. Shahbazi, M.-A., Herranz, B. & Santos, H. A. Nanostructured porous Si-based nanoparticles for targeted drug delivery. *Biomatter* **2**, 296–312 (2012).

49. Shahbazi, M.-A. *et al.* Surface chemistry dependent immunostimulative potential of porous silicon nanoplatforms. *Biomaterials* **35**, 9224–9235 (2014).

50. Low, S. P., Voelcker, N. H., Canham, L. T. & Williams, K. A. The biocompatibility of porous silicon in tissues of the eye. *Biomaterials* **30**, 2873–2880 (2009).

51. Tasciotti, E. *et al.* Near-Infrared Imaging Method for the In Vivo Assessment of the Biodistribution of Nanoporous Silicon Particles. *Mol Imaging* **10**, 56–68 (2011).

52. Tölli, M. A. *et al.* In vivo biocompatibility of porous silicon biomaterials for drug delivery to the heart. *Biomaterials* **35**, 8394–8405 (2014).

53. Cheng, L. *et al.* Intravitreal properties of porous silicon photonic crystals: a potential self-reporting intraocular drug-delivery vehicle. *British Journal of Ophthalmology* **92**, 705–711 (2008).

54. Salonen, J. *et al.* Mesoporous silicon microparticles for oral drug delivery: loading and release of five model drugs. *J Control Release* **108**, 362–374 (2005).

55. Foraker, A. B. *et al.* Microfabricated porous silicon particles enhance paracellular delivery of insulin across intestinal Caco-2 cell monolayers. *Pharm Res* **20**, 110–116 (2003).

56. Park, J.-H. *et al.* Biodegradable luminescent porous silicon nanoparticles for in vivo applications. *Nature Mater* **8**, 331–336 (2009).

57. Shabir, Q. Biodegradability of Porous Silicon. in *Handbook of Porous Silicon* (ed. Canham, L.) 1–7 (Springer International Publishing, 2021). doi:10.1007/978-3-319-04508-5_39-1.

58. Porous Silicon in Practice: Preparation, Characterization and Applications | Wiley. *Wiley.com* https://www.wiley.com/en-us/Porous+Silicon+in+Practice%3A+Preparation%2C+Characterization+and+Applications-p-9783527313785.

59. Tzur-Balter, A., Shatsberg, Z., Beckerman, M., Segal, E. & Artzi, N. Mechanism of erosion of nanostructured porous silicon drug carriers in neoplastic tissues. *Nat Commun* **6**, 6208 (2015).

60. Canham, L. Routes of Formation for Porous Silicon. in *Handbook of Porous Silicon* (ed. Canham, L.) 3–11 (Springer International Publishing, 2018). doi:10.1007/978-3-319-71381-6_1.

61. Valiullin, R. Mesoporous Silicon. in *Handbook of Porous Silicon* (ed. Canham, L.) 133–147 (Springer International Publishing, 2018). doi:10.1007/978-3-319-71381-6_11.

62. Sailor, M. J. Color Me Sensitive: Amplification and Discrimination in Photonic Silicon Nanostructures. *ACS Nano* **1**, 248–252 (2007).

63. Canham, L. Tunable Properties of Porous Silicon. in *Handbook of Porous Silicon* (ed. Canham, L.) 201–206 (Springer International Publishing, 2014). doi:10.1007/978-3-319-05744-6_19.

64. Salonen, J. & Lehto, V.-P. Fabrication and chemical surface modification of mesoporous silicon for biomedical applications. *Chemical Engineering Journal* **1**, 162–172 (2008).

65. Frotscher, U. *et al.* Investigation of different oxidation processes for porous silicon studied by spectroscopic ellipsometry. *Thin Solid Films* **276**, 36–39 (1996).

66. Halimaoui, A. *et al.* Electroluminescence in the visible range during anodic oxidation of porous silicon films. *Appl. Phys. Lett.* **59**, 304–306 (1991).

67. Riikonen, J. *et al.* Surface chemistry, reactivity, and pore structure of porous silicon oxidized by various methods. *Langmuir* **28**, 10573–10583 (2012).

68. Schwartz, M. P. *et al.* Using an oxidized porous silicon interferometer for determination of relative protein binding affinity through non-covalent capture probe immobilization. *physica status solidi (a)* **204**, 1444–1448 (2007).

69. Bateman, J. E., Eagling, R. D., Worrall, D. R., Horrocks, B. R. & Houlton, A. Alkylation of Porous Silicon by Direct Reaction with Alkenes and Alkynes. *Angew Chem Int Ed Engl* **37**, 2683–2685 (1998).

70. Salonen, J., Laine, E. & Niinistö, L. Thermal analysis of hydrosilylation of 1-dodecene on porous silicon surface. *Physica Status Solidi Applied Research* **197**, 246–250 (2003).

71. Anglin, E. J., Cheng, L., Freeman, W. R. & Sailor, M. J. Porous silicon in drug delivery devices and materials. *Adv Drug Deliv Rev* **60**, 1266–1277 (2008).

72. Boukherroub, R. *et al.* Ideal Passivation of Luminescent Porous Silicon by Thermal, Noncatalytic Reaction with Alkenes and Aldehydes. *Chem. Mater.* **13**, 2002–2011 (2001).

73. Kovalainen, M. *et al.* Mesoporous silicon (PSi) for sustained peptide delivery: effect of psi microparticle surface chemistry on peptide YY3-36 release. *Pharm Res* **29**, 837–846 (2012).

74. Jalkanen, T., Mäkilä, E., Sakka, T., Salonen, J. & Ogata, Y. H. Thermally promoted addition of undecylenic acid on thermally hydrocarbonized porous silicon optical reflectors. *Nanoscale Res Lett* **7**, 311 (2012).

75. Gelloz, B. Photoluminescence of Porous Silicon. in *Handbook of Porous Silicon* (ed. Canham, L.) 449–462 (Springer International Publishing, 2018). doi:10.1007/978-3-319-71381-6_32.

76. Iyer, S. S. & Xie, Y.-H. Light Emission from Silicon. *Science* **260**, 40–46 (1993).

77. Kanemitsu, Y. *et al.* Microstructure and optical properties of free-standing porous silicon films: Size dependence of absorption spectra in Si nanometer-sized crystallites. *Phys. Rev. B* **48**, 2827–2830 (1993).

78. Gösele, U. & Lehmann, V. Light-emitting porous silicon. *Materials Chemistry and Physics* **40**, 253–259 (1995).

79. Ledoux, G. *et al.* Photoluminescence properties of silicon nanocrystals as a function of their size. *Phys. Rev. B* **62**, 15942–15951 (2000).

80. Delerue, C., Allan, G. & Lannoo, M. Theoretical aspects of the luminescence of porous silicon. *Phys. Rev. B* **48**, 11024–11036 (1993).

81. Stewart, M. P. & Buriak, J. M. Exciton-Mediated Hydrosilylation on Photoluminescent Nanocrystalline Silicon. *J. Am. Chem. Soc.* **123**, 7821–7830 (2001).

82. Stewart, M. P. & Buriak, J. M. Photopatterned Hydrosilylation on Porous Silicon. *Angewandte Chemie International Edition* **37**, 3257–3260 (1998).

83. Korotcenkov, G., Han, S. H. & Cho, B. K. Material Design for Metal Oxide Chemiresistive Gas Sensors. *Journal of Sensor Science and Technology* **22**, 1–17 (2013).

84. Maniya, N. H., Patel, S. R. & Murthy, Z. V. P. Study on surface chemistry and particle size of porous silicon prepared by electrochemical etching. *Materials Research Bulletin* **57**, 6–12 (2014).

85. Infrared and Raman Characteristic Group Frequencies: Tables and Charts, 3rd Edition | Wiley. *Wiley.com* https://www.wiley.com/en-it/Infrared+and+Raman+Characteristic+Group+Frequencies%3A+Tables+and+Charts%2C+3rd+Edition-p-9780470093078.

86. Canham, L. Processing Techniques and Process Flows with Porous Silicon. in *Handbook of Porous Silicon* (ed. Canham, L.) 787–796 (Springer International Publishing, 2018). doi:10.1007/978-3-319-71381-6_53.

87. Taurozzi, J. S., Hackley, V. A. & Wiesner, M. R. Ultrasonic dispersion of nanoparticles for environmental, health and safety assessment--issues and recommendations. *Nanotoxicology* **5**, 711–729 (2011).

88. Adhesion of cells to surfaces coated with polylysine. Applications to electron microscopy. *J Cell Biol* **66**, 198–200 (1975).

89. Schiattarella, C. *et al.* Time-gated luminescence imaging of positively charged poly-l-lysine-coated highly microporous silicon nanoparticles in living Hydra polyp. *Journal of Biophotonics* **13**, e202000272 (2020).

90. Zheng, M. *et al.* Poly(α-l-lysine)-based nanomaterials for versatile biomedical applications: Current advances and perspectives. *Bioactive Materials* **6**, 1878–1909 (2021).

91. Jang, J. *et al.* Surfactant-based selective assembly approach for Si-embedded silicon oxycarbide composite materials in lithium-ion batteries. *Chemical Engineering Journal* **401**, 126091 (2020).

92. Bryleva, E. Yu. *et al.* Interfacial properties of cetyltrimethylammonium-coated SiO2 nanoparticles in aqueous media as studied by using different indicator dyes. *Journal of Colloid and Interface Science* **316**, 712–722 (2007).

93. Bachelder, E. M., Beaudette, T. T., Broaders, K. E., Dashe, J. & Fréchet, J. M. J. Acetal-Derivatized Dextran: An Acid-Responsive Biodegradable Material for Therapeutic Applications. *J. Am. Chem. Soc.* **130**, 10494–10495 (2008).

94. Cohen, J. A. *et al.* Acetal-Modified Dextran Microparticles with Controlled Degradation Kinetics and Surface Functionality for Gene Delivery in Phagocytic and Non-Phagocytic Cells. *Advanced Materials* **22**, 3593–3597 (2010).

95. Peine, K. J. *et al.* Efficient Delivery of the Toll-like Receptor Agonists Polyinosinic:Polycytidylic Acid and CpG to Macrophages by Acetalated Dextran Microparticles. *Mol. Pharmaceutics* **10**, 2849–2857 (2013).

96. Fontana, F. *et al.* Multistaged Nanovaccines Based on Porous Silicon@Acetalated Dextran@Cancer Cell Membrane for Cancer Immunotherapy. *Advanced Materials* **29**, 1603239 (2017).

97. Broaders, K. E., Cohen, J. A., Beaudette, T. T., Bachelder, E. M. & Fréchet, J. M. J. Acetalated dextran is a chemically and biologically tunable material for particulate immunotherapy. *Proceedings of the National Academy of Sciences* **106**, 5497–5502 (2009).

98. Wang, Y., Li, P., Truong-Dinh Tran, T., Zhang, J. & Kong, L. Manufacturing Techniques and Surface Engineering of Polymer Based Nanoparticles for Targeted Drug Delivery to Cancer. *Nanomaterials* **6**, 26 (2016).

99. Shkodra-Pula, B. *et al.* Encapsulation of the dual FLAP/mPEGS-1 inhibitor BRP-187 into acetalated dextran and PLGA nanoparticles improves its cellular bioactivity. *Journal of Nanobiotechnology* **18**, 73 (2020).

100. Gongalsky, M. B. *et al.* Enhanced photoluminescence of porous silicon nanoparticles coated by bioresorbable polymers. *Nanoscale Res Lett* **7**, 446 (2012).

101. Fallacara, A., Baldini, E., Manfredini, S. & Vertuani, S. Hyaluronic Acid in the Third Millennium. *Polymers* **10**, 701 (2018).

102. Mattheolabakis, G., Milane, L., Singh, A. & Amiji, M. M. Hyaluronic acid targeting of CD44 for cancer therapy: from receptor biology to nanomedicine. *Journal of Drug Targeting* **23**, 605–618 (2015).

103. Kamat, M. *et al.* Hyaluronic Acid Immobilized Magnetic Nanoparticles for Active Targeting and Imaging of Macrophages. *Bioconjugate Chem.* **21**, 2128–2135 (2010).

104. Ai, T. *et al.* A Historical Overview of Magnetic Resonance Imaging, Focusing on Technological Innovations. *Investigative Radiology* **47**, 725 (2012).

105. Wolf, M. *et al.* Magnetic resonance imaging T1- and T2-mapping to assess renal structure and function: a systematic review and statement paper. *Nephrology Dialysis Transplantation* **33**, ii41–ii50 (2018).

106. Anik, M. I., Hossain, M. K., Hossain, I., Ahmed, I. & Doha, R. M. 18 - Biomedical applications of magnetic nanoparticles. in *Magnetic Nanoparticle-Based Hybrid Materials* (eds. Ehrmann, A., Nguyen, T. A., Ahmadi, M., Farmani, A. & Nguyen-Tri, P.) 463–497 (Woodhead Publishing, 2021). doi:10.1016/B978-0-12-823688-8.00002-8.

107. Zhu, Y.-C., Dufouil, C., Tzourio, C. & Chabriat, H. Silent Brain Infarcts. *Stroke* **42**, 1140–1145 (2011).

108. Stephen, Z. R., Kievit, F. M. & Zhang, M. Magnetite nanoparticles for medical MR imaging. *Materials Today* **14**, 330–338 (2011).

109. Dumas, S. *et al.* High relaxivity MRI contrast agents part 1: Impact of single donor atom substitution on relaxivity of serum albumin-bound gadolinium complexes. *Invest Radiol* **45**, 600–612 (2010).

110. Na, H. B., Song, I. C. & Hyeon, T. Inorganic Nanoparticles for MRI Contrast Agents. *Advanced Materials* **21**, 2133–2148 (2009).

111. Wahsner, J., Gale, E. M., Rodríguez-Rodríguez, A. & Caravan, P. Chemistry of MRI Contrast Agents: Current Challenges and New Frontiers. *Chem. Rev.* **119**, 957–1057 (2019).

112. Tran, H.-V. *et al.* Multifunctional Iron Oxide Magnetic Nanoparticles for Biomedical Applications: A Review. *Materials* **15**, 503 (2022).

113. Samrot, A. V., Sahithya, C. S., Selvarani A, J., Purayil, S. K. & Ponnaiah, P. A review on synthesis, characterization and potential biological applications of superparamagnetic iron oxide nanoparticles. *Current Research in Green and Sustainable Chemistry* **4**, 100042 (2021).

114. Vakili-Ghartavol, R. *et al.* Toxicity assessment of superparamagnetic iron oxide nanoparticles in different tissues. *Artificial Cells, Nanomedicine, and Biotechnology* **48**, 443–451 (2020).

115. Farinha, P., Coelho, J. M. P., Reis, C. P. & Gaspar, M. M. A Comprehensive Updated Review on Magnetic Nanoparticles in Diagnostics. *Nanomaterials* **11**, (2021).

116. Malvindi, M. A. *et al.* Toxicity Assessment of Silica Coated Iron Oxide Nanoparticles and Biocompatibility Improvement by Surface Engineering. *PLOS ONE* **9**, e85835 (2014).

117. Gu, L., Park, J.-H., Duong, K. H., Ruoslahti, E. & Sailor, M. J. Magnetic Luminescent Porous Silicon Microparticles for Localized Delivery of Molecular Drug Payloads. *Small* **6**, 2546–2552 (2010).

118. Serda, R. E. *et al.* Cellular association and assembly of a multistage delivery system. *Small* **6**, 1329–1340 (2010).

119. Chaix, A. *et al.* Cell penetrating peptide decorated magnetic porous silicon nanorods for glioblastoma therapy and imaging. *RSC Adv.* **12**, 11708–11714 (2022).

120. Yang, G. W. Laser ablation in liquids: Applications in the synthesis of nanocrystals. *Progress in Materials Science* **52**, 648–698 (2007).

121. Huang, H., Lai, J., Lu, J. & Li, Z. Pulsed laser ablation of bulk target and particle products in liquid for nanomaterial fabrication. *AIP Advances* **9**, 015307 (2019).

122. DeVita, V. T., Jr. & Chu, E. A History of Cancer Chemotherapy. *Cancer Research* **68**, 8643–8653 (2008).

123. Pearce, A. *et al.* Incidence and severity of self-reported chemotherapy side effects in routine care: A prospective cohort study. *PLOS ONE* **12**, e0184360 (2017).

124. Benjamin, D. J., Xu, A., Lythgoe, M. P. & Prasad, V. Cancer Drug Approvals That Displaced Existing Standard-of-Care Therapies, 2016-2021. *JAMA Network Open* **5**, e222265 (2022).

125. Doxorubicin. in *LiverTox: Clinical and Research Information on Drug-Induced Liver Injury* (National Institute of Diabetes and Digestive and Kidney Diseases, 2012).

126. Bonadonna, G., Monfardini, S., de Lena, M. & Fossati-Bellani, F. Clinical Evaluation of Adriamycin, a New Antitumour Antibiotic. *BMJ* **3**, 503–506 (1969).

127. Asensio-López, M. C., Soler, F., Pascual-Figal, D., Fernández-Belda, F. & Lax, A. Doxorubicin-induced oxidative stress: The protective effect of nicorandil on HL-1 cardiomyocytes. *PLOS ONE* **12**, e0172803 (2017).

128. Zhao, L. & Zhang, B. Doxorubicin induces cardiotoxicity through upregulation of death receptors mediated apoptosis in cardiomyocytes. *Sci Rep* **7**, 44735 (2017).

129. Bhinge, K. *et al.* The opposite effects of Doxorubicin on bone marrow stem cells versus breast cancer stem cells depend on glucosylceramide synthase. *Int J Biochem Cell Biol* **44**, 1770–1778 (2012).

130. Arnouk, H., Hassan, B. A. R., Arnouk, H. & Hassan, B. A. R. *Advances in Precision Medicine Oncology*. (2021). doi:10.5772/intechopen.91507.

131. Kartal-Yandim, M., Adan-Gokbulut, A. & Baran, Y. Molecular mechanisms of drug resistance and its reversal in cancer. *Critical Reviews in Biotechnology* **36**, 716–726 (2016).

132. Nam, Y.-S. *et al.* Down-regulation of intracellular reactive oxygen species attenuates P-glycoprotein-associated chemoresistance in Epstein-Barr virus-positive NK/T-cell lymphoma. *Am J Transl Res* **11**, 1359–1373 (2019).

133. Ji, X. *et al.* Chemoresistance mechanisms of breast cancer and their countermeasures. *Biomedicine & Pharmacotherapy* **114**, 108800 (2019).

134. Mansoori, B., Mohammadi, A., Davudian, S., Shirjang, S. & Baradaran, B. The Different Mechanisms of Cancer Drug Resistance: A Brief Review. *Adv Pharm Bull* **7**, 339–348 (2017).

135. Engelberth, S. A., Hempel, N. & Bergkvist, M. Development of Nanoscale Approaches for Ovarian Cancer Therapeutics and Diagnostics. *CRO* **19**, (2014).

136. Wang, S. *et al.* Nanoparticle-based medicines in clinical cancer therapy. *Nano Today* **45**, 101512 (2022).

137. Sayed, E. *et al.* Porous Inorganic Drug Delivery Systems—a Review. *AAPS PharmSciTech* **18**, 1507–1525 (2017).

138. Na, H. B., Song, I. C. & Hyeon, T. Inorganic Nanoparticles for MRI Contrast Agents. *Advanced Materials* **21**, 2133–2148 (2009).

139. Shi, Z. *et al.* Inorganic nano-carriers based smart drug delivery systems for tumor therapy. *Smart Materials in Medicine* **1**, 32–47 (2020).

140. Tieu, T., Alba, M., Elnathan, R., Cifuentes-Rius, A. & Voelcker, N. H. Advances in Porous Silicon–Based Nanomaterials for Diagnostic and Therapeutic Applications. *Advanced Therapeutics* **2**, 1800095 (2019).

141. Xu, W. *et al.* Smart Porous Silicon Nanoparticles with Polymeric Coatings for Sequential Combination Therapy. *Mol. Pharmaceutics* **12**, 4038–4047 (2015).

142. Janoniene, A. *et al.* A Versatile Carbonic Anhydrase IX Targeting Ligand-Functionalized Porous Silicon Nanoplatform for Dual Hypoxia Cancer Therapy and Imaging. *ACS Appl. Mater. Interfaces* **9**, 13976–13987 (2017).

143. Xia, B. *et al.* Photothermal and biodegradable polyaniline/porous silicon hybrid nanocomposites as drug carriers for combined chemo-photothermal therapy of cancer. *Acta Biomaterialia* **51**, 197–208 (2017).

144. Liang, J. *et al.* Simple and rapid monitoring of doxorubicin using streptavidin-modified microparticle-based time-resolved fluorescence immunoassay. *RSC Adv.* **8**, 15621–15631 (2018).

145. Wu, E. C., Andrew, J. S., Buyanin, A., Kinsella, J. M. & Sailor, M. J. Suitability of porous silicon microparticles for the long-term delivery of redox-active therapeutics. *Chem. Commun.* **47**, 5699–5701 (2011).

146. Xia, B., Wang, B., Zhang, W. & Shi, J. High loading of doxorubicin into styrene-terminated porous silicon nanoparticles via π-stacking for cancer treatments in vitro. *RSC Adv.* **5**, 44660–44665 (2015).

147. Xia, B., Zhang, W., Shi, J. & Xiao, S. A novel strategy to fabricate doxorubicin/bovine serum albumin/porous silicon nanocomposites with pH-triggered drug delivery for cancer therapy in vitro. *J. Mater. Chem. B* **2**, 5280–5286 (2014).

148. Alken, S. & Kelly, C. M. Benefit risk assessment and update on the use of docetaxel in the management of breast cancer. *Cancer Management and Research* **5**, 357–365 (2013).

149. Vakili-Ghartavol, R., Rezayat, S. M., Faridi-Majidi, R., Sadri, K. & Jaafari, M. R. Optimization of Docetaxel Loading Conditions in Liposomes: proposing potential products for metastatic breast carcinoma chemotherapy. *Sci Rep* **10**, 5569 (2020).

150. Chin, V., Collins, B. E., Sailor, M. J. & Bhatia, S. N. Compatibility of Primary Hepatocytes with Oxidized Nanoporous Silicon. *Advanced Materials* **13**, 1877–1880 (2001).

151. Ghasemi, M., Turnbull, T., Sebastian, S. & Kempson, I. The MTT Assay: Utility, Limitations, Pitfalls, and Interpretation in Bulk and Single-Cell Analysis. *Int J Mol Sci* **22**, 12827 (2021).

152. Laaksonen, T. *et al.* Failure of MTT as a Toxicity Testing Agent for Mesoporous Silicon Microparticles. *Chem. Res. Toxicol.* **20**, 1913–1918 (2007).

153. Chittasupho, C., Lirdprapamongkol, K., Kewsuwan, P. & Sarisuta, N. Targeted delivery of doxorubicin to A549 lung cancer cells by CXCR4

antagonist conjugated PLGA nanoparticles. *European Journal of Pharmaceutics and Biopharmaceutics* **88**, 529–538 (2014).

154. Sawpari, R. *et al.* Recent advances and futuristic potentials of nano-tailored doxorubicin for prostate cancer therapy. *Journal of Drug Delivery Science and Technology* **81**, 104212 (2023).

155. Shu, Y., Xie, B., Liang, Z. & Chen, J. Quercetin reverses the doxorubicin resistance of prostate cancer cells by downregulating the expression of c-met. *Oncology Letters* **15**, 2252–2258 (2018).

156. Melguizo, C. *et al.* Enhanced antitumoral activity of doxorubicin against lung cancer cells using biodegradable poly(butylcyanoacrylate) nanoparticles. *Drug Des Devel Ther* **9**, 6433–6444 (2015).

157. Cancino-Marentes, M. E. *et al.* Sensitizing the cytotoxic action of Docetaxel induced by Pentoxifylline in a PC3 prostate cancer cell line. *BMC Urology* **21**, 38 (2021).

158. Chen, X. *et al.* Significant Suppression of Non-small-cell Lung Cancer by Hydrophobic Poly(ester amide) Nanoparticles with High Docetaxel Loading. *Frontiers in Pharmacology* **9**, (2018).

159. Kuo, W.-T., Tu, D.-G., Chiu, L.-Y., Sheu, G.-T. & Wu, M.-F. High pemetrexed sensitivity of docetaxel-resistant A549 cells is mediated by TP53 status and downregulated thymidylate synthase. *Oncol Rep* **38**, 2787–2795 (2017).

160. Sharma, P., Hu-Lieskovan, S., Wargo, J. A. & Ribas, A. Primary, Adaptive, and Acquired Resistance to Cancer Immunotherapy. *Cell* **168**, 707–723 (2017).

161. Busch, W. *Aus der Sitzung der medicinischen Section vom 13 November 1867. Berlin Klin Wochenschr 1868;5:137. (in German)*.

162. Fehleisen, N. Ueber die Züchtung der Erysipelkokken auf künstlichem Nährboden und ihre Uebertragbarkeit auf den Menschen. *Dtsch Med Wochenschr* **8**, 553–554 (1882).

163. Dobosz, P. & Dzieciątkowski, T. The Intriguing History of Cancer Immunotherapy. *Front Immunol* **10**, 2965 (2019).

164. Oiseth, S. J. & Aziz, M. S. Cancer immunotherapy: a brief review of the history, possibilities, and challenges ahead. *Journal of Cancer Metastasis and Treatment* **3**, 250–261 (2017).

165. Morales, A., Eidinger, D. & Bruce, A. W. Intracavitary Bacillus Calmette-guerin in the Treatment of Superficial Bladder Tumors. *Journal of Urology* **116**, 180–182 (1976).

166. Old, L. J., Clarke, D. A. & Benacerraf, B. Effect of Bacillus Calmette-Guérin Infection on Transplanted Tumours in the Mouse. *Nature* **184**, 291–292 (1959).

167. Carswell, E. A. *et al.* An endotoxin-induced serum factor that causes necrosis of tumors. *Proceedings of the National Academy of Sciences* **72**, 3666–3670 (1975).

168. Foster, J. R. The functions of cytokines and their uses in toxicology. *Int J Exp Pathol* **82**, 171–192 (2001).

169. Peterson, C., Denlinger, N. & Yang, Y. Recent Advances and Challenges in Cancer Immunotherapy. *Cancers* **14**, 3972 (2022).

170. Michot, J. M. *et al.* Immune-related adverse events with immune checkpoint blockade: a comprehensive review. *European Journal of Cancer* **54**, 139–148 (2016).

171. Wang, S., Xie, K. & Liu, T. Cancer Immunotherapies: From Efficacy to Resistance Mechanisms – Not Only Checkpoint Matters. *Frontiers in Immunology* **12**, (2021).

172. Reed, S. G., Orr, M. T. & Fox, C. B. Key roles of adjuvants in modern vaccines. *Nat Med* **19**, 1597–1608 (2013).

173. Verdijk, P. *et al.* Morphological changes during dendritic cell maturation correlate with cofilin activation and translocation to the cell membrane. *European Journal of Immunology* **34**, 156–164 (2004).

174. Xing, F. *et al.* Comparison of immature and mature bone marrow-derived dendritic cells by atomic force microscopy. *Nanoscale Res Lett* **6**, 455 (2011).

175. Khan, F. U. *et al.* Dendritic Cells and Their Immunotherapeutic Potential for Treating Type 1 Diabetes. *International Journal of Molecular Sciences* **23**, 4885 (2022).

176. Zhu, F., Tong, Y., Sheng, Z. & Yao, Y. Role of dendritic cells in the host response to biomaterials and their signaling pathways. *Acta Biomaterialia* **94**, 132–144 (2019).

177. Banchereau, J. *et al.* Immunobiology of dendritic cells. *Annu Rev Immunol* **18**, 767–811 (2000).

178. de Oliviera Nascimento, L., Massari, P. & Wetzler, L. The Role of TLR2 in Infection and Immunity. *Frontiers in Immunology* **3**, (2012).

179. Liu, Z. & Roche, P. A. Macropinocytosis in phagocytes: regulation of MHC class-II-restricted antigen presentation in dendritic cells. *Frontiers in Physiology* **6**, (2015).

180. Jia, J. *et al.* Interactions Between Nanoparticles and Dendritic Cells: From the Perspective of Cancer Immunotherapy. *Front Oncol* **8**, 404 (2018).

181. Joshi, V. B., Geary, S. M. & Salem, A. K. Biodegradable Particles as Vaccine Delivery Systems: Size Matters. *AAPS J* **15**, 85–94 (2012).

182. Fytianos, K. *et al.* Uptake efficiency of surface modified gold nanoparticles does not correlate with functional changes and cytokine secretion in human dendritic cells in vitro. *Nanomedicine* **11**, 633–644 (2015).

183. Palucka, K., Ueno, H. & Banchereau, J. Recent Developments in Cancer Vaccines. *The Journal of Immunology* **186**, 1325–1331 (2011).

184. Lanzavecchia, A. & Sallusto, F. Regulation of T Cell Immunity by Dendritic Cells. *Cell* **106**, 263–266 (2001).

185. Marrack, P., McKee, A. S. & Munks, M. W. Towards an understanding of the adjuvant action of aluminium. *Nat Rev Immunol* **9**, 287–293 (2009).

186. Klippstein, R. & Pozo, D. Nanotechnology-based manipulation of dendritic cells for enhanced immunotherapy strategies. *Nanomedicine: Nanotechnology, Biology and Medicine* **6**, 523–529 (2010).

187. TLR2 Ligands Induce NF-κB Activation from Endosomal Compartments of Human Monocytes | PLOS ONE. https://journals.plos.org/plosone/article?id=10.1371/journal.pone.0080743.

188. Murgueitio, M. S. *et al.* Enhanced immunostimulatory activity of in silico discovered agonists of Toll-like receptor 2 (TLR2). *Biochimica et Biophysica Acta (BBA) - General Subjects* **1861**, 2680–2689 (2017).

189. Engel, A. L., Holt, G. E. & Lu, H. The pharmacokinetics of Toll-like receptor agonists and the impact on the immune system. *Expert Review of Clinical Pharmacology* **4**, 275–289 (2011).

190. Lamrayah, M. *et al.* Molecular modelling of TLR agonist Pam3CSK4 entrapment in PLA nanoparticles as a tool to explain loading efficiency and functionality. *International Journal of Pharmaceutics* **568**, 118569 (2019).

191. Rosalia, R. A. *et al.* CD40-targeted dendritic cell delivery of PLGA-nanoparticle vaccines induce potent anti-tumor responses. *Biomaterials* **40**, 88–97 (2015).

192. Megy, S. *et al.* Molecular Dynamics Studies of Poly(Lactic Acid) Nanoparticles and Their Interactions with Vitamin E and TLR Agonists Pam1CSK4 and Pam3CSK4. *Nanomaterials* **10**, 2209 (2020).

193. Alkie, T. N. *et al.* Characterization of Innate Responses Induced by PLGA Encapsulated- and Soluble TLR Ligands In Vitro and In Vivo in Chickens. *PLOS ONE* **12**, e0169154 (2017).

194. Katebi, A., Varshochian, R., Riazi-Rad, F., Ganjalikhani-Hakemi, M. & Ajdary, S. Combinatorial delivery of antigen and TLR agonists via PLGA nanoparticles modulates Leishmania major-infected-macrophages activation. *Biomed Pharmacother* **137**, 111276 (2021).

195. Bal, S. M., Slütter, B., Verheul, R., Bouwstra, J. A. & Jiskoot, W. Adjuvanted, antigen loaded N-trimethyl chitosan nanoparticles for nasal and

intradermal vaccination: Adjuvant- and site-dependent immunogenicity in mice. *European Journal of Pharmaceutical Sciences* **45**, 475–481 (2012).

196. Haddadi, A., Chaffey, A., Ng, S. H., Yalamati, D. & Wilson, H. L. Combination of Innate Immune Modulators as Vaccine Adjuvants in Mice. *Vaccines* **8**, 569 (2020).
197. Tsolmongyn, B. *et al.* A Toll-like receptor 2 ligand, Pam3CSK4, augments interferon-γ-induced nitric oxide production via a physical association between MyD88 and interferon-γ receptor in vascular endothelial cells. *Immunology* **140**, 352–361 (2013).
198. Boguszewska, K., Szewczuk, M., Urbaniak, S. & Karwowski, B. T. Review: immunoassays in DNA damage and instability detection. *Cell. Mol. Life Sci.* **76**, 4689–4704 (2019).
199. Godwin, A. K. Immune Priming: Overview and its Mechanism.
200. Gogolák, P., Réthi, B., Hajas, G. & Rajnavölgyi, É. Targeting dendritic cells for priming cellular immune responses. *Journal of Molecular Recognition* **16**, 299–317 (2003).
201. Karwacki, J. *et al.* Boosting the Immune Response-Combining Local and Immune Therapy for Prostate Cancer Treatment. *Cells* **11**, 2793 (2022).
202. Lamrayah, M. *et al.* Molecular modelling of TLR agonist Pam3CSK4 entrapment in PLA nanoparticles as a tool to explain loading efficiency and functionality. *International Journal of Pharmaceutics* **568**, 118569 (2019).
203. Uronen-Hansson, H. *et al.* Toll-like receptor 2 (TLR2) and TLR4 are present inside human dendritic cells, associated with microtubules and the Golgi apparatus but are not detectable on the cell surface: integrity of microtubules is

required for interleukin-12 production in response to internalized bacteria. *Immunology* **111**, 173–178 (2004).

204. Lundquist, C. M. *et al.* Characterization of Free and Porous Silicon-Encapsulated Superparamagnetic Iron Oxide Nanoparticles as Platforms for the Development of Theranostic Vaccines. *Medical Sciences* **2**, 51–69 (2014).
205. Meraz, I. M. *et al.* Multivalent Presentation of MPL by Porous Silicon Microparticles Favors T Helper 1 Polarization Enhancing the Anti-Tumor Efficacy of Doxorubicin Nanoliposomes. *PLOS ONE* **9**, e94703 (2014).
206. Friedmann, T. A brief history of gene therapy. *Nat Genet* **2**, 93–98 (1992).
207. Arabi, F., Mansouri, V. & Ahmadbeigi, N. Gene therapy clinical trials, where do we go? An overview. *Biomedicine & Pharmacotherapy* **153**, 113324 (2022).
208. Scheller, E. L. & Krebsbach, P. H. Gene Therapy. *J Dent Res* **88**, 585–596 (2009).
209. Ledford, H. & Callaway, E. Pioneers of revolutionary CRISPR gene editing win chemistry Nobel. *Nature* **586**, 346–347 (2020).
210. Zhang, W.-W. *et al.* The First Approved Gene Therapy Product for Cancer Ad-p53 (Gendicine): 12 Years in the Clinic. *Human Gene Therapy* **29**, 160–179 (2018).
211. Mullard, A. 2022 FDA approvals. *Nature Reviews Drug Discovery* **22**, 83–88 (2023).
212. Shahryari, A., Burtscher, I., Nazari, Z. & Lickert, H. Engineering Gene Therapy: Advances and Barriers. *Advanced Therapeutics* **4**, 2100040 (2021).

213. Sayed, N. *et al.* Gene therapy: Comprehensive overview and therapeutic applications. *Life Sciences* **294**, 120375 (2022).

214. Nguyen, J. & Szoka, F. C. Nucleic Acid Delivery: The Missing Pieces of the Puzzle? *Acc. Chem. Res.* **45**, 1153–1162 (2012).

215. Grimm, D. & Kay, M. A. RNAi and Gene Therapy: A Mutual Attraction. *Hematology* **2007**, 473–481 (2007).

216. Alshaer, W. *et al.* siRNA: Mechanism of action, challenges, and therapeutic approaches. *European Journal of Pharmacology* **905**, 174178 (2021).

217. Lam, J. K. W., Chow, M. Y. T., Zhang, Y. & Leung, S. W. S. siRNA Versus miRNA as Therapeutics for Gene Silencing. *Mol Ther Nucleic Acids* **4**, e252 (2015).

218. Dana, H. *et al.* Molecular Mechanisms and Biological Functions of siRNA. *Int J Biomed Sci* **13**, 48–57 (2017).

219. Lee, S. J., Kim, M. J., Kwon, I. C. & Roberts, T. M. Delivery Strategies and Potential Targets for siRNA in Major Cancer Types. *Adv Drug Deliv Rev* **104**, 2–15 (2016).

220. Tatiparti, K., Sau, S., Kashaw, S. K. & Iyer, A. K. siRNA Delivery Strategies: A Comprehensive Review of Recent Developments. *Nanomaterials (Basel)* **7**, 77 (2017).

221. Tanaka, T. *et al.* Sustained Small Interfering RNA Delivery by Mesoporous Silicon Particles. *Cancer Research* **70**, 3687–3696 (2010).

222. Tieu, T. *et al.* Maximizing RNA Loading for Gene Silencing Using Porous Silicon Nanoparticles. *ACS Appl. Mater. Interfaces* **11**, 22993–23005 (2019).

223. Chaix, A. *et al.* Amino-acid functionalized porous silicon nanoparticles for the delivery of pDNA. *RSC Adv.* **9**, 31895–31899 (2019).

224. Kang, J. *et al.* Self-Sealing Porous Silicon-Calcium Silicate Core-Shell Nanoparticles for Targeted siRNA Delivery to the Injured Brain. *Adv Mater* **28**, 7962–7969 (2016).

225. Schroeder, A., Levins, C. G., Cortez, C., Langer, R. & Anderson, D. G. Lipid-based nanotherapeutics for siRNA delivery. *J Intern Med* **267**, 9–21 (2010).

226. Kang, J. *et al.* Enhanced Performance of a Molecular Photoacoustic Imaging Agent by Encapsulation in Mesoporous Silicon Nanoparticles. *Advanced Materials* **30**, 1800512 (2018).

227. Hyaluronidase as a Therapeutic Target in Cancer: A Matter of Too Little or Too Much. *Cancer Biology & Therapy* **4**, 917–917 (2005).

228. Weber, G. C., Buhren, B. A., Schrumpf, H., Wohlrab, J. & Gerber, P. A. Clinical Applications of Hyaluronidase. in *Therapeutic Enzymes: Function and Clinical Implications* (ed. Labrou, N.) 255–277 (Springer, 2019). doi:10.1007/978-981-13-7709-9_12.

229. Tieu, T. *et al.* Nanobody-displaying porous silicon nanoparticles for the co-delivery of siRNA and doxorubicin. *Biomater. Sci.* **9**, 133–147 (2021).

230. Wu, Z., Zhu, L., Mai, J., Shen, H. & Xu, R. Rad51 Silencing with siRNA Delivered by Porous Silicon-Based Microparticle Enhances the Anti-Cancer Effect of Doxorubicin in Triple-Negative Breast Cancer. *Journal of Biomedical Nanotechnology* **17**, 2351–2363 (2021).

231. Meng, H. *et al.* Co-delivery of an Optimal Drug/siRNA Combination Using Mesoporous Silica Nanoparticle to Overcome Drug Resistance in Breast Cancer In Vitro and In Vivo. *ACS Nano* **7**, 994–1005 (2013).

232. Ding, J. *et al.* Hyaluronidase-triggered anticancer drug and siRNA delivery from cascaded targeting nanoparticles for drug-resistant breast cancer therapy. *Nano Res.* **10**, 690–703 (2017).

APPENDIX A1: Characterization techniques

Here, the techniques used for the sample characterization are reported, organized by type of characterization.

Surface and chemical characterization

- FT-IR Spectroscopy

The surface characterization, in particular the chemical groups present at the surface were investigated by a *Thermo Scientific, Nicolet iN10* micro-FTIR (Fourier Transform InfraRed) instrument, with a liquid nitrogen cooled detector. A drop of each sample was deposited on a ZnSe slab and let dry with a flow of nitrogen in the case of samples in ethanol or let evaporate in oven at 50°C overnight in the case of aqueous samples. The spectra were acquired in transmission mode from 900 to 3600 cm^{-1} with a resolution of 4 cm^{-1}.

- Raman spectroscopy

Vibrational modes of the samples were analysed by triple-monochromator *T-64000, Horiba-Jobin Yvon* Raman spectrometer, equipped with Olympus (BX-41) microscope (100x objective), a CCD detector (256×1024 pixels) cooled by liquid nitrogen, and under water cooled Ar/Kr gas laser (*Stabilite RM2018, Spectra Physics*) excitation. The coated pSi microparticles samples were investigated 514,5 nm laser (5 mW) with 600 s integration time.

SPIONs were investigated by *Thermo Scientific, DXR2* Raman microscope equipped with a 633 nm laser (3mW power) and single exposure CCD detector.

- Z-potential measurement (Dynamic light scattering)

The microparticles surface charge (ζ-potential) was analysed by Zetasizer Nano-SZ (Malvern) instrument, with a 633 nm laser beam. The ζ-Potential was determined after resuspension of the microparticles in phosphate-buffered saline (PBS at pH 7.4). The measurements were performed at 25 °C, repeated three times and

averaged. Before the measurements, the samples were sonicated in a thermal bath for 45 minutes to homogenize the samples and reduce the agglomeration.

Optical characterization

- Fluorescence spectroscopy

Fluorescence spectroscopy was used to determine steady state and time resolved photoluminescence. The samples under investigation were analysed by a *Horiba Jobin-Yvon Nanolog* Spectrofluorometer, with a 54W xenon lamp and PMT detector.

The samples photoluminescence (PL) spectra were acquired by excitation at 350 nm, 3 nm slit size, 1200 g/mm density grating (blazed at 500 nm), 0.2 s integration time and with a 370 nm cut-off filter. For the PLE experiments, PL was investigated for each sample as a function of the exciting wavelength, which was varied from 325nm to 450nm, with a step of 25nm. Photoluminescence decay curve were studied by TCSPC (time correlated single photon counting) method.

The PL lifetime of the orange-red band (600 - 700 nm, characterized by a μs range lifetime) was analysed by a xenon pulsed lamp with a pulse width of 1.1 μs, exciting at 325 nm and fixing the emission at the maximum wavelength of the PL band for each sample. The lifetime values τ were obtained by fitting the decay curve with a stretched exponential $I = I_o\, e^{-(t/\tau)^{\beta}}$, where β is the stretched parameter. The lifetime of the small blue band, characterized by a ns range lifetime, was investigated by a 335 nm nanoLED source with a pulse width < 1 ns. The emission wavelength was fixed at 420 nm (i.e. the center of the blue band) and the data were fitted with an exponential decay curve, $I = I_o\, e^{-(\mathrm{t}/\tau)}$, to obtain the average lifetime.

The light efficiency of the samples was evaluated by quantum yield (QY) measurements by means of the comparative method, where the unknown QYs is determined starting from a known QYr of a reference material through the following formula, where s and r refers to 'sample' and 'reference', respectively

$$QY_s = QY_r \frac{I_s}{I_r} \frac{A_r}{A_s} \left(\frac{n_s}{n_r}\right)^2$$

The integrated emission intensity I is recorded as a function the absorbance A of the sample and n is the refractive index of the buffer solution. For the measurements

to be reliable and to minimize the non-uniform radiation, the samples concentration was less than 0.1 mg/mL. pSi-COOH microparticles were used as standard, whose QY was previously determine with respect to Rhodamine 101 and Fluorescein.

Structural and morphological characterization

- Size measurement (Dynamic light scattering)

The microparticles size distribution were analysed by Zetasizer Nano-SZ (Malvern) instrument, with a 633 nm laser beam. The size measurements were performed at 25 °C in ethanol, repeated three times and averaged. Before the measurements, the samples were sonicated in a thermal bath for 45 minutes to homogenize the samples and reduce the agglomeration.

- TEM (Transmission electron microscopy) – EDS (energy dispersive X-rays spectroscopy)

Dimension, shape and microparticles size were analysed by TEM imaging, with a Philips CM12 microscope operating at 120 keV, after depositing a drop of each sample (about 30 μL) on a copper grid coated with a perforated carbon film. The coupling to the EDS (Energy dispersion X-Ray) spectroscopy allows the chemical composition analysis. The integration spectrum relative to the diffraction pattern obtained by TEM was evaluated by using the software *ProcessDiffraction*.

- SEM (Scanning electron microscopy)

The morphology of the samples was studied by SEM Jeol JSM IT300 operating at 20 keV in high vacuum condition. The sample preparation consists in the deposition of a drop of each sample (about 30 μL) on a copper grid coated with a perforated carbon film.

Magnetic characterization

- MRI (magnetic resonance imaging)

The magnetic properties of the samples were investigated by using a *Pharmascan* system operating at 7 T (*Bruker, Germany*).

Each sample under investigation was prepared in different concentrations and stored in Eppendorf vials, which were placed in a polystyrene box, to be imaged at the same time. The longitudinal (T_1) and transversal (T_2) relaxation times were measured by acquiring a MSME (multi spin multi echo) pulse sequence [230]. It consists in a 90° excitation RF pulse, followed by repeated 180° refocusing pulses, separated by a constant interval or echo-time. The signals coming from each point of the images were mediated to obtain the relaxation curve decays, that were fitted with an exponential decay function to obtain the T_1 and T_2 values.

Afterward, the longitudinal and transversal relaxivities r_1 and r_2 were determined by plotting the relaxation rate against the sample concentration and fitting the data with the formula:

$$\frac{1}{T_i} = \frac{1}{T_{i,0}} + r_i \cdot c$$

APPENDIX A2: In-vitro cellular studies

Cytotoxicity and immune response evaluation

- alamarBlue® assay

The monocytes, dendritic cell and lymphocytes cell viability was evaluated using an alamarBlue® assay (Invitrogen, Thermo Fischer Scientific, Waltham, MA, USA) under the manufacturer's instructions. alamarBlue® is a colorimetric redox assay of metabolic activity, which contains a fluorescent blue dye (resazurin), that becomes highly pink fluorescent when it is reduced: the higher the emission, the higher the number of living cells. The cells were incubated for 24 hours with different microparticle concentrations, the reagent was added to the culture medium at 10% concentration and then, the absorbance was measured at 570 and 600 nm.

- ELISA assays

Enzyme-linked immunosorbent assay (ELISA) was used to estimate the cytokine production in culture supernatants: TNF-α, IL-6 and IL-12 presence was investigated. After DCs stimulation with microparticles (for 24 hours), the supernatants were collected. The protein levels of TNF-α (4–500 pg/mL), IL-6 (10–1000 pg/mL) and IL-12 (p70) (6–600 pg/mL) were tested by ELISA development kits purchased from Mabtech (Nacka Strand, Sweden). The plates were read at 450 nm using a *Perkin Elmer Victor 1420 Multilabel Counter (Waltham, MA, USA)*.

- Superoxide anion production

The superoxide anion production was evaluated by Cytochrome C reduction assay [231]. The cell culture medium is replaced with HBSS at pH 7.4, containing 80 mM ferricytochrome C and the required stimulus. The reduction of Cytochrome C was assessed by measuring the absorbance at 550 nm by *ELx808t Absorbance Microplate Reader (BioTek Instruments, Inc).*

The statistical analysis was performed by one-way ANOVA followed by the Dunnett's Multiple Comparison Test, by considering statistically significant the p-values lower than 0.05.

Cell imaging

- TEM (Transmission electron microscopy)

The up-taking of the pSi-TiO_2 microparticles by DCs was evaluated by TEM Morgagni 268D Electron microscope (Philips). The sample was prepared by 2 h fixation in 2% glutaraldehyde in Sorensen buffer (pH 7.4), 2 hours fixation in 1% OsO4 in aqueous solution, dehydrated in graded concentrations of acetone and then, embedded in an Epon–Araldite mixture (Electron Microscopy Sciences, Fort Washington, PA). The sample was cut into 1 mm-thick sections, examined by light microscopy and stained with toluidine blue. Then, ultrathin section, of about 70 nm, was cut and deposited on Cu/Rh grids by an Ultracut E (Reichert, Wien, Austria).

- Two photon absorption (2PA) experiments

The two photon absorption (2PA) experiments were performed by Multiphoton microscope TCS SP5 AOBS (Leica), with a Chameleon ULTRA II laser (Coherent) and a 20 objective, immersed in water, with a NA of 1, to verify if the microparticles were still luminescent after the cell internalization. The DCs incubated with pSi microparticles were washed with PBS and deposited on a microscope slide for the observation. The sample was observed by 488 nm laser in total reflection modality. The fluorescence images were obtained upon 700 nm excitation (perfectly matching the 350 nm excitation of standard PL measurements) and z-stack images were acquired and merged to obtain a maximum projection image.

APPENDIX B

Conferences contributions and schools

15th International Summer Schools on Nanotechnologies, Organic Electronics & Nanomedicine (ISSON21), 3-10 July 2021, Thessaloniki, Greece.

Summer School for Silicon Nanotechnology 2022, June 19th - August 19th 2022, San Diego, USA.

18th International Conference on Nanosciences & Nanotechnologies (NN21), 6-9 July 2021- Thessaloniki (Greece) with poster presentation on "Porous silicon microparticles for immune adjuvant delivery".

Conference NANOINNOVATION2021 (online) - 21-24 September 2021 - Rome with poster presentation on "Porous silicon microparticles for immunologic adjuvant delivery".

Conference Smart NanoMaterials 2021 (SNAIA2021) - 7th-10th of December 2021 - Paris (France) with oral presentation on "Porous silicon microparticles as a multimodal drug delivery system".

16th European Symposium on Controlled Drug Delivery (ESCDD22) - 13th - 15th of April 2022 Egmond Aan Zee (The Netherlands) with poster presentation on: "Organic and inorganic nanosystems for drug delivery in anticancer therapy"

Conference PSST (Porous Semiconductors – Science and Technology) 2022, 27th of March-1st of April 2022 – Lido di Camaiore (Italy) with two oral presentations on: "Magnetic nanospheres within porous silicon light emitting microparticles" and "Porous silicon microparticles for immune adjuvant delivery".

2022 Summer Research Conference (SRC) at UC San Diego, 11th - 12th of August 2022 - San Diego (CA, USA) with oral presentation on "Porous silicon nanoparticles coated with hyaluronic acid for targeted cancer therapy"